

## Accurate Modeling of Advanced Reflectarrays

**Zhou, Min; Breinbjerg, Olav; Jørgensen, Erik; Kim, Oleksiy S.**

*Publication date:*  
2013

*Document Version*  
Publisher's PDF, also known as Version of record

[Link back to DTU Orbit](#)

*Citation (APA):*  
Zhou, M., Breinbjerg, O., Jørgensen, E., & Kim, O. S. (2013). Accurate Modeling of Advanced Reflectarrays. Kgs. Lyngby: Technical University of Denmark (DTU).

## DTU Library

Technical Information Center of Denmark

---

### General rights

Copyright and moral rights for the publications made accessible in the public portal are retained by the authors and/or other copyright owners and it is a condition of accessing publications that users recognise and abide by the legal requirements associated with these rights.

- Users may download and print one copy of any publication from the public portal for the purpose of private study or research.
- You may not further distribute the material or use it for any profit-making activity or commercial gain
- You may freely distribute the URL identifying the publication in the public portal

If you believe that this document breaches copyright please contact us providing details, and we will remove access to the work immediately and investigate your claim.

# ACCURATE MODELING OF ADVANCED REFLECTARRAYS

---

Ph.D. Thesis  
Min Zhou  
October 2012



Supervisors:

Erik Jørgensen, Ph.D.  
Peter Meincke, Ph.D.  
TICRA

Olav Breinbjerg, Professor, Ph.D.  
Oleksiy S. Kim, Associate Professor, Ph.D.  
Electromagnetic Systems, DTU Elektro,  
Technical University of Denmark



# ABSTRACT

---

Analysis and optimization methods for the design of advanced printed reflector-arrays have been investigated, and the study is focused on developing an accurate and efficient simulation tool.

For the analysis, a good compromise between accuracy and efficiency can be obtained using the spectral domain method of moments (SDMoM) assuming local periodicity (LP) and the focus in this work has therefore been on this technique.

In the LP-SDMoM, several factors contribute to errors in the analysis and these include: the periodicity assumption, the assumption of infinite ground plane, the representation of the incident field, the choice of basis functions, and the technique to calculate the far-field. Based on accurate reference measurements of two offset reflectarrays carried out at the DTU-ESA Spherical Near-Field Antenna Test Facility, it was concluded that the three latter factors are particularly important for an accurate analysis. Solutions for these sources of error have been proposed, implemented, and validated.

Based on the techniques for the enhanced analysis, a generalized direct optimization technique (GDOT) has been developed. The GDOT is based on the LP-SDMoM and a minimax optimization algorithm. Contrary to the conventional phase-only optimization technique (POT), the geometrical parameters of the array elements are directly optimized to fulfill the far-field requirements, thus maintaining a direct relation between optimization goals and optimization variables. As a result, better designs can be obtained compared to the POT.

The GDOT can optimize for the size as well as the orientation and position of arbitrarily shaped array elements. Both co- and cross-polar radiation can be optimized for multiple frequencies, dual polarization, and several feed illuminations. Several contoured beam reflectarrays have been designed using the GDOT to demonstrate its capabilities. To verify the accuracy of the GDOT, two offset contoured beam reflectarrays that radiate a high-gain beam on a European coverage have been designed and manufactured, and subsequently measured at the DTU-ESA Spherical Near-Field Antenna Test Facility. An excellent agreement between the simulated and measured patterns is obtained, showing accuracies that are comparable to those obtained for shaped reflectors.





# RESUMÉ

---

Analyse- og optimeringsmetoder til design af avancerede printede reflectarray antenner er blevet undersøgt, og fokus er lagt på udvikling af et nøjagtigt og effektivt simuleringsværktøj.

Et hensigtsmæssigt kompromis mellem nøjagtighed og effektivitet af analysen kan opnås ved at anvende momentmetoden i den spektrale domæne (SDMoM) med antagelse af lokal periodicitet (LP), hvorfor fokus blev lagt på denne metode i dette arbejde.

Ved brugen af LP-SDMoM er der flere forhold, der fører til fejl og unøjagtighed i analysen af et fysisk reflectarray antenne. Disse omfatter antagelsen af periodicitet, jordplanets endelighed, repræsentation af det indfaldende felt, valg af basis funktioner samt metoden der anvendes til fjernfeltsberegning. Det kan konkluderes, at særligt de tre sidstnævnte forhold er afgørende for en nøjagtig analyse, hvilket er dokumenteret med referencemålinger fra DTU-ESA Spherical Near-Field Antenna Test Facility af to offset reflectarray antenner. Løsninger til disse fejlkilder er blevet foreslået, implementeret og valideret.

En direkte optimeringsmetode er udviklet på baggrund af de ovennævnte løsninger. Optimeringsmetoden er baseret på LP-SDMoM og en minimax optimeringsalgoritme. I modsætning til den konventionelle fase-optimeringsmetode, er de geometriske parametre for array-elementerne direkte optimerede for at opfylde fjernfeltskravene. Dermed bevares relationen mellem optimeringsvariable og -målsætninger. Som konsekvens heraf kan bedre antennedesigns opnås.

Den nævnte metode kan optimere størrelse, orientering og position af vilkårligt udformede array-elementer. De co- og krydspolariserede feltkomponenter kan optimeres for flere frekvenser, polarisationer samt for anvendelsen af flere fødehorn. En række reflectarray antenner, der belyser et geografisk afgrænset område er blevet designet ved hjælp af optimeringsmetoden og illustrerer metodens egenskaber. To offset reflectarray antenner, hvis dækning er afgrænset til netop at dække Europa, er blevet designet og fremstillet med henblik på at verificere metodens nøjagtighed. Disse antenner er efterfølgende målt på DTU-ESA Spherical Near-Field Antenna Test Facility. Der er en god overensstemmelse mellem simuleringer og målinger.



# PREFACE

---

The work presented in this thesis was carried out partly at TICRA and partly at the Electromagnetics Systems (EMS) group at the Department of Electrical Engineering at the Technical University of Denmark (DTU) between October 2009 and October 2012. The study was funded by TICRA with the support of the Danish Industrial Ph.D. program. However, the manufacturing and measurements of the reflectarray antennas were supported by the European Space Research and Technology Centre at the European Space Agency (ESA-ESTEC) under the ESTEC contract no. 4000101041.

There are many people to whom I wish to extend my gratitude. Especially, my supervisors at TICRA and DTU, Erik Jørgensen, Peter Meincke, Oleksiy S. Kim, and Olav Breinbjerg. With their extensive experience and knowledge within the area of antennas and electromagnetics, they have formed the ideal team. Without them, this work would not have been possible. A special thanks to Stig B. Sørensen for his invaluable assistance during the project. His support is highly appreciated and has been essential for the outcome of the project. I would also like to thank all of TICRA for accepting me as an industrial Ph.D. student and for giving me the opportunity to work at such a relaxed and special working environment, which greatly contributed to making the project much more enjoyable.

A number of other people have contributed to this work by providing reference measurements, valuable feedbacks, useful comments, and the manufacture of reflectarray antennas. From TICRA, Niels C. Albertsen, Niels Vesterdal, and Cecilia Cappellin, from DTU, Thomas G. Smith, Martin Nielsen, Frank Persson, Jan N. Mortensen, and Sergey Pivnenko, and from ESA-ESTEC, Giovanni Toso.

Finally, I thank my friends and family, especially Emilie, for the patience and constant support during this study.

Min Zhou, October 2012.



# CONTENTS

---

<b>Abstract</b>	<b>i</b>
<b>Resumé</b>	<b>iii</b>
<b>Preface</b>	<b>v</b>
<b>Contents</b>	<b>vii</b>
<b>List of Publications</b>	<b>xi</b>
<b>1 Introduction</b>	<b>1</b>
<b>2 Reflectarray Analysis</b>	<b>5</b>
2.1 Survey . . . . .	5
2.2 Reflectarray Measurement Campaign I . . . . .	7
2.2.1 Reflectarray Samples . . . . .	8
2.3 Sources of Error . . . . .	10
2.3.1 Incident Field . . . . .	11
2.3.2 Basis Functions . . . . .	12
2.3.3 Far-field Calculations . . . . .	15
2.3.4 Infinite Ground Plane . . . . .	19
2.3.5 Periodicity . . . . .	20
2.4 Summary . . . . .	21
<b>3 Reflectarray Optimization</b>	<b>23</b>
3.1 Survey . . . . .	23
3.2 Generalized Direct Optimization Technique . . . . .	25
3.2.1 Optimization Procedure . . . . .	25
3.2.2 Incident Field . . . . .	27
3.2.3 Basis Functions . . . . .	27

3.2.4	Far-field Calculations . . . . .	27
3.2.5	Irregularly Positioned Array Elements . . . . .	27
3.2.6	Scattering Matrix Look-Up Table . . . . .	29
3.2.7	Spline Representation . . . . .	31
3.3	Reflectarray Designs . . . . .	31
3.3.1	Single-Polarized Broadband Design . . . . .	32
3.3.2	Dual-Polarized Broadband Design . . . . .	33
3.3.3	Circularly Polarized Design . . . . .	35
3.3.4	Electrically Large Design . . . . .	36
3.4	Reflectarray Measurement Campaign II . . . . .	37
3.4.1	Reflectarray Samples . . . . .	38
3.4.2	Simulations Versus Measurements . . . . .	39
3.5	Summary . . . . .	44
<b>4</b>	<b>Conclusions</b>	<b>45</b>
	<b>Appendices</b>	<b>51</b>
<b>A</b>	<b>Design of the Reflectarray Samples</b>	<b>51</b>
A.1	Geometrical and Electrical Parameters . . . . .	51
A.2	Measurement Campaign I . . . . .	52
A.2.1	Sample I-I . . . . .	52
A.2.2	Sample I-II . . . . .	53
A.2.3	Feed Horns . . . . .	54
A.3	Measurement Campaign II . . . . .	54
A.3.1	Choice of Design . . . . .	55
A.3.2	Sample II-I . . . . .	57
A.3.3	Sample II-II . . . . .	59
<b>B</b>	<b>Measurement Results</b>	<b>61</b>
B.1	Measurement Campaign I . . . . .	61
B.2	Measurement Campaign II . . . . .	66
<b>C</b>	<b>Spectral Domain MoM for Periodic Multilayer Configurations</b>	<b>69</b>
C.1	Configuration . . . . .	69
C.2	Outline of the Formulation . . . . .	69
C.3	SDMoM Formulation . . . . .	72
C.3.1	Periodic Multilayer Configuration . . . . .	72

C.3.2	Setting up the MoM Equation . . . . .	80
C.3.3	Scattering due to Propagating Floquet Harmonics . . . . .	83
<b>D</b>	<b>Fourier Transforms of Basis Functions</b>	<b>85</b>
D.1	Higher-order Hierarchical Legendre Basis Functions . . . . .	85
D.2	Singular Basis Functions weighted by Chebyshev Polynomials . . . . .	86
<b>E</b>	<b>SEA and ELP</b>	<b>89</b>
E.1	Surrounded Element Approach . . . . .	89
E.2	Extended Local Periodicity . . . . .	91
<b>F</b>	<b>Integral Equation Formulation for Grounded Dielectric Slab</b>	<b>97</b>
F.1	Integral Equation Formulation . . . . .	97
F.2	Vector and Scalar Potential Green's Functions . . . . .	98
F.3	Computation of the Vector and Scalar Potential Green's Functions	100
F.3.1	Discrete Complex Image Method . . . . .	101
F.3.2	Asymptotic Behavior of $\mathcal{R}_{\text{TM}}$ . . . . .	102
F.3.3	Validation of the DCIM . . . . .	103
F.4	Other Formulations of the Spatial Green's Functions . . . . .	103
<b>Publications</b>		<b>107</b>
<b>Paper I</b>		<b>107</b>
<b>Paper II</b>		<b>113</b>
<b>Paper III</b>		<b>119</b>
<b>Paper IV</b>		<b>131</b>
<b>Conference Paper I</b>		<b>145</b>
<b>Conference Paper II</b>		<b>155</b>
<b>Bibliography</b>		<b>165</b>





# LIST OF PUBLICATIONS

---

The following publications have been prepared during the study: journal papers [J1–J4], conference papers [C1–C5], and technical reports [R1–R5]. The journal papers [J1–J4] and conference papers [C2, C5] are included in the last part of the thesis on pages 107–164.

## Journal Publications

- [J1] M. Zhou, S. B. Sørensen, E. Jørgensen, P. Meincke, O. S. Kim, and O. Breinbjerg, “An accurate technique for calculation of radiation from printed reflectarrays,” *IEEE Antennas Wireless Propag. Lett.*, vol. 10, pp. 1081–1084, 2011.
- [J2] M. Zhou, E. Jørgensen, O. S. Kim, S. B. Sørensen, P. Meincke, and O. Breinbjerg, “Accurate and efficient analysis of printed reflectarrays with arbitrary elements using higher-order hierarchical Legendre basis functions,” *IEEE Antennas Wireless Propag. Lett.*, vol. 11, pp. 814–817, 2012.
- [J3] M. Zhou, S. B. Sørensen, O. S. Kim, E. Jørgensen, P. Meincke, and O. Breinbjerg, “Direct optimization of printed reflectarrays for contoured beam satellite antenna applications,” *Submitted to IEEE Trans. Antennas Propag.*, 2012.
- [J4] M. Zhou, S. B. Sørensen, O. S. Kim, E. Jørgensen, P. Meincke, O. Breinbjerg, and G. Toso, “The generalized direct optimization technique for printed reflectarrays,” *Submitted to IEEE Trans. Antennas Propag.*, 2012.

## Conference Publications

- [C1] M. Zhou, S. B. Sørensen, E. Jørgensen, P. Meincke, O. S. Kim, and O. Breinbjerg, “Analysis of printed reflectarrays using extended local periodicity,” in *Proc. EuCAP*, Rome, Italy, 2011.
- [C2] M. Zhou, S. B. Sørensen, O. S. Kim, S. Pivnenko, and G. Toso, “Investigations on accurate analysis of microstrip reflectarrays,” in *Proc. 33rd ESA Antenna Workshop*, Noordwijk, The Netherlands, 2011.

- [C3] M. Zhou, S. B. Sørensen, P. Meincke, E. Jørgensen, O. S. Kim, O. Breinbjerg, and G. Toso, “Design and analysis of printed reflectarrays with irregularly positioned array elements,” in *Proc. EuCAP*, Prague, Czech Republic, 2012.
- [C4] —, “Design of dual-polarized contoured beam reflectarrays with cross-polar and sidelobe suppressions,” in *Proc. IEEE AP-S Int. Symp.*, Chicago, Illinois, USA, 2012.
- [C5] —, “An accurate and efficient design tool for large contoured beam reflectarrays,” in *Proc. ESA Workshop on Large Deployable Antennas*, Noordwijk, The Netherlands, 2012.

## Reports

- [R1] S. B. Sørensen, N. C. Albertsen, and M. Zhou, “Advanced Reflectarray Antennas, WP1000 report,” TICRA, Copenhagen, Denmark, Tech. Rep. S-1529-09, November 2010.
- [R2] —, “Advanced Reflectarray Antennas, WP3000 report,” TICRA, Copenhagen, Denmark, Tech. Rep. S-1529-13, March 2012.
- [R3] S. B. Sørensen, N. C. Albertsen, P. E. Frandsen, and M. Zhou, “Advanced Reflectarray Antennas, WP5000 report,” TICRA, Copenhagen, Denmark, Tech. Rep. S-1529-15, March 2012.
- [R4] S. B. Sørensen and M. Zhou, “Advanced Reflectarray Antennas, WP6000 report,” TICRA, Copenhagen, Denmark, Tech. Rep. S-1529-17, March 2012.
- [R5] S. B. Sørensen, N. C. Albertsen, P. E. Frandsen, and M. Zhou, “Advanced Reflectarray Antennas, Final report,” TICRA, Copenhagen, Denmark, Tech. Rep. S-1529-18, April 2012.

# INTRODUCTION

---

Printed reflectarrays provide a way for realizing low-cost, high-gain antennas for space applications and are the subject of increasing research interest [1–4]. The reflectarray combines some of the best features of the reflector antenna and the array antenna. It usually consists of a flat surface with many printed elements and a feed antenna that illuminates the surface. The printed elements are designed to reflect the incident field such that a desired far-field can be achieved.

The reflectarray eliminates the need for the bulky, expensive, and relatively high-loss feeding network required by conventional array antennas, as well as the requirement of curved surfaces in conventional reflector antennas. Reflectarrays are light, easy and cheap to manufacture, and can be packed more compactly.

The key feature of reflectarray design is how the individual array elements are designed to reflect the incident field with electrical phases that form a given far-field. The first reflectarray was proposed several decades ago by Berry et al. [5] where short-ended waveguides with variable lengths were used to achieve the required phases. The printed reflectarray was introduced in [6] and due to the rapid development of printed antenna technology and the need for low-cost high-gain antennas, printed elements have been the preferred choice in reflectarray configurations.

One method to adjust the electrical phase of the reflected field is to utilize identical microstrip patches with stubs of variable length [7–14]. These phase delay stubs are designed to compensate for the phase differences of the different path lengths from the illuminating feed. Thus with appropriate stub-lengths, a given phase distribution over the reflectarray surface can be obtained to form the required far-field.

Another approach to control the phase is to employ printed elements with variable sizes [15–19]. By adjusting the size of each printed element, a small shift in the resonant frequency is introduced, thus changing the phase of the reflected field. Many types of printed elements can be employed, e.g. variable-sized loops [20], crossed dipoles [21], patches loaded with slots [22], etc.

In the last decade, research and development of reflectarrays have gained momentum and a large number of advanced reflectarrays has been designed. The capabilities for reflectarrays include circular polarized reflectarrays [23–26], dual/multi-band reflectarrays [26–34], variable polarized reflectarrays [35], shaped/contoured beam [36–41] and multi-beam [42, 43] reflectarrays, amplifying [44] and reconfigurable [45–53] reflectarrays, folded compact reflectarrays [54–57], inflatable reflectarrays [58, 59], etc. Despite these advanced capabilities, reflectarrays have not yet gained widespread acceptance for space applications, and conventional reflectors are still the preferred choice for satellite communications. This is presumably due to two reasons: the narrow bandwidth, and the lack of accurate design tools.

The bandwidth of printed reflectarrays is controlled by two main factors: the bandwidth of the array element, and the bandwidth limitation introduced by the differential spatial phase delay from the feed [60, 61]. The differential spatial phase delay is due to the different electrical path length the incident field must propagate before impinging the reflectarray surface. These delays are compensated by an appropriate phase delay at each array element by using the aforementioned phasing arrangements. However, the design and the compensating phase for each element are often fixed for the center frequency, thus as the frequency varies, a frequency excursion error will occur and the required phase for each array element will be incorrect, resulting in narrowband performance. While the differential spatial phase delay is the limiting factor for reflectarrays of large electrical sizes ( $> 50$  wavelengths) and small focal distance to diameter (F/D) ratios, the bandwidth of the array elements is the dominating factor for smaller reflectarrays.

Recent developments circumvent the bandwidth issue by designing multi-resonance array elements e.g. stacked multiple patches [62, 63], loop/ring elements [64–71], aperture-coupled patches [72–74], subwavelength array elements [75–78], and other types of broadband element shapes [79–84]. To alleviate the differential spatial phase delay limitation, true-time delay lines [85] and a parabolic reflectarray surface [86] have been suggested.

Most of the solutions listed above do not attempt to solve the bandwidth limitation by means of simulation tools, as the existing design tools for reflectarrays are inadequate compared to those for conventional reflector and array antennas, both in terms of accuracy and capability.

To ensure high-gain performance, the electrical size of reflectarrays is usually very large and full-wave analysis on the entire reflectarray sets prohibitively heavy computational requirements. In addition, several degrees of freedom can be utilized in printed reflectarrays to obtain a certain antenna performance, e.g. the size [15, 17, 62], the shape [64, 79, 81, 87], the orientation [23, 25, 29], and the position [88, 89] of the array elements, as well as the surface [86] of

the reflectarray. Thus, an accurate and efficient design procedure, capable of including all these parameters, is a demanding task.

The commonly adopted analysis method for printed reflectarrays is based on a spectral domain method of moments (SDMoM) [90–92]. Each element in the reflectarray is analyzed by assuming local periodicity (LP), that is, the individual array element is analyzed assuming it is located in an infinite array of identical elements [17]. Using this approach, mutual coupling effects are accounted for and it is a fairly accurate approximation when the variation in element dimensions is smooth from one cell to the adjacent cells [1, p.32].

Although the LP-SDMoM is efficient and many advanced reflectarrays have been designed using this approach, the technique currently can not reach the analysis accuracy of conventional reflector and array modeling algorithms. Without an accurate simulation tool, genuine routines for optimizing reflectarrays are not available.

The primary objective of this work is to develop an accurate yet efficient simulation tool for the design of passive printed reflectarrays with a level of accuracy that is customary for conventional reflector and array antennas.

As a first step in the process, existing modeling techniques are investigated and reference measurements on simple reflectarray antennas are conducted at the DTU-ESA Spherical Near-Field Antenna Test Facility [93]. The purpose of this preliminary study is to obtain an overview of the existing modeling techniques, but also to provide the fundamental knowledge needed to identify the main reasons for the lack of accuracy in current reflectarray modeling. Based on this study, techniques to enhance the modeling accuracy will be proposed, tested, and verified. These improvements are subsequently implemented in an optimization tool for the design of printed reflectarrays. The developed optimization tool should be able to optimize both co- and cross-polar radiation patterns for multiple frequencies, dual polarization, and several feed illuminations. It should include the optimization of several geometrical parameters as well as being applicable for the design of electrically large reflectarrays. It is expected that such an enhanced simulation tool can improve the bandwidth and the performance of printed reflectarrays, and thereby also their usability.

This thesis is intended to provide an overview of the most important results obtained during the study. The main outcome of the study has been documented in the six papers [J1–J4] and [C2, C5] according to the list of publications on page xi, which are included in the last part of the thesis. While the overview summarizes the main contributions presented in the papers, it also contains results and discussions which are not covered in the papers. In addition, three conference papers [C1, C3, C4], have been prepared during the study, but are not included in this thesis. Furthermore, the author has contributed to five technical reports [R1–R5]. A list of these works can be found on page xi.

The thesis is organized as follows: Following the present introduction in Chapter 1, Chapter 2 deals with the analysis of printed reflectarrays. A survey of existing modeling techniques for printed reflectarrays is presented and the main sources of error in current reflectarray modeling are identified. Techniques to reduce these errors are proposed and verified by means of accurate measurements of reference reflectarrays designed specifically for this purpose. These improvements are subsequently implemented in an optimization routine, which is described in Chapter 3. Herein, the analysis and optimization methods used in the optimization technique are briefly reviewed, followed by the description of several advanced reflectarrays, which are designed to demonstrate the capabilities of the new optimization technique. Two offset contoured beam reflectarrays have been designed, manufactured, and measured, and simulations and measurements are presented in this chapter. Conclusion and suggestions for future work are given in Chapter 4. In addition to these chapters, a series of appendices are included followed by selected publications that have been prepared during the study.

The techniques presented in this work have been implemented into the TICRA software packages GRASP [94] and POS [95], thus the capabilities of these software packages were available and integrated with the techniques in this work.

Throughout the thesis the harmonic time dependence  $e^{j\omega t}$ , with  $\omega = 2\pi f$  being the angular frequency, is assumed and suppressed.

## REFLECTARRAY ANALYSIS

---

This chapter deals with the analysis of printed reflectarrays. First, a survey of the existing modeling techniques is presented. This survey serves the purpose of providing an overview of the existing modeling techniques as well as to identify the main sources of error in the analysis of printed reflectarrays. To investigate these sources, two reflectarrays are designed and manufactured, and subsequently measured at the DTU-ESA Spherical Near-Field Antenna Test Facility. These reflectarrays are intentionally designed to exaggerate some of the sources of error such that they can be separated. Based on these measurements, techniques that enhance the modeling accuracy are proposed, tested, and verified.

The contents of this chapter will provide the necessary background for the implementation of the accurate and efficient optimization technique presented in Chapter 3.

The most significant parts of the work in this chapter are presented in papers [J1, J2], [C1] and summarized in [C2]. Papers [J1, J2] are included in the thesis as Paper I and Paper II, respectively, and [C2] as Conference Paper I.

### 2.1 Survey

Numerous techniques to analyze reflectarrays have been presented in the literature. The most common procedure is to analyze each array element separately and sum the element contributions to determine the overall performance of the entire reflectarray.

In the early designs, the analysis of each array element was done without including the neighboring elements, thus mutual coupling was neglected [9, 10, 13, 14, 96]. These results can be used to get a rough estimate of the radiation properties, but in order to obtain an accurate prediction, the mutual coupling has to be included in the analysis.

The LP approach [17] is the commonly adopted approach to account for the mutual coupling in printed reflectarrays. Here, each array element is analyzed



assuming that the individual element is located in an infinite array of identical elements. The advantage of the LP approach is that the problem is restricted to a single periodic unit-cell, thus reducing the complexity of the problem and thereby also the computation time.

Different numerical methods can be used to solve the periodic problem e.g. finite element method (FEM) [97], or finite difference time domain (FDTD) [98]. For printed reflectarrays, the periodic problem is usually formulated in terms of an integral equation and solved by the SDMoM [90–92]. This approach has proven to be very efficient, and is therefore the most popular choice in printed reflectarrays [15–17, 20, 28, 36–40, 42, 57, 62, 63, 73–75, 99, 100]. Although the LP-SDMoM is very efficient and several advanced reflectarrays have been designed using this approach, a realistic reflectarray is not periodic and hence the assumption of periodicity can be inaccurate. In addition to the periodicity assumption, other sources of error, e.g. the representation of the incident field, and the choice of basis functions, also exist.

To account for the lack of periodicity, an approach called the surrounded-element approach (SEA) was presented in [101, 102]. It includes the actual neighboring elements that surround the element under consideration, thus accounting for the mutual coupling more realistically. The analysis in [101, 102] was based on a FDTD implementation assuming plane wave incidence, and many neighboring elements were required to obtain an accurate result. Even though the mutual coupling is accounted for in a realistic way, the reported computation time was in terms of hours, and thus not suitable for optimization. A similar approach was presented in [103], where the commercial software FEKO was used to analyze the array element and its neighboring elements.

In the LP-SDMoM, each array element is assumed to be illuminated by a locally plane wave. The pattern of the feed is usually approximated by a far-field model using a  $\cos^q(\theta)$  function or a Gaussian beam [1, Sec. 3.8]. This pattern is used to compute the polarization, amplitude, and phase of the incident plane wave on each array element. It was shown in [104] that the accuracy of the analysis can be improved by using the near-field of the feed, obtained either by measurements or an accurate commercial software. In addition, the scattered field depends on the incidence angle [16, 19], hence to accurately predict the response of the array elements, the real incidence angle should be used.

Suitable basis functions must be selected in the LP-SDMoM to ensure an accurate and efficient analysis. For canonically shaped array elements, e.g. rectangular patches, the common choices are non-singular entire domain basis functions, e.g. trigonometrical basis functions. For arbitrarily shaped elements, the electric currents on the array elements are usually represented by non-singular first-order basis functions, e.g. Rao-Wilton-Glisson (RWG) [105] or rooftop [106] basis functions. Alternatively, a set of non-singular entire-domain basis functions

can be determined for arbitrarily shaped patches by using the boundary integral-resonant mode expansion (BI-RME) method as described in [79, 107]. However, it was shown in [108] that non-singular basis functions tend to have poor convergence rates and can in certain cases give inaccurate results. Thus, singular basis functions with the correct edge conditions, reproducing the singular behavior of the electric currents at the edges, are required to ensure accurate results.

Due to the periodicity assumption in the LP approach, the truncation of the ground plane is not taken into account and an infinite ground plane is assumed when calculating the currents on the array elements. It is expected that this assumption can have an effect on the accuracy of the analysis of the array elements at the edges of the reflectarray. This effect has received little attention in the literature, presumably due to its small contribution in electrically large reflectarrays. Nevertheless, this should be investigated and verified.

As an alternative to the techniques described above, efficient full-wave method of moments (MoM) techniques have been applied on entire reflectarrays for the accurate determination of the electric currents on the array elements [109–112]. These techniques take into account the exact mutual coupling between the array elements and therefore require heavy computational power. These full-wave techniques are appropriate for an accurate analysis of the reflectarray, but the large computation time and memory requirements make them unsuitable for optimization processes.

In the works cited above, the main focus has been on the accurate determination of the currents on the array elements, while the calculation of the far-field has received very little attention. However, the latter is equally important. Some of the few reported techniques in the literature include approximate formulas based on array element summations [10, 17, 72] and the field equivalence principle [42, 103, 113]. As will be shown later, the technique used to calculate the far-field is very important for an accurate analysis.

Several research groups have used commercial software for the analysis and design of printed reflectarrays, e.g. HFSS [22, 24, 29–31, 52, 65–70, 82, 83, 114–120], CST [64, 71, 121, 122], FEKO [103, 123], and Ansoft Designer [44, 49, 72]. Several of these electromagnetic software packages incorporate the possibility of applying periodic boundary conditions, thus allowing the use of the LP assumption. However, these general-purpose codes are slow and impractical for the analysis and design of a reflectarray antenna.

## 2.2 Reflectarray Measurement Campaign I

To serve as reference solutions for the results presented in this chapter, two offset pencil beam reflectarray samples have been measured at the DTU-ESA Spherical Near-Field Antenna Test Facility. The reflectarray samples are de-

signed to exaggerate some of the sources of error that are presented in Section 2.3 such that they can be separated.

In this section, the reflectarray samples are briefly described. For more details on the design and measurements of the samples, the reader is referred to Appendix A and Appendix B, respectively.

### 2.2.1 Reflectarray Samples

The mask layouts of the two reflectarray samples are shown in Figure 2.1.

The reflectarray in Figure 2.1a (sample I-I) is designed to exaggerate the incorrect analysis of the elements at the edges of the reflectarray due to assumption of infinite ground plane. To achieve this, a strong edge illumination is required and the error introduced by the periodicity assumption must be reduced, so as not to influence the conclusions. To this end, a smooth patch variation is obtained by reducing the differential spatial phase delay by placing the feed far from the reflectarray surface, and by having the main beam directed towards the specular direction.

The reflectarray in Figure 2.1b (sample I-II) is designed to exaggerate the errors introduced by the periodicity assumption by having a pencil beam towards  $\theta = 35^\circ$  and  $\phi = 135^\circ$  in the coordinate system shown in Figure 2.2. To ensure that the effects due to the truncation of the ground plane are negligible, the feed is located close to the reflectarray surface such that a low edge illumination can be achieved with a high-gain feed.

As feeds, two horn antennas were used: a corrugated horn, and a Potter horn. Each horn was used with both reflectarrays giving a total of four different reflectarray configurations to be measured.

The reflectarrays and their support structures were manufactured by the mechanical workshop at the Electromagnetics Systems (EMS) group at the Department of Electrical Engineering at the Technical University of Denmark (DTU). For the manufacturing accuracy of the reflectarrays and their support structures, requirements such as the planarity of the reflectarrays, the deviations of the support structures in the gravity field under rotation during the spherical measurements, the deviations of the feed horn pointing and position, have been specified. Due to the large weight of the corrugated feed horn, it was concluded that the most appropriate way to fulfill the manufacturing requirements was to mount the feed horn on the mounting frame, see Figure 2.3. Simulations of the mechanical deformations in the gravity field were carried out at the mechanical workshop and showed that the structures comply with the mechanical requirements.

The reflectarray samples were measured at a series of frequencies from 9.6 GHz to 10.5 GHz for two orthogonal polarizations, H- and V-polarization. H-polarization

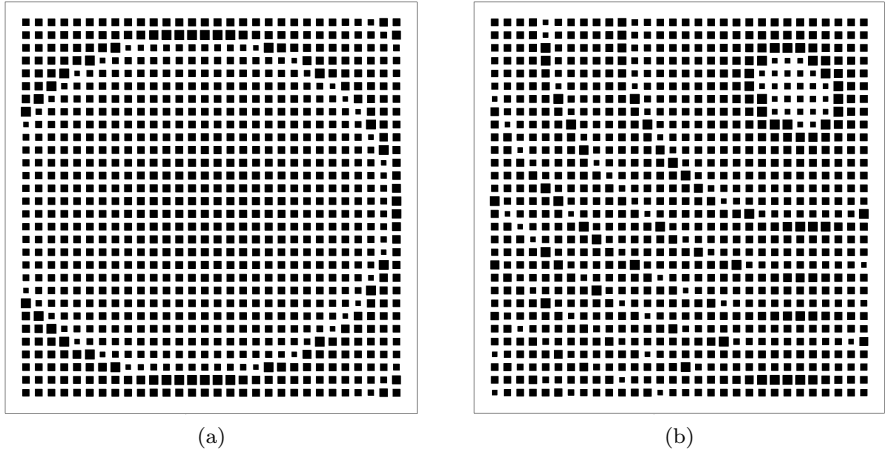


**Figure 2.1** The mask layout of the reflectarrays samples for measurement campaign I, (a) sample I-I and (b) sample I-II.

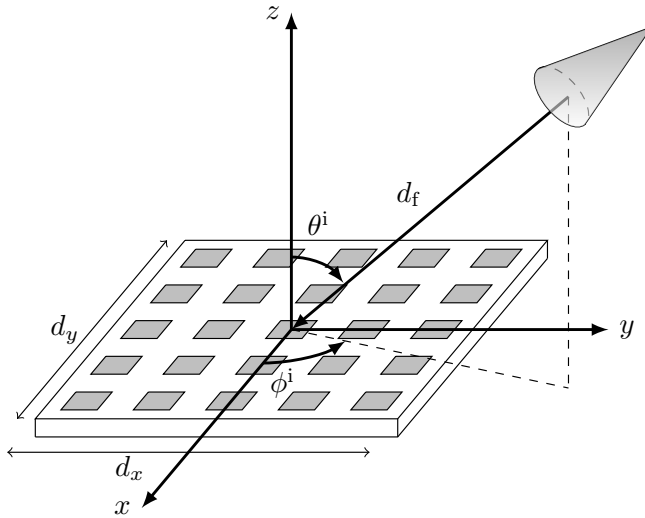


**Figure 2.2** Reflectarray geometrical parameters.

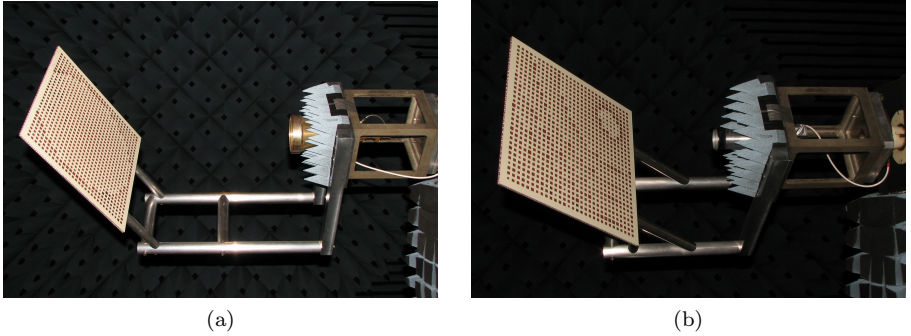


**Figure 2.3** Reflectarray (a) sample I-I and (b) sample I-II at the DTU-ESA Spherical Near-Field Antenna Test Facility.

is defined to be in the  $xz$ -plane in Figure 2.2 and V-polarization in the orthogonal plane. The measurement results will be shown and discussed in the following sections.

## 2.3 Sources of Error

Based on the survey in Section 2.1, it is deemed that a good compromise between accuracy and efficiency can be obtained using the LP-SDMoM, and it is therefore considered as the most suitable technique for optimization purposes. Thus, the focus in this work has been on this technique.

An integral equation (IE) for periodic multilayer configurations has been formulated, where the Green's function in the IE consists of a double summation of Floquet harmonics [90–92]. An SDMoM routine was implemented and integrated into the GRASP MoM add-on. The existing geometry handling in the MoM add-on is used and extended to reflectarray configurations. A detailed description of the IE formulation and the SDMoM is provided in Appendix C.

In the LP-SDMoM, several factors contribute to errors in the analysis of printed reflectarrays. These include: the representation of the incident field, the choice of basis functions, the periodicity assumption, the assumption of infinite ground plane, and the technique used to calculate the far-field. These factors should be correctly accounted for to obtain an accurate analysis and will be treated in the following.

All radiation patterns presented in this section are shown in a coordinate system defined with its  $z$ -axis directed in the main beam direction. For the simulations, unless otherwise stated, the LP-SDMoM is used, measured feed patterns

are used to represent the incident field (see Section 2.3.1), higher-order Legendre basis functions are applied in the SDMoM (see Section 2.3.2), and the far-field is calculated using the continuous spectrum technique (see Section 2.3.3). To account for the presence of the support structures, the struts have been analyzed using the GRASP MoM add-on, see Figure 2.4, and the scattering from these is included in the radiation patterns.

### 2.3.1 Incident Field

In the LP-SDMoM, each array element is assumed to be illuminated by a locally plane wave. The pattern of the feed is usually approximated by a far-field model using a  $\cos^q(\theta)$  function or, for e.g. corrugated horns, a Gaussian beam [1, Sec. 3.8]. This idealized pattern is used to compute the polarization, amplitude, and phase of the incident plane wave on each array element.

The analysis accuracy can be improved by using the real pattern of the feed obtained by either measurements or commercially available simulation tools e.g. CHAMP [104]. This is also illustrated in Figure 2.5. In this figure, the simulated (red and blue) and measured (black) radiation pattern from sample I-II when illuminated by the corrugated horn are shown. In the red curve, the feed is approximated by a Gaussian beam with a taper of  $-17.5$  dB at  $30^\circ$ , whereas in the blue curve the measured feed pattern is used. For the latter, spherical wave expansions of the measured feed patterns are used to compute the polarization, amplitude, and phase of the incident plane wave on each array element. It is seen that an improved accuracy is obtained using the measured feed pattern, both in the prediction of the peak directivity and the sidelobes. The measured peak directivity is 29.4 dBi, whereas 29.7 dBi and 29.4 dBi are predicted using the Gaussian beam and the measured pattern, respectively. Even though sample I-II is a rather aperiodic design, the accuracy obtained using the LP-SDMoM is very good.

Although the accuracy for this case is very good, the assumption of plane wave incidence in the LP-SDMoM is only valid if the reflectarray surface is located sufficiently far away from the feed. Alternatively, a plane wave expansion

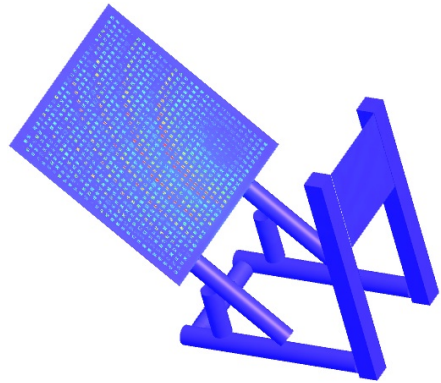


**Figure 2.4** *Electrical currents on sample I-II and its support structures.*

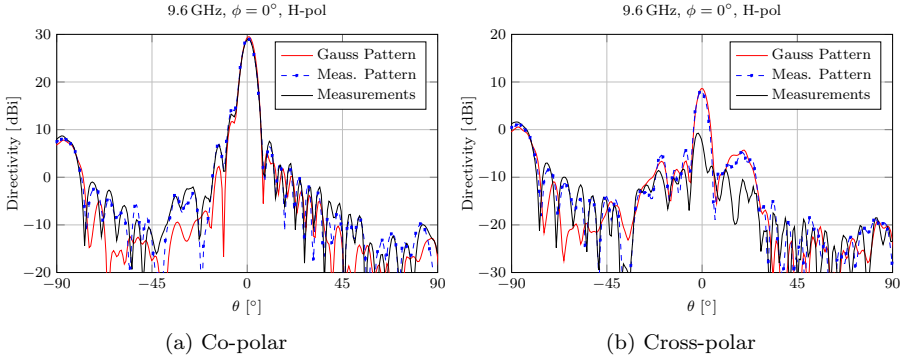


**Figure 2.5** Simulated and measured radiation pattern from sample I-II with the corrugated horn as feed. In the red curve, a Gaussian beam is used to approximate the feed pattern, whereas the measured feed pattern is used in the blue curve.

(PWE) of the feed radiation over the reflectarray surface can be computed. The LP-SDMoM analysis is then performed for each plane wave and subsequently added to yield the final result. In this approach, the representation of the incident field is exact, but the overall computation becomes very time consuming. This approach was used on both samples and the results were compared to the results obtained using the plane wave incidence assumption. Identical results were obtained, both for the corrugated horn and the Potter horn, thus validating the plane wave incidence assumption for both cases.

### 2.3.2 Basis Functions

In the LP-SDMoM, the spectral representation of the basis functions is required rather than their spatial form. To ensure an accurate and efficient result, suitable basis function must be selected to minimize the number of basis functions ( $N_b$ ) as well as the number of Floquet harmonics ( $N_f$ ).

Generally, the electric currents on the array elements are modeled by non-singular basis functions e.g. trigonometric or rooftop basis functions. However, for resonant printed elements, the convergence of the SDMoM solution becomes poor and in certain cases convergence is never achieved using these non-singular basis functions [108]. The latter is particularly true for very thin substrates with thickness below  $0.05\lambda$ , with  $\lambda$  being the wavelength in the dielectric substrate. Consequently, singular basis functions with the correct edge condition, reproducing the singular behavior of the electric currents at the edges, are required

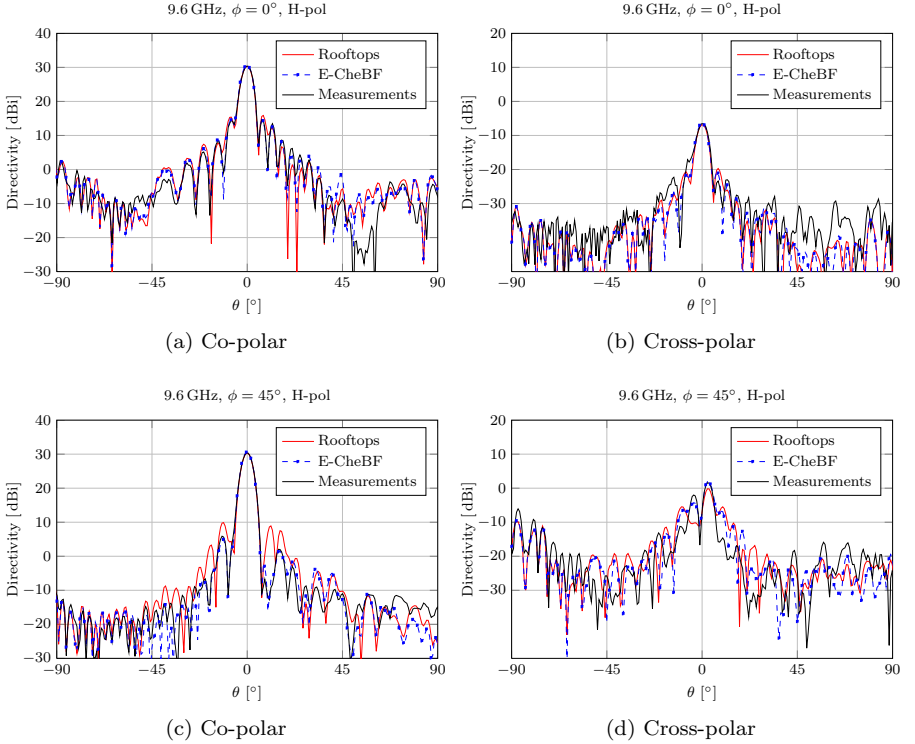


**Figure 2.6** Simulated and measured radiation pattern from sample I-I with the corrugated horn as feed. Rooftops (red) and E-CheBFs (blue) are used in the LP-SDMoM simulations.

for the accurate modeling of the unknown currents [108]. This is also illustrated in Figure 2.6, where the radiation pattern of sample I-I when illuminated by the corrugated horn is shown.

The analysis is done using rooftops (red) and the entire domain singular basis functions weighted by Chebyshev polynomials of first and second kind (E-CheBF) from [124] (blue). For the rooftops,  $\lambda_0/50 \times \lambda_0/50$  subdomain mesh elements are used, where  $\lambda_0$  is the free-space wavelength. This resulted in approximately 300 rooftop basis functions per array element, whereas 18 basis functions are used per array element for the E-CheBFs.

It is seen in Figure 2.6 that the accuracy of the rooftops is good in the  $\phi = 0^\circ$  plane, yielding a pattern close to that obtained using E-CheBFs. However, they are inaccurate in the  $\phi = 45^\circ$  plane. This is due to the thin substrate



(approximately  $0.045 \lambda$ ) used in the sample. A similar observation was made for sample I-II.

Although the entire domain singular basis functions are very accurate and efficient with respect to  $N_b$ , the value of  $N_f$  is high. Owing to their singular behavior, the Fourier spectrum is wide, thus increasing  $N_f$ , and thereby the overall computation time. In addition, entire domain singular basis functions are not easily applied to arbitrarily shaped array elements and one often has to resort to first-order basis functions e.g. RWG and rooftops, which can give inaccurate results. To circumvent these issues, higher-order hierarchical Legendre basis functions (LegBF) as described in [125] can be used. The LegBFs have several advantages, which will be outlined in the following.

The LegBFs are subdomain non-singular basis functions. For array elements where the shape can be described using a single mesh element, e.g. rectangular patches, the LegBFs can be defined on the entire patch, hence becoming entire domain basis functions.

The LegBFs do not possess the singularity behavior at the edges of the array elements. However, contrary to first-order basis functions, they have good convergence properties. This was demonstrated in [J2] where the LegBFs are compared to rooftops, the entire domain singular basis functions weighted by sinusoidal functions (E-SinBF) from [108], and the E-CheBFs. It was shown that the singular basis functions have a superior convergence rate with respect to  $N_b$ , whereas higher  $N_b$  was required for the LegBFs to obtain the same accuracy. For the rooftops, the same accuracy can not be obtained.

Although the convergence rate of the LegBFs with respect to  $N_b$  is lower compared to the singular basis functions, they have better convergence regarding  $N_f$ . In [J2], the LegBFs and E-CheBFs were applied in the analysis of sample I-I and it was shown that  $N_f$  for the E-CheBFs was more than 5 times larger than for the LegBFs. The overall computation times for E-CheBFs and LegBFs were 25 and 17 seconds, respectively, on a 2.8-GHz Intel processor laptop. The radiation pattern obtained using the two types of basis functions were practically identical and very close to the measured pattern. Thus, the LegBFs are capable of giving results of the same accuracy as those obtained using singular basis functions with less computation time. This is also demonstrated for sample I-II in Figure 2.7, where the Potter horn has been used as feed. The simulated results are very close to each other, and agree very well with the measurements, despite the reflectarray being highly aperiodic.

In addition to their good convergence properties and narrow Fourier spectrum, the LegBFs can be applied to any arbitrarily shaped array element. The choice of element shape is often dictated by requirements such as bandwidth and polarization, and much research has been carried out to investigate the performance of different element shapes [29, 64, 81, 84, 87, 114], see Figure 2.8. The

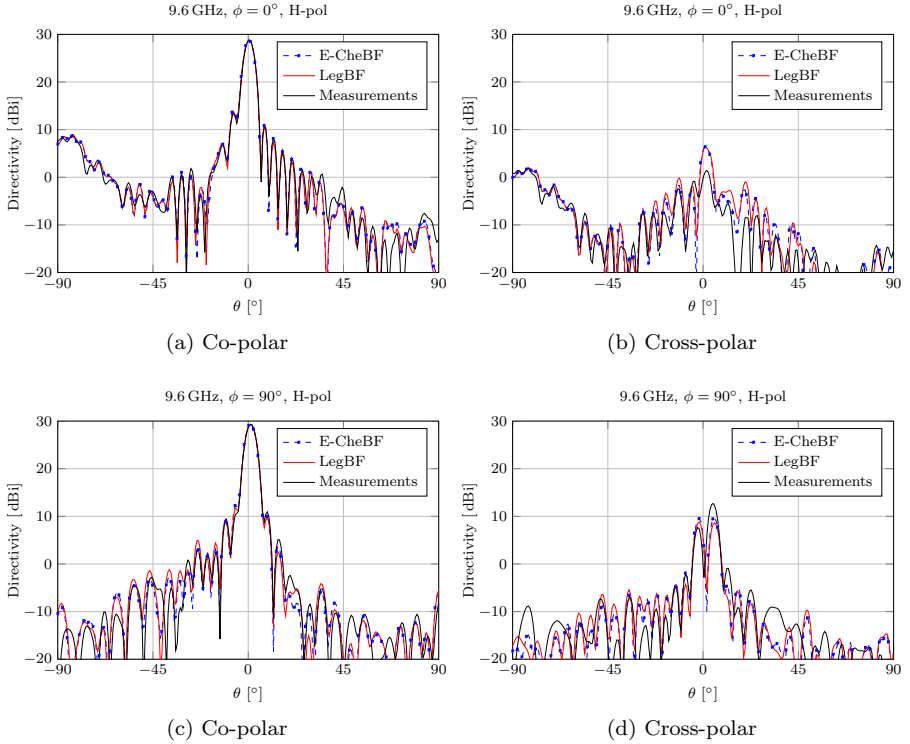


**Figure 2.7** Simulated radiation pattern from sample I-II with the Potter horn as feed. *E-CheBFs* (blue) and *LegBFs* (red) are used in the LP-SDMoM simulations.

*LegBFs* are defined on higher-order curvilinear mesh elements [125], hence any curved boundary can be modeled very accurately. Thus, the *LegBFs* can be applied to any of those element shapes and with a good efficiency [J2].

The expressions for the Fourier transforms of the basis functions used in this section are in closed form, and some of these are provided in Appendix D.

### 2.3.3 Far-field Calculations

In the analysis of printed reflectarrays, the main focus in the literature has been on the accurate determination of the currents on the array elements, while the calculation of the radiation pattern has received less attention. However, the latter is equally important and should not be neglected. In this section, the

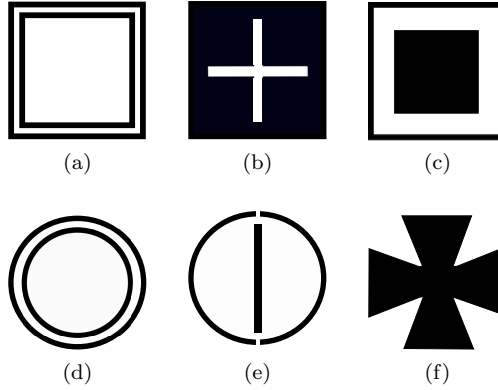


**Figure 2.8** *Different element shapes used for reflectarray applications [29, 64, 81, 84, 87, 114].*

two techniques that are used throughout this work will be described. For more details, the reader is referred to the publications [J1] and [C2].

In [J1], several techniques to calculate the far-field from reflectarrays are compared and two techniques yielded accurate results; the Floquet harmonics technique [J1, Technique II], and the continuous spectrum technique [J1, Technique III]. Both techniques are based on the field equivalence principle [126, p.106]. Equivalent currents are constructed on a surface enclosing the entire reflectarray and are defined by

$$\mathbf{J}_S = \hat{n} \times \mathbf{H}, \quad \mathbf{M}_S = -\hat{n} \times \mathbf{E}, \quad (2.1)$$

where  $\mathbf{E}$  and  $\mathbf{H}$  are the total electric and magnetic fields at the surface and  $\hat{n}$  is the outward unit vector normal to that surface, see Figure 2.9a. The total field in the entire half space behind the reflectarray is assumed to be zero and the equivalent currents are computed only in the plane of the array elements as illustrated in Figure 2.9b.

In the Floquet harmonics technique, the equivalent currents are calculated using the fundamental Floquet harmonic from the LP-SDMoM formulation. Due to the periodicity, the equivalent currents for each array element is calculated only within its own unit-cell, as illustrated in Figure 2.10a. The equivalent currents for the  $i$ th and  $j$ th element are shown with solid and dashed lines, respectively. Thus, the contribution from each array element to the equivalent currents is restricted to its unit-cell. By repeating this procedure for all array elements, equivalent currents on the surface,  $\mathcal{S}$ , covering all elements/unit-cells

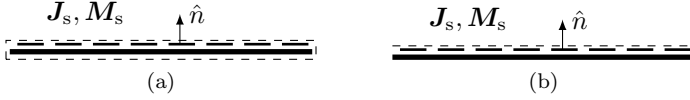


**Figure 2.9** The field equivalence principle for calculating the far-field: (a) equivalent currents computed on a surface enclosing the entire reflectarray, (b) equivalent currents computed only in the plane of the array elements.

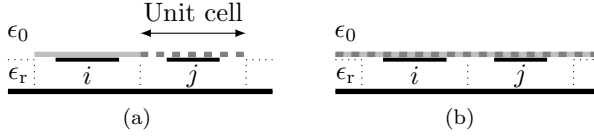


**Figure 2.10** Calculation of the equivalent currents for (a) the Floquet harmonics technique and (b) the continuous spectrum technique. The equivalent currents for the  $i$ th and  $j$ th element are shown with solid and dashed lines, respectively.

are constructed. For details on the computation of the equivalent currents using the fundamental Floquet harmonic, see Appendix C.3.3.

There are several disadvantages associated with the Floquet harmonics technique. First, the substrate and ground plane in reflectarrays are often extended beyond the elements at the edges, and the physical substrate size is larger than  $S$ , see Figure 2.11. To correct for this, unit-cells with no array elements are placed at the edges such that the extended substrate area  $S_{\text{ext}}$  is also covered. The electric and magnetic fields scattered by these empty unit-cells, which are readily obtained from the reflection of the incident field, are then used to form the equivalent currents on  $S_{\text{ext}}$ . In this way, equivalent currents on the entire surface  $S_{\text{tot}} = S + S_{\text{ext}}$  are constructed. However, this procedure is impractical. Second, the equivalent currents are discontinuous at cell boundaries due to the truncation of the currents at the border of each unit-cell. These discontinuities can contribute to phase and amplitude errors in the equivalent currents, thus resulting in an erroneous relation between the electric and magnetic currents. As a result, an erroneous far-field can be obtained, particularly for the radiation in the back hemisphere [J1].

The use of the Floquet harmonics technique is not new, and has been applied in the previous works [42, 113]. However, in these works, only one of the equivalent currents in (2.1) is used together with the image principle, thus limiting the radiation to only the forward hemisphere. Furthermore, these works do not account for  $S_{\text{ext}}$ .

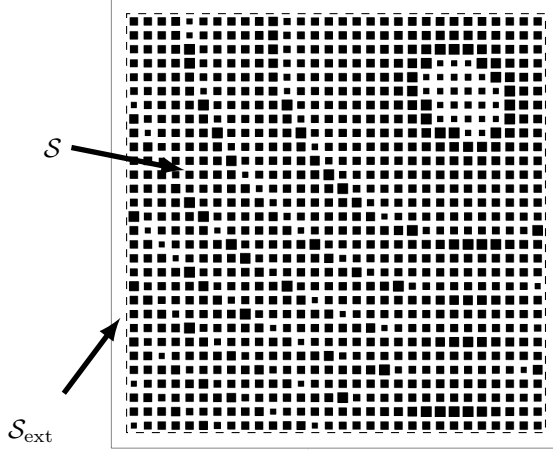


**Figure 2.11** The surface  $\mathcal{S}$  is the area confined with the dashed lines covering the unit-cells, and  $\mathcal{S}_{\text{ext}}$  covers the extended substrate area. The total surface area is  $\mathcal{S}_{\text{tot}} = \mathcal{S} + \mathcal{S}_{\text{ext}}$ .

To circumvent the issues associated with the Floquet harmonics technique, the continuous spectrum technique was proposed in [J1]. Similar to the Floquet harmonics technique, the equivalent currents are calculated at the plane of the array elements as given by (2.1). However, the tangential electric field at the plane of the array elements is determined using a continuous plane wave spectrum

$$\mathbf{E}(x, y) = \frac{1}{4\pi^2} \iint_{k_x^2 + k_y^2 < k_0^2} \mathcal{E}(k_x, k_y) e^{-j(k_x x + k_y y)} dk_x dk_y, \quad (2.2)$$

and evaluated over the entire reflectarray surface, not only within each unit-cell. Herein,  $k_0$  is the free-space wave number, and the expressions for the spectral amplitude  $\mathcal{E}(k_x, k_y)$  can be found in [J1]. Once  $\mathcal{E}(k_x, k_y)$  is determined, the magnetic field can be obtained using the plane wave relation

$$\mathbf{H}(x, y) = \frac{1}{4\pi^2} \iint_{k_x^2 + k_y^2 < k_0^2} \frac{1}{\eta_0} \hat{k} \times \mathcal{E}(k_x, k_y) \cdot e^{-j(k_x x + k_y y)} dk_x dk_y, \quad (2.3)$$

where  $\hat{k} = \hat{x}k_x + \hat{y}k_y \pm \hat{z}\gamma_0$  describes the direction of propagation,  $\eta_0$  is the free-space impedance, and  $\gamma_0 = \sqrt{k_0^2 - k_x^2 - k_y^2}$ . Upon substitution in (2.1), the

equivalent currents are calculated over the entire surface  $\mathcal{S}_{\text{tot}}$ , thus automatically accounting for  $\mathcal{S}_{\text{ext}}$ . A graphical illustration is shown in Fig. 2.10b, where the equivalent currents for the  $i$ th and  $j$ th element are shown again with solid and dashed lines, respectively. The currents cover the entire  $\mathcal{S}_{\text{tot}}$ , and the contribution from each array element over  $\mathcal{S}_{\text{tot}}$  is taken into account. The electric and magnetic fields at the reflectarray surface are related through the continuous plane wave spectrum and no discontinuities are present at the borders of the unit-cells.

In [J1] and [C2], the Floquet harmonics and continuous spectrum techniques were used to calculate the far-field from sample I-II and the results were compared to the measurements. The comparison showed, in the forward hemisphere, accurate results for both techniques if  $\mathcal{S}_{\text{ext}}$  is taken into account. However, the continuous spectrum technique was slightly more accurate in predicting the peak directivity. For the back hemisphere, the Floquet harmonics technique predicted, for both the co- and cross-polar components, an erroneous beam in the direction of the main beam's image. The source of this error is the incorrect relation between the electric and magnetic equivalent currents in the Floquet harmonics technique as previously mentioned. This problem is circumvented using the continuous spectrum technique, and a very good agreement with measurements is obtained in the back hemisphere using this technique.

Although the continuous spectrum technique is more accurate, it has the drawback of higher computation time. For moderately sized reflectarrays ( $< 20\lambda_0$ ) the computation time is similar to that required for the Floquet harmonics technique, which is in the order of seconds. However, for increasing antenna size, the number of plane waves needed in the PWE in (2.2) increases accordingly, thus resulting in a slightly higher computation time in the order of a couple of minutes.

### 2.3.4 Infinite Ground Plane

Due to the periodicity assumption in the LP approach, the truncation of the ground plane is not taken into account in the determination of the currents on the array elements. Thus, the analysis of the elements at the edges of the reflectarray is incorrect and this, in principle, contributes to errors.

Sample I-I was designed with the aim to exaggerate exactly these errors. In Figure 2.12 the radiation from sample I-I is shown. The Potter horn is used as feed to give a strong edge illumination varying between  $-7$  to  $-1$  dB along the edges. It is seen that an extremely good agreement between simulations and measurements is obtained, even with the strong edge illumination. The discrepancies observed around  $\theta = 60^\circ$  are due to the blockage of the feed and/or the measurement tower. This good agreement indicates that the errors introduced

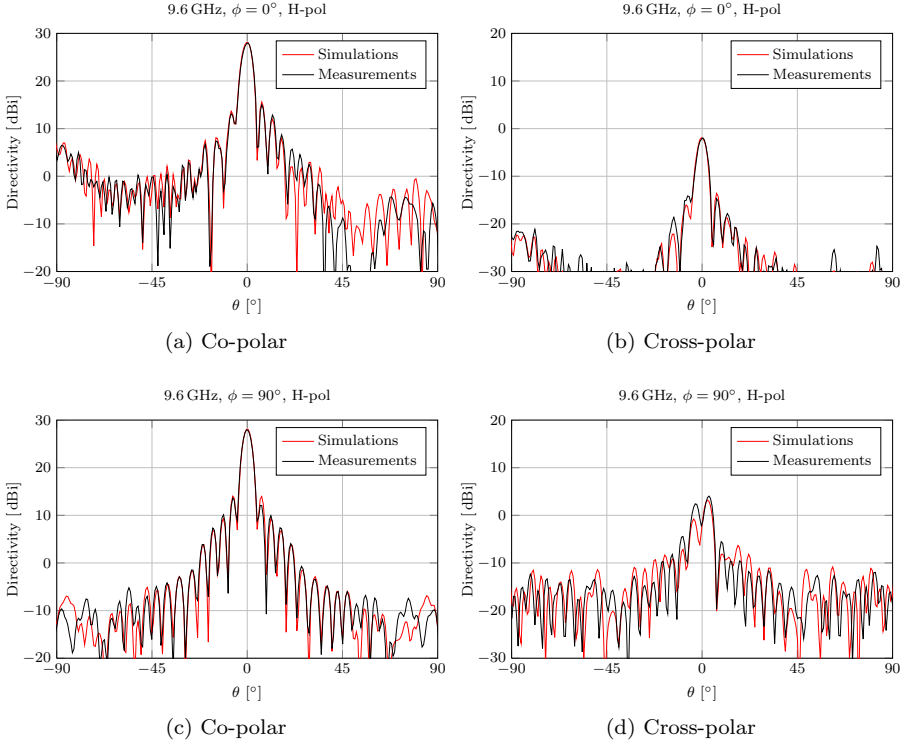


**Figure 2.12** Simulated radiation pattern from sample I-I with the Potter horn as feed. The discrepancies around  $\theta = 60^\circ$  in (a) are due to the blockage of the feed and /or the measurement tower.

by the assumption of infinite ground plane are of small importance for the determination of the currents on the array elements. However, as mentioned in Section 2.3.3, the finite size of the reflectarray, and thereby also the truncation of the ground plane, has to be taken into account when calculating the far-field.

### 2.3.5 Periodicity

Reflectarrays are inherently aperiodic due to the need to compensate for the differential spatial phase delay from the feed. Thus the periodicity assumption in the LP-SDMoM can give inaccurate results.

It has been stated by several research groups that the periodicity assumption is one of the main sources of error in the LP-SDMoM, and is only accurate

when the variation in patch dimensions is smooth from one cell to the adjacent cells [2, 38, 101, 104, 127]. However, as already demonstrated, the accuracy of the LP-SDMoM is extremely good if the aforementioned sources of error are correctly accounted for. Even for sample I-II, which is designed to exaggerate this particular source of error, the accuracy is impressive. This points to the fact that the errors due to the periodicity assumption are of less importance. Nevertheless, two techniques to reduce these errors have been examined during this study, the surrounded element approach (SEA) [101], and the extended local periodicity (ELP) approach [C1].

Both approaches attempt to account for the mutual coupling more realistically by including the actual neighboring elements in the analysis of each array element. The SEA is a finite approach where no periodicity is applied, whereas the ELP is based on periodicity but applied to an extended unit-cell.

Although both techniques have advantages, they do not necessarily produce more accurate results than the LP-SDMoM, quite the contrary. In addition, the overall computation time associated with both techniques is very high ( $> 45$  min) and thus not suitable for optimization purposes. Therefore, neither of the techniques are used in the optimization technique presented in the next chapter. Even though a great amount of time during the study was devoted to the investigation of these techniques, details will not be provided in this chapter. However, they can be found in Appendix E. There, the advantages and drawbacks of each technique are discussed and representative results are provided.

## 2.4 Summary

A survey of existing modeling techniques for the analysis of printed reflectarrays has been performed. Based on this survey, it was concluded that the LP-SDMoM was most attractive for optimization purposes and several sources of inaccuracy in this technique have been identified. To exaggerate some of these sources, two reflectarray samples have been designed and manufactured, and subsequently measured at the DTU-ESA Spherical Near-Field Antenna Test Facility to serve as reference solutions.

The sources of error that have been treated in this work are the periodicity assumption, the assumption of infinite ground plane, the representation of the incident field, the choice of basis functions, and the technique to calculate the far-field. The three latter sources are particularly important for an accurate analysis.

The representation of the incident field in the LP-SDMoM must be correct, thus measured or accurately simulated patterns must be used to compute the



polarization, amplitude, and phase of the incident plane wave on each array element.

The choice of basis functions in the LP-SDMoM also has a great impact on the accuracy and the efficiency of the solution. It was demonstrated that higher-order hierarchical Legendre basis functions are capable of yielding very accurate results and at the same time being applicable to arbitrarily shaped array elements.

Finally, it was shown that the technique to calculate the far-field is very important with respect to the analysis accuracy. The finite substrate and ground plane size of the reflectarray must be accounted for, and techniques that neglect this yield inaccurate results.

It is often believed that the periodicity assumption is the one of the main sources of error in the LP-SDMoM. However, it was demonstrated that the accuracy of the LP-SDMoM is extremely good, even for highly aperiodic reflectarrays, as long as the aforementioned sources of error are correctly accounted for.

## REFLECTARRAY OPTIMIZATION

---

Based on the techniques for the enhanced analysis accuracy presented in Chapter 2, a generalized direct optimization technique (GDOT) has been implemented and is presented in this chapter.

This chapter begins with a survey of existing techniques for the design of printed reflectarrays, followed by a description of the GDOT. Subsequently, several reflectarrays designed using the GDOT are described. Finally, two reference reflectarrays have been measured at the DTU-ESA Spherical Near-Field Antenna Test Facility with the goal to verify the accuracy of the GDOT and simulations and measurements are presented.

Most of the results presented in this chapter are presented in [J3,J4], [C3,C4], and summarized in [C5]. Papers [J3] and [J4] are included in the thesis as Paper III and Paper IV, respectively, and [C5] is included as Conference Paper II.

### 3.1 Survey

To obtain a specific far-field pattern with a printed reflectarray, several degrees of freedom can be used: the size, the shape, the orientation, and the position of the array elements, as well as the shape of the reflectarray surface. An accurate and efficient design procedure, capable of including all these parameters, is a challenging task.

The conventional approach for the design of printed reflectarrays is based on a phase-only optimization technique (POT) [37,38] involving the following steps:

- 1) Determine the phase distribution over the reflectarray surface using a phase-only pattern synthesis such that a specific far-field can be realized,
- 2) Each array element is designed, element by element, to match the required phase distribution found in step 1.

Several phase-only pattern synthesis techniques have been reported in the literature for the determination of the phase distribution in step 1 [37, 43, 128].

Alternatively, commercial software packages for the design of shaped reflectors, e.g. POS, can be used to obtain the required phase distribution [36, 129].

For simple designs e.g. pencil beam reflectarrays, the design part in step 2) is usually done by means of phase curves [17]. These phase curves relate the phase of the scattered field to one or two of the geometrical parameters of the array element when illuminated by a given plane wave. From these curves, the geometry of the array element can be extracted.

In [130–132], a geometrical optimization strategy is proposed. The purpose of this approach is to maximize the geometrical similarity between consecutive array elements in the reflectarray layout. The goal is to comply with the LP assumption and thus improve the prediction accuracy of the antenna performance. However, this strategy is only enforced at the center frequency and is thus not suitable for broadband designs since the phase distribution is different over a given frequency band.

For broadband designs, each array element is optimized to comply with the phase specifications at the central and extreme frequencies by minimizing a given error function [37, 38, 40]. However, to find array elements that match all phase distributions simultaneously is impossible in most cases and the array elements are determined as a compromise between the different phase distributions, thus resulting in non-optimal designs. Nevertheless, this approach is the most common and many advanced reflectarrays have been designed using this technique [37–40, 42, 57].

In [41, 129], a more refined approach that utilizes the scattering matrix has been presented. Herein, the magnitude and phase of coefficients in the scattering matrix can be tuned by adjusting some of the geometrical parameters of the array elements. Starting from a design obtained using the POT, the cross-polar coefficients in the scattering matrix for the array elements can be controlled, thus offering the possibility of reducing the overall cross-polar radiation.

Although the POT is efficient since the analysis of all array elements at each iteration is avoided, it suffers the drawback that intermediate optimization steps are necessary to fulfill a given phase distribution. This intermediate step breaks the direct relation between the geometrical parameters and the far-field performance and can give non-optimal designs. It is therefore expected that a direct optimization technique where all the array elements are simultaneously optimized, can potentially produce better designs. Such techniques have been presented in [133, 134]. In [133], a small contoured beam reflectarray was designed, manufactured, and measured. However, significant discrepancies between simulations and measurements were observed, and it was concluded that further work is needed to improve the accuracy of the reflectarray analysis. The work in [134] is an extension of the technique presented in [133] where also the position of the array elements can be included in the optimization. Since the

array elements can be located in a strongly distorted grid, a full-wave MoM including the nearest neighboring elements is used in the optimization. As a result, the overall synthesis becomes very time consuming.

The techniques in [133, 134] can optimize both co- and cross-polar radiation. Previous works on minimizing the cross-polar radiation from the entire reflectarray has mostly focused on the scattering response of the periodic cell [41, 135, 136] or on appropriate arrangement of the array elements [10, 119], but not by means of direct optimization of the cross-polar radiation. Thus, the optimization of the cross-polar radiation from the entire reflectarray is an important feature. However, a high analysis accuracy is required to realize the low cross-polar radiation.

## 3.2 Generalized Direct Optimization Technique

A new generalized direct optimization technique (GDOT) for the design of printed reflectarrays using arbitrarily shaped array elements with irregular orientation and position is presented in this section. The GDOT is developed by considering the accuracy and efficiency as the most important parameters.

The LP-SDMoM is used in the GDOT since the technique is very efficient and has proven to yield very accurate results. The flow chart for the GDOT is shown in Figure 3.1 and is described in detail in the publications [J3, J4] and [C3–C5].

### 3.2.1 Optimization Procedure

The far-field objectives are specified in a number of far-field points in the  $(u, v)$ -plane, where  $u = \sin \theta \cos \phi$  and  $v = \sin \theta \sin \phi$ . At each optimization iteration, the maximum difference between realized and specified objectives is minimized. The optimization variables are the geometrical parameters of the array elements, e.g. the size, orientation, and position. By optimizing directly on the geometrical parameters to fulfill the far-field specifications, the direct relation between optimization variables and optimization goals is maintained. Both co- and cross-polar radiation can be optimized for a number of frequencies for multiple polarizations, and for different feed illuminations, to obtain a desired bandwidth for different feeds.

The GDOT uses the same optimization procedure that is used in POS. It uses a gradient minimax algorithm for non-linear optimization. Since it is a gradient based method, a good initial point is required to ensure rapid convergence and to avoid non-optimum local minima.

Depending on the complexity and the requirements of the specified contour, identical array elements can be used as the initial start. This produces an initial pattern that resembles the feed pattern and is a good initial start in certain cases, e.g. multi-frequency designs. Another choice is to use an initial

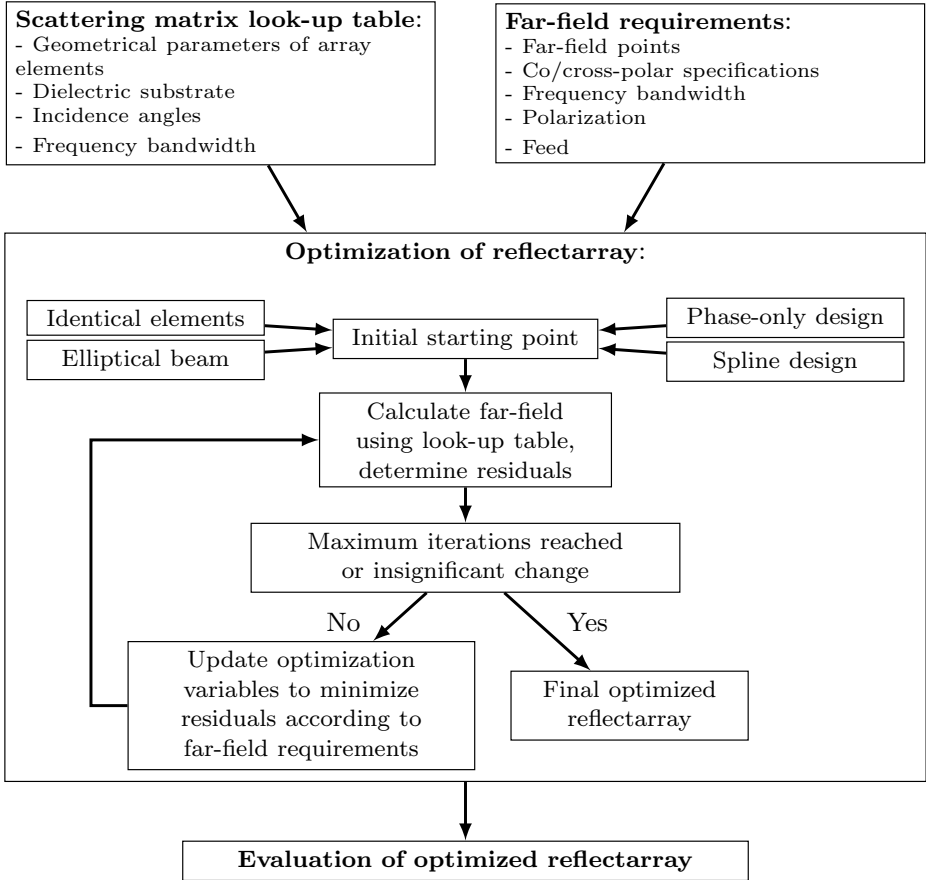


**Figure 3.1** Flow chart of the GDOT.

defocused elliptical beam. This approach is used in POS and has proven to be an effective starting point for the optimization of shaped reflector antennas. For reflectarrays, an elliptical beam can be accomplished by requiring a proper phase variation over the reflectarray surface. However, this is problematic for multi-frequency designs as the phases depend on the frequency. On the other hand for single frequency designs, an elliptical beam can be a very good starting point. Alternatively, a reflectarray designed using a POT can be used as initial start.

### 3.2.2 Incident Field

As described in Section 2.3.1, the analysis accuracy can be improved if an accurate feed pattern is obtained by either measurements or an accurate simulation tool. This is particularly important during the optimization process to obtain an accurate design that fulfills the requirements. Thus, measured or accurately simulated feed patterns can be included in the GDOT to ensure that the reflectarray is optimized for the correct feed illumination.

### 3.2.3 Basis Functions

For the accurate and efficient computation in the LP-SDMoM, the LegBFs are used. As described in Section 2.3.2, the LegBFs can be applied to any arbitrarily shaped array elements, and have been demonstrated to yield very accurate results. The versatility of the LegBFs is a key feature in the GDOT as it enables the optimization of reflectarrays consisting of arbitrarily shaped array elements.

### 3.2.4 Far-field Calculations

Regarding the technique to calculate the far-field, the two techniques presented in Section 2.3.3 have been considered for the GDOT, namely the Floquet harmonics technique, and the continuous spectrum technique. Although the continuous spectrum technique is superior in terms of accuracy compared to the Floquet harmonics technique, it is not suited for optimization purposes, since it needs higher computation time and storage requirements as will be discussed in Section 3.2.6. Consequently, the Floquet harmonics technique is used for the calculation of the far-field during the optimization. However, for the evaluation of the final optimized reflectarray, the continuous spectrum technique is utilized.

### 3.2.5 Irregularly Positioned Array Elements

The GDOT can be used for the optimization of reflectarrays with arbitrary element orientation and position. To utilize the position of the array elements in the GDOT, an irregular distribution of element positions is obtained through a mapping from a regular grid to an irregular grid. In this work, the mapping is obtained by adding a distortion to the regular grid.

Define  $(\alpha, \beta)$  as normalized coordinates in the regular grid such that  $|\alpha| \leq 1$  and  $|\beta| \leq 1$ . Then, the new normalized coordinate in the irregular grid is given

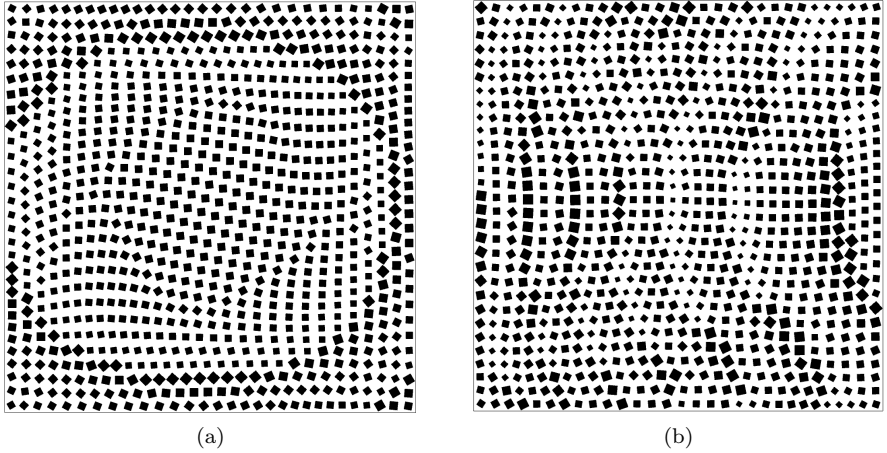


**Figure 3.2** Offset pencil beam reflectarrays with irregularly positioned array elements. The reflectarrays are designed to radiate a pencil beam towards (a) the specular direction and (b) the broadside direction.

by  $(\alpha', \beta') = (\alpha + f_x, \beta + f_y)$ , where

$$f_x(\alpha, \beta) = (\alpha - 1)(\alpha + 1) \sum_{p=0}^P \sum_{q=0}^Q c_{pq} T_p(\alpha) T_q(\beta), \quad (3.1a)$$

$$f_y(\alpha, \beta) = (\beta - 1)(\beta + 1) \sum_{p=0}^P \sum_{q=0}^Q d_{pq} T_p(\alpha) T_q(\beta). \quad (3.1b)$$

Herein,  $T_p$  and  $T_q$  are the Chebyshev polynomials of order  $p$  and  $q$ , respectively, and  $c_{pq}$  and  $d_{pq}$  are the distortion coefficients, which are the variables used to optimize the positions of the array elements. The terms in front of the summations are to ensure that the edges of the reflectarray are kept fixed to avoid any undesired increase in antenna size introduced by the mapping. Some examples of irregular reflectarrays are illustrated in Figure 3.2. Here, the mask layouts for two offset pencil beam reflectarrays with irregularly positioned and oriented array elements are shown. The weighted polynomials are selected empirically to ensure a strong but realistic distortion.

Due to the distortion of the grid, the array elements are no longer positioned in a periodic lattice and the LP-SDMoM can not be directly applied. Thus, equivalent square unit-cells with the same area as the distorted cells have been defined to approximate these distorted cells. An example of a distorted cell and

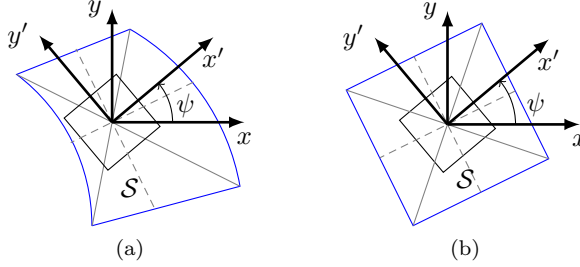


**Figure 3.3** An example of (a) a distorted cell and (b) its equivalent square cell. Both cells have the area  $S$ . The center of the array element is located at the intersection of the two solid diagonal lines of the distorted cell. The rotation of the array element, which also can be optimized, is given by the rotation angle  $\psi$ .

its equivalent unit-cell is shown in Figure 3.3, and details on the equivalent unit-cell are given in [J4]. These equivalent square unit-cells, which are of different sizes, are used in the LP-SDMoM computations. In [C3] and [J4], several irregular reflectarrays, including those shown in Figure 3.2, have been analyzed using the LP-SDMoM and compared to reference solutions obtained using a full-wave MoM<sup>1</sup>. The comparison showed that the LP-SDMoM is very accurate despite the strong irregularities. For more details, see [J4].

### 3.2.6 Scattering Matrix Look-Up Table

Although the LP-SDMoM using LegBFs is computationally efficient with only a fraction of a second in computation time per array element, it is not efficient enough for optimization as the analysis must be performed repeatedly. To circumvent this, the scattering matrices can be calculated in advance and stored in a look-up table. The use of look-up tables has been successfully applied in other works [41, 131, 134, 140] and is also used in the GDOT.

In this work, the representation of the scattering matrices in the look-up table is done by means of local cubic interpolation. For a given frequency and substrate, the scattering matrices depend on: illumination angles, geometrical parameters of the array element, and unit-cell dimensions. It was found that a

<sup>1</sup>The full-wave MoM was developed during the investigation of the surrounded element approach, see Appendix E. The reflectarray problem is formulated using the mixed-potential form of the electric field integral equation (EFIE) [137–139] and solved using the MoM algorithm from the GRASP MoM add-on [94] where the spatial Green's functions have been included. A description of the IE formulation and the calculation of the spatial Green's functions is given in Appendix F.



sufficient accuracy can be obtained using relatively few scattering matrix samples values, for specific values see [J3, J4]. For complex array element geometries where several geometrical parameters can be adjusted, the size of the look-up table becomes huge in terms of memory requirements and the process of calculating the look-up table becomes time consuming. However, once the look-up table has been calculated, it can be reused in the optimization and needs only to be recalculated if another substrate or frequency is used.

Using local cubic interpolation, the derivatives with respect to the geometrical parameters of the array element can be computed by differentiation of the local cubic interpolation expression. Thus, the gradients needed during the optimization can be determined analytically, which is more accurate and faster than using numerical difference approximations. More details on the look-up table can be found in [J3, J4].

It was stated in Section 3.2.4 that the Floquet harmonics technique is more suitable for optimization purposes compared to the continuous spectrum technique and this will be clarified in the following.

The equivalent currents in the Floquet harmonics technique are determined through the scattering matrices of the array elements, which are independent of the position of the array element. The positions are accounted for in the Floquet harmonics technique by the multiplication of appropriate phase shifts in the equivalent currents. From the equivalent currents, the radiation in a given far-field point can be calculated analytically since the equivalent currents are determined assuming the electric and magnetic field on the unit-cell surface being related through plane waves. Thus, the scattering matrices can be computed and tabulated in the look-up table without any a priori knowledge of the far-field specifications nor of the position of the array elements.

The equivalent currents in the continuous spectrum technique on the other hand are determined using a PWE, and this involves several complications. The PWE depends on the size of the reflectarray and the position of the array elements. In addition, the radiation in a given far-field point can not be calculated analytically due to the continuous spectrum of plane waves. These issues combined makes the look-up table for this technique complicated since many parameters need to be stored.

Nevertheless, a version of the look-up table for the continuous spectrum technique was implemented, where the co- and cross-polar radiation in the specified far-field points from each array element has been tabulated as function of illumination angles and geometrical parameters. Although good designs were obtained, the computation time to calculate the look-up table and the storage requirements were much higher compared to the case using the Floquet harmonics technique. In addition, it could not be used for the design of reflectarrays with irregularly positioned elements as the positions of the array elements are

fixed a priori. Thus, to optimize the positions, recalculation of the look-up table at each optimization iteration is required. As a result, the continuous spectrum technique was considered unsuitable for the GDOT and the Floquet harmonics technique was selected.

### 3.2.7 Spline Representation

For large reflectarrays consisting of many array elements, the number of optimization variables becomes excessively high and the optimization becomes slow.

To reduce the number of optimization variables, cubic splines have been included in the GDOT to represent the sizes of the array elements

$$s(x, y) = \sum_i^I \sum_j^J b_{ij} B_i(x) B_j(y). \quad (3.2)$$

Herein,  $s(x, y)$  describes the sizes of the array elements at coordinate  $(x, y)$ ,  $b_{ij}$  are the spline coefficients, and  $B_i(x)$  and  $B_j(y)$  are the cubic splines, which can be defined over several array elements. The spline coefficients  $b_{ij}$  are the optimization variables used to determine the sizes of the array elements, and in this way the number of optimization variables can be reduced.

However, the variation of the dimensions of the array element over the reflectarray surface can have discontinuities when the scattered phase is required to jump after a complete 360° cycle, see e.g. Figure 2.1b. Such discontinuities are hard to represent using splines, and thus, a design obtained using splines is inferior compared to a design where the array elements are directly optimized (unless the number of splines and array elements are equal). Without the use of splines, the optimization time for electrically large reflectarrays is still high compared to POS for the design of shaped reflectors [C5], and techniques to improve the spline implementation should be investigated. One solution to improve the spline representation is to implement a periodic mapping between  $s(x, y)$  and the sizes of the array elements such that the discontinuities can be taken into account.

Nevertheless, the current spline representation can be used to generate a design that can be used as a starting point for the more rigorous optimization where the array elements are directly optimized. In this way, the number of optimization iterations that is needed for the rigorous optimization can be reduced.

## 3.3 Reflectarray Designs

To demonstrate the capabilities of the GDOT, several offset contoured beam reflectarrays have been designed and presented in [J3, J4] and [C5], and some of

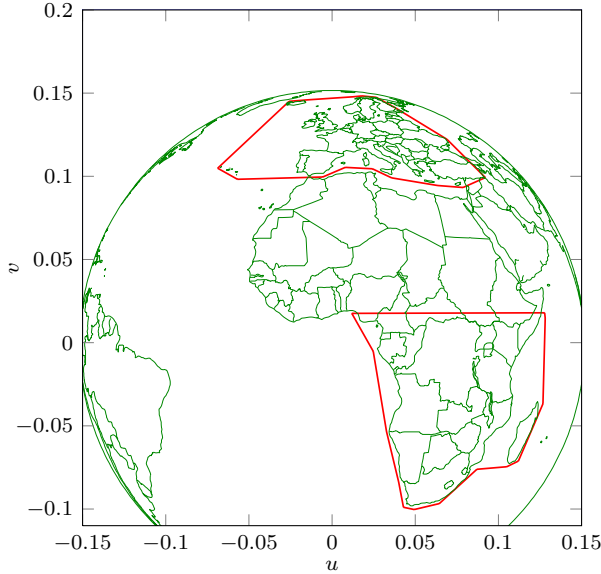


**Figure 3.4** *European and southern African coverages seen from the longitude  $0^\circ$  geostationary orbital position.*

the results are presented in this section. A high-gain European coverage with the possibility of enforcing sidelobe suppression within a southern African coverage is considered. The coverages seen from the longitude  $0^\circ$  geostationary orbital position are shown as red polygons in Figure 3.4.

Four reflectarray designs are presented: a single-polarized broadband design, a dual-polarized broadband design, a circularly polarized design based on the variable rotation technique (VRT), and an electrically large dual-polarized design.

### 3.3.1 Single-Polarized Broadband Design

The purpose of this design is to illustrate the improvements obtained using the GDOT compared to the POT. To this end, three reflectarrays were designed, one using the conventional POT (Design A-I), and two using the GDOT. The reflectarrays were optimized to radiate a high gain beam on the European cove-

**Table 3.1** *Performance of single-polarized broadband reflectarray (Design A)*

	Design A-I	Design A-II	Design A-III
Frequency (GHz)	Minimum Directivity (dBi)	Minimum Directivity (dBi)	Minimum Directivity (dBi)
8.5	24.2	24.9	24.9
9.0	25.4	26.5	26.5
9.5	25.5	26.7	26.7
10.0	25.4	26.8	26.8
10.5	25.4	26.6	26.8
11.0	25.4	26.5	26.7
11.5	23.2	23.4	23.3

range in the frequency range 9 – 11 GHz for a single polarization, H-polarization<sup>2</sup>. Square patches are used as array elements, and a linearly polarized Gaussian beam with a taper of  $-15$  dB at  $30^\circ$  is used as feed.

All three designs consist of  $50 \times 50$  elements ( $20 \times 20 \lambda_0^2$ ) and the performance of the reflectarrays is summarized in Table 3.1. The two designs obtained using the GDOT were synthesized using different starting points: the first (Design A-II) uses identical patches, whereas the second (Design A-III) uses Design A-I. The comparison of the three designs clearly shows the advantages of the GDOT, where more than 1 dB in the minimum directivity is gained compared to the phase-only design. Furthermore, it demonstrates that a design obtained using the POT can be useful as the starting point for the GDOT.

A similar comparison was also performed for a dual-polarized reflectarray design optimized at a single frequency, and it was again shown that the performance of the design optimized using the GDOT was superior compared to the phase-only design. For more details, see [J3].

### 3.3.2 Dual-Polarized Broadband Design

The goal of this design (Design B) is to maximize the directivity within the European coverage in the frequency range 9 – 11 GHz for the two orthogonal polarizations, H- and V-polarization, and at the same time minimize the cross-polar radiation within the same coverage.

<sup>2</sup>The reflectarray is assumed to be mounted on a satellite such that H-polarization is defined to be in the feed offset plane ( $xz$ -plane in Figure 2.2), and V-polarization in the orthogonal plane. This is the same definition as used in Chapter 2.

For this design the square loop/patch combination [83] (see Figure 3.5) has been selected due to its good phase response [J4]. As a starting point for the optimization, identical elements are used, and a Gaussian beam is used as a feed. The optimized reflectarray consists of  $57 \times 57$  elements ( $20 \times 20 \lambda_0^2$ ) and the mask layout of the design is shown in Figure 3.6.

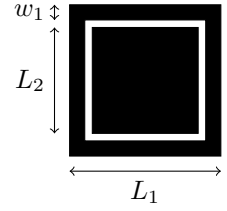


**Figure 3.5** *Square loop/patch combination element [83].*

The minimum directivity and the minimum cross polarization discrimination (XPD) of the design for both V- and H-polarizations in the frequency range 8.5 – 11.5 GHz are tabulated in Table 3.2. It is seen that the minimum directivity within the European coverage is above 26.4 dBi for both polarizations between 9 – 11 GHz and drops to approximately 25 dBi at 8.5 GHz and 11.5 GHz. This demonstrates that the reflectarray has been successfully optimized to operate in the specified frequency range of 20% bandwidth.

In this design, only the length of the outer loop  $L_1$  has been optimized, while the width of the outer loop  $w$  and the size of the inner patch  $L_2$  were fixed. More details on this design can be found in [J4].

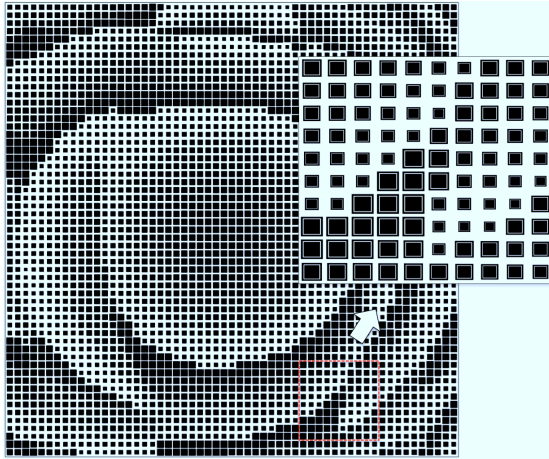


**Figure 3.6** *Mask layout of dual-polarized broadband reflectarray (Design B).*

**Table 3.2** *Performance of dual-polarized broadband reflectarray (Design B)*

Frequency (GHz)	H-polarization		V-polarization	
	Minimum Directivity (dBi)	Minimum XPD (dB)	Minimum Directivity (dBi)	Minimum XPD (dB)
8.5	24.7	27.1	24.8	28.1
9.0	26.6	26.7	26.5	26.6
9.5	26.4	26.4	26.4	26.9
10.0	26.6	26.4	26.5	27.6
10.5	26.5	25.0	26.4	27.4
11.0	26.6	24.1	26.4	28.4
11.5	24.9	22.9	25.1	26.3

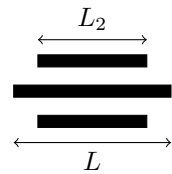
### 3.3.3 Circularly Polarized Design

In this design (Design C), which is presented in [J4], a right hand circularly polarized (RHCP) reflectarray radiating a high-gain beam on the European coverage in the frequency range 9 – 11 GHz is realized by using the VRT [23]. In the VRT, identical array elements with different angular rotations are used to achieve a given far-field beam.

The key for the use of the VRT is to have array elements that can realize a  $180^\circ$  phase difference between two orthogonal polarizations, e.g. V- and H-polarization [23,141]. In this design, the triple dipole element [82] (see Figure 3.7) is used and only the rotation angles of the dipoles are optimized.

The optimized reflectarray consists of  $50 \times 50$  elements ( $20 \times 20 \lambda_0^2$ ) and the mask layout is depicted in Figure 3.8. It is seen in Table 3.3, where the performance of the design in the frequency range 8.5 – 11.5 GHz is listed, that a minimum directivity above 26.6 dBi is achieved between 9 – 11 GHz. As expected, the minimum directivity decreases outside of the specified frequency range. The minimum XPD within the frequency range is relatively low with the best value of 24.7 dB. This is a direct consequence of the large bandwidth specified in the optimization. More details can be found in [J4].

It is expected that better performance can be obtained if an array element with  $180^\circ$  phase difference between V- and H-polarization in a wider frequency range can be found.

**Figure 3.7** *Triple dipole element [82].*

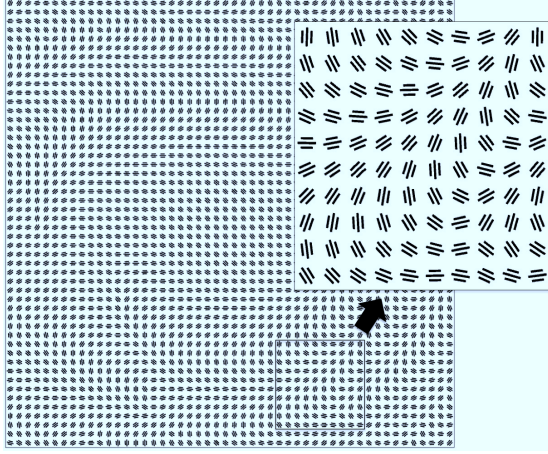


**Figure 3.8** Mask layout of circularly polarized reflectarray (Design C).

**Table 3.3** Performance of circularly polarized reflectarray (Design C)

Frequency (GHz)	Minimum Directivity (dBi)	Minimum XPB (dB)
8.5	25.0	16.4
9.0	26.6	24.7
9.5	26.7	23.0
10.0	26.8	20.7
10.5	26.8	20.5
11.0	26.7	17.3
11.5	25.1	14.8

### 3.3.4 Electrically Large Design

The reflectarrays presented up until now are all of a moderate size,  $20 \times 20 \lambda_0^2$ . To demonstrate GDOT's ability to design electrically large reflectarrays, a  $50 \times 50 \lambda_0^2$  design (Design D) has been optimized and presented in [C5]. It is optimized to radiate a high-gain beam on the European coverage with cross-polar suppression within the same coverage, and for both V- and H-polarizations. Square patches are used as array elements. Due to their non-optimal performance for dual polarization, the antenna is optimized to operate in a 10% bandwidth, specifically 9.5 – 10.5 GHz.

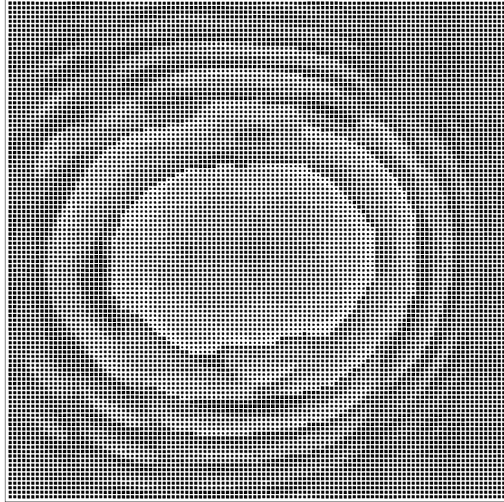


**Figure 3.9** Mask layout of  $50 \times 50 \lambda_0^2$  reflectarray (Design D).

Initially, a reflectarray optimized using  $50 \times 50$  splines is designed. A minimum directivity of 27.5 dBi was achieved in the specified frequency range for both polarizations. This design was subsequently used as a starting point for the final design where the patches were directly optimized. The mask layout of the final design is shown in Figure 3.9 and the performance is summarized in Table 3.4. The minimum directivity and XPD in the specified frequency range for both polarizations are 28.3 dBi and 26.7 dB, respectively. Outside this frequency range, the minimum directivity drops several dBs, again showing that the reflectarray has been successfully optimized for the given frequency range. Even though square patches are used as array elements, the design has low cross-polar radiation and operates for dual polarization for a 10% bandwidth.

The optimization was carried out on an 1.86 GHz 8 core Intel Xeon processor computer, and the overall optimization time, including the calculation of the look-up table and the optimization of the spline design, took slightly below 20 hours. As previously mentioned, this is still high compared to POS for the design of shaped reflectors, and techniques to reduce this are being investigated.

### 3.4 Reflectarray Measurement Campaign II

To verify the accuracy of the GDOT, a second measurement campaign at the DTU-ESA Spherical Near-Field Antenna Test Facility was planned. The initial



**Table 3.4** *Performance of  $50 \times 50 \lambda_0^2$  reflectarray (Design D)*

Frequency (GHz)	H-polarization		V-polarization	
	Minimum Directivity (dBi)	Minimum XPD (dB)	Minimum Directivity (dBi)	Minimum XPD (dB)
9.0	23.4	25.2	22.8	18.8
9.5	28.7	27.0	28.4	26.7
10.0	28.7	27.8	28.3	28.0
10.5	28.5	28.0	28.3	27.5
11.0	23.5	23.1	25.0	27.1

plan was to design two advanced offset contoured beam reflectarray samples, which could be used to demonstrate the capabilities of the GDOT. However, the measurements were scheduled at a time where the implementation of the GDOT was incomplete. At that time, the GDOT was restricted to the optimization of reflectarrays consisting of square patches at a single frequency. Thus, the aforementioned designs (Designs A-D), which were designed after the second measurement campaign, could not be measured. Instead, two offset contoured beam reflectarrays consisting of square patches were manufactured and measured.

In this section, the reflectarray samples and the measurements of these are briefly described. A more detailed description of the design of the samples is given in Appendix A and additional measurement results can be found in Appendix B.

### 3.4.1 Reflectarray Samples

For the two samples, it was decided that one should be a reflectarray where the array elements are positioned in a regular grid, whereas the other should be a reflectarray where the array elements are positioned in an irregular grid. Both samples should be optimized to radiate a high-gain beam on the European coverage with cross-polar suppression within the same coverage, and sidelobe suppression within a southern African coverage.

Prior to the final designs, a large number of design iterations were performed from which the two final designs were selected. For dual polarization, it was observed that the performance of an irregular reflectarray is similar to that of a regular reflectarray, thus no improvement was gained by using an irregular grid. However, for a single polarization, the comparison between the regular and irregular designs showed an improvement of 1 dB in the XPD level for the irregular

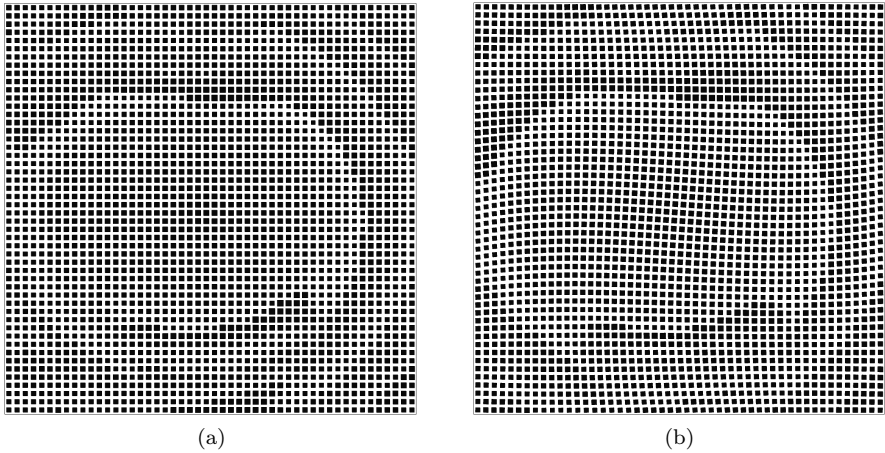


**Figure 3.10** *The mask layouts of the reflectarrays for measurement campaign II, (a) sample II-I and (b) sample II-II.*

design, indicating that better performance in the cross-polar radiation can be achieved using an irregular grid. It was thus decided to have a regular reflectarray optimized for dual polarization, and an irregular reflectarray optimized for a single polarization.

The mask layouts of the two final reflectarray samples are shown in Figure 3.10. The sample in Figure 3.10a is the regular reflectarray (sample II-I). It was optimized for both V- and H-polarization and at 10 GHz. The sample in Figure 3.10b is the irregular design and was optimized with the same goals as sample II-I, but only for H-polarization (sample II-II).

For both samples, the corrugated horn used in the previous measurement campaign was used as feed, and its measured pattern was used in the optimization of the two reflectarray samples.

Similar to the first measurement campaign, both samples were measured for both V- and H-polarizations at a series of frequencies between 9.6 GHz and 10.5 GHz.

### 3.4.2 Simulations Versus Measurements

In this section, comparisons of simulated and measured radiation patterns of the reflectarray samples are presented. To account for the presence of the support structures, the scattering from the struts is included in the analysis using the MoM add-on in GRASP.

### 3.4.2.1 Sample II-I

In the initial comparison of the simulated and measured radiation patterns of sample II-I, it was observed that the co-polar radiation on the southern African contour was higher than expected. Instead of an expected isolation level above 25 dB for both V- and H-polarization, the measurement showed an isolation level of only 17 dB. The source of this error was found to be an inadequate number of basis functions used in the LP-SDMoM to model the electric currents on the patches during the design process. The analysis did not entirely converge in the forward hemisphere and this resulted in a non-optimum design.

The number of basis functions was initially selected based on the previous reflectarray samples from measurement campaign I since the same substrate was used. However, this number was not sufficient. This is explained by the strong resonance of the patches. Identical patches of resonant size were used as the initial starting point for the optimization. Thus, the final design consists of patches that are all very close to their resonance. As a result, the singular behavior of the electric currents at the edges of the patches has a strong effect and additional basis functions are required. By increasing the number of basis functions, the results shown in Figure 3.11 were obtained.

The agreement between simulations and measurements is very good, where the high gain curves practically coincide. Also the accuracy for the lower levels is very good. The performance of the sample for both polarizations at 10 GHz is summarized in Table 3.5. It is seen that an excellent agreement is obtained for the peak directivity and minimum directivity within the European coverage. Also the isolation levels are accurately predicted. Regarding the XPD, the accuracy is slightly lower where discrepancies up to a few dBs are observed. This is expected since the cross-polar radiation is approximately 30 dB below the co-polar peak, and phenomena such as scattering from the edges come into play. The accuracy for the other measured frequencies is also very good, where the maximum discrepancy in the minimum directivity is  $\pm 0.1$  dB.

### 3.4.2.2 Sample II-II

In the design of sample II-II, the same number of basis functions was used as in sample II-I. However, convergence was reached despite the fact that the initial starting point for the optimization also consisted of identical patches of resonant size. However, the resonance issue is not as severe as in sample II-I. This is explained by the fact that the patches in sample II-II are slightly rotated due to the irregular grid. The mutual coupling between the patches is less dominant and the singularities of the electric currents may have a smaller effect.

Simulated and measured radiation patterns of sample II-II are depicted in Figure 3.12, and the performance is summarized in Table 3.6. An excellent

**Table 3.5** *Measured versus simulated data at 10 GHz – Sample II-I*

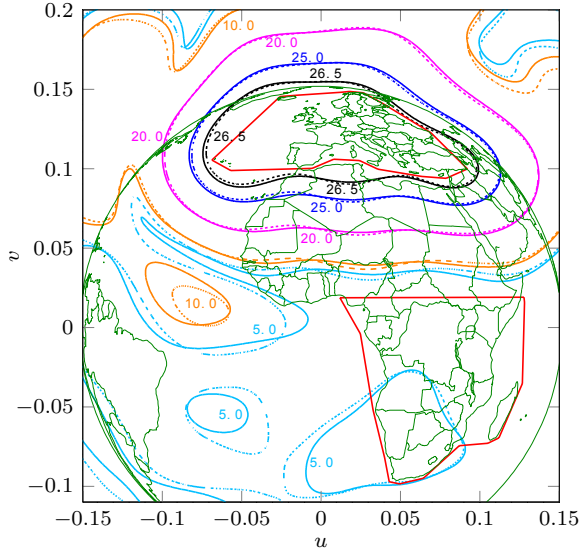
	Peak directivity (dBi)	Min. directivity (dBi)	Min. XPD (dB)	Min. isolation (dB)
Measurement (H-pol.)	28.3	26.5	27.1	17.5
Simulation (H-pol.)	28.2	26.6	25.0	17.8
Measurement (V-pol.)	27.9	26.5	27.7	18.4
Simulation (V-pol.)	27.9	26.5	25.5	17.2

**Table 3.6** *Measured versus simulated data at 10 GHz – Sample II-II*

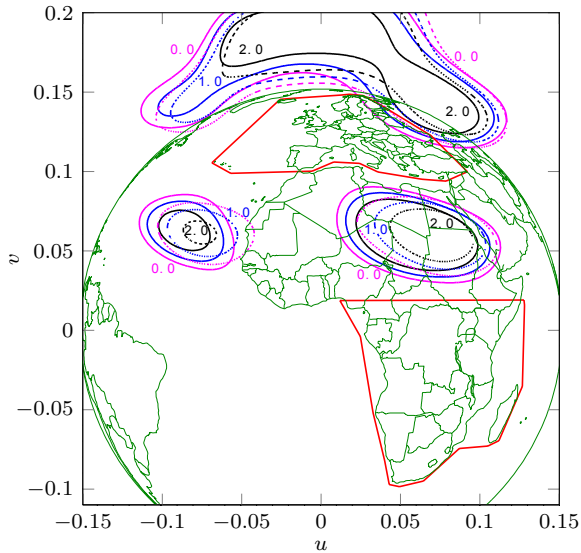
	Peak directivity (dBi)	Min. directivity (dBi)	Min. XPD (dB)	Min. isolation (dB)
Measurement (H-pol.)	29.2	27.3	27.2	24.3
Simulation (H-pol.)	29.2	27.3	27.8	27.2
Measurement (V-pol.)	29.4	27.1	24.5	20.2
Simulation (V-pol.)	29.4	27.1	21.0	20.5

agreement between simulations and measurements is obtained for both polarizations, even though the array elements are positioned in an irregular grid. The sample was only optimized for H-polarization, hence the lower minimum XPD and isolation levels in V-polarization. A similar accuracy has been obtained for the other measured frequencies as well.

These excellent agreements between simulated and measured patterns are close to those obtained for conventional shaped reflectors and thereby verify the accuracy of the GDOT.

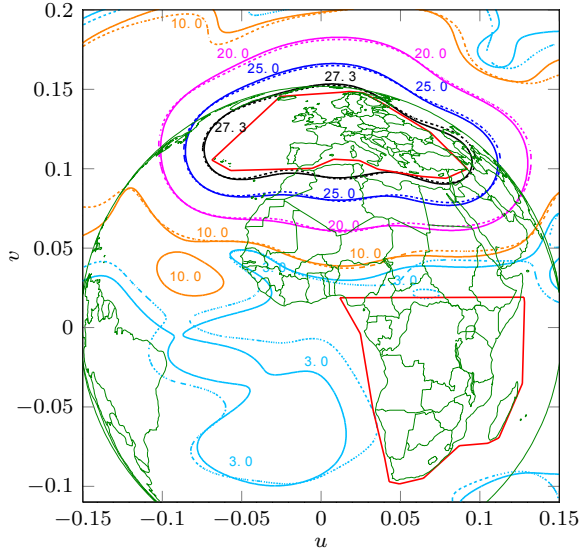


(a)

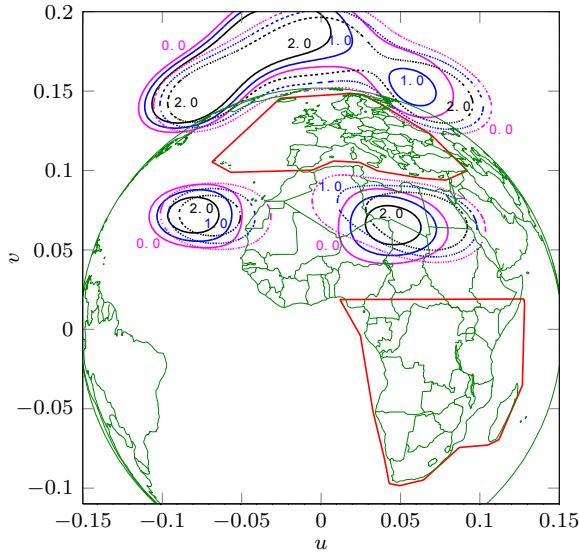


(b)

**Figure 3.11** Simulated (solid lines) and measured (dotted lines) radiation patterns of sample II-I for H-polarization at 10 GHz, (a) co-polar pattern and (b) cross-polar pattern.



(a)



(b)

**Figure 3.12** Simulated (solid lines) and measured (dotted lines) radiation patterns of sample II-II for H-polarization at 10 GHz, (a) co-polar pattern and (b) cross-polar pattern.

### 3.5 Summary

In this chapter, an accurate and efficient generalized direct optimization technique for the design of printed reflectarrays using arbitrarily shaped array elements with irregular orientation and position is presented. It is based on the LP-SDMoM and a minimax optimization algorithm. The geometrical parameters of the array elements, i.e. size, orientation, and position, are directly optimized to fulfill the far-field requirements, thus maintaining a direct relation between optimization goals and optimization variables. As a result, better designs can be obtained compared to the conventional POT.

To ensure high accuracy, efficiency, and flexibility, LegBFs are used in the LP-SDMoM computations and the Floquet harmonics technique is used to calculate the far-field during the optimization. The Floquet harmonics technique uses scattering matrices which are calculated in advance, stored in a look-up table, and accessed during the optimization. Both co- and cross-polar radiation can be optimized for multiple frequencies, dual polarization, and several feed illuminations.

To show the capabilities of the GDOT, several offset contoured beam reflectarrays forming a high-gain beam on a European coverage have been designed: a single-polarized broadband design, a dual-polarized broadband design, a circularly polarized design using the VRT, and an electrically large dual-polarized design.

Finally, to verify the accuracy of the GDOT, two reference reflectarrays designed using the GDOT have been manufactured and measured at the DTU-ESA Spherical Near-Field Antenna Test Facility. An excellent agreement between simulated and measured patterns is obtained.

## CONCLUSIONS

---

In this study, analysis and optimization methods have been investigated with the aim to develop an accurate and efficient simulation tool for the design of printed reflectarrays. The work was divided in two main parts: the investigation of accurate analysis of printed reflectarrays; and the implementation and validation of an accurate and efficient design tool.

As the first step in the process, a survey of existing modeling techniques was presented. The emphasis was on identifying the sources for the lack of accuracy in current reflectarray modeling. Based on this survey, it was deemed that the spectral domain method of moments (SDMoM) assuming local periodicity (LP) is the most attractive technique in terms of the tradeoff between accuracy and efficiency. Therefore, focus in this work was on this technique. Several sources of error in the LP-SDMoM were identified and investigated: the representation of the incident field, the choice of basis functions, the calculation of the far-field, the periodicity assumption, and the assumption of infinite ground plane. To serve as reference for the investigations, two offset pencil beam reflectarrays have been designed and manufactured, and subsequently measured at the DTU-ESA Spherical Near-Field Antenna Test Facility.

The incident field in LP-SDMoM must be correctly represented to ensure accurate results. To this end, measured or accurately simulated feed patterns should be used to calculate the polarization, amplitude, and phase of the incident plane wave on each array element.

In the LP-SDMoM, the choice of basis functions must be carefully selected to ensure an accurate and efficient solution. It was shown that higher-order hierarchical Legendre basis functions (LegBF) can be applied to arbitrarily shaped array elements and have better convergence rate compared to first-order basis functions, e.g. rooftop basis functions. For canonically shaped array elements, e.g. rectangular patches, entire domain singular basis functions are known to accurately account for the singularities of the electric current on the patch edges and for providing very accurate results. It was demonstrated that the LegBFs are capable of producing results of the same accuracy as those obtained using



entire domain singular basis functions using less computation time.

It was shown in this work that the technique to calculate the far-field has a great impact on the analysis accuracy. The finite size of the reflectarray must be accounted for, and techniques that neglect this yield inaccurate results. Several techniques have been considered in this work, and two techniques were capable of yielding accurate results: the Floquet harmonics technique and the continuous spectrum technique. Both techniques are based on the field equivalence principle and can calculate the radiation in the entire hemisphere. Whereas the continuous spectrum technique is more accurate, particularly in the back hemisphere, the Floquet harmonics technique is more efficient and most suitable for optimization purposes.

It has been stated by several research groups that the periodic assumption in the LP-SDMoM can be inaccurate. However, comparisons of simulated and measured radiation patterns showed that the accuracy of the LP-SDMoM is very good, even for highly aperiodic reflectarrays, as long as the three aforementioned sources of error are taken into account. Nevertheless, two techniques to reduce the possible errors introduced by the periodicity assumption have been examined, the surrounded element approach (SEA) and the extended local periodicity (ELP) approach. Both approaches attempt to account for the mutual coupling more realistically by including the actual neighboring elements in the analysis. The SEA is a finite approach where no periodicity is applied, whereas the ELP is based on periodicity but applied to an extended unit-cell. Although both techniques have advantages, they do not necessarily produce more accurate results than the LP-SDMoM, quite the contrary. Furthermore, the overall computation time associated with each technique is high, thus unsuitable for optimization purposes.

Finally, it was shown that the finite size of the ground plane is of little importance for the calculation of the electric currents on the array elements, but has to be taken into account when calculating the far-field.

The aforementioned techniques for the enhanced analysis accuracy have been used to develop a generalized direct optimization technique (GDOT), which can be used for the optimization and design of printed reflectarrays using arbitrarily shaped array elements with irregular orientation and position. The GDOT is based on the LP-SDMoM and a minimax optimization algorithm. Contrary to the conventional phase-only optimization technique (POT), the geometrical parameters of the array elements are directly optimized to fulfill the far-field requirements, thus maintaining a direct relation between optimization goals and optimization variables. Consequently, improved designs can be obtained. Both co- and cross-polar radiation can be optimized for multiple frequencies, dual polarization, and several feed illuminations.

To ensure high accuracy, efficiency, and flexibility, the LegBFs are used to-

gether with the Floquet harmonics technique in the GDOT. The Floquet harmonics technique uses scattering matrices, which are calculated in advance, stored in a look-up table, and accessed during the optimization using local cubic interpolation. This circumvents the calculation of the scattering matrices at each iteration and greatly reduces the overall optimization time. Furthermore, measured or accurately simulated feed patterns can be included in the GDOT to ensure that the reflectarray is optimized for the correct feed illuminations.

For the optimization of the position of the array elements, an irregular distribution of element positions is achieved by adding a distortion to the regular grid. The distortion used in this work is based on Chebyshev polynomials. Due to the distortion of the grid, the array elements are positioned in a non-periodic lattice and the accuracy of the LP-SDMoM had to be investigated. It was demonstrated by comparisons with full-wave method of moments that the LP-SDMoM is very accurate, despite the strong irregularities.

To demonstrate the capabilities of the GDOT, several offset contoured beam reflectarrays have been designed and presented in this thesis. These designs illustrated that the GDOT is capable of designing reflectarrays with improved performance compared to those obtained using the conventional POT. Furthermore, they demonstrated that the GDOT can optimize for the size, orientation, and the position of arbitrarily shaped array elements. Finally, the designs demonstrated the GDOT's ability to design electrically large reflectarrays as well as broadband reflectarrays with low cross-polarization.

For verification of the accuracy of the GDOT, two of the aforementioned contoured beam reflectarrays have been manufactured and measured at the DTU-ESA Spherical Near-Field Antenna Test Facility. An excellent agreement between simulations and measurements was obtained for both reflectarrays. The prediction accuracy between simulated and measured patterns is close to those obtained for conventional shaped reflectors, thus verifying the accuracy of the GDOT.

It is expected that with the GDOT, advanced reflectarrays with enhanced performance can be designed, thereby improving the usability of printed reflectarrays.

The work presented in this thesis can be extended in many ways. First, only reflectarrays on a single layer substrate with rectangular rim are presented in this work. The GDOT should be developed to allow multi-layer configurations with circular or elliptical rim. Second, for large reflectarrays consisting of many array elements, the number of optimization variables is exceedingly high and the optimization becomes slow. To alleviate this problem, cubic splines are included in the GDOT to represent the sizes of the array elements. However, the variation of the dimensions of the array elements can have discontinuities due to the  $360^\circ$  phase jump, and these discontinuities are hard to represent using

splines. Techniques to improve the spline implementation, and thereby reducing the overall optimization time, are currently being investigated. Finally, the GDOT could be extended to allow array elements to be located on a curved surface. This eliminates the differential spatial phase delay from the feed and increases the bandwidth for large reflectarrays. Although this complicates the manufacturing of the reflectarrays, it is, however, an attractive technique for contoured beam applications because a single mold can then be reused for several shaped beam applications.

# Appendices



## DESIGN OF THE REFLECTARRAY SAMPLES

---

In this appendix, the choice and design of the reflectarray samples measured in the two measurement campaigns are presented. The reflectarray samples were manufactured at the workshop at EMS-DTU and measured at the DTU-ESA Spherical Near-Field Antenna Test Facility.

### A.1 Geometrical and Electrical Parameters

The geometrical parameters of the reflectarrays are shown in Figure A.1. The dimensions of the reflectarray along  $x$  and  $y$  are denoted  $d_x$  and  $d_y$ , respectively,  $d_f$  denotes the distance from the aperture center of the feed to the center of the reflectarray,  $\theta^i$  and  $\phi^i$  describe the incidence angles from the feed to the reflectarray center. The number of array elements along  $x$  and  $y$  are denoted  $N_x$  and  $N_y$ , respectively.

Feed horns operating around 10 GHz were available at the DTU-ESA Spherical Near-Field Antenna Test Facility and the reflectarrays were designed for this frequency.

Square patches with varying sizes are used as array elements in all the samples. The dielectric substrate is Rogers 4350 with dielectric constant  $\epsilon_r = 3.66$ , loss tangent  $\tan \delta = 0.0037$ , and substrate thickness 0.762 mm.<sup>1</sup>

To avoid any blockage from the support structures or the feed, only offset configurations have been considered.

---

<sup>1</sup>The reflectarray samples for the first measurement campaign were initially designed using a dielectric constant of  $\epsilon_r = 3.48$  as was stated in the Rogers Data sheet. However, it was not before after the measurements were completed that it was discovered that the actual value was  $\epsilon_r = 3.66$ . As a result, the resonance frequency was shifted from 10 GHz to 9.6 GHz, where the best performance of the reflectarray samples was observed.

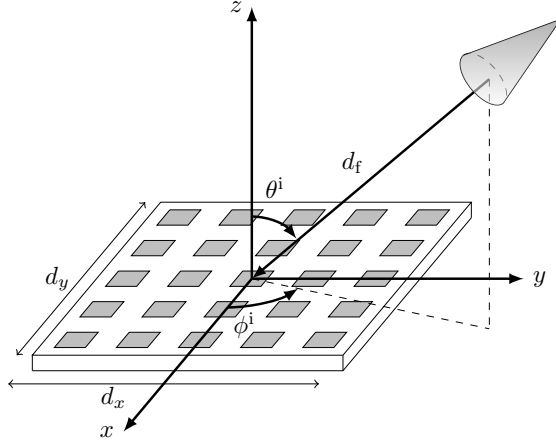


**Figure A.1** *Reflectarray geometrical parameters.*

## A.2 Measurement Campaign I

Two reflectarrays have been designed for the first measurement campaign. The reflectarrays were designed to exaggerate two of the sources of error as described in Chapter 2, and to serve as reference solutions for the algorithms developed during the study.

At the time of the first measurement campaign, no optimization routine was implemented, thus the reflectarrays were designed by means of phase curves.

### A.2.1 Sample I-I

The mask layout of sample I-I is shown in Figure A.2 and aims to exaggerate the incorrect analysis of the elements at the edges of the reflectarray due to the assumption of infinite ground plane. To this end, the patch variations must be as smooth as possible to reduce the errors introduced by the periodicity assumption when using the local periodicity (LP) approach. To achieve this, the main beam of this reflectarray is directed towards the specular direction. The incidence angle from the feed to the center of the reflectarray is  $\theta^i = 30^\circ$  and  $\phi^i = 0^\circ$ , hence the reflectarray is synthesized to have its main beam towards  $\theta = -30^\circ$  and  $\phi = 0^\circ$ .

To reduce the aperiodicity, the differential spatial phase delay has to be small. This was achieved by increasing the distance between the feed and the reflectarray surface. For this sample, the feed is located  $d_f = 600$  mm from the reflectarray center. In addition, a low-gain feed is preferred to ensure a high

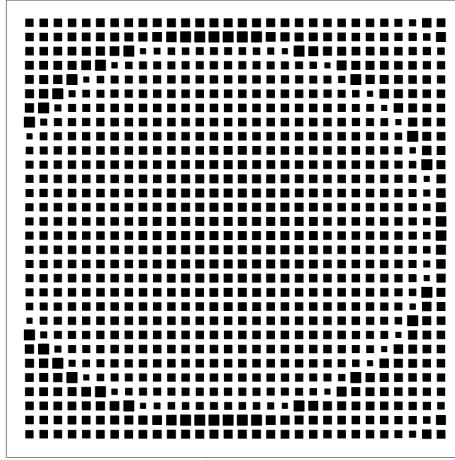


**Figure A.2** *The mask layout of sample I-I. The sample is designed to have main beam towards  $\theta = -30^\circ$  and  $\phi = 0^\circ$ .*

edge illumination of the reflectarray. Based on the main beam direction and the feed's position, the required phase distribution was determined and the patch sizes were readily obtained from the phase curve. The geometrical parameters are summarized in Table A.1.

**Table A.1** *Geometrical parameters for sample I-I*

$f$ [GHz]	$N_x \times N_y$	$d_x/d_y$ [mm]	$d_f$ [mm]	$\theta^i/\phi^i$ [ $^\circ$ ]
10	$30 \times 30$	435/435	600	30/0

### A.2.2 Sample I-II

This sample attempts to exaggerate the errors introduced by the periodicity assumption, thus a strong aperiodicity was created by steering the main beam towards  $\theta = 35^\circ$  and  $\phi = 135^\circ$ . To reduce the errors due to the assumption of infinite ground plane, the edge illumination should be low. Thus a high gain feed is preferred and the distance between the feed and the reflectarray should be small. The feed is located  $d_f = 350$  mm from the reflectarray center with an incidence angle of  $\theta^i = 45^\circ$  and  $\phi^i = 0^\circ$  towards the center. This results in the mask layout shown in Figure A.3. The geometrical parameters are summarized in Table A.2.



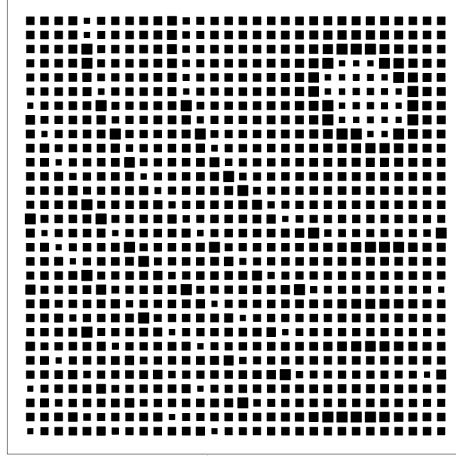


**Figure A.3** The mask layout of sample I-II. The sample is designed to have main beam towards  $\theta = 35^\circ$  and  $\phi = 135^\circ$ .

**Table A.2** Geometrical parameters for reflectarray sample I-II

$f$ [GHz]	$N_x \times N_y$	$d_x/d_y$ [mm]	$d_f$ [mm]	$\theta^i/\phi^i$ [ $^\circ$ ]
10	$30 \times 30$	435/435	350	45/0

### A.2.3 Feed Horns

Two horns were used as feed for the reflectarray samples: a high-gain corrugated horn (Figure A.4a), and a low-gain Potter horn (Figure A.4b). Each horn was used on both samples giving a total of 4 different reflectarray configurations to be measured. At 10 GHz, the corrugated horn has a taper of  $-17.5$  dB at  $30^\circ$ , whereas the Potter horn has a taper of  $-7$  dB at  $30^\circ$ .

## A.3 Measurement Campaign II

The purpose of the reflectarray samples in the second measurement campaign was to verify the accuracy of the generalized direct optimization technique (GDOT) that is presented in Chapter 3.

At the time of the measurements, the GDOT was restricted to the optimization of reflectarrays consisting of square patches at a single frequency. Thus, multi-frequency designs with advanced element types were not possible for this measurement campaign.

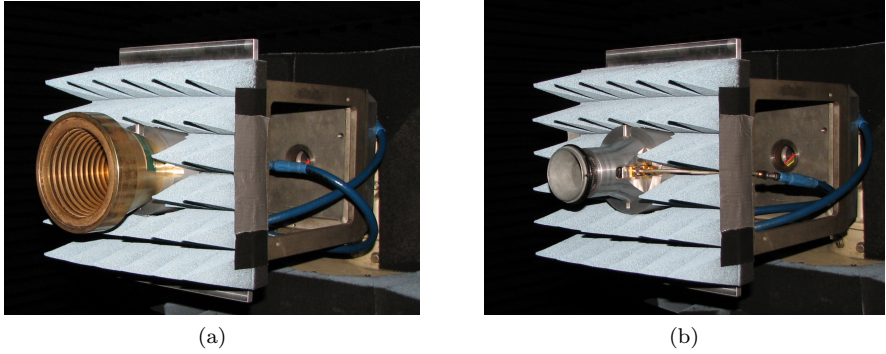


**Figure A.4** *The two horn antennas used in the measurement campaigns, (a) the corrugated horn and (b) the Potter horn.*

It was decided to design two reflectarray samples, a regular design and an irregular design. To reuse as much as possible from the first measurement campaign, the support structures from sample I-I were reused. Thus the feed position and orientation were maintained. The corrugated horn from Figure A.4a was used as feed and the measured pattern obtained in the first measurement campaign was used in the optimization of the reflectarray samples.

The two samples were designed to radiate contoured beams. To ensure reasonable results, the dimension of the reflectarrays was increased to  $600 \times 600 \text{ mm}^2$  corresponding to  $20 \times 20$  square wavelengths at 10 GHz. Square patches were used as array elements. The geometrical parameters for the two samples are summarized in Table A.3.

**Table A.3** *Geometrical parameters for samples II-I and II-II.*

$f [\text{GHz}]$	$N_x \times N_y$	$d_x/d_y [\text{mm}]$	$d_f [\text{mm}]$	$\theta^i/\phi^i [^\circ]$	$\theta^f/\phi^f [^\circ]$
10	$50 \times 50$	600/600	600	30/0	30/0

### A.3.1 Choice of Design

For both samples, a European high-gain coverage with cross-polar suppression within the same coverage and sidelobe suppressions within a southern African contour was considered. The coverages are shown in Figure A.5 as the red polygons. Prior to the final designs, a large number of design iterations were performed and many interesting results were found. Details will not be described, but the observations can be summarized as follows:

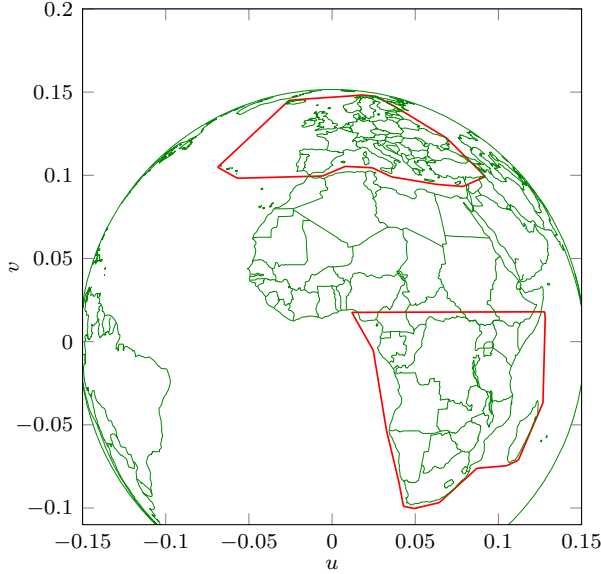


**Figure A.5** *European and southern African coverages seen from the longitude  $0^\circ$  geostationary orbital position.*

- 1 If only a co-polar beam is optimized for a single polarization, a reflectarray with irregular grid performs just as well as a reflectarray with a regular grid<sup>2</sup>. Thus, nothing is gained by using an irregular design in this case.
- 2 If cross-polar suppression (within Europe) and sidelobe suppression (within southern Africa) are included, but still for a single polarization, some performance improvements can be obtained with an irregular grid. The improvements are small, but worthwhile to investigate.
- 3 If cross-polar suppression (within Europe) and sidelobe suppression (within southern Africa) are included and optimized for two orthogonal polarizations i.e. V- and H-polarization, good results can be obtained with a regular grid, but no further improvement is gained with an irregular grid.

These conclusions are preliminary and restricted to the particular type of grid distortions considered in this work. More general grids e.g. polar or elliptical grids have not been investigated and may lead to different results.

---

<sup>2</sup>For more information on reflectarrays with irregular grids, see Section 3.2.5.

Based on these observations, it was decided that the two samples should be designed for different specifications.

The first sample (sample II-I) uses a regular grid and was optimized according to 3). The second sample (sample II-II) was optimized according to 2) and has an irregular grid.

### A.3.2 Sample II-I

The design procedure for sample II-I involved several steps and is briefly described in the following.

In the first optimization (Design I), the goal was to achieve maximum co-polar directivity within the European coverage, and no cross-polar or sidelobe suppressions were specified in the optimization. The initial starting point for the optimization consisted of identical patches of resonant size. In this design, the minimum directivity within the European coverage for both polarizations was 27.4 dBi. The minimum cross polarization discrimination (XPD) was 21.5 dB and the minimum high/low (Europe/Africa) isolation was 18 dB.

In the second optimization (Design II), cross-polar suppression within the European coverage was added and Design I was used as the initial starting point. The minimum XPD was improved to 26 dB. However, this was at the cost of almost 1 dB reduction in the minimum co-polar directivity, which was approximately 26.7 dBi. The minimum isolation was unchanged.

Sidelobe suppression within the southern African coverage was finally added in the optimization and Design II was used as the initial starting point. The radiation of the final design for H-polarization at 10 GHz is shown in Figure A.6. The co-polar radiation in the southern African coverage for both polarizations have been greatly reduced to a minimum isolation above 25 dB, while maintaining the minimum co-polar level on the European coverage at 26.7 dBi. This improvement was obtained at the cost of the cross-polar radiation where the minimum XPD was decreased to 25.5 dB. The mask of the final sample is shown in Figure A.7.

The performance of the different designs are summarized in Table A.4.

**Table A.4** *Summary of the design iterations for sample II-I*

	Design I	Design II	Sample II-I
Min. directivity (dBi)	27.4	26.7	26.7
Min. XPD (dB)	21.5	26.0	25.5
Min. isolation (dB)	18.0	18.0	25.0

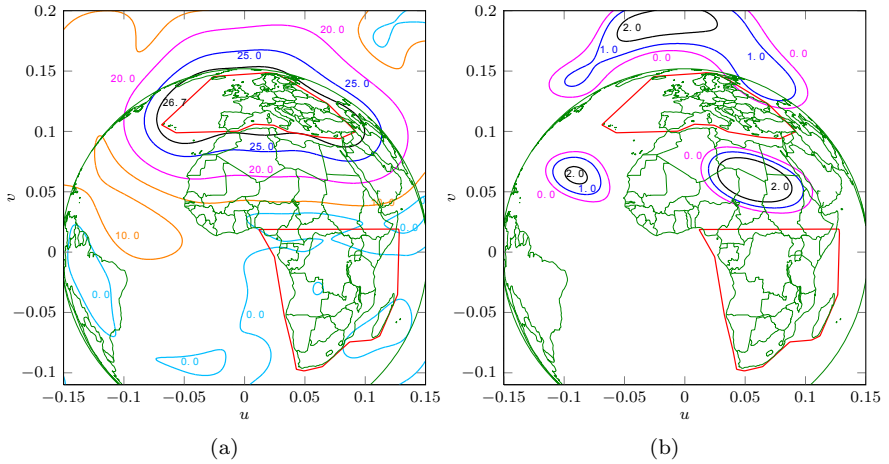


**Figure A.6** Simulated radiation patterns of sample II-I for H-polarization at 10 GHz, (a) co-polar pattern and (b) cross-polar pattern.

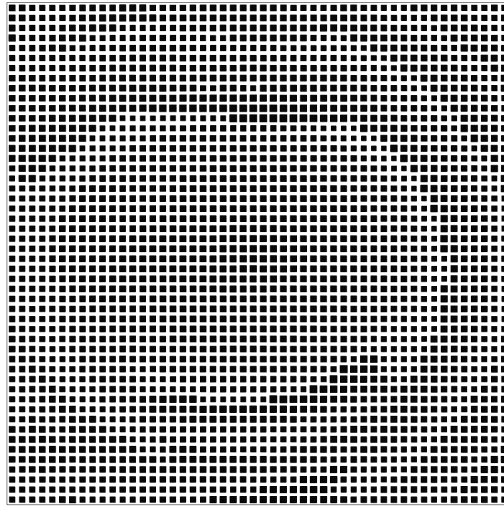


**Figure A.7** Mask layout of sample II-I.

### A.3.3 Sample II-II

Sample II-II was designed with the same goals as sample II-I, but optimized only for H-polarization. The design process was similar to sample II-I except that the reflectarray uses an irregular grid. A detailed description of the design process will not be given. The mask layout of sample II-II is shown in Figure A.8 and the radiation patterns for H-polarization at 10 GHz are shown in Figure A.9. A minimum directivity of 27.3 dBi is obtained within the European coverage with a minimum XPD of 28.3 dB. The isolation level is at 27.6 dB.

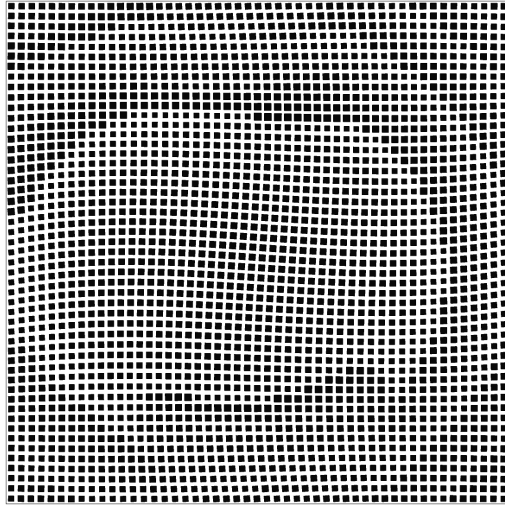
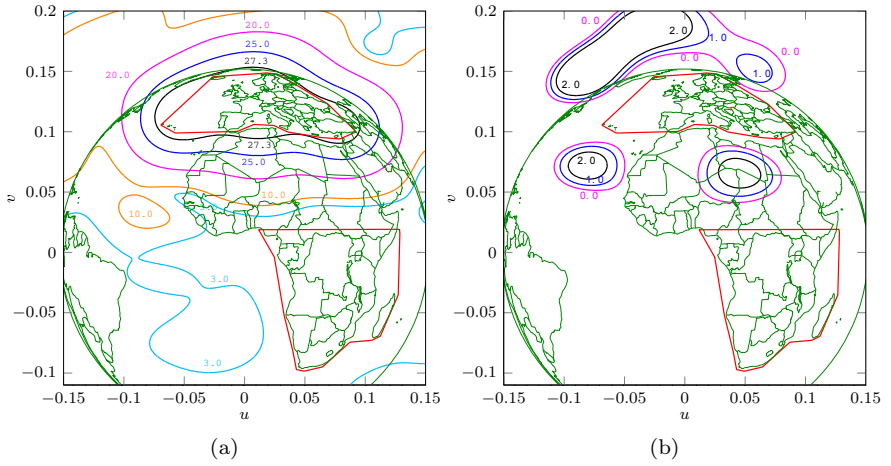


Figure A.8 *Mask layout of sample II-II.*



**Figure A.9** Simulated radiation patterns of sample II-II for H-polarization at 10 GHz, (a) co-polar pattern and (b) cross-polar pattern.

## MEASUREMENT RESULTS

---

Additional measurement results from the two measurement campaigns at DTU-ESA Spherical Near-Field Antenna Test Facility are presented in this appendix.

All the simulated results shown in this appendix are obtained using the spectral domain method of moments (SDMoM) assuming local periodicity. Higher-order hierarchical Legendre basis functions are used in the SDMoM and the far-field is calculated using the continuous spectrum technique<sup>1</sup>. In addition, the scattering from the support structures have been included using the GRASP MoM add-on.

### B.1 Measurement Campaign I

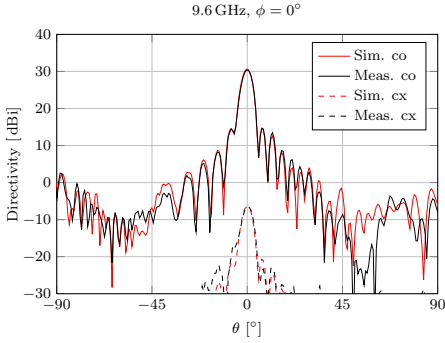
During the design of the reflectarray samples for the first measurement campaign, the dielectric constant was initially selected to  $\epsilon_r = 3.48$  as was stated in the substrate data sheet. However, after the measurements were complete, it was discovered that the actual value was  $\epsilon_r = 3.66$ . This resulted in a shift in the resonance frequency from 10 GHz to 9.6 GHz, where the best performance of the reflectarray samples was observed. Therefore, radiation patterns are shown for 9.6 GHz in this section, even though the measurements were carried out in a series of frequencies between 9.6 – 10.5 GHz. The results are shown in Figures B.1-B.4. The accuracy in the other measured frequencies is very similar to those shown in this section.

The radiation patterns are shown in a coordinate system defined with its  $z$ -axis directed towards the main beam direction. In Figure B.1a, B.1c, B.2a, and B.2c, strong discrepancies between simulations and measurements around  $\theta = 60^\circ$  are observed. These errors are due to the blockage of the feed and/or the measurement tower. Overall, the agreement between simulations and measurements is very good.

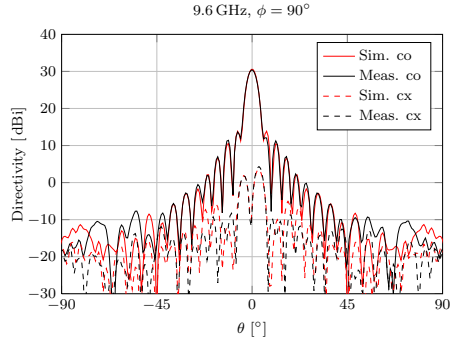
---

<sup>1</sup>For more information on the higher-order hierarchical Legendre basis functions and the continuous spectrum technique, see Chapter 2.

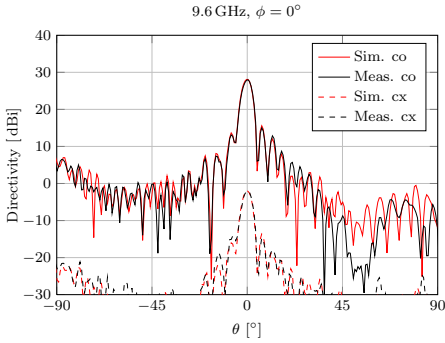




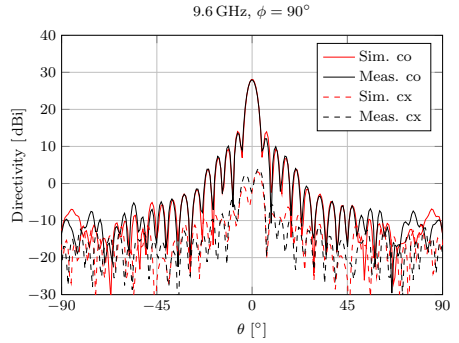
(a) Sample I-I, corrugated horn, H-pol.



(b) Sample I-I, corrugated horn, H-pol.

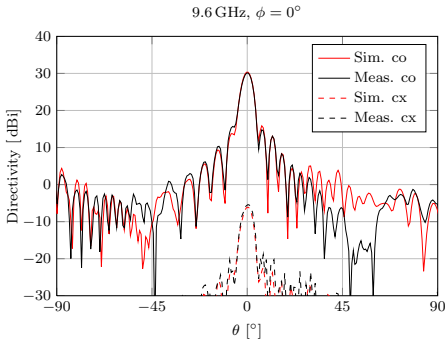


(c) Sample I-I, Potter horn, H-pol.

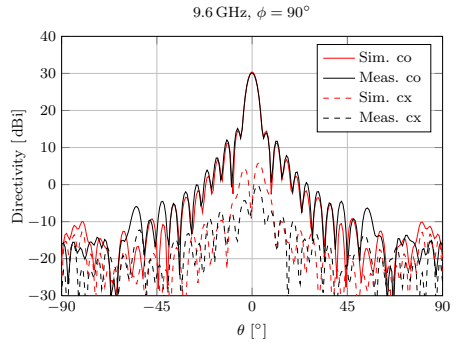


(d) Sample I-I, Potter horn, H-pol.

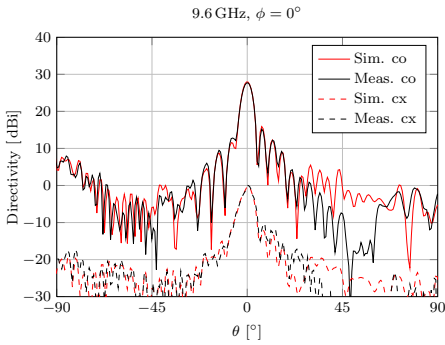
**Figure B.1**



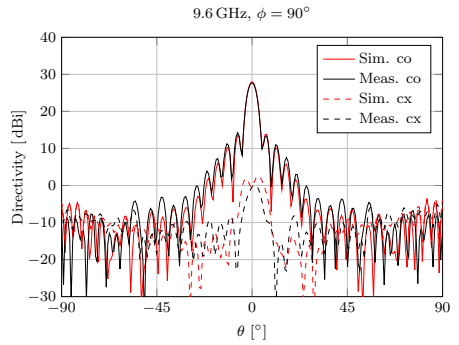
(a) Sample I-I, corrugated horn, V-pol.



(b) Sample I-I, corrugated horn, V-pol.

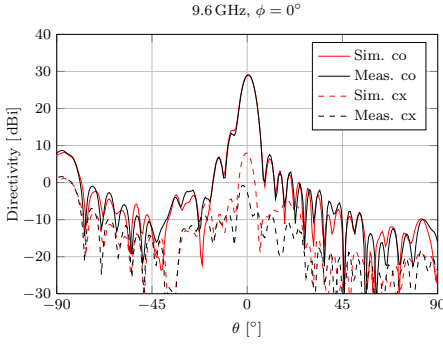


(c) Sample I-I, Potter horn, V-pol

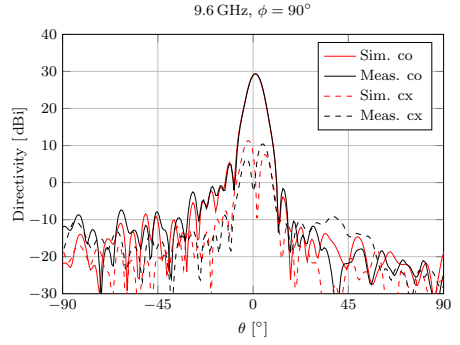


(d) Sample I-I, Potter horn, V-pol.

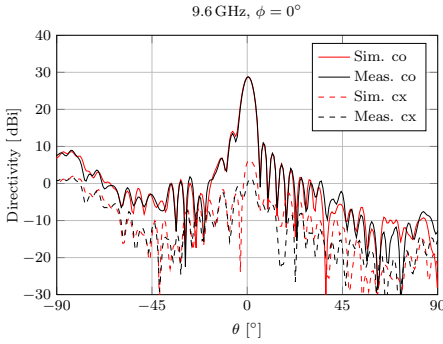
**Figure B.2**



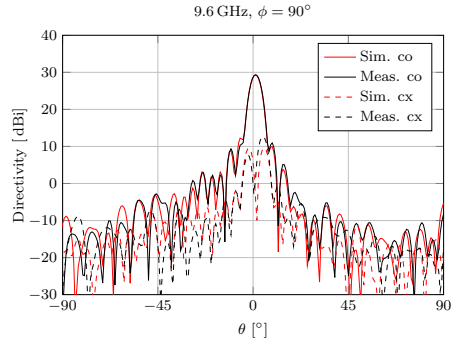
(a) Sample I-II, corrugated horn, H-pol.



(b) Sample I-II, corrugated horn, H-pol.

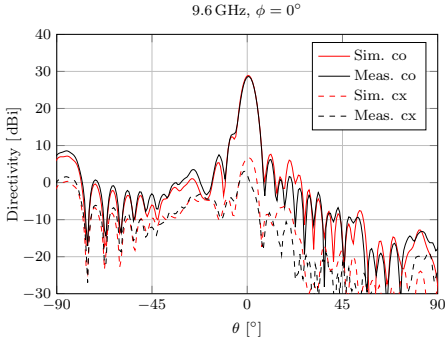


(c) Sample I-II, Potter horn, H-pol.

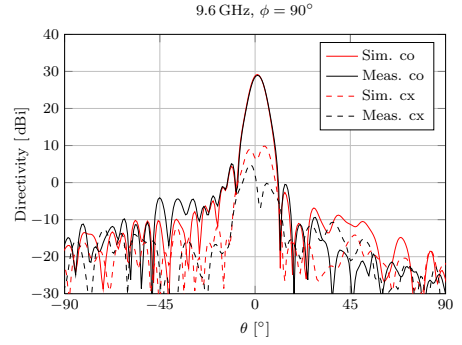


(d) Sample I-II, Potter horn, H-pol.

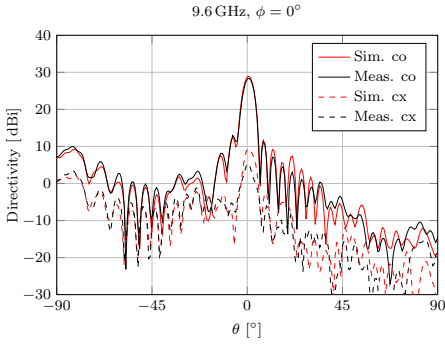
**Figure B.3**



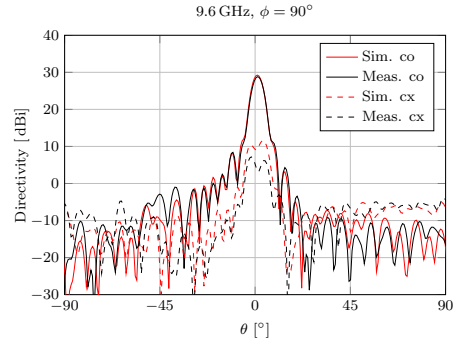
(a) Sample I-II, corrugated horn, V-pol.



(b) Sample I-II, corrugated horn, V-pol.



(c) Sample I-II, Potter horn, V-pol.



(d) Sample I-II, Potter horn, V-pol.

**Figure B.4**

## B.2 Measurement Campaign II

In the initial comparison of the simulations and measurements of sample II-I, it was observed that the measured results were slightly shifted in  $v = \sin \theta \sin \phi$  compared to the simulations. The same offset existed in the other measured fre-

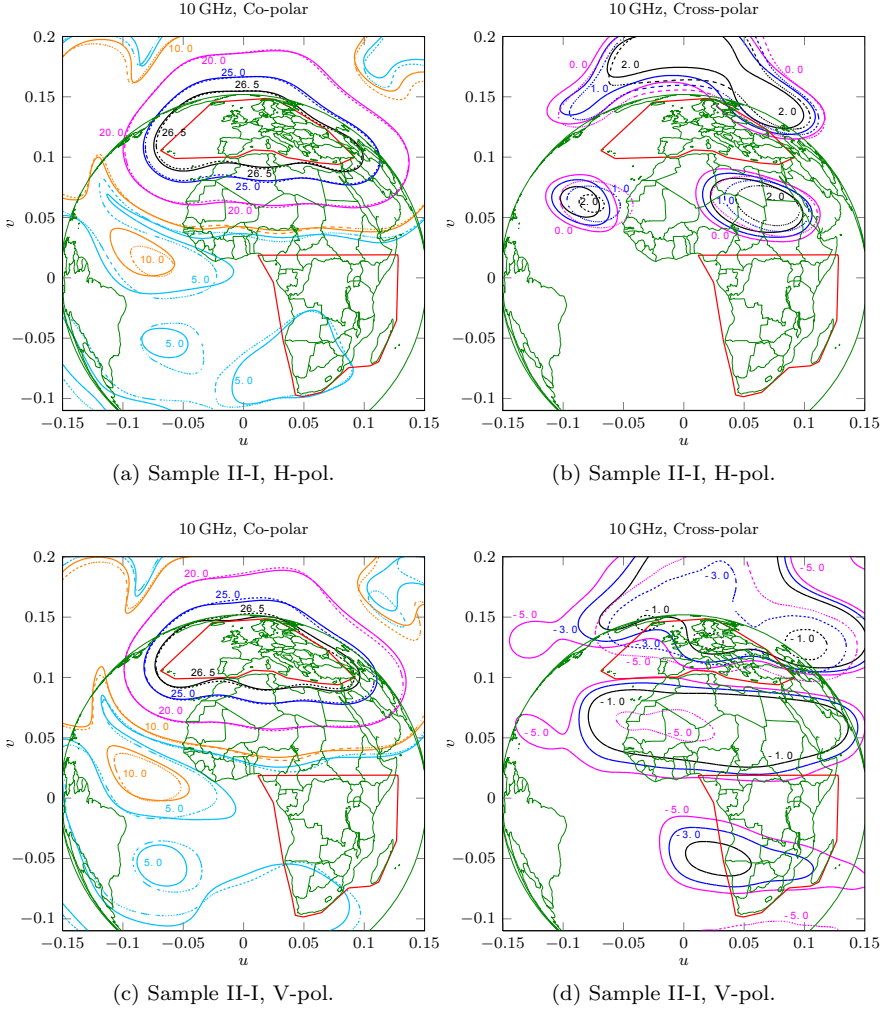


Figure B.5

quencies as well, thus indicating that the source could be by manufacturing errors. After thorough numerical investigations, it is found that the offset can be caused by a slight tilt or shift of the reflectarray plane in the manufactured sample. This was indeed the case and was confirmed by the workshop. It was discovered that the reflectarray plane was shifted by 1 mm in the  $y$ -direction, and that it also was tilted by  $\theta = -0.2^\circ$  at  $\phi = 90^\circ$ . These manufacturing errors were included

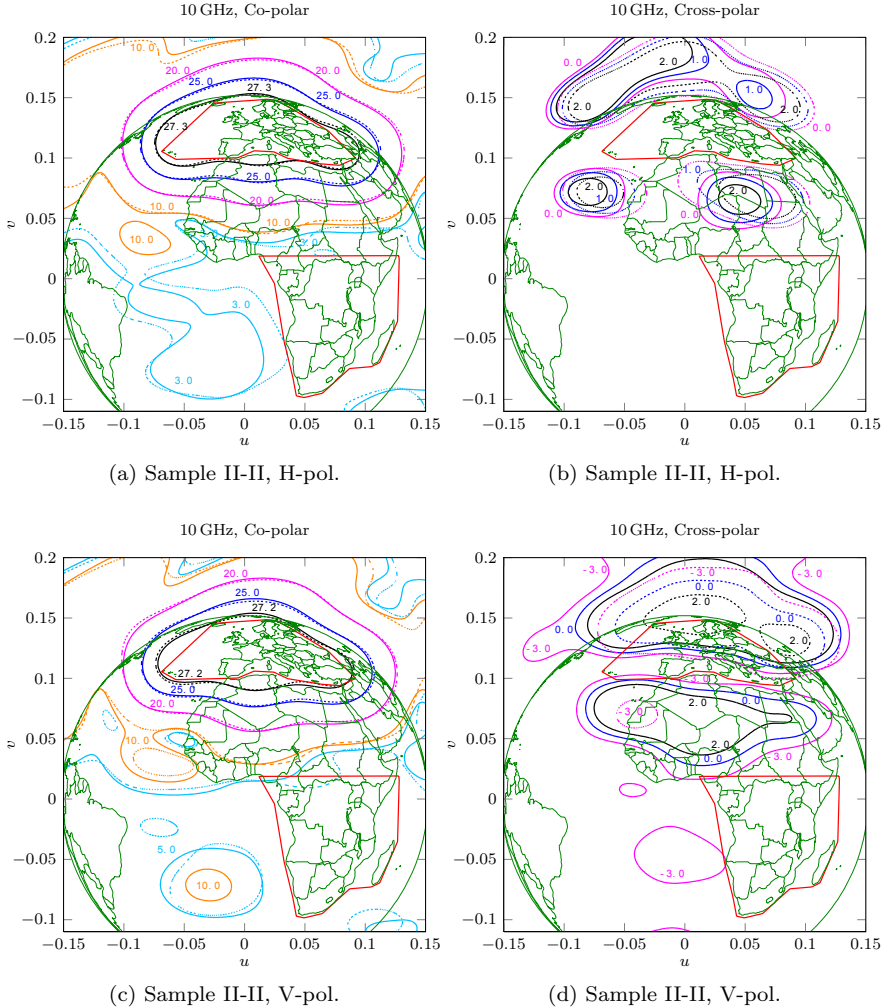


Figure B.6

in the analysis and the simulation showed a result that corresponds very well to the original measured data.

If the measured data is shifted  $v = \sin \theta \sin \phi = -0.0075$ , which corresponds to  $\theta = -0.4^\circ$ , the results shown in Figure B.5 are obtained. It is seen that a very good agreement between simulations and measurements is obtained.

A similar offset was observed for the measured data of sample II-II. By shifting the measured data by  $u = \sin \theta \cos \phi = 0.001$  and  $v = \sin \theta \sin \phi = -0.004$ , the results shown in Figure B.6 are obtained. Similar to sample II-I, the offset was frequency independent and was observed in all measured frequencies. It is expected that a similar manufacturing error is the cause of this offset. However, this could not be confirmed by the workshop as the reflectarray was already dismantled at the time.

The accuracy in the other measured frequencies was also very good for both samples. The co-polar radiations for sample II-I at the extreme frequencies 9.6 GHz and 10.5 GHz are shown in Figure B.7 showing a very good agreement. The radiation patterns for both samples II-I and II-II for all measured frequencies show that the maximum deviation between simulations and measurements of the minimum directivity within the European coverage is within  $\pm 0.1$  dB.

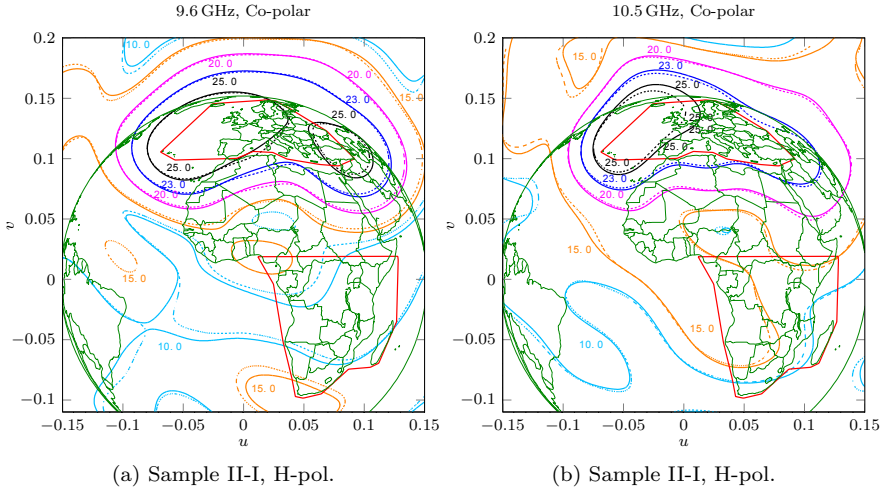


**Figure B.7**

# SPECTRAL DOMAIN MoM FOR PERIODIC MULTILAYER CONFIGURATIONS

---

This appendix deals with the derivation of the integral equation formulation and the spectral domain method of moments (SDMoM) for periodic multilayer configurations.

## C.1 Configuration

Consider a multilayer configuration consisting of  $S$  interfaces as shown in Figure C.1a where the interfaces are located at  $z = z_1, z_2, \dots, z_S$ . Each layer is characterized by the constitutive parameters  $\epsilon_s$  and  $\mu_s$  and has a width of  $d_s = z_{s+1} - z_s$ . At each interface, there is an infinite array of periodically located patches. The periodicity is shown in Figure C.1b, where the parallelograms indicate the periodic unit-cells in the infinite structure seen in the  $xy$ -plane. The quantities  $d_x$  and  $d_y$  are the side lengths of the parallelogram and  $\Omega$  is the angle between the two sides. In the configuration in Figure C.1a, layer  $S$  is extended to infinity and no ground plane is included. For reflectarrays, layer  $S$  is truncated by a perfectly electrically conducting (PEC) ground plane as shown in Figure C.2.

## C.2 Outline of the Formulation

The formulation of the multilayer configuration solution will be outlined in the following.

Due to the periodicity of the configuration, the electric currents on the printed elements as well as the electric/magnetic fields can be expressed, using Floquet's theorem, by summations of Floquet spatial harmonics. These spatial harmonics are plane waves, thus if one plane wave solution can be found, the problem can be solved by summing all the plane wave solutions. The boundary conditions imply that the tangential electric field is continuous across any inter-



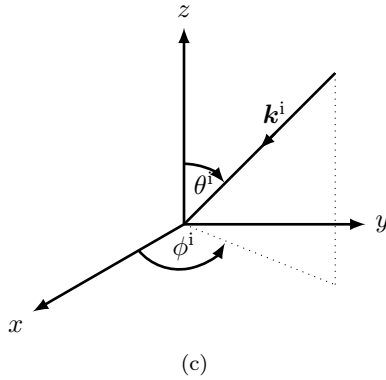
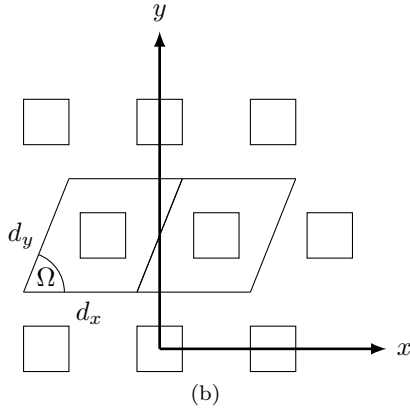
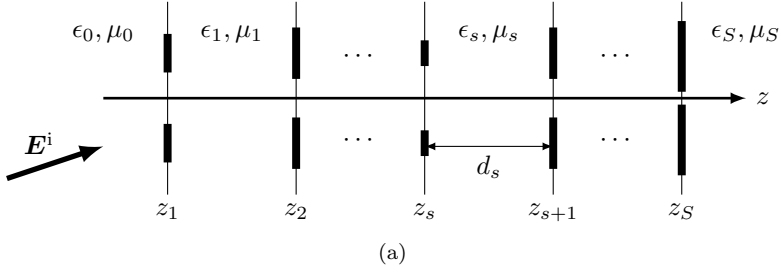


**Figure C.1** (a) Multilayer configuration with periodically located patches at each interface. (b) An infinite array of periodically located patches. (c) Coordinates for the incident plane wave.

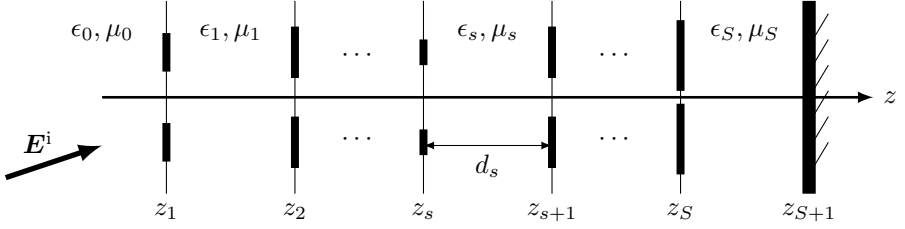


**Figure C.2** Multilayer configuration with periodically located patches at each interface with a PEC ground plane located at  $z = z_{S+1}$ .

face whereas the tangential magnetic field is continuous over any non-metallic interface. Since the printed elements are placed at each interface, the tangential components of the magnetic field will experience a discontinuity due to the induced surface currents on the metallic patches. The unknown surface currents are the objectives of this formulation. The following steps must be done to determine these currents:

1. Express the field and current quantities as double summations of Floquet harmonics.
2. Express the electric field in terms of its tangential components.
3. Determine the magnetic field in terms of the tangential components of the electric field.
4. Enforce the boundary condition for the magnetic field to relate the unknown current densities to the tangential components of the electric field.
5. The interfaces at  $z_1$  and  $z_S$  need to be treated separately since these interfaces include a half space.
6. Enforce the boundary condition for the electric field on the metallic patches to arrive at a formulation where the unknown currents densities can be expanded by basis functions, which can then be solved by using method of moments (MoM).

### C.3 SDMoM Formulation

#### C.3.1 Periodic Multilayer Configuration

From Floquet's theorem the unknown current density on interface  $s$  can be expressed as summations of spatial harmonics in a Fourier series

$$\mathbf{J}_s(\boldsymbol{\rho}, z_s) = \sum_{m,n=-\infty}^{\infty} \mathbf{j}_{mns} e^{-j\boldsymbol{\beta}_{mn} \cdot \boldsymbol{\rho}}, \quad (\text{C.1})$$

where  $\boldsymbol{\rho} = \hat{x}x + \hat{y}y$ , and  $\mathbf{j}_{mns}$  is the Fourier coefficient given by

$$\mathbf{j}_{mns} = \frac{1}{A_U} \iint_U \mathbf{J}_s(\boldsymbol{\rho}, z_s) e^{j\boldsymbol{\beta}_{mn} \cdot \boldsymbol{\rho}} dxdy. \quad (\text{C.2})$$

Herein,  $A_U = d_x d_y \sin \Omega$  is the area of the unit-cell and  $\boldsymbol{\beta}_{mn}$  is defined as

$$\begin{aligned} \boldsymbol{\beta}_{mn} &= \hat{x}\beta_{xmn} + \hat{y}\beta_{ymn} \\ &= \hat{x} \left( k_x^i + \frac{2\pi m}{d_x} \right) + \hat{y} \left( k_y^i + \frac{2\pi n}{d_y \sin \Omega} - \frac{2\pi m}{d_x} \cot \Omega \right), \end{aligned} \quad (\text{C.3})$$

where  $k_x^i$  and  $k_y^i$  are given by the incident propagation vector

$$\mathbf{k}^i = \hat{x}k_x^i + \hat{y}k_y^i + \hat{z}k_z^i, \quad (\text{C.4})$$

as shown in Figure C.1c. Similarly, the electric/magnetic field in layer  $s$  can be expressed using spatial harmonics. However, contrary to  $\mathbf{J}_s$ , the electric/magnetic fields are also present between the interfaces and both forward and backward propagating waves exist in each layer. Thus the electric field in layer  $s$  is expressed as summations of forward and backward propagating plane waves

$$\begin{aligned} \mathbf{E}_s(\mathbf{r}) &= \sum_{m,n=-\infty}^{\infty} \boldsymbol{\mathcal{E}}_{mns}^+ e^{-j\mathbf{k}_{mns}^+ \cdot \mathbf{r}_s} + \sum_{m,n=-\infty}^{\infty} \boldsymbol{\mathcal{E}}_{mns}^- e^{-j\mathbf{k}_{mns}^- \cdot \mathbf{r}_s} \\ &= \sum_{m,n=-\infty}^{\infty} \left( \boldsymbol{\mathcal{E}}_{mns}^+ e^{-j\gamma_s^{mn}(z-z_s)} + \boldsymbol{\mathcal{E}}_{mns}^- e^{j\gamma_s^{mn}(z-z_s)} \right) e^{-j\boldsymbol{\beta}_{mn} \cdot \boldsymbol{\rho}}. \end{aligned} \quad (\text{C.5})$$

Here,  $\mathbf{k}_{mns}^{\pm} = \boldsymbol{\beta}_{mn} \pm \hat{z}\gamma_s^{mn}$  where

$$\gamma_s^{mn} = \begin{cases} \left| \sqrt{k_s^2 - \beta_{xmn}^2 - \beta_{ymn}^2} \right|, & \beta_{xmn}^2 + \beta_{ymn}^2 \leq k_s^2, \\ -j \left| \sqrt{\beta_{xmn}^2 + \beta_{ymn}^2 - k_s^2} \right|, & \beta_{xmn}^2 + \beta_{ymn}^2 > k_s^2, \end{cases} \quad (\text{C.6})$$

with  $k_s = \omega\sqrt{\epsilon_s\mu_s}$  being the wave number in layer  $s$ . Likewise, the magnetic field in layer  $s$  can be determined using

$$\begin{aligned} \mathbf{H}_s(\mathbf{r}) &= \sum_{m,n=-\infty}^{\infty} \mathcal{H}_{mns}^+ e^{-j\mathbf{k}_{mn}^+ \cdot \mathbf{r}_s} + \sum_{m,n=-\infty}^{\infty} \mathcal{H}_{mns}^- e^{-j\mathbf{k}_{mn}^- \cdot \mathbf{r}_s} \\ &= \sum_{m,n=-\infty}^{\infty} \left( \mathcal{H}_{mns}^+ e^{-j\gamma_s^{mn}(z-z_s)} + \mathcal{H}_{mns}^- e^{j\gamma_s^{mn}(z-z_s)} \right) e^{-j\boldsymbol{\beta}_{mn} \cdot \boldsymbol{\rho}}. \end{aligned} \quad (\text{C.7})$$

The boundary conditions at the patches state that

$$\mathbf{J}_s(\boldsymbol{\rho}, z_s) = \hat{z} \times \left[ \mathbf{H}_s(\boldsymbol{\rho}, z_s) - \mathbf{H}_{s-1}(\boldsymbol{\rho}, z_s) \right], \quad s = 1, 2, \dots, S. \quad (\text{C.8})$$

Substituting (C.1) and (C.7) in the above yields

$$\begin{aligned} \sum_{m,n=-\infty}^{\infty} \mathbf{j}_{mns} e^{-j\boldsymbol{\beta}_{mn} \cdot \boldsymbol{\rho}} &= \hat{z} \times \left[ \sum_{m,n=-\infty}^{\infty} \left( \mathcal{H}_{mns}^+ + \mathcal{H}_{mns}^- - \right. \right. \\ &\quad \left. \left. \mathcal{H}_{mn(s-1)}^+ e^{-j\gamma_{s-1}^{mn} d_{s-1}} - \mathcal{H}_{mn(s-1)}^- e^{j\gamma_{s-1}^{mn} d_{s-1}} \right) e^{-j\boldsymbol{\beta}_{mn} \cdot \boldsymbol{\rho}} \right]. \end{aligned} \quad (\text{C.9})$$

It is now utilized that (C.9) must be fulfilled term-wise

$$\mathbf{j}_{mns} = \hat{z} \times \left( \mathcal{H}_{mns}^+ + \mathcal{H}_{mns}^- - \mathcal{H}_{mn(s-1)}^+ e^{-j\gamma_{s-1}^{mn} d_{s-1}} - \mathcal{H}_{mn(s-1)}^- e^{j\gamma_{s-1}^{mn} d_{s-1}} \right). \quad (\text{C.10})$$

If a solution of the above can be found, then the uniqueness theorem states that the solution is unique and is the correct solution.

The spatial harmonics in (C.5) are plane waves. Consequently, the complex amplitude of each spatial harmonic is orthogonal to the propagating vector of the plane wave

$$\boldsymbol{\mathcal{E}}_{mns}^{\pm} \cdot \mathbf{k}_{mns}^{\pm} = 0. \quad (\text{C.11})$$

This can also be written as

$$\boldsymbol{\mathcal{E}}_{mns}^{\pm} \cdot \mathbf{k}_{mns}^{\pm} = \boldsymbol{\mathcal{E}}_{mns}^{\pm, \text{t}} \cdot \boldsymbol{\beta}_{mn} \pm \mathcal{E}_{zmns}^{\pm} \gamma_s^{mn} = 0, \quad (\text{C.12})$$

where  $\boldsymbol{\mathcal{E}}_{mns}^{\pm, \text{t}}$  is the tangential components of  $\boldsymbol{\mathcal{E}}_{mns}^{\pm}$ , indicated by a superscript t, and  $\mathcal{E}_{zmns}^{\pm}$  is the  $z$ -component. It follows from (C.12) that

$$\mathcal{E}_{zmns}^{\pm} = \mp \frac{\boldsymbol{\mathcal{E}}_{mns}^{\pm, \text{t}} \cdot \boldsymbol{\beta}_{mn}}{\gamma_s^{mn}}, \quad (\text{C.13})$$

and the complex amplitude of the spatial harmonics can be expressed in terms of its tangential components

$$\boldsymbol{\mathcal{E}}_{mns}^{\pm} = \boldsymbol{\mathcal{E}}_{mns}^{\pm,t} \mp \hat{z} \frac{\boldsymbol{\mathcal{E}}_{mns}^{\pm,t} \cdot \boldsymbol{\beta}_{mn}}{\gamma_s^{mn}}. \quad (\text{C.14})$$

With this in mind, (C.5) can be rewritten as

$$\begin{aligned} \mathbf{E}_s(\mathbf{r}) &= \sum_{m,n=-\infty}^{\infty} \left( \boldsymbol{\mathcal{E}}_{mns}^{+,t} e^{-j\gamma_s^{mn}(z-z_s)} + \boldsymbol{\mathcal{E}}_{mns}^{-,t} e^{j\gamma_s^{mn}(z-z_s)} \right) e^{-j\boldsymbol{\beta}_{mn} \cdot \boldsymbol{\rho}} \\ &\quad + \hat{z} \sum_{m,n=-\infty}^{\infty} \left( -\boldsymbol{\mathcal{E}}_{zmn}^{+} e^{-j\gamma_s^{mn}(z-z_s)} + \boldsymbol{\mathcal{E}}_{zmn}^{-} e^{j\gamma_s^{mn}(z-z_s)} \right) e^{-j\boldsymbol{\beta}_{mn} \cdot \boldsymbol{\rho}} \\ &= \sum_{m,n=-\infty}^{\infty} \mathbf{E}_{mns}^t(z) e^{-j\boldsymbol{\beta}_{mn} \cdot \boldsymbol{\rho}} + \hat{z} \sum_{m,n=-\infty}^{\infty} E_{zmn}(z) e^{-j\boldsymbol{\beta}_{mn} \cdot \boldsymbol{\rho}}. \end{aligned} \quad (\text{C.15})$$

At interface  $s$  ( $z = z_s$ )

$$\mathbf{E}_{mns}^t(z_s) = \boldsymbol{\mathcal{E}}_{mns}^{+,t} + \boldsymbol{\mathcal{E}}_{mns}^{-,t}. \quad (\text{C.16})$$

Since the tangential components of the electrical fields are continuous across the interfaces, it implies that  $\mathbf{E}_{mn(s+1)}^t(z_{s+1}) = \mathbf{E}_{mns}^t(z_{s+1})$ , hence

$$\mathbf{E}_{mn(s+1)}^t(z_{s+1}) = \boldsymbol{\mathcal{E}}_{mns}^{+,t} e^{-j\gamma_s^{mn}d_s} + \boldsymbol{\mathcal{E}}_{mns}^{-,t} e^{j\gamma_s^{mn}d_s}. \quad (\text{C.17})$$

For convenience

$$\mathbf{C}_{mns} = \mathbf{E}_{mns}^t(z_s), \quad (\text{C.18})$$

denotes the complex amplitude of the total tangential electric field for the  $(m, n)$ 'th Floquet harmonic at interface  $s$ . It can be shown by combining (C.16) and (C.17) that

$$\boldsymbol{\mathcal{E}}_{mns}^{\pm,t} = \frac{\pm \mathbf{C}_{mn(s+1)} \mp \mathbf{C}_{mns} e^{\pm j\gamma_s^{mn}d_s}}{-2j \sin(\gamma_s^{mn}d_s)}. \quad (\text{C.19})$$

The electric field in the different layers is now related to  $\mathbf{C}_{mns}$ ,  $s = 1, 2, \dots, S$ .

The spatial harmonics of the magnetic fields can be related to the spatial harmonics of the electric field by

$$\boldsymbol{\mathcal{H}}_{mns}^{\pm} = \frac{1}{\eta_s} \hat{k}_{mns}^{\pm} \times \boldsymbol{\mathcal{E}}_{mns}^{\pm}, \quad (\text{C.20})$$

with  $\eta_s = \sqrt{\mu_s/\epsilon_s}$  being the intrinsic impedance for layer  $s$  and  $\hat{k}_{mns}^\pm = \mathbf{k}_{mns}^\pm/k_s$ . Note that only the tangential components of  $\mathcal{H}_{mns}^\pm$  are of interest since the  $z$ -components will be cancelled out by the cross product in (C.10). Substituting (C.14) in (C.20) yields the following relation

$$\begin{aligned} \mathcal{H}_{mns}^\pm &= \pm \frac{1}{\eta_s k_s} \hat{z} \times \left( \gamma_s^{mn} \mathcal{E}_{mns}^{\pm,t} + \beta_{mn} \frac{\mathcal{E}_{mns}^{\pm,t} \cdot \beta_{mn}}{\gamma_s^{mn}} \right) + \hat{z} \mathcal{H}_{zmns}^\pm, \\ &= \pm \frac{1}{\eta_s k_s \gamma_s^{mn}} \left\{ \hat{y} \left[ (k_s^2 - \beta_{ymn}^2) \mathcal{E}_{mns}^{\pm,x} + \beta_{xmn} \beta_{ymn} \mathcal{E}_{mns}^{\pm,y} \right] - \right. \\ &\quad \left. \hat{x} \left[ (k_s^2 - \beta_{xmn}^2) \mathcal{E}_{mns}^{\pm,y} + \beta_{xmn} \beta_{ymn} \mathcal{E}_{mns}^{\pm,x} \right] \right\} + \hat{z} \mathcal{H}_{zmns}^\pm. \end{aligned} \quad (\text{C.21})$$

By applying (C.19), the complex amplitude of the magnetic spatial harmonics is now expressed in terms of the tangential components of the electric fields evaluated at the interfaces.

Now that the complex amplitude of the magnetic spatial harmonics are known, these can be substituted into (C.10) to relate the unknown currents to the tangential components of the electric fields. This procedure must be divided in four different cases, namely the  $z_s$ ,  $1 < s < S$  interfaces, the  $z_1$  interface, the  $z_S$  interface without ground plane (FSS configurations) and the  $z_S$  interface with ground plane (reflectarray configurations). These will be treated separately in the following, starting with the most general case, the  $z_s$  interface.

### The intermediate interfaces ( $z = z_s$ )

This is the general case and one merely has to substitute (C.21) into (C.10). The  $z$ -component in (C.21) is cancelled out by the cross product and only the  $x$ - and  $y$ -components remain. Using the relation

$$\hat{z} \times \hat{z} \times \hat{a}_t = -\hat{a}_t, \quad (\text{C.22})$$

where  $\hat{a}_t$  is a unit vector transversal to  $\hat{z}$ , it can be shown that the electric current density can be expressed in terms of the tangential components of the electric fields evaluated at the adjacent interfaces

$$\begin{aligned} j_{mns} &= \left( \frac{2}{\Omega_s} \cos(\gamma_s^{mn} d_s) \mathcal{L}_s^{mn} + \frac{2}{\Omega_{s-1}} \cos(\gamma_{s-1}^{mn} d_{s-1}) \mathcal{L}_{s-1}^{mn} \right) \mathbf{C}_{mns} \\ &\quad + \left( \frac{-2}{\Omega_{s-1}} \mathcal{L}_{s-1}^{mn} \right) \mathbf{C}_{mn(s-1)} + \left( \frac{-2}{\Omega_s} \mathcal{L}_s^{mn} \right) \mathbf{C}_{mn(s+1)}. \end{aligned} \quad (\text{C.23})$$

Herein,  $\Omega_s = -2j \sin(\gamma_s^{mn} d_s)$  and the operator  $\mathcal{L}_s^{mn}$  is defined as

$$\begin{aligned}\mathcal{L}_s^{mn} &= \frac{1}{\eta_s k_s} \left( \gamma_s^{mn} + \frac{|\beta_{mn}|^2}{\gamma_s^{mn}} + \frac{1}{\gamma_s^{mn}} \overline{\mathbf{B}}_{mn} \right), \\ &= \frac{1}{\eta_s k_s \gamma_s^{mn}} \left( \gamma_s^{mn2} + \beta_{mn} \beta_{mn} \right), \\ &= \frac{1}{\eta_s k_s \gamma_s^{mn}} \left( k_s^2 + \overline{\mathbf{B}}_{mn} \right),\end{aligned}\tag{C.24}$$

where

$$\overline{\mathbf{B}}_{mn} = \begin{pmatrix} -\beta_{ymn}^2 & \beta_{xmn} \beta_{ymn} \\ \beta_{xmn} \beta_{ymn} & -\beta_{xmn}^2 \end{pmatrix}.\tag{C.25}$$

### The first interface ( $z = z_1$ )

For this special case, the layer to the left of the interface is a half space and (C.9) has to be modified. In the layer to the right side of the interface (layer 1), the magnetic field still consists of summations of forward and backward propagating waves, thus no changes are needed. However, in the layer to the left side of the interface (free space), the reflected field (backward propagating field) is decomposed by spatial harmonics and the forward propagating field consists of only the incident field. As a result, the boundary condition at the first interface is

$$\begin{aligned}\sum_{m,n=-\infty}^{\infty} \mathbf{j}_{mn1} e^{-j\beta_{mn} \cdot \boldsymbol{\rho}} \\ = \hat{\mathbf{z}} \times \left[ \sum_{m,n=-\infty}^{\infty} (\mathcal{H}_{mn1}^+ + \mathcal{H}_{mn1}^- - \mathcal{H}_{mn0}^-) e^{-j\beta_{mn} \cdot \boldsymbol{\rho}} - \mathbf{H}^i(z_1) \right],\end{aligned}\tag{C.26}$$

where  $\mathbf{H}^i(z_1) = \mathcal{H}^i e^{-j\mathbf{k}^i \cdot \boldsymbol{\rho}}$  is the incident magnetic field evaluated at the first interface. The complex amplitude  $\mathcal{H}^i$  can be found from the incident electric field  $\mathbf{E}^i(z_1)$ . The incident magnetic field corresponds to the fundamental Floquet harmonic,  $(m, n) = (0, 0)$ ,

$$\mathbf{H}^i(z_1) = \mathcal{H}_{000}^+ e^{-j\beta_{00} \cdot \boldsymbol{\rho}}.\tag{C.27}$$

Thus, the treatment of the first interface has to be divided up in two cases,  $(m, n) = (0, 0)$  and  $(m, n) \neq (0, 0)$ . Consider first the latter case.

Using the term-wise fulfillment, the boundary condition for the  $(m, n) \neq (0, 0)$  case is

$$\mathbf{j}_{mn1} = \hat{z} \times (\mathcal{H}_{mn1}^+ + \mathcal{H}_{mn1}^- - \mathcal{H}_{mn0}^-). \quad (\text{C.28})$$

The term  $\hat{z} \times (\mathcal{H}_{mn1}^+ + \mathcal{H}_{mn1}^-)$  is treated in a similar manner as in the case of the intermediate interfaces and additional comments on this will not be given.  $\mathcal{H}_{mn0}^-$  can be found using (C.21) to yield

$$\mathcal{H}_{mn0}^- = \frac{-1}{\eta_0 k_0} \hat{z} \times \left( \gamma_0^{mn} \mathcal{E}_{mn0}^{-,t} + \beta_{mn} \frac{\mathcal{E}_{mn0}^{-,t} \cdot \beta_{mn}}{\gamma_0^{mn}} \right) + \hat{z} \mathcal{H}_{zmn0}^-. \quad (\text{C.29})$$

Due to the continuity of the tangential components of the electric field,  $\mathcal{E}_{mn0}^{-,t} = \mathbf{C}_{mn1}$  since only the reflected fields are present. Thus the  $\mathcal{E}_{mn0}^{-,t}$  terms in (C.29) can be replaced by  $\mathbf{C}_{mn1}$ . It can be shown by combining all the above that

$$\begin{aligned} \mathbf{j}_{mn1} = & \left( \frac{2}{\Omega_1} \cos(\gamma_1^{mn} d_1) \mathcal{L}_1^{mn} - \mathcal{L}_0^{mn} \right) \mathbf{C}_{mn1} \\ & + \left( \frac{-2}{\Omega_1} \mathcal{L}_1^{mn} \right) \mathbf{C}_{mn2}, \quad (m, n) \neq (0, 0). \end{aligned} \quad (\text{C.30})$$

For the  $(m, n) = (0, 0)$  case, the boundary condition is

$$\mathbf{j}_{001} = \hat{z} \times (\mathcal{H}_{001}^+ + \mathcal{H}_{001}^- - \mathcal{H}_{000}^+ - \mathcal{H}_{000}^-). \quad (\text{C.31})$$

$\mathcal{H}_{000}^+$  can be expressed in terms of the tangential components of the incident electric field by using (C.21)

$$\mathcal{H}_{000}^+ = \frac{1}{\eta_0 k_0} \hat{z} \times \left( \gamma_0^{00} \mathcal{E}^{i,t} + \beta_{00} \frac{\mathcal{E}^{i,t} \cdot \beta_{00}}{\gamma_0^{00}} \right) + \hat{z} \mathcal{H}_{z000}^+, \quad (\text{C.32})$$

where  $\mathcal{E}^{i,t}$  is the tangential components of the complex amplitude of the incident electric field, evaluated at  $z = z_1$ .

$\mathcal{H}_{000}^-$  is given by (C.21)

$$\mathcal{H}_{000}^- = \frac{-1}{\eta_0 k_0} \hat{z} \times \left( \gamma_0^{00} \mathcal{E}_{000}^{-,t} + \beta_{00} \frac{\mathcal{E}_{000}^{-,t} \cdot \beta_{00}}{\gamma_0^{00}} \right) + \hat{z} \mathcal{H}_{z000}^-. \quad (\text{C.33})$$

Contrary to the  $(m, n) \neq (0, 0)$  case,  $\mathcal{E}_{000}^{-,t} \neq \mathbf{C}_{001}$  due to the incident field. Hence the incident field must be subtracted to give  $\mathcal{E}_{000}^{-,t} = \mathbf{C}_{001} - \mathcal{E}^{i,t}$ . This can then be substituted into (C.33) yielding

$$\mathbf{j}_{001} = \left( \frac{2}{\Omega_1} \cos(\gamma_1^{00} d_1) \mathcal{L}_1^{00} - \mathcal{L}_0^{00} \right) \mathbf{C}_{001} + \left( \frac{-2}{\Omega_1} \mathcal{L}_1^{00} \right) \mathbf{C}_{002} + 2 \mathcal{L}_0^{00} \mathcal{E}^{i,t}. \quad (\text{C.34})$$



### The last interface ( $z = z_S$ ) without ground plane

In the layer to the left of the last interface (layer  $S - 1$ ), the field is decomposed of forward and backward propagating spatial harmonics. In the layer to the right of the last interface (layer  $S$ ), only forward propagating spatial harmonics are present. Hence the boundary condition at the last interface is

$$\mathbf{j}_{mnS} = \hat{z} \times \left( \mathcal{H}_{mnS}^+ - \mathcal{H}_{mn(S-1)}^+ e^{-j\gamma_{S-1}^{mn} d_{S-1}} - \mathcal{H}_{mn(S-1)}^- e^{j\gamma_{S-1}^{mn} d_{S-1}} \right). \quad (\text{C.35})$$

The treatment of this interface is identical to the first interface case where  $(m, n) \neq (0, 0)$ . Further explanation will not be given and the final equation is

$$\mathbf{j}_{mnS} = \left( \frac{2}{\Omega_{S-1}} \cos(\gamma_{S-1}^{mn} d_{S-1}) \mathcal{L}_{S-1}^{mn} - \mathcal{L}_S^{mn} \right) \mathbf{C}_{mnS} + \left( \frac{-2}{\Omega_{S-1}} \mathcal{L}_{S-1}^{mn} \right) \mathbf{C}_{mn(S-1)}. \quad (\text{C.36})$$

### The last interface ( $z = z_S$ ) with ground plane

Due to the presence of the ground plane, the field in the layer to the right of the last interface (layer  $S$ ) no longer consists of only forward propagating spatial harmonics, but also reflected backward propagating waves. Thus the boundary condition at the last interface is

$$\mathbf{j}_{mnS} = \hat{z} \times \left( \mathcal{H}_{mnS}^+ + \mathcal{H}_{mnS}^- - \mathcal{H}_{mn(S-1)}^+ e^{-j\gamma_{S-1}^{mn} d_{S-1}} - \mathcal{H}_{mn(S-1)}^- e^{j\gamma_{S-1}^{mn} d_{S-1}} \right). \quad (\text{C.37})$$

$\mathcal{H}_{mnS}^+$  and  $\mathcal{H}_{mnS}^-$  are related to  $\mathcal{E}_{mnS}^+$  and  $\mathcal{E}_{mnS}^-$ , respectively, and the relation between the latter quantities are easily determined by imposing the boundary conditions at the PEC ground plane. The complex amplitude of the electric field in a given layer is related to the complex amplitude of the total tangential electric field at its adjacent interfaces by (C.19). At the last interface, the relation is

$$\mathcal{E}_{mnS}^{\pm, t} = \frac{\pm \mathbf{C}_{mn(S+1)} \mp \mathbf{C}_{mnS} e^{\pm j\gamma_S^{mn} d_S}}{-2j \sin(\gamma_S^{mn} d_S)}. \quad (\text{C.38})$$

To satisfy the boundary condition at the PEC ground plane, the total tangential electric field at  $z = z_{S+1}$  has to be zero, hence  $\mathbf{C}_{mn(S+1)} = 0$ . Equation (C.21) is still applicable and the complex amplitude of the magnetic spatial harmonics can still be expressed using the tangential components of the electric fields. The procedure to relate the current densities to the tangential components of the electric fields is exactly the same as for the intermediate interfaces. As a consequence of  $\mathbf{C}_{mn(S+1)} = 0$ , the resulting equation is the same as the intermediate

interfaces (C.23), but without the last term. That is

$$\begin{aligned} \mathbf{j}_{mnS} = & \left( \frac{2}{\Omega_S} \cos(\gamma_S^{mn} d_S) \mathcal{L}_S^{mn} + \frac{2}{\Omega_{S-1}} \cos(\gamma_{S-1}^{mn} d_{S-1}) \mathcal{L}_{S-1}^{mn} \right) \mathbf{C}_{mnS} \\ & + \left( \frac{-2}{\Omega_{S-1}} \mathcal{L}_{S-1}^{mn} \right) \mathbf{C}_{mn(S-1)}. \end{aligned} \quad (\text{C.39})$$

### Summary of Currents

The intermediate interfaces:

$$\begin{aligned} \mathbf{j}_{mns} = & \left( \frac{2}{\Omega_s} \cos(\gamma_s^{mn} d_s) \mathcal{L}_s^{mn} + \frac{2}{\Omega_{s-1}} \cos(\gamma_{s-1}^{mn} d_{s-1}) \mathcal{L}_{s-1}^{mn} \right) \mathbf{C}_{mns} \\ & + \left( \frac{-2}{\Omega_{s-1}} \mathcal{L}_{s-1}^{mn} \right) \mathbf{C}_{mn(s-1)} + \left( \frac{-2}{\Omega_s} \mathcal{L}_s^{mn} \right) \mathbf{C}_{mn(s+1)}. \end{aligned} \quad (\text{C.40a})$$

The first interface:

$$\begin{aligned} \mathbf{j}_{mn1} = & \left( \frac{2}{\Omega_1} \cos(\gamma_1^{mn} d_1) \mathcal{L}_1^{mn} - \mathcal{L}_0^{mn} \right) \mathbf{C}_{mn1} \\ & + \left( \frac{-2}{\Omega_1} \mathcal{L}_1^{mn} \right) \mathbf{C}_{mn2}, \quad (m, n) \neq (0, 0), \end{aligned} \quad (\text{C.40b})$$

$$\mathbf{j}_{001} = \left( \frac{2}{\Omega_1} \cos(\gamma_1^{00} d_1) \mathcal{L}_1^{00} - \mathcal{L}_0^{00} \right) \mathbf{C}_{001} + \left( \frac{-2}{\Omega_1} \mathcal{L}_1^{00} \right) \mathbf{C}_{002} + 2\mathcal{L}_0^{00} \boldsymbol{\varepsilon}^{\text{i,t}}. \quad (\text{C.40c})$$

The last interface without ground plane:

$$\mathbf{j}_{mnS} = \left( \frac{2}{\Omega_{S-1}} \cos(\gamma_{S-1}^{mn} d_{S-1}) \mathcal{L}_{S-1}^{mn} - \mathcal{L}_S^{mn} \right) \mathbf{C}_{mnS} + \left( \frac{-2}{\Omega_{S-1}} \mathcal{L}_{S-1}^{mn} \right) \mathbf{C}_{mn(S-1)}. \quad (\text{C.40d})$$

The last interface with ground plane:

$$\begin{aligned} \mathbf{j}_{mnS} = & \left( \frac{2}{\Omega_S} \cos(\gamma_S^{mn} d_S) \mathcal{L}_S^{mn} + \frac{2}{\Omega_{S-1}} \cos(\gamma_{S-1}^{mn} d_{S-1}) \mathcal{L}_{S-1}^{mn} \right) \mathbf{C}_{mnS} \\ & + \left( \frac{-2}{\Omega_{S-1}} \mathcal{L}_{S-1}^{mn} \right) \mathbf{C}_{mn(S-1)}. \end{aligned} \quad (\text{C.40e})$$

### C.3.2 Setting up the MoM Equation

(C.40a)-(C.40d) can be expressed in matrix form as

$$\begin{pmatrix} A_{1,1} & A_{1,2} & \cdots & A_{1,2S} \\ A_{2,1} & A_{2,2} & \cdots & A_{2,2S} \\ \vdots & \vdots & \ddots & \vdots \\ A_{2S,1} & A_{2S,2} & \cdots & A_{2S,2S} \end{pmatrix} \cdot \begin{pmatrix} C_{mn1} \\ C_{mn2} \\ \vdots \\ C_{mnS} \end{pmatrix} = \begin{pmatrix} j_{mn1} \\ j_{mn2} \\ \vdots \\ j_{mnS} \end{pmatrix}$$

$$\Leftrightarrow \bar{\mathbf{A}}_{mn} \cdot \mathbf{C}_{mn} = \mathbf{j}_{mn}, \quad (m, n) \neq (0, 0). \quad (\text{C.41})$$

To include the  $(m, n) = (0, 0)$  term

$$\bar{\mathbf{A}}_{mn} \cdot \mathbf{C}_{mn} = \mathbf{j}_{mn} - \mathbf{b}_{mn}, \quad (\text{C.42})$$

where

$$\mathbf{b}_{mn} = \begin{pmatrix} 2\mathcal{L}_0^{00} \boldsymbol{\varepsilon}^{\text{i,t}} \\ 0 \\ \vdots \\ 0 \end{pmatrix}, \quad (m, n) = (0, 0) \text{ else } \mathbf{b}_{mn} = \mathbf{0}. \quad (\text{C.43})$$

The matrix  $\bar{\mathbf{A}}_{mn}$  is a regular matrix, thus by multiplying  $\bar{\mathbf{A}}_{mn}^{-1}$  on both sides of (C.42) one gets

$$\bar{\mathbf{A}}_{mn}^{-1} \cdot \mathbf{j}_{mn} = \mathbf{C}_{mn} + \bar{\mathbf{A}}_{mn}^{-1} \cdot \mathbf{b}_{mn}. \quad (\text{C.44})$$

Recall from (C.2) that

$$\mathbf{j}_{mns} = \frac{1}{A_U} \iint_U \mathbf{J}_s(\boldsymbol{\rho}, z_s) e^{j\boldsymbol{\beta}_{mn} \cdot \boldsymbol{\rho}} dxdy, \quad (\text{C.45})$$

where  $\mathbf{J}_s(\boldsymbol{\rho}, z_s)$  is the quantity to be found. This quantity can be expressed in terms of a set of basis functions

$$\mathbf{J}_s(\boldsymbol{\rho}, z_s) = \sum_{p=1}^{P_s} c_p^s \mathbf{J}_p^s, \quad (\text{C.46})$$

where  $P_s$  is the number of basis functions used in layer  $s$ . Inserting into (C.45) yields

$$\mathbf{j}_{mns} = \frac{1}{A_U} \sum_{p=1}^{P_s} c_p^s \iint_U \mathbf{J}_p^s e^{j\boldsymbol{\beta}_{mn} \cdot \boldsymbol{\rho}} dxdy = \sum_{p=1}^{P_s} c_p^s \mathbf{j}_{pmn}^s, \quad (\text{C.47})$$

where

$$\mathbf{j}_{pmn}^s = \frac{1}{A_U} \iint_U \mathbf{J}_p^s e^{j\boldsymbol{\beta}_{mn} \cdot \boldsymbol{\rho}} dx dy, \quad (\text{C.48})$$

is the Fourier transform of the basis function  $\mathbf{J}_p^s$  evaluated at a given Floquet harmonic. Since the vector  $\mathbf{j}_{mn}$  includes all  $\mathbf{j}_{mns}$ ,  $\mathbf{j}_{mn}$  can also be expressed in matrix form as

$$\begin{aligned} \mathbf{j}_{mn} &= \begin{pmatrix} \mathbf{j}_{mn1} \\ \mathbf{j}_{mn2} \\ \vdots \\ \mathbf{j}_{mnS} \end{pmatrix} = \begin{pmatrix} c_1^1 \mathbf{j}_{1mn}^1 + c_2^1 \mathbf{j}_{2mn}^1 + \cdots \\ c_1^2 \mathbf{j}_{1mn}^2 + c_2^2 \mathbf{j}_{2mn}^2 + \cdots \\ \vdots \\ c_1^S \mathbf{j}_{1mn}^S + c_2^S \mathbf{j}_{2mn}^S + \cdots \end{pmatrix} \\ &= \begin{pmatrix} \mathbf{j}_{1mn}^1 & \cdots & \mathbf{j}_{P_1mn}^1 & 0 & \cdots & \cdots & \cdots & \cdots & 0 \\ 0 & \cdots & 0 & \mathbf{j}_{1mn}^2 & \cdots & \mathbf{j}_{P_2mn}^2 & 0 & \cdots & \vdots \\ \vdots & \ddots & \ddots & \ddots & \cdots & \cdots & \mathbf{j}_{1mn}^3 & \cdots & \vdots \\ \vdots & \ddots & \ddots & \ddots & \ddots & \ddots & \ddots & \ddots & \vdots \\ \vdots & \ddots & \ddots & \ddots & \ddots & \ddots & \ddots & \ddots & \vdots \\ 0 & \cdots & \cdots & \cdots & \cdots & \cdots & \cdots & \cdots & \mathbf{j}_{P_Smn}^S \end{pmatrix} \cdot \begin{pmatrix} c_1^1 \\ \vdots \\ c_{P_1}^1 \\ c_1^2 \\ \vdots \\ c_{P_2}^2 \\ c_1^3 \\ \vdots \\ c_{P_S}^S \end{pmatrix} \\ &= \bar{\mathbf{J}}_{mn} \cdot \mathbf{c}. \end{aligned} \quad (\text{C.49})$$

Substituting in (C.44) gives

$$\bar{\mathbf{A}}_{mn}^{-1} \cdot \bar{\mathbf{J}}_{mn} \cdot \mathbf{c} = \mathbf{C}_{mn} + \bar{\mathbf{A}}_{mn}^{-1} \cdot \mathbf{b}_{mn}. \quad (\text{C.50})$$

To get the correct representation of the tangential field components,  $e^{-j\boldsymbol{\beta}_{mn} \cdot \boldsymbol{\rho}}$  is multiplied on both sides of (C.50)

$$\bar{\mathbf{A}}_{mn}^{-1} \cdot \bar{\mathbf{J}}_{mn} e^{-j\boldsymbol{\beta}_{mn} \cdot \boldsymbol{\rho}} \cdot \mathbf{c} = \left( \mathbf{C}_{mn} + \bar{\mathbf{A}}_{mn}^{-1} \cdot \mathbf{b}_{mn} \right) e^{-j\boldsymbol{\beta}_{mn} \cdot \boldsymbol{\rho}}. \quad (\text{C.51})$$

$\sum_{mn} \mathbf{C}_{mn} e^{-j\boldsymbol{\beta}_{mn} \cdot \boldsymbol{\rho}}$  describes the total tangential electric field at the interfaces. On the metallic patches, the total tangential electric field is equal to the product of the surface impedance and the surface current density

$$\mathbf{E}_s^t(\boldsymbol{\rho}, z_s) = Z_{\text{sur}} \mathbf{J}_s(\boldsymbol{\rho}, z_s), \quad (\text{C.52})$$

where  $Z_{\text{sur}}$  is the surface impedance. To ensure an averaged fulfillment of the impedance boundary condition, a set of appropriate weighting functions  $\mathbf{w}_q^s$ ,

which are only supported on the patches, is multiplied in (C.51). In Galerkin's method,  $\mathbf{J}_q^{s*}$  is used

$$\begin{aligned} \iint_{\mathbf{U}} \mathbf{J}_q^{s*} \cdot \sum_{m,n=-\infty}^{\infty} \mathbf{C}_{mns} e^{-j\beta_{mn} \cdot \boldsymbol{\rho}} dxdy &= \iint_{\mathbf{U}} \mathbf{J}_q^{s*} \cdot Z_{\text{sur}} \sum_{p=1}^{P_s} c_p^s \mathbf{J}_p^s dxdy \quad \Leftrightarrow \\ \sum_{m,n=-\infty}^{\infty} \mathbf{j}_{qmn}^{s*} \cdot \mathbf{C}_{mns} &= Z_{\text{sur}} \sum_{m,n=-\infty}^{\infty} \sum_{p=1}^{P_s} c_p^s \mathbf{j}_{qmn}^{s*} \cdot \mathbf{j}_{pmn}^s. \end{aligned} \quad (\text{C.53})$$

The asterisk indicates the complex conjugate. The quantity  $\mathbf{j}_{qmn}^s$  is the Fourier transform of the weighting function  $\mathbf{J}_q^s$  evaluated at a given Floquet harmonic. Consequently, an appropriate weighting matrix is

$$\overline{\mathbf{W}}_{mn} = \overline{\mathbf{J}}_{mn}^*, \quad (\text{C.54})$$

where the asterisk means Hermitian transpose of the matrix  $\overline{\mathbf{J}}_{mn}$ . Substituting in (C.51) and summing all Floquet harmonics, the equation that needs to be solved becomes

$$\left( \sum_{m,n=-\infty}^{\infty} \overline{\mathbf{J}}_{mn}^* \cdot \overline{\mathbf{A}}_{mn}^{-1} \cdot \overline{\mathbf{J}}_{mn} - Z_{\text{sur}} \sum_{m,n=-\infty}^{\infty} \overline{\mathbf{J}}_{mn}^* \cdot \overline{\mathbf{J}}_{mn} \right) \cdot \mathbf{c} = \overline{\mathbf{J}}_{00}^* \cdot \overline{\mathbf{A}}_{00}^{-1} \cdot \mathbf{b}_{00}, \quad (\text{C.55})$$

where the MoM impedance matrix is

$$\overline{\mathbf{Z}} = \sum_{m,n=-\infty}^{\infty} \left( \overline{\mathbf{J}}_{mn}^* \cdot \overline{\mathbf{A}}_{mn}^{-1} \cdot \overline{\mathbf{J}}_{mn} - Z_{\text{sur}} \overline{\mathbf{J}}_{mn}^* \cdot \overline{\mathbf{J}}_{mn} \right), \quad (\text{C.56})$$

and the voltage vector is

$$\mathbf{V} = \overline{\mathbf{J}}_{00}^* \cdot \overline{\mathbf{A}}_{00}^{-1} \cdot \mathbf{b}_{00}. \quad (\text{C.57})$$

For the single layer with ground plane case,  $\overline{\mathbf{A}}$  is

$$A_{11} = \frac{k_1^2 - \beta_{ymn}^2}{j \tan(\gamma_1^{mn} d_1) \eta_1 k_1 \gamma_1^{mn}} - \frac{k_0^2 - \beta_{ymn}^2}{\eta_0 k_0 \gamma_0^{mn}}, \quad (\text{C.58a})$$

$$A_{12} = \frac{\beta_{xmn} \beta_{ymn}}{j \tan(\gamma_1^{mn} d_1) \eta_1 k_1 \gamma_1^{mn}} - \frac{\beta_{xmn} \beta_{ymn}}{\eta_0 k_0 \gamma_0^{mn}}, \quad (\text{C.58b})$$

$$A_{21} = A_{12}, \quad (\text{C.58c})$$

$$A_{22} = \frac{k_1^2 - \beta_{xmn}^2}{j \tan(\gamma_1^{mn} d_1) \eta_1 k_1 \gamma_1^{mn}} - \frac{k_0^2 - \beta_{xmn}^2}{\eta_0 k_0 \gamma_0^{mn}}, \quad (\text{C.58d})$$

and the inverse of  $\overline{\mathbf{A}}$  corresponds to the dyadic Green's function reported in e.g. [90, Eqn.(2)-(4)].

The size of  $\overline{\mathbf{Z}}$  is determined by the number of layers and the number of basis functions. The number of Floquet harmonics needed depends on the choice of the basis functions and their convergence properties. For a description of the basis functions used in this work and their Fourier transforms, the reader is referred to Section 2.3.2 and Appendix D.

### C.3.3 Scattering due to Propagating Floquet Harmonics

Two techniques to calculate the far-field from reflectarrays are used in this work, namely the Floquet harmonics technique and the continuous spectrum technique.<sup>1</sup>

To calculate the far-field using the Floquet harmonics technique, the propagating Floquet harmonics are used to determine the equivalent currents within each unit-cell. These propagating Floquet harmonics can be readily obtained from the SDMoM formulation.

The total field to the left of layer 1 consists of a single forward propagating wave (incident field) and infinite back propagating waves (scattered field)

$$\mathbf{E}_0(\mathbf{r}) = \mathcal{E}^i e^{-j\mathbf{k}^i \cdot \mathbf{r}_1} + \sum_{m,n=-\infty}^{\infty} \mathcal{E}_{mn0}^- e^{j\gamma_0^{mn}(z-z_1)} e^{-j\beta_{mn} \cdot \boldsymbol{\rho}}. \quad (\text{C.59})$$

The second term is the total scattered field. Using (C.14) this is rewritten as

$$\mathbf{E}_0(\mathbf{r}) = \mathcal{E}^i e^{-j\mathbf{k}^i \cdot \mathbf{r}_1} + \sum_{m,n=-\infty}^{\infty} \left( \mathcal{E}_{mn0}^{-,t} + \hat{z} \frac{\mathcal{E}_{mn0}^{-,t} \cdot \beta_{mn}}{\gamma_0^{mn}} \right) e^{j\gamma_0^{mn}(z-z_1)} e^{-j\beta_{mn} \cdot \boldsymbol{\rho}}. \quad (\text{C.60})$$

From the MoM solution,  $\mathbf{j}_{mn}$  is determined. This can be substituted into (C.42) to calculate the complex amplitude of the total tangential electric field at all interfaces

$$\mathbf{C}_{mn} = \overline{\mathbf{A}}_{mn}^{-1} \cdot (\mathbf{j}_{mn} - \mathbf{b}_{mn}). \quad (\text{C.61})$$

The complex amplitude of the total tangential electric field at interface 1 is

$$\mathbf{C}_{mn1} = \mathcal{E}_{mn0}^{-,t} + \delta_{mn0} \mathcal{E}^{i,t}, \quad (\text{C.62})$$

where the delta is Kronecker's delta. With  $\mathbf{C}_{mn1}$  known, the complex amplitude of the tangential component of the back propagating waves  $\mathcal{E}_{mn0}^{-,t}$  can be readily determined and used in (C.60) to find the scattered electric field. The scattered magnetic field is obtained through (C.20).

---

<sup>1</sup>For more information on the calculation of the far-field, see Section 2.3.3.



## FOURIER TRANSFORMS OF BASIS FUNCTIONS

---

In the spectral domain method of moments (SDMoM), the spectral representation of the basis functions is required rather than their spatial form. In this appendix, the Fourier transforms of some of the basis functions used in this work are given.

The basis functions that have been used in this work are rooftop basis functions [106], higher-order hierarchical Legendre basis functions (LegBF) [125], entire domain singular basis functions weighted by sinusoidal functions (E-SinBF) from [108], and entire domain singular basis functions weighted by Chebyshev polynomials of first and second kind (E-CheBF) from [124]. The rooftops are the first-order cases of the LegBFs [125] and are therefore not treated here. In addition, the Fourier transform of the E-SinBFs are comprehensively given in [108] and will therefore also not be treated here.

We define the Fourier transformation as

$$\mathcal{F}\{f(x)\} = \tilde{F}(k) = \int_{-a/2}^{a/2} f(x) e^{jkx} dx, \quad (\text{D.1})$$

where  $a$  denotes the spatial support of the basis function and  $k$  is the spectral variable.

### D.1 Higher-order Hierarchical Legendre Basis Functions

The LegBFs are defined on higher-order curvilinear mesh elements, thus any curved surface can be modeled very accurately. In the spatial domain, the LegBF consists of Legendre polynomials of different order and the expressions can be found in [125]. The spatial support for the LegBFs is always between  $[-1 : 1]$ , resulting in  $a = 2$ .



The Fourier transform of the Legendre polynomial of order  $n$ ,  $P_n$ , is given by

$$\tilde{P}_n(k) = 2j^n j_n(k), \quad n \in \mathbb{N}_0, \quad (\text{D.2})$$

where  $j_n(k)$  is the spherical Bessel function of order  $n$ . With (D.2), the Fourier transforms of the LegBFs can be readily obtained. Recurrence formulas for the spherical Bessel functions [142] can be used for an efficient implementation of the LegBFs in the spectral domain.<sup>1</sup>

## D.2 Singular Basis Functions weighted by Chebyshev Polynomials

Expressions for the Fourier transforms of the E-CheBFs are provided in [124]. However, the expressions are somewhat ambiguous due to their notation. In this section, the Fourier transforms of the basis functions will be explicitly provided.

Using the E-CheBFs, which are only applicable for rectangular patches of size  $a \times b$ , the  $x$ - and  $y$ -currents are expanded as

$$J_x(x, y) = \sum_{s=0}^S \sum_{r=0}^R F_s^U(x, a) F_r^T(y, b), \quad (\text{D.3a})$$

$$J_y(x, y) = \sum_{s=0}^S \sum_{r=0}^R F_s^U(y, b) F_r^T(x, a), \quad (\text{D.3b})$$

where

$$F_n^T(x, a) = T_n\left(\frac{2x}{a}\right) \frac{1}{\sqrt{1 - \left(\frac{2x}{a}\right)^2}}, \quad (\text{D.4a})$$

$$F_n^U(x, a) = U_n\left(\frac{2x}{a}\right) \sqrt{1 - \left(\frac{2x}{a}\right)^2}. \quad (\text{D.4b})$$

Herein,  $U_n(x)$  and  $T_n(x)$  are the Chebyshev polynomials of first and second kind, respectively, of the order  $n$ . The Fourier transforms of (D.4) are given by

$$\tilde{F}_n^T(k) = \frac{a}{2} j^n \pi J_n\left(\frac{ka}{2}\right), \quad (\text{D.5a})$$

$$\tilde{F}_n^U(k) = j^n \pi \frac{n+1}{k} J_{n+1}\left(\frac{ka}{2}\right), \quad (\text{D.5b})$$

---

<sup>1</sup>Dr. Erik Jørgensen, TICRA, is acknowledged for the implementation of the Fourier transforms of the LegBFs.

where  $J_n(x)$  is the Bessel function of first kind of the order  $n$ . It is seen in (D.5b) that division by zero occurs if  $k = 0$ . Thus, this term has to be treated separately for small arguments. Using the small argument expansion for the Bessel function, it can be shown that

$$\frac{J_{n+1}\left(\frac{ka}{2}\right)}{k} \simeq \frac{1}{(n+1)!} \left(\frac{a}{4}\right)^{(n+1)} k^n, \quad k \rightarrow 0. \quad (\text{D.6})$$

Thus, for small arguments

$$\tilde{F}_0^U(k) = \begin{cases} \pi a/4, & n = 0 \\ 0, & n > 0 \end{cases} \quad k \rightarrow 0. \quad (\text{D.7})$$

Similar to the LegBFs, recurrence formulas for the Bessel functions [142] can be used for the efficient calculation of the higher-order Bessel functions.



## SEA AND ELP

---

The surrounded element approach (SEA) and extended local periodicity (ELP) approach are techniques proposed to reduce the errors introduced by the periodicity assumption in the local periodicity (LP) approach. In this appendix, the advantages and drawbacks of each technique will be discussed and representative results will be shown.

### E.1 Surrounded Element Approach

The SEA was introduced in [101] and is based on a finite approach where no periodicity is applied. The concept is shown in Figure E.1. For the analysis of each array element, the actual neighboring elements that surround the element under consideration are included in the analysis, thus this approach should account for the mutual coupling more accurately than the LP approach. In [101], the analysis was based on a finite difference time domain (FDTD) implementation assuming plane wave incidence, and many neighboring elements were required to obtain an improved result. Even though the reported computation time were in terms of hours, the technique was considered interesting. Therefore, an integral equation (IE) formulation of the SEA using spatial Green's functions assuming infinite ground plane has been implemented. The reflectarray problem is formulated using the mixed-potential form of the electric field inte-

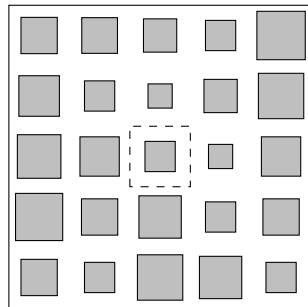


**Figure E.1** *Surrounded element approach: the actual neighboring elements that surrounds the element under consideration (center element within the dashed lines) are included in the analysis.*

gral equation (EFIE) [137–139, 143] and solved using the method of moments (MoM) from the GRASP MoM add-on [94] where the spatial Green’s functions have been included. With an IE formulation, the total computation time may be reduced compared to a FDTD implementation since it is more suited for open radiation problems. In addition, the plane wave incidence assumption is avoided, since the real feed pattern is used in the IE formulation. With the IE, it is also possible to perform a full-wave MoM of the entire reflectarray. However, due to the memory consumption, only reflectarrays of moderate sizes (approximately  $15 \times 15 \lambda_0^2$ ) can be considered. For a more detailed description of the IE formulation and the calculation of the spatial Green’s functions, the reader is referred to Appendix F.

To examine the performance of the SEA, the technique was applied on samples I-I and I-II.<sup>1</sup> However, the convergence rate with respect to the number of neighboring elements was very poor. In Figure E.2 the radiation of sample I-II calculated using the LP approach and SEA are compared to the measurements. The Potter horn is used as feed. For the SEA, 120 neighboring elements were included in the simulations resulting in an overall simulation time of approximately 20 hours on an 1.86 GHz 8 core Intel Xeon processor computer. For the LP approach, the computation time was 20 seconds. The results show that the overall accuracy of both techniques is rather good. It is seen that the cross-polar level is better predicted using the SEA. However, for the co-polar radiation, the LP approach is more accurate, despite the large number of included neighboring elements in the SEA. The measured peak directivity is 29.4 dBi, the SEA predicts 28.8 dBi whereas the LP approach gives a more accurate value of 29.3 dBi. Also the sidelobes are better predicted using the LP approach, see Figure E.2c. The same phenomenon was observed for sample I-I. This observation indicates that the mutual coupling between the array elements is strong and the effect of the elements positioned far from the element under consideration can not be neglected. It also implies that the actual size of the neighboring elements are of less importance compared to the inclusion of the elements positioned far from the element under consideration.

Based on a number of simulations, it was observed that the performance of the SEA was particularly bad for very thin substrates where the  $Q$ -factor of the printed elements is high. It was shown by comparison with full-wave MoM solutions that the number of included neighboring elements can be reduced for thicker substrates. In general, the mutual coupling between printed elements may be due to both space waves and surface waves, however, for thin substrates, the effects of the surface waves are of less importance [144, 145]. These effects can be separated by selecting appropriate integration paths for the integrals involved in the calculation of the spatial Green’s functions [145–147]. It could

---

<sup>1</sup>For information on samples I-I and I-II, see Section 2.2 or Appendix A.

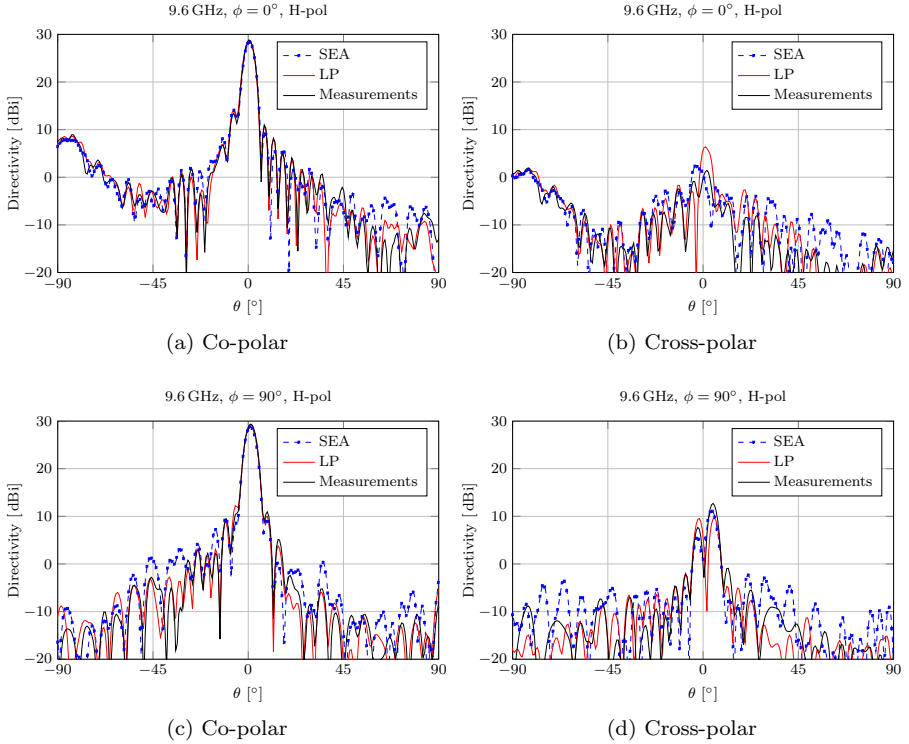


**Figure E.2** Simulated radiation pattern from sample I-II with the Potter horn as feed. The SEA (blue) and LP approach (red) have been used in the simulations.

been interesting to study these effects in more detail to see how they affect the solution for different substrate thickness and frequency etc. However, this does not change the fact that the overall computation time associated with the SEA is extremely high. This is a major limitation for optimization purposes, and due to this sole reason, the SEA was not investigated further.

## E.2 Extended Local Periodicity

The ELP approach was introduced in [C1] and is a combination of the LP approach and the SEA. Similar to the LP approach, the ELP approach is also based on periodicity, but the periodicity is applied to an extended unit-cell which includes the actual 8 neighboring elements that surround the element un-

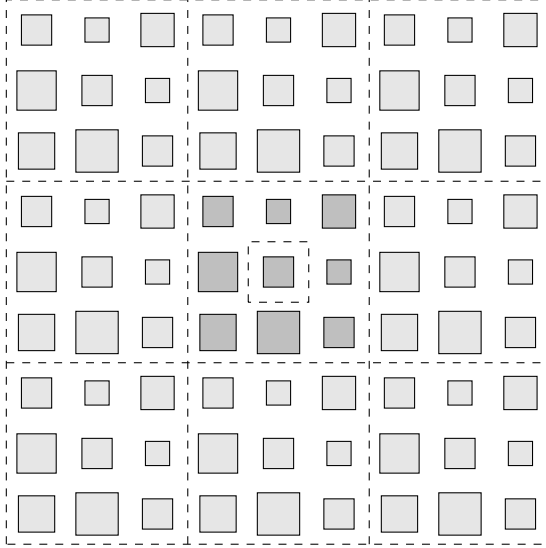


**Figure E.3** *Extended local periodicity: periodicity is applied on an extended unit-cell which includes the actual 8 neighboring elements that surround the element under consideration (center element within the dashed lines).*

der consideration, see Figure E.3. The spectral domain method of moments is applied to the extended unit-cell and the unknown currents on the element under consideration is determined. This is repeated for the next element with the extended unit-cell now including the new element under consideration and its 8 neighbors. The inclusion of the nearest surrounding neighbors increases the total computation time due to additional basis functions and Floquet harmonics, but it accounts for the mutual coupling in a more accurate way.

The performance of the ELP approach has been tested on samples I-I and I-II and compared to the LP approach. It was shown in [C2] for sample I-II, that a slight improvement was obtained in the prediction of the peak directivity using the ELP approach at 10 GHz. For sample I-I, nothing was gained by using the ELP approach.

Although the ELP approach has in some cases shown to have superior accuracy compared to the LP approach, this is obtained at the cost of higher computation time. While an analysis of a realistic reflectarray takes a couple of seconds using the LP approach, the ELP approach requires 45-60 minutes. This increase is significant and makes the ELP approach unaffordable for optimization purposes. Several acceleration techniques to reduce the computation time

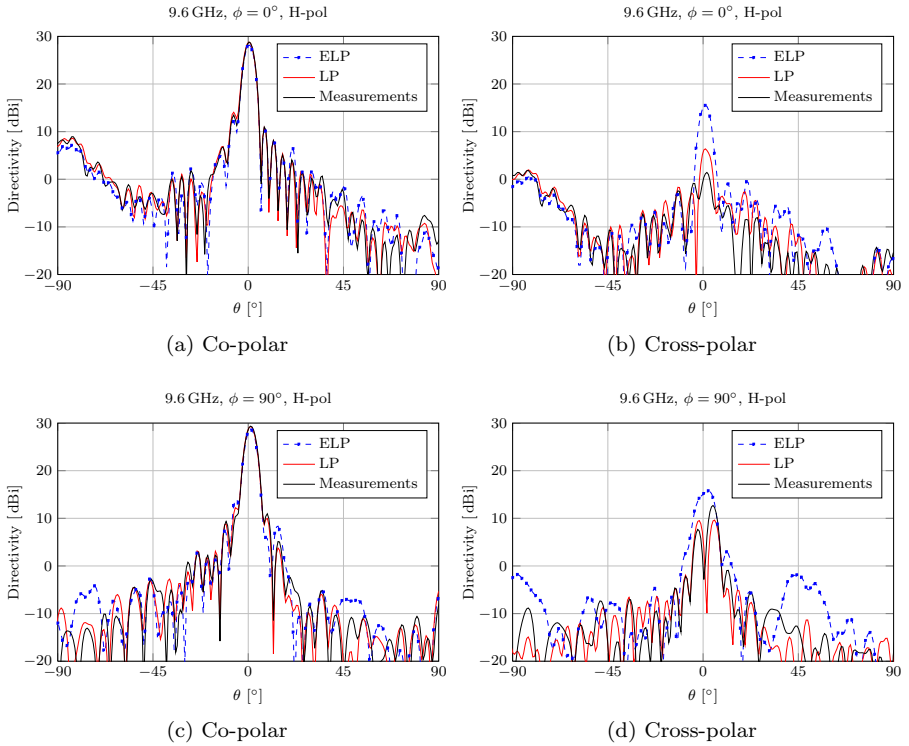


**Figure E.4** Simulated radiation pattern from sample I-II with the Potter horn as feed. The ELP (blue) and LP approach (red) have been used in the simulations.

have been proposed in the literature [148–150]. However, these techniques are unsuitable for arbitrarily shaped elements and were therefore considered outside the scope for this project.

The main disadvantage of the ELP approach is, however, not the high computation time associated with the technique. Simulations showed that the ELP approach tends to give inaccurate results when the array elements in the extended unit-cell are highly resonant. An example is shown in Figure E.4. Here, the radiation of sample I-II at 9.6 GHz, which is the resonance frequency, is analyzed using the LP and ELP approaches and compared to the measurements. It is seen that the prediction of the ELP is faulty, especially for the cross-polar radiation. For a frequency slightly away from the resonance frequency, e.g. 10 GHz, the spurious radiation disappears and the accuracy of the ELP approach is very



good as demonstrated in [C2]. The same behavior was observed for sample I-II with the corrugated horn, and sample I-I for both feeds. A large simulation campaign was carried out to identify and understand the source of this error. Details will not be given but the main observations are summarized in the following for brevity

- The errors occur only in the presence of a dielectric substrate when the elements in the extended unit-cell are highly resonant. Away from the resonance (by changing the frequency or the dielectric constant), the errors disappear. This is also the case if additional losses are added to the substrate.
- The errors are particularly large for the cross-polar radiation.
- An excessive number of basis functions and Floquet harmonics have been used in the ELP approach to guarantee that convergence was reached. However, this did not improve the results.
- A plane wave has been used to illuminate the reflectarray samples to investigate the influence of the incident field. The ELP approach still produced faulty results.
- Reflectarrays with different feed positions have been tested to see the influence of the incidence angle. However, the ELP approach still produced erroneous results.
- When unit-cell sizes are above  $0.5\lambda_0$ , which is often the case for the ELP approach, additional propagating Floquet harmonics exist. To investigate the effect of these additional propagating Floquet harmonics, several reflectarrays with unit-cells of size  $d = 0.15\lambda_0$  have been designed. This gives an extended unit-cell size of  $d = 0.45\lambda_0$ . For these cases, only the fundamental Floquet harmonic is a propagating wave. However, also in these cases, the ELP approach gives faulty results at the resonance frequency.
- To verify the implementation of the ELP approach, instead of including the actual neighboring elements, identical patches were used in the extended unit-cell, thus imitating the LP approach. Results identical to that obtained using LP were obtained.
- In continuation of the test case, where identical patches were used in the extended unit-cell, the size of one of the nine patches were slightly changed. This resulted in a big change in the response of the array elements, indicating that the problem is very sensitive and susceptible to changes. This was confirmed by simulations in HFSS.

Based on these observations, it is still unclear why the ELP approach produces erroneous results at the resonance frequency.

At a certain point, it was decided that the time devoted to investigating the ELP approach was too high. It was already concluded that the computation time associated with the technique was high and therefore not suitable for optimization purposes. Therefore, even though the source of this error has not been identified, the investigation was brought to an end, and the ELP approach was not investigated further.



# INTEGRAL EQUATION FORMULATION FOR GROUNDED DIELECTRIC SLAB

---

This appendix deals with the integral equation (IE) formulation and the calculation of the spatial Green's functions for a grounded dielectric slab.

## F.1 Integral Equation Formulation

The field radiated by electric surface currents and charges can be described by the vector potential  $\mathbf{A}$  and the scalar potential  $\Phi$ . These are defined as

$$\mathbf{A}(\mathbf{r}) = \mu_0 \int_S \overline{\mathbf{G}}(\mathbf{r}, \mathbf{r}') \cdot \mathbf{J}_s(\mathbf{r}') dS', \quad (\text{F.1a})$$

$$\Phi(\mathbf{r}) = \frac{1}{\epsilon_0} \int_S G_\Phi(\mathbf{r}, \mathbf{r}') \rho_s(\mathbf{r}') dS', \quad (\text{F.1b})$$

where  $\mathbf{J}_s(\mathbf{r})$  and  $\rho_s(\mathbf{r})$  are the surface current density and surface charge density, respectively,  $\mu_0$  and  $\epsilon_0$  are the free-space permeability and permittivity, respectively,  $\overline{\mathbf{G}}(\mathbf{r}, \mathbf{r}')$  is the spatial dyadic Green's function for the vector potential, and  $G_\Phi$  is the spatial scalar Green's function for the scalar potential. The scattered electric field due to the sources  $\mathbf{J}_s(\mathbf{r})$  and  $\rho_s(\mathbf{r})$  are then expressed as

$$\mathbf{E}^s(\mathbf{r}) = -j\omega \mathbf{A}(\mathbf{r}) - \nabla \Phi(\mathbf{r}). \quad (\text{F.2})$$

The reflectarray problem is formulated using the mixed-potential form of the electric field integral equation (EFIE) [137–139, 143]

$$\begin{aligned} \hat{n} \times \mathbf{E}^i(\mathbf{r}) = \hat{n} \times & \left( j\omega\mu_0 \int_S \overline{\mathbf{G}}(\mathbf{r}, \mathbf{r}') \cdot \mathbf{J}_s(\mathbf{r}') dS' \right. \\ & \left. + \frac{1}{\epsilon_0} \nabla \int_S G_\Phi(\mathbf{r}, \mathbf{r}') \rho_s(\mathbf{r}') dS' \right), \quad \mathbf{r} \in S. \end{aligned} \quad (\text{F.3})$$

Herein,  $\mathbf{E}^i(r)$  is the incident field and  $\hat{n}$  is the outward unit vector normal to the surface  $S$ . Since only single layer configurations have been considered in this work,  $\overline{\mathbf{G}}$  and  $G_\Phi$  for a grounded dielectric slab is required. The configuration is shown in Figure F.1. For reflectarray configurations, only the tangential components of the dyadic  $\overline{\mathbf{G}}$  is of interest since the electric currents will always be oriented in the  $xy$ -plane. The expressions for the Green's functions can be derived in closed form in the spectral domain, but in the spatial domain, one needs to evaluate Sommerfeld integrals which are improper integrals [137, 138, 151]. The spatial Green's functions are integrated in GRASP, and the EFIE is solved using the method of moments (MoM) from the GRASP MoM add-on [94]. In the following, the spatial Green's functions will be briefly described.

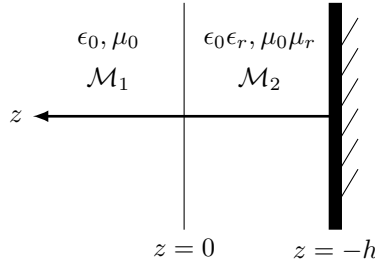


**Figure F.1** *A grounded dielectric slab.*

## F.2 Vector and Scalar Potential Green's Functions

The goal is to determine the vector and scalar potentials generated by a Hertzian dipole in the presence of the dielectric and ground plane. Consider an  $x$ -directed Hertzian dipole located at the origin of the configuration shown in Figure F.1. The expression for such a dipole is given by

$$\mathbf{J} = \hat{x} I_0 \delta(x) \delta(y), \quad (\text{F.4})$$

and this can be expanded in a plane wave spectrum [152]

$$\mathbf{J} = \hat{x} I_0 \frac{1}{4\pi^2} \iint_{-\infty}^{\infty} e^{-j(k_x x + k_y y)} dk_x dk_y. \quad (\text{F.5})$$

The vector and scalar potentials can be derived by considering the Fresnel reflection and transmission coefficients for each plane wave. The derivation is rather

lengthy and only the final result is shown here. The vector potential is given by<sup>1</sup>

$$\begin{aligned} \mathbf{A} = & \frac{\mu_0 I_0 k}{j 8 \pi} \int_0^\infty \left\{ \left[ \hat{x} (J_0(k s \rho) - J_2(k s \rho) \cos 2\phi) + \hat{y} (-J_2(k s \rho) \sin 2\phi) \right] (1 + \mathcal{R}_{\text{TM}}) \right. \\ & \left. - \left[ -\hat{x} (J_0(k s \rho) + J_2(k s \rho) \cos 2\phi) + \hat{y} (-J_2(k s \rho) \sin 2\phi) \right] (1 + \mathcal{R}_{\text{TE}}) \right\} \\ & \frac{s}{\sqrt{1-s^2}} e^{-j k \sqrt{1-s^2} z} ds. \end{aligned} \quad (\text{F.6})$$

and the scalar potential

$$\Phi = \frac{1}{\epsilon_0} \frac{\rho_0 k}{j 4 \pi} \int_0^\infty J_0(k s \rho) (1 + \mathcal{R}_{\text{TM}}) \frac{s}{\sqrt{1-s^2}} e^{-j k \sqrt{1-s^2} z} ds. \quad (\text{F.7})$$

Herein,  $k$  is the free-space wave number,  $\rho, \phi, z$  are the observation points in polar coordinates,  $J_\nu$  is the Bessel function of first kind and order  $\nu$ , and the reflection coefficients can be expressed in terms of the integration variable  $s$  as

$$\mathcal{R}_{\text{TM}} = \frac{\frac{1}{\epsilon_r} \sqrt{\epsilon_r - s^2} - \sqrt{1-s^2} - \left( \frac{1}{\epsilon_r} \sqrt{\epsilon_r - s^2} + \sqrt{1-s^2} \right) e^{-2j k h \sqrt{\epsilon_r - s^2}}}{\frac{1}{\epsilon_r} \sqrt{\epsilon_r - s^2} + \sqrt{1-s^2} - \left( \frac{1}{\epsilon_r} \sqrt{\epsilon_r - s^2} - \sqrt{1-s^2} \right) e^{-2j k h \sqrt{\epsilon_r - s^2}}}, \quad (\text{F.8a})$$

$$\mathcal{R}_{\text{TE}} = \frac{\sqrt{1-s^2} - \sqrt{\epsilon_r - s^2} - \left( \sqrt{1-s^2} + \sqrt{\epsilon_r - s^2} \right) e^{-2j k h \sqrt{\epsilon_r - s^2}}}{\sqrt{1-s^2} + \sqrt{\epsilon_r - s^2} - \left( \sqrt{1-s^2} - \sqrt{\epsilon_r - s^2} \right) e^{-2j k h \sqrt{\epsilon_r - s^2}}}. \quad (\text{F.8b})$$

For sources located at  $(\rho', z')$ ,  $\rho$  and  $z$  in (F.6) and (F.7) are replaced by  $|\rho - \rho'|$  and  $|z - z'|$ , respectively.

The equations (F.6) and (F.7) are essentially computed by considering 4 integrals

$$I_1 = -j k \int_{\text{SIP}} J_0(k s \rho) \frac{s}{\sqrt{1-s^2}} e^{-j k \sqrt{1-s^2} z} ds, \quad (\text{F.9a})$$

$$I_2 = -j k \int_{\text{SIP}} J_2(k s \rho) \frac{s}{\sqrt{1-s^2}} e^{-j k \sqrt{1-s^2} z} ds, \quad (\text{F.9b})$$

$$I_3^{\text{TM/TE}} = -j k \int_{\text{SIP}} J_0(k s \rho) \frac{s}{\sqrt{1-s^2}} e^{-j k \sqrt{1-s^2} z} \mathcal{R}_{\text{TM/TE}} ds, \quad (\text{F.9c})$$

$$I_4^{\text{TM/TE}} = -j k \int_{\text{SIP}} J_2(k s \rho) \frac{s}{\sqrt{1-s^2}} e^{-j k \sqrt{1-s^2} z} \mathcal{R}_{\text{TM/TE}} ds, \quad (\text{F.9d})$$

---

<sup>1</sup>Dr. Stig B. Sørensen, TICRA, is acknowledged for his contributions to this section. Among other things, he provided the derivation of the expressions for the vector and scalar potentials (F.6)-(F.8).

where  $\mathcal{R}_{\text{TM/TE}}$  denotes the TM or TE reflection coefficient in (F.8) and SIP the Sommerfeld integration path. Equations (F.6) and (F.7) then reduce to

$$\mathbf{A} = \frac{\mu_0 I_0}{8\pi} \left\{ \hat{x} [2I_1 + I_3^{\text{TM}} + I_3^{\text{TE}} + \cos 2\phi (I_4^{\text{TE}} - I_4^{\text{TM}})] + \hat{y} [\sin 2\phi (I_4^{\text{TE}} - I_4^{\text{TM}})] \right\}, \quad (\text{F.10a})$$

$$\Phi = \frac{1}{\epsilon_0} \frac{\rho_0}{4\pi} (I_1 + I_3^{\text{TM}}). \quad (\text{F.10b})$$

For a  $y$ -directed Hertzian dipole, the vector potential can be obtained by an appropriate coordinate transformation of (F.10a). By comparison with (F.1), it is identified that the tangential components of the dyadic  $\mathbf{\bar{G}}$  are

$$G_{xx} = \frac{1}{4\pi} \left( I_1 + \frac{I_3^{\text{TM}} + I_3^{\text{TE}} + \cos 2\phi (I_4^{\text{TE}} - I_4^{\text{TM}})}{2} \right), \quad (\text{F.11a})$$

$$G_{yy} = \frac{1}{4\pi} \left( I_1 + \frac{I_3^{\text{TM}} + I_3^{\text{TE}} + \cos 2\phi (I_4^{\text{TM}} - I_4^{\text{TE}})}{2} \right), \quad (\text{F.11b})$$

$$G_{xy} = G_{yx} = \frac{1}{4\pi} \left( \frac{\sin 2\phi (I_4^{\text{TE}} - I_4^{\text{TM}})}{2} \right), \quad (\text{F.11c})$$

and that the scalar Green's function is

$$G_\Phi = \frac{1}{4\pi} (I_1 + I_3^{\text{TM}}). \quad (\text{F.12})$$

### F.3 Computation of the Vector and Scalar Potential Green's Functions

In this section, the computation of  $\mathbf{\bar{G}}$  and  $G_\Phi$  is described.

Integral  $I_1$  is given by the Sommerfeld identity [152]

$$-jk \int_{\text{SIP}} J_0(k\rho) \frac{s}{\sqrt{1-s^2}} e^{-jk\sqrt{1-s^2}z} ds = \frac{e^{-jkr}}{r}, \quad (\text{F.13})$$

where  $r = \sqrt{\rho^2 + z^2}$ . A similar expression can be derived for  $I_2$  using recurrence formulas for the Bessel functions<sup>2</sup>

$$-jk \int_{\text{SIP}} J_2(k\rho) \frac{s}{\sqrt{1-s^2}} e^{-jk\sqrt{1-s^2}z} ds = -\frac{e^{-jkr}}{r} + \frac{2j}{k\rho^2} (e^{-jkr} - e^{-jzk}). \quad (\text{F.14})$$

---

<sup>2</sup>Dr. Niels C. Albertsen, TICRA, is acknowledged for providing the derivation of (F.14).

Analytical expressions for integrals  $I_3^{\text{TM/TE}}$  and  $I_4^{\text{TM/TE}}$  are not readily obtained and computing these numerically can be time consuming, thus special treatment of the equations is required in order to accelerate the computational time. One solution is to use the discrete complex image method (DCIM) [146,147,153–155].

### F.3.1 Discrete Complex Image Method

Suppose the reflection coefficient can be written in terms of a sum of complex exponentials of the kind

$$\mathcal{R}_{\text{TM/TE}} = \sum_m^M c_m e^{\beta_m k \sqrt{1-s^2}}, \quad (\text{F.15})$$

then upon substitution in (F.9c) the integral  $I_3^{\text{TM/TE}}$  becomes

$$\begin{aligned} I_3^{\text{TM/TE}} &= -jk \int_{\text{SIP}} J_0(k s \rho) \frac{s}{\sqrt{1-s^2}} e^{-jk\sqrt{1-s^2}z} \sum_m^M c_m e^{\beta_m k \sqrt{1-s^2}} ds, \\ &= -jk \sum_m^M c_m \int_{\text{SIP}} J_0(k s \rho) \frac{s}{\sqrt{1-s^2}} e^{-jk\sqrt{1-s^2}z + \beta_m k \sqrt{1-s^2}} ds, \\ &= -jk \sum_m^M c_m \int_{\text{SIP}} J_0(k s \rho) \frac{s}{\sqrt{1-s^2}} e^{-jk\sqrt{1-s^2}\tilde{z}_m} ds, \\ &= \sum_m^M c_m \frac{e^{-jk\sqrt{\rho^2 + \tilde{z}_m^2}}}{\sqrt{\rho^2 + \tilde{z}_m^2}}, \end{aligned} \quad (\text{F.16})$$

where  $\tilde{z}_m = z + j\beta_m$ . To approximate the reflection coefficients in the form (F.15), the generalized pencil-of-function (GPOF) method [156] is used. The GPOF method takes a number of uniform samples of the function  $f(x)$  that is to be expanded, and approximate it in the form

$$f(x) \simeq \sum_m^M a_m e^{b_m x}. \quad (\text{F.17})$$

This does not satisfy the form in (F.15), thus a deformed path on the  $s$  plane is defined as a mapping of a real variable  $t$  onto the complex  $k\sqrt{1-s^2}$  plane [155]

$$\sqrt{1-s^2} = 1 - \frac{t}{T_0} - jt, \quad 0 \leq t \leq T_0. \quad (\text{F.18})$$

For each value of  $t$ , the corresponding  $s$  value is computed and the reflection coefficient is sampled at that value. The function is then approximated using



the GPOF method in terms of  $t$  which returns

$$\mathcal{R}_{\text{TM/TE}} = \sum_m^M c'_m e^{\beta'_m t}. \quad (\text{F.19})$$

By comparison between (F.15) and (F.19), it can be shown that

$$c_m = c'_m e^{\beta'_m \frac{T_0}{1+jT_0}}, \quad (\text{F.20a})$$

$$\beta_m = \beta'_m \frac{T_0}{k(1+jT_0)}. \quad (\text{F.20b})$$

The same procedure can be applied for integral  $I_4^{\text{TM/TE}}$  using the identity for  $I_2$  in (F.14). To summarize, the integrals are

$$I_1 = \frac{e^{-jkr}}{r}, \quad (\text{F.21a})$$

$$I_2 = -\frac{e^{-jkr}}{r} + \frac{2j}{k\rho^2} (e^{-jkr} - e^{-jkz}), \quad (\text{F.21b})$$

$$I_3^{\text{TM/TE}} = \sum_m^M c_m \frac{e^{-jk\sqrt{\rho^2 + \tilde{z}_m^2}}}{\sqrt{\rho^2 + \tilde{z}_m^2}}, \quad (\text{F.21c})$$

$$I_4^{\text{TM/TE}} = \sum_m^M c_m \left[ -\frac{e^{-jk\sqrt{\rho^2 + \tilde{z}_m^2}}}{\sqrt{\rho^2 + \tilde{z}_m^2}} + \frac{2j}{k\rho^2} (e^{-jk\sqrt{\rho^2 + \tilde{z}_m^2}} - e^{-jk\tilde{z}_m}) \right]. \quad (\text{F.21d})$$

### F.3.2 Asymptotic Behavior of $\mathcal{R}_{\text{TM}}$

Looking at the asymptotic behavior of the reflection coefficients, it is seen that

$$\lim_{s \rightarrow \infty} \mathcal{R}_{\text{TM}} = -\frac{\epsilon_r - 1}{\epsilon_r + 1}, \quad (\text{F.22a})$$

$$\lim_{s \rightarrow \infty} \mathcal{R}_{\text{TE}} = 0. \quad (\text{F.22b})$$

The convergence of the GPOF procedure can be enhanced by subtracting the asymptotic value of  $\mathcal{R}_{\text{TM}}$

$$I'_3 = I_3^{\text{TM}} - \lim_{s \rightarrow \infty} I_3^{\text{TM}} = \int_{\text{SIP}} J_0(ks\rho) \frac{-jks}{\sqrt{1-s^2}} e^{-jk\sqrt{1-s^2}z} \left( \mathcal{R}_{\text{TM}} + \frac{\epsilon_r - 1}{\epsilon_r + 1} \right) ds, \quad (\text{F.23a})$$

$$I'_4 = I_4^{\text{TM}} - \lim_{s \rightarrow \infty} I_4^{\text{TM}} = \int_{\text{SIP}} J_2(ks\rho) \frac{-jks}{\sqrt{1-s^2}} e^{-jk\sqrt{1-s^2}z} \left( \mathcal{R}_{\text{TM}} + \frac{\epsilon_r - 1}{\epsilon_r + 1} \right) ds. \quad (\text{F.23b})$$

The term  $\mathcal{R}_{\text{TM}} + \frac{\epsilon_r - 1}{\epsilon_r + 1}$  is then expanded using GPOF and used in (F.21) to approximate  $I'_3$  and  $I'_4$ . To obtain  $I_3^{\text{TM}}$  and  $I_4^{\text{TM}}$  the asymptotic values must be added again. The asymptotic values are

$$\lim_{s \rightarrow \infty} I_3^{\text{TM}} = -\frac{\epsilon_r - 1}{\epsilon_r + 1} I_1, \quad (\text{F.24a})$$

$$\lim_{s \rightarrow \infty} I_4^{\text{TM}} = -\frac{\epsilon_r - 1}{\epsilon_r + 1} I_2. \quad (\text{F.24b})$$

### F.3.3 Validation of the DCIM

A routine using the DCIM to determine the spatial Green's functions has been implemented. A GPOF algorithm was available at TICRA and was used directly in the DCIM implementation.

To facilitate a reference solution for the implementation of the DCIM, a numerical integration of  $\overline{\mathbf{G}}$  and  $G_\Phi$  has been implemented. The integrals are precomputed for a number of  $\rho$  values and stored in a look-up table, which is accessed when filling the MoM matrix by means of local cubic interpolation. Although numerical integration is required, the look-up table led to a particularly efficient solution with a computation time that is comparable to that of the DCIM.

The comparison between the two solutions showed that the DCIM is rather unstable and the approximated Green's functions using DCIM did not agree with the numerical integration solution for small values of  $\rho$ , and the accuracy was highly dependent on the choice of  $T_0$ . Thus, to use the DCIM to obtain accurate results, several iterations must be performed and compared to the reference solution to determine the optimal value of  $T_0$ . Solutions to this issue has been proposed, e.g. [155], but was not pursued as it was out of the scope of the project. As a result, the numerical integration in conjunction with the look-up table has been used to calculate  $\overline{\mathbf{G}}$  and  $G_\Phi$  in this work.

## F.4 Other Formulations of the Spatial Green's Functions

It is known that the vector and scalar potentials for layered media are not unique [157] and to satisfy the boundary conditions at the interfaces of the layered media, two components of the vector potential (and its corresponding scalar potential) are needed [137]. In the formulation described above, the  $x$  and  $y$  components are used. Traditionally, the  $z$  component is selected in addition to the  $x$  component, e.g. [146, 151]. For validation purposes, the expressions in [146, Eqn.(1)-(5)] have been implemented and compared to results obtained using the expressions presented in this appendix. Identical results were obtained thus verifying the derivation of  $\overline{\mathbf{G}}$  and  $G_\Phi$ .



# Publications



# PAPER I

---

## AN ACCURATE TECHNIQUE FOR CALCULATION OF RADIATION FROM PRINTED REFLECTARRAYS

Min Zhou, Stig B. Sørensen, Erik Jørgensen, Peter Meincke,  
Oleksiy S. Kim, and Olav Breinbjerg

*Status*

Published: October 2011

### **Bibliography**

- [J1] M. Zhou, S. B. Sørensen, E. Jørgensen, P. Meincke, O. S. Kim, and O. Breinbjerg, “An accurate technique for calculation of radiation from printed reflectarrays,” *IEEE Antennas Wireless Propag. Lett.*, vol. 10, pp. 1081–1084, 2011.



# An Accurate Technique for Calculation of Radiation From Printed Reflectarrays

Min Zhou, Stig B. Sørensen, *Member, IEEE*, Erik Jørgensen, *Member, IEEE*, Peter Meincke, *Member, IEEE*, Oleksiy S. Kim, and Olav Breinbjerg, *Member, IEEE*

**Abstract**—The accuracy of various techniques for calculating the radiation from printed reflectarrays is examined, and an improved technique based on the equivalent currents approach is proposed. The equivalent currents are found from a continuous plane wave spectrum calculated by use of the spectral dyadic Green's function. This ensures a correct relation between the equivalent electric and magnetic currents and thus allows an accurate calculation of the radiation over the entire far-field sphere. A comparison to DTU-ESA Facility measurements of a reference offset reflectarray designed and manufactured specifically for this purpose is presented to demonstrate the accuracy of the proposed technique.

**Index Terms**—Accurate antenna analysis, antenna radiation pattern, dyadic Green's function (DGF), equivalent currents, method of moments (MoM), reflectarray.

## I. INTRODUCTION

PRINTED reflectarrays provide a way for realizing low-cost, high-gain antennas for satellite applications and have been the subject of increasing research interest [1], [2]. In the analysis of printed reflectarrays, the main focus has been on the accurate determination of the currents on the array elements [3]–[5], while the calculation of the radiation pattern has received less attention. However, the latter is equally important, and for space applications where the accuracy demands are high, an accurate prediction of the radiation pattern is required and should not be neglected. Some of the few reported techniques in the literature include approximate formulas based on array element summations [6]–[8], stationary phase approximation of the spatial dyadic Green's function (DGF) [9], and the field equivalence principle [5], [10]–[12]. The objective of this letter is to compare different techniques for calculating the radiation from printed reflectarrays and to propose and validate an improved method.

The commonly adopted method for determining the currents is based on the spectral domain method of moments (SDMoM).

Manuscript received July 11, 2011; revised August 19, 2011; accepted September 21, 2011. Date of publication October 06, 2011; date of current version October 17, 2011. The reflectarray antenna production and measurement was supported by the European Space Agency under ESTEC Contract No. 4000101041.

M. Zhou is with TICRA, Copenhagen 1201, Denmark, and also with the Department of Electrical Engineering, Electromagnetic Systems, Technical University of Denmark, Kgs. Lyngby 2800, Denmark (e-mail: mz@ticra.com).

S. B. Sørensen, E. Jørgensen, and P. Meincke are with TICRA, Copenhagen 1201, Denmark (e-mail: ticra@ticra.com).

O. S. Kim and O. Breinbjerg are with the Department of Electrical Engineering, Electromagnetic Systems, Technical University of Denmark, Kgs. Lyngby 2800, Denmark (e-mail: osk@elektro.dtu.dk; ob@elektro.dtu.dk).

Color versions of one or more of the figures in this letter are available online at <http://ieeexplore.ieee.org>.

Digital Object Identifier 10.1109/LAWP.2011.2170652

It assumes local periodicity such that the individual array element is embedded in an infinite array consisting of identical elements [7]. This method is also used to determine the unknown currents on the array elements in this letter.

This letter is organized as follows. Section II discusses the different techniques for radiation pattern calculation. The reference antenna is described in Section III. In Section IV, simulations are compared to the measured data, and conclusions are given in Section V.

The time factor  $e^{j\omega t}$  is assumed and suppressed throughout the letter.

## II. TECHNIQUES FOR CALCULATION OF RADIATION

Three techniques to calculate the radiation from printed reflectarrays will be considered in this letter, and they will be described in this section.

### A. Technique I: Stationary Phase Evaluation of DGF

A simple technique to determine the radiation from printed reflectarrays is the direct calculation from the currents on the array elements using a spatial DGF assuming an infinite ground plane [9]. The spatial DGF is found through its spectral counterpart and expressed in terms of infinite integrals. The numerical evaluation of these integrals is computationally expensive [13]. However, for far-field radiation pattern calculations, the stationary phase approximation can be used [9].

The drawback of this technique is that the DGF assumes infinite substrate and ground plane, thus the finite substrate size is not taken into account and the radiation in the backward hemisphere cannot be determined.

### B. Technique II: Equivalent Currents From Floquet Spectrum

This technique utilizes the equivalent currents approach [14, p. 106]. Equivalent currents are constructed on a surface enclosing the entire reflectarray. The currents are defined by

$$\mathbf{J}_S = \hat{n} \times \mathbf{H} \quad \mathbf{M}_S = -\hat{n} \times \mathbf{E} \quad (1)$$

where  $\mathbf{E}$  and  $\mathbf{H}$  are the total electric and magnetic fields at the surface and  $\hat{n}$  is the outward unit vector normal to the surface. Usually, the total field in the entire half-space behind the reflectarray is assumed to be zero, and the equivalent currents are computed only in the plane of the array elements. By placing a perfect electric or magnetic conductor behind this planar surface, the electric or magnetic current, respectively, is short-circuited. The image principle is then employed to double the magnetic or electric current [10], [11]. On the other hand, if both electric and magnetic currents are used, the radiation over the



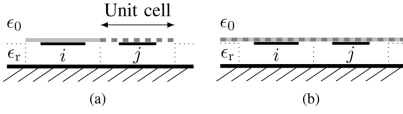


Fig. 1. Calculation of the equivalent currents for (a) technique II and (b) technique III. The equivalent currents for the  $i$ th and  $j$ th element are shown with solid and dashed lines, respectively.

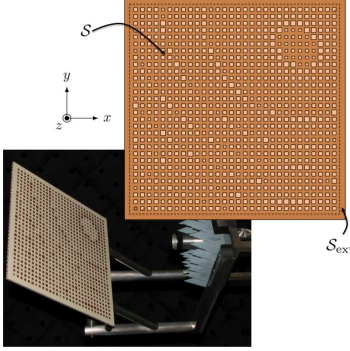


Fig. 2. Reflectarray designed with a pencil beam directed toward  $\theta = 35^\circ$  and  $\phi = 135^\circ$  in the shown coordinate system and measured at the DTU-ESA Spherical Near-Field Antenna Test Facility. The surface  $S$  is the area confined within the dashed lines covering the unit cells, and  $S_{\text{ext}}$  covers the extended substrate area.

entire far-field sphere can be calculated. In this case, the equivalent currents on the back side and at the edges of the reflectarray are assumed to be zero [5].

The equivalent currents are determined through the Floquet space harmonics from the SDMoM formulation. Due to the periodicity, the equivalent currents for each array element are calculated only within its own unit cell, as illustrated in Fig. 1(a). The equivalent currents for the  $i$ th and  $j$ th element are shown with solid and dashed lines, respectively. Thus, the contribution from each array element to the equivalent current is confined to its unit cell. By repeating this procedure for all array elements, equivalent currents on the surface,  $S$ , covering all elements/unit cells are constructed. For practical reasons, the substrate and ground plane in reflectarrays are often extended at the edges, and the physical substrate size is then larger than  $S$ . To correct for this, unit cells with no array elements are placed at the edges such that the extended substrate area  $S_{\text{ext}}$  is also covered; see Fig. 2. In this way, equivalent currents on the entire surface  $S_{\text{tot}} = S + S_{\text{ext}}$  are constructed.

It is sufficient to approximate the equivalent currents on each unit cell using the fundamental Floquet space harmonic. This is valid since the distance between the array elements is usually selected to avoid grating lobes, and all higher-order Floquet space harmonics are thus evanescent waves that do not contribute to the far-field radiation. As a result, the equivalent currents are calculated assuming the electric and magnetic field on the unit-cell surface being related through the plane wave

relation. In addition, discontinuities in the equivalent currents are created due to the truncation of the currents at the border of each unit cell. These issues may result in erroneous radiation patterns, as will be shown in Section IV.

### C. Technique III: Equivalent Currents From Continuous Spectrum

We propose a novel technique combining techniques I and II. This technique is based on the equivalent currents approach, but these equivalent currents are calculated using a continuous spectrum formulation.

Like in techniques I and II, the currents on the array elements are calculated under the local periodicity assumption. The equivalent currents are constructed on a surface enclosing the entire reflectarray as given by (1). The total field on the back side and at the edges of the reflectarray are assumed to be zero. The tangential electric field at the plane of the array elements  $z = 0$  can be expanded in a spectrum of plane waves [15]

$$\mathbf{E}(x, y) = \frac{1}{4\pi^2} \iint_{-\infty}^{\infty} \mathbf{E}(k_x, k_y) e^{-j(k_x x + k_y y)} dk_x dk_y \quad (2)$$

where the spectral amplitude  $\mathbf{E}(k_x, k_y)$  is

$$\mathbf{E}(k_x, k_y) = \tilde{\mathbf{G}}(k_x, k_y) \cdot (\tilde{\mathbf{J}}(k_x, k_y) - \mathbf{b}(k_x, k_y)). \quad (3)$$

Herein,  $\tilde{\mathbf{J}}(k_x, k_y)$  is the Fourier transformation of the electric current on the array elements, and  $\mathbf{b}(k_x, k_y)$  is given by

$$\mathbf{b}(k_x, k_y) = \frac{2}{\eta_0 k_0 \gamma_0} \begin{pmatrix} k_0^2 - k_y^2 & k_x k_y \\ k_x k_y & k_0^2 - k_x^2 \end{pmatrix} \cdot \mathbf{E}^i(k_x, k_y). \quad (4)$$

In the above,  $\eta_0$  is the free-space impedance,  $k_0$  the free-space wavenumber, and  $\gamma_0 = \sqrt{k_0^2 - k_x^2 - k_y^2}$ . The quantity  $\mathbf{E}^i(k_x, k_y)$  is the spectral amplitude of the plane wave expansion of the incident electric field. The dyad  $\tilde{\mathbf{G}}(k_x, k_y)$  is the multilayer Green's function in the spectral domain. For the specific case of a single dielectric layer backed with an infinite ground plane, the terms in the spectral DGF can be found in [16, eqs. (2)–(4)].

The numerical computation of (2) is cumbersome, but since only propagating waves contribute to the far-field radiation, the evanescent waves can be excluded in the integration to yield

$$\mathbf{E}(x, y) = \frac{1}{4\pi^2} \iint_{k_x^2 + k_y^2 < k_0^2} \mathbf{E}(k_x, k_y) e^{-j(k_x x + k_y y)} dk_x dk_y. \quad (5)$$

Consequently, the need of pole residue calculation or other cumbersome methods [17] can be avoided. The spectral integrals can be done in polar variables and performed efficiently using standard integration rules. Once  $\mathbf{E}(k_x, k_y)$  is determined, the magnetic field can be readily obtained using the plane wave relation

$$\mathbf{H}(x, y) = \frac{1}{4\pi^2} \iint_{k_x^2 + k_y^2 < k_0^2} \frac{1}{\eta_0} \hat{k} \times \mathbf{E}(k_x, k_y) \cdot e^{-j(k_x x + k_y y)} dk_x dk_y \quad (6)$$

TABLE I  
 REFERENCE REFLECTARRAY DATA

Frequency	9.6 GHz
Number of elements	30 × 30
Reflectarray dimensions	435 mm × 435 mm
Substrate thickness	0.762 mm
Relative permittivity ( $\epsilon_r$ )	3.66
Loss tangent ( $\tan \delta$ )	0.0037
Feed distance to center of array	0.35 m
Feed offset angle	$\theta = 45^\circ$ , $\phi = 0^\circ$
Main beam direction	$\theta = 35^\circ$ , $\phi = 135^\circ$

where  $\hat{k} = \hat{x}k_x + \hat{y}k_y + \hat{z}\gamma_0$  describes the direction of propagation. Upon substitution in (1), the equivalent currents are calculated over the entire surface  $S_{\text{tot}}$ , thus automatically accounting for the area  $S_{\text{ext}}$ . A graphical illustration is shown in Fig. 1(b), where the equivalent currents for the  $i$ th and  $j$ th element are again shown with solid and dashed lines, respectively. The currents cover the entire  $S_{\text{tot}}$ , and the contribution from each array element over the entire surface is taken into account. Contrary to technique II, the electric and magnetic field at the reflectarray surface are related through the continuous plane wave spectrum and not through the plane wave relation of the fundamental Floquet space harmonic.

An overhead associated with the numerical evaluation of (5)–(6) does not significantly increase the overall computation time. For the reflectarray to be described in Section III, the computation times for techniques I–III using a 2.8-GHz Intel processor laptop are 25, 28, and 30 s, respectively.

### III. REFERENCE ANTENNA

The reflectarray antenna first reported in [5] is used as a reference, and its geometrical parameters are summarized in Table I. The antenna is designed to exaggerate the lack of periodicity by having a pencil beam toward  $\theta = 35^\circ$  and  $\phi = 135^\circ$  in the coordinate system shown in Fig. 2. The feed is an  $x$ -polarized Potter horn with a 3-dB beamwidth of  $40^\circ$ , yielding an edge illumination varying from approximately  $-20$  to  $-5$  dB. The reflectarray and its support structures are manufactured at the Technical University of Denmark (DTU), Kgs. Lyngby, Denmark, and measured at the DTU-ESA-Spherical Near-Field Antenna Test Facility [18]. For the peak directivity, the measurements have a  $1\sigma$  uncertainty of 0.07 dB. The measured gain of the reflectarray is 28.74 dB. In addition to the reflectarray measurements, the Potter horn is also measured, and the measured data are used in the SDMoM calculations.

### IV. SIMULATIONS VERSUS MEASUREMENTS

The radiation patterns at 9.6 GHz obtained by measurements and simulations using techniques I–III are shown in Fig. 3. To account for the presence of the support structures, the scattering from the struts is included in the analysis using the MoM add-on in GRASP [19]. For techniques II and III, both electric and magnetic currents are used. Results using only electric or magnetic currents are not shown since they yield patterns similar to those obtained using both currents but limited to the forward hemisphere.

All three techniques are capable of determining the main beam direction and beamwidth with good accuracy. However,

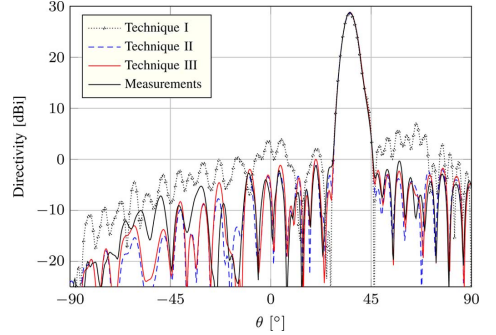


Fig. 3. Simulated and measured radiation patterns of the copolar component at  $\phi = 135^\circ$ . Both electric and magnetic currents are used in techniques II and III.

technique I is very inaccurate in predicting the sidelobes since the finite substrate size is not accounted for. Techniques II and III, on the other hand, account for the finite substrate size and therefore yield patterns that are in good agreement with the measurements. The peak directivity is measured to  $D_{\text{meas}} = 29.35$  dB. Techniques I and II yield  $D_I = 29.11$  dB and  $D_{II} = 29.10$  dB, respectively, whereas technique III gives an improved value of  $D_{III} = 29.30$  dB.

To illustrate the accuracy in the back hemisphere, the radiation in the entire sphere is shown in Fig. 4. The agreement with the measurement is good for both techniques II and III. However, it is seen that in the direction of the main beam's image around  $\theta = 145^\circ$  and  $\phi = 135^\circ$ , technique II gives an erroneous beam, both for the copolar and the cross-polar component. Usually, the equivalent electric and magnetic currents each give strong contributions in the direction of the image, but in sum they cancel each other. Thus, such an erroneous beam should not exist if the currents are correctly related. There are several error sources that can introduce such an incorrect relation as described in the following.

In technique II, the equivalent currents are calculated under the approximation that the electric and magnetic fields in each unit cell are related by the plane wave relation. This approximation is inaccurate for configurations where the reflectarray is located close to the feed. Thus, errors are introduced in the equivalent currents, resulting in an incorrect relation between them. In addition, the total equivalent currents are composed of truncated currents, and jumps in phase and amplitude can occur at the borders of the unit cells. This can give phase and amplitude errors, especially for aperiodic reflectarrays, thus further deteriorating the relation between the equivalent currents. These sources of error give an incorrect relation between the equivalent currents, thus causing the erroneous beam. For reflectarrays made of slowly varying-sized elements and with large feed distances, the errors diminish, and no erroneous beams are created.

This problem is circumvented in technique III. No discontinuities are created in the equivalent currents, and the electric and magnetic currents are correctly related through the continuous

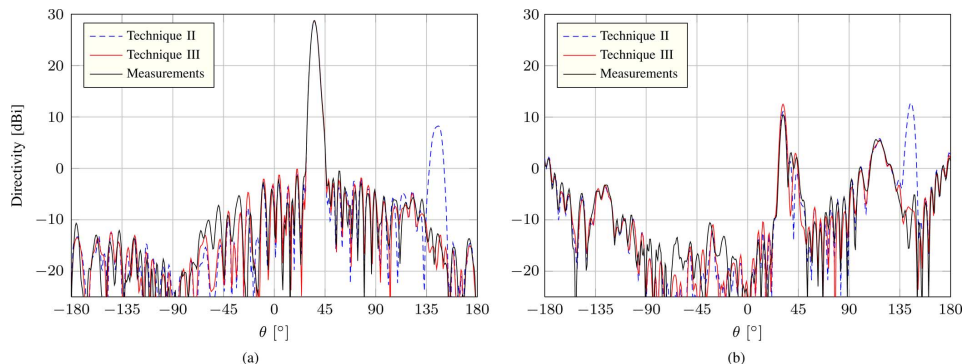


Fig. 4. Simulated and measured radiation patterns of the (a) copolar and (b) cross-polar components at  $\phi = 135^\circ$ .

plane wave spectrum. Hence, the sum of the two gives an accurate pattern in the entire far-field sphere. The remaining discrepancies seen in Figs. 3 and 4 are mainly attributed to the local periodicity approximation in the SDMoM analysis [5].

## V. CONCLUSION

Several techniques to calculate the radiation from printed reflectarrays have been compared, and an improved technique based on the equivalent currents approach has been proposed. The equivalent currents are determined from a continuous plane wave spectrum computed using the spectral dyadic Green's function. This ensures the correct relation between the equivalent electric and magnetic currents and enables an accurate calculation of the radiation over the entire sphere. An offset reflectarray has been manufactured and measured to serve as reference. Comparisons of simulated and measured radiation patterns show that the choice of the technique to calculate the radiation is very important with respect to the analysis accuracy. The finite substrate and ground plane size of the reflectarray must be accounted for, and techniques that neglect this yield inaccurate radiation patterns. The comparisons also show that the proposed technique improves the accuracy of calculating the radiation from printed reflectarrays.

## ACKNOWLEDGMENT

Dr. S. Pivnenko, DTU, is acknowledged for the high-accuracy measurements of the reflectarray samples.

## REFERENCES

- [1] J. Huang and J. A. Encinar, *Reflectarray Antennas*. Piscataway, NJ: IEEE Press, 2008.
- [2] J. A. Encinar, "Recent advances in reflectarray antennas," in *Proc. EuCAP*, Barcelona, Spain, 2010, pp. 1–6.
- [3] M. A. Milon, D. Cadoret, R. Gillard, and H. Legay, "Surrounded-element approach for the simulation of reflectarray radiating cells," *Microw. Antennas Propag.*, vol. 1, no. 2, pp. 289–293, 2007.
- [4] M. Arrebola, Y. Alvarez, J. A. Encinar, and F. Las-Heras, "Accurate analysis of printed reflectarrays considering the near field of the primary feed," *Microw. Antennas Propag.*, vol. 3, no. 2, pp. 187–194, 2009.
- [5] M. Zhou, S. B. Sørensen, E. Jørgensen, P. Meincke, O. S. Kim, and O. Breinbjerg, "Analysis of printed reflectarrays using extended local periodicity," in *Proc. EuCAP*, Rome, Italy, 2011, pp. 1408–1412.
- [6] D. C. Chang and M. C. Huang, "Multiple-polarization microstrip reflectarray antenna with high efficiency and low cross-polarization," *IEEE Trans. Antennas Propag.*, vol. 43, no. 8, pp. 829–834, Aug. 1995.
- [7] D. M. Pozar, S. D. Targonski, and H. D. Syrigos, "Design of millimeter wave microstrip reflectarrays," *IEEE Trans. Antennas Propag.*, vol. 45, no. 2, pp. 287–296, Feb. 1997.
- [8] A. W. Robinson, M. E. Bialkowski, and H. J. Song, "A passive reflect array with dual-feed microstrip patch elements," *Microw. Opt. Technol. Lett.*, vol. 23, no. 5, pp. 295–299, 1999.
- [9] D. M. Pozar, "Radiation and scattering from a microstrip patch on a uniaxial substrate," *IEEE Trans. Antennas Propag.*, vol. AP-35, no. 6, pp. 613–621, Jun. 1987.
- [10] S. R. Rengarajan, "Reciprocity considerations in microstrip reflectarrays," *IEEE Antennas Wireless Propag. Lett.*, vol. 8, pp. 1206–1209, 2009.
- [11] M. Arrebola, J. A. Encinar, and M. Barba, "Multifed printed reflectarray with three simultaneous shaped beams for LMDS central station antenna," *IEEE Trans. Antennas Propag.*, vol. 56, no. 6, pp. 1518–1527, Jun. 2008.
- [12] H. Li, B.-Z. Wang, L. Guo, W. Shao, and P. Du, "A far field pattern analysis technique for reflectarrays including mutual coupling between elements," *J. Electromagn. Waves Appl.*, vol. 23, pp. 87–95, 2009.
- [13] K. Michalski and J. R. Mosig, "Multilayered media Green's functions in integral equation formulations," *IEEE Trans. Antennas Propag.*, vol. 45, no. 3, pp. 508–519, Mar. 1997.
- [14] R. F. Harrington, *Time-Harmonic Electromagnetic Fields*. New York: McGraw-Hill, 1961.
- [15] G. Kristensson, S. Poulsen, and S. Rikte, "Propagators and scattering of electromagnetic waves in planar bianisotropic slabs—An application to frequency selective structures," *Progr. Electromagn. Res.*, vol. 48, pp. 1–25, 2004.
- [16] D. Pozar and D. Schaubert, "Analysis of an infinite array of rectangular microstrip patches with idealized probe feeds," *IEEE Trans. Antennas Propag.*, vol. AP-32, no. 10, pp. 1101–1107, Oct. 1984.
- [17] Y. Chow, J. Yang, D. Fang, and G. Howard, "A closed-form spatial Green's function for the thick microstrip substrate," *IEEE Trans. Microw. Theory Tech.*, vol. 39, no. 3, pp. 588–592, Mar. 1991.
- [18] "DTU-ESA spherical near-field antenna test facility," Technical University of Denmark, Kgs. Lyngby, Denmark [Online]. Available: <http://www.dtu.dk/centre/ems/English/research/facilities.aspx>
- [19] K. Pontopidan, Ed., "GRASP9," TICRA Engineering Consultants, Copenhagen, Denmark, Tech. Description, 2008.

## PAPER II

---

# ACCURATE AND EFFICIENT ANALYSIS OF PRINTED REFLECTARRAYS WITH ARBITRARY ELEMENTS USING HIGHER-ORDER HIERARCHICAL LEGENDRE BASIS FUNCTIONS

Min Zhou, Erik Jørgensen, Oleksiy S. Kim, Stig B. Sørensen,  
Peter Meincke, and Olav Breinbjerg

*Status*

Published: July 2012

### Bibliography

- [J2] M. Zhou, E. Jørgensen, O. S. Kim, S. B. Sørensen, P. Meincke, and O. Breinbjerg, “Accurate and efficient analysis of printed reflectarrays with arbitrary elements using higher-order hierarchical Legendre basis functions”, *IEEE Antennas Wireless Propag. Lett.*, vol. 11, pp. 814–817, 2012.



# Accurate and Efficient Analysis of Printed Reflectarrays With Arbitrary Elements Using Higher-Order Hierarchical Legendre Basis Functions

Min Zhou, *Student Member, IEEE*, Erik Jørgensen, *Member, IEEE*, Oleksiy S. Kim, Stig B. Sørensen, Peter Meincke, *Member, IEEE*, and Olav Breinbjerg, *Member, IEEE*

**Abstract**—It is demonstrated that nonsingular higher-order hierarchical Legendre basis functions are capable of accounting for the singularities of the electric currents at the edges of the reflectarray elements, thus yielding good convergence properties and very accurate results. In addition, the number of Floquet harmonics needed in the spectral domain method of moments is reduced by using higher-order hierarchical Legendre basis functions as compared to singular basis functions. At the same time, higher-order hierarchical Legendre basis functions can be applied to any arbitrarily shaped array elements, thus providing the flexibility required in the analysis of printed reflectarrays. A comparison to DTU-ESA Facility measurements of a reference offset reflectarray shows that higher-order hierarchical Legendre basis functions produce results of the same accuracy as those obtained using singular basis functions.

**Index Terms**—Accurate antenna analysis, basis functions, Floquet harmonics, method of moments (MoM), reflectarray.

## I. INTRODUCTION

PRINTED reflectarrays are becoming viable alternatives to reflector antennas, and they are the subject of increasing research interest [1]. In the analysis and design of reflectarrays, the commonly adopted technique for the calculation of the electric currents on the printed array elements is based on the Local Periodicity approach, where each array element is analyzed assuming that it is located in an infinite array of identical elements [2]. The periodic problem is usually formulated in terms of an integral equation and solved by the spectral domain method of moments (SDMoM) [3]. The Green's function in the integral equation consists of a double summation of Floquet harmonics.

To ensure an accurate yet efficient analysis, suitable basis functions must be selected to minimize the number of basis functions ( $N_b$ ) and Floquet harmonics ( $N_f$ ). For canonically

shaped array elements, e.g., rectangular patches, entire domain basis functions with the correct edge conditions, reproducing the singular behavior of the electric currents at the edges, are known for providing fast convergence in the SDMoM with respect to  $N_b$  [4], [5]. However, due to their singular behavior, the Fourier spectrum is wide, which increases  $N_f$ . For arbitrarily shaped elements, the common choices are first-order basis functions, e.g., Rao–Wilton–Glisson (RWG) [6] or rooftop [7] basis functions. However,  $N_b$  is high for these cases.

The objective of this letter is to present the use of nonsingular higher-order hierarchical Legendre basis functions as described in [8] in the analysis of printed reflectarrays. The higher-order hierarchical Legendre basis functions can be applied to any arbitrarily shaped elements and, at the same time, maintain a good compromise between  $N_b$  and  $N_f$ .

The Fourier transforms of all the basis functions used in this letter are closed-form expressions.

## II. HIGHER-ORDER HIERARCHICAL LEGENDRE BASIS FUNCTIONS

The higher-order hierarchical Legendre basis functions (LegBF) [8] are subdomain nonsingular basis functions. For array elements where the shape can be described using a single mesh element, e.g., rectangular patches, the LegBF can be defined on the entire patch, thus becoming entire domain basis functions.

The LegBF do not possess the singularity behaviors on the edges of the array elements. However, they have—contrary to first-order basis functions, e.g., rooftop basis functions—good convergence properties. This is illustrated in Fig. 1, where the relative error of the magnitude of the reflection coefficient of a square patch in a periodic environment is displayed. The reflection coefficient for a normally incident plane wave is calculated at 9.6 GHz and displayed as a function of the total  $N_b$  on the patch. Five different basis functions are employed: rooftops, subdomain LegBF (S-LegBF), entire-domain LegBF (E-LegBF), the entire-domain singular basis functions weighted by sinusoidal functions (E-SinBF) from [9], and the entire-domain singular basis functions weighted by Chebyshev polynomials of first and second kind (E-CheBF) from [4]. For the S-LegBF, the square patch is divided into  $2 \times 2$  mesh elements. The substrate dielectric constant and thickness are  $\epsilon_r = 3.66$  and  $h = 0.762$  mm, respectively, and the loss tangent is  $\tan \delta = 0.0037$ . The dimension of the unit cell is  $d^2 = 13.5 \times 13.5$  mm<sup>2</sup>, and the square patch is at resonance

Manuscript received June 14, 2012; accepted July 05, 2012. Date of publication July 11, 2012; date of current version July 20, 2012. The reflectarray antenna production and measurement was supported by the European Space Agency under ESTEC Contract No. 4000101041.

M. Zhou is with TICRA, Copenhagen 1201, Denmark, and also with the Department of Electrical Engineering, Electromagnetic Systems, Technical University of Denmark, Kgs. Lyngby 2800, Denmark (e-mail: mz@ticta.com).

E. Jørgensen, S. B. Sørensen, and P. Meincke are with TICRA, Copenhagen 1201, Denmark (e-mail: ticta@ticta.com).

O. S. Kim and O. Breinbjerg are with the Department of Electrical Engineering, Electromagnetic Systems, Technical University of Denmark, Kgs. Lyngby 2800, Denmark (e-mail: osk@elektro.dtu.dk; ob@elektro.dtu.dk).

Color versions of one or more of the figures in this letter are available online at <http://ieeexplore.ieee.org>.

Digital Object Identifier 10.1109/LAWP.2012.2208174

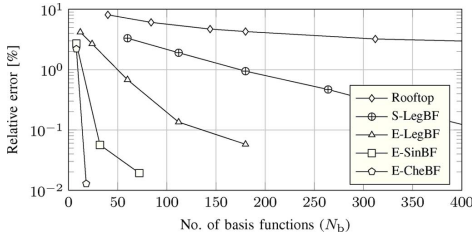


Fig. 1. Relative error of the magnitude of the reflection coefficient of a square patch in a periodic environment as a function of the number of basis functions  $N_b$ .

with a side length of 7.65 mm. As a reference, 512 E-CheBF are used.

It is seen that a relative error below 0.1% is achieved by using 32 E-SinBF and only 18 E-CheBF. For the same accuracy, 180 E-LegBF and 480 S-LegBF are required. For the rooftops, a relative error below 0.1% cannot be obtained due to the high  $Q$ -factor of the patch. The same convergence issues exist for conventional nonsingular entire-domain basis function, e.g., trigonometric basis functions [9]. As expected,  $N_b$  required for the LegBF is higher compared to the singular basis functions. However, it demonstrates their superior convergence capabilities compared to the first-order basis functions.

Usually, the double summation of the Floquet harmonics is truncated according to [3]

$$\sum_{n=-N}^N \sum_{m=-M}^M \quad (1)$$

where  $n, m$  are the indices for the Floquet harmonics. The main contribution in this summation originates from the combinations of the lower-order Floquet harmonics, thus an appropriate choice for  $M$  is  $M = N - |n|$ , yielding a total number of Floquet harmonics of  $N_f = 2(N^2 + N) + 1$ . This choice of  $M$  corresponds to summing the Floquet harmonics within a rhombus instead of a square when  $M = N$ . To ensure convergent results in Fig. 1, the number of Floquet harmonics used in the SDMoM calculations has been overestimated. For E-SinBF and E-CheBF, approximately 24 000 Floquet harmonics are used, whereas approximately 3300 are used for the rooftops and the LegBF.

Although the convergence rate of the LegBF with respect to  $N_b$  is lower compared to the singular basis functions, the convergence rate with respect to  $N_f$  is better. Let us define the spatial support of the basis function as  $a$  and the spectral variable as  $k$ , then for a fixed  $a$ , the Fourier spectrum of the LegBF decays as  $1/(ka)$ , whereas it decays as  $1/\sqrt{ka}$  for the singular basis functions. As a result, the Fourier spectrum is narrower for the LegBF, thus decreasing  $N_f$ .

Using the same test case as for Fig. 1, the relative error of the magnitude of the reflection coefficient as function of  $N_f$  is displayed in Fig. 2. A relative error below 0.1% is desired, thus 18 E-CheBF, 32 E-SinBF, 180 E-LegBF, and 480 S-LegBF are used. It is seen that the required accuracy is obtained using

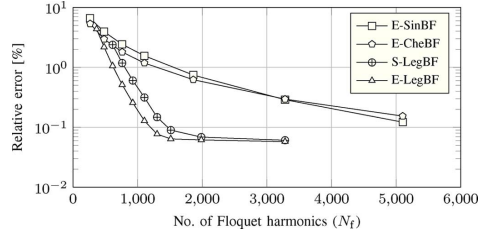


Fig. 2. Relative error of the magnitude of the reflection coefficient of a square patch in a periodic environment as a function of the number of Floquet harmonics  $N_f$ .

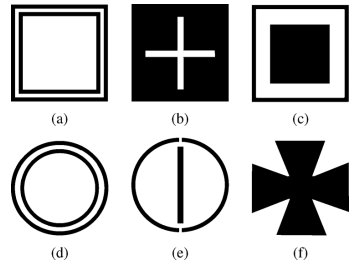


Fig. 3. (a)–(f) Different element shapes used for reflectarray applications.

approximately 1300 and 2000 Floquet harmonics for E-LegBF and S-LegBF, respectively, whereas over 5000 Floquet harmonics are needed for E-SinBF and E-CheBF.

There exist several acceleration techniques for the efficient computation of (1), e.g., the application of Kummer's transformation [10]–[12], and the two-dimensional fast Fourier transform (2-D FFT) technique [3]. In Kummer's transformation, an asymptotic part is subtracted from the Floquet summation, resulting in a fast converging summation, and the summation of the asymptotic part is treated separately in an efficient way. However, the treatment of the asymptotic part depends on the choice of basis function and the element shape, thus making the technique unsuitable for arbitrarily shaped elements. The 2-D FFT technique is another efficient way of computing the double summation of (1), but it is restricted to basis functions that are defined in a uniform rectangular mesh, thus not applicable for arbitrarily shaped elements. This is a limitation for the analysis of arbitrary reflectarrays, as different element shapes are used for different applications.

The choice of element shape is heavily dictated by requirements such as bandwidth and polarization, and much research has been carried out to investigate the performance of different element shapes [13]–[18]; see Fig. 3. Suitable entire-domain basis functions can be defined only for some of the element shapes, e.g., the concentric circular loops [Fig. 3(d)]. Rooftops and RWG basis functions can be used on arbitrary-shaped elements, but at the cost of high  $N_b$ . The LegBF are defined on higher-order curvilinear mesh elements [8], hence any curved boundary can be modeled very accurately. Thus, the LegBF can

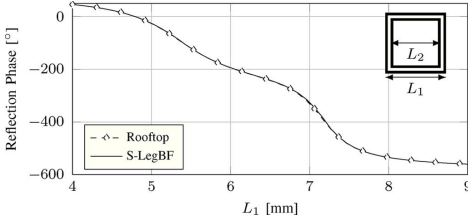


Fig. 4. Phase of the reflection coefficient of concentric square loops in a periodic environment as function of the outer loop length  $L_1$ . The inner loop length is  $L_2 = 0.75L_1$ ; the widths of the loops are  $w = 0.35$  mm.

be applied to any of those element shapes and with a good efficiency. As an example, the phase of the reflection coefficient of the concentric square loop [Fig. 3(a)] in a periodic environment is shown in Fig. 4. The reflection coefficient for a normally incident plane wave is calculated at 9.6 GHz using rooftops and S-LegBF, and the phase is displayed as function of the outer loop length  $L_1$ . The inner loop length is  $L_2 = 0.75L_1$ , and the widths of the loops are  $w = 0.35$  mm. The setup is the same as in Figs. 1 and 2, but the substrate thickness is increased to  $h = 3.175$  mm. This is to ensure convergence of the rooftops by reducing the  $Q$ -factor of the printed element. The phase curve is obtained using a total of 80 rooftops, whereas only 28 S-LegBF are required for the same accuracy. For both cases,  $N_f = 1861$ . A similar reduction in  $N_b$  has been observed for other element shapes.

We have observed in the analysis of various reflectarrays that convergence using LegBF is achieved when the largest Floquet harmonic,  $k_{\max}$ , satisfies the criterium  $k_{\max}a = 60$ , where  $a$  is the average spatial support of the basis functions. Consequently the Floquet harmonic summation can be truncated at approximately  $N = 30d/(a\pi)$ .

The LegBF's ability to model arbitrary-shaped elements together with their good convergence properties make the LegBF well suited for general codes and is an appropriate choice for the analysis of arbitrary reflectarrays.

### III. VALIDATION BY MEASUREMENTS

#### A. Reference Antenna

To demonstrate the capabilities of the LegBF, a 900-element reflectarray with a pencil beam toward  $\theta = -30^\circ$  and  $\phi = 0^\circ$  in the coordinate system shown in Fig. 5 has been designed. It consists of square patches, and its geometrical parameters are summarized in Table I. The feed is a linearly polarized corrugated horn with a taper of  $-17.5$  dB at  $30^\circ$  at 9.6 GHz, yielding an illumination along the edges varying from approximately  $-12$  to  $-5$  dB. The reflectarray and its support structures have been manufactured at the Technical University of Denmark (DTU), Kgs. Lyngby, Denmark, and measured at the DTU-ESA Spherical Near-Field Antenna Test Facility [19]; see Fig. 5. For the peak directivity, the measurements have a  $1\sigma$  uncertainty of 0.07 dB. In addition to the reflectarray measurements, the corrugated horn has also been measured, and the measured data are

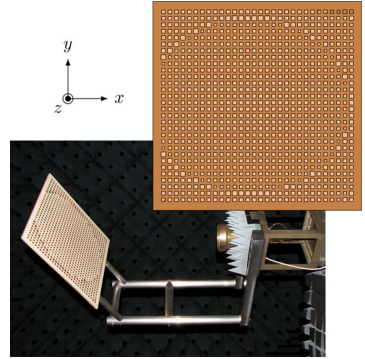


Fig. 5. Reflectarray designed with a pencil beam directed toward  $\theta = -30^\circ$  and  $\phi = 0^\circ$  in the shown coordinate system and measured at the DTU-ESA Spherical Near-Field Antenna Test Facility.

TABLE I  
REFERENCE REFLECTARRAY DATA

Frequency	9.6 GHz
Number of elements	$30 \times 30$
Reflectarray dimensions	435 mm $\times$ 435 mm
Substrate thickness	0.762 mm
Relative permittivity $\epsilon_r$	3.66
Loss tangent $\tan \delta$	0.0037
Feed distance to center of array	0.6 m
Feed offset angle	$\theta = 30^\circ$ , $\phi = 0^\circ$
Main beam direction	$\theta = -30^\circ$ , $\phi = 0^\circ$

used in the SDMoM calculations for accurate representation of the incident field.

#### B. Simulations Versus Measurements

For the calculation of the radiation pattern, the continuous spectrum technique from [20, Technique III] is employed. This technique is based on the field equivalence principle and allows the finite extent of the reflectarray to be included. To account for the presence of the support structures, the scattering from the struts is included in the analysis using the MoM add-on in GRASP [21].

The radiation pattern obtained using the E-CheBF and E-LegBF is compared to the measurement results and shown in Fig. 6. The patterns calculated using the two types of basis functions are almost identical. The agreement between the simulated and measured patterns is very good, even for the cross-polar radiation. The discrepancies observed around  $\theta = 30^\circ$  are due to the blockage by the feed and/or the measurement tower.

The analysis of the reference antenna has also been carried out using rooftops, E-sinBF, and S-LegBF, and the performance is summarized in Table II. Due to the thin substrate, and thus highly resonant patches, convergence was not obtained using rooftops, hence the results for the rooftops are omitted in Table II.

This comparison shows that the LegBF is capable of producing results of the same accuracy as those obtained using entire-domain singular basis functions, and for this specific case,



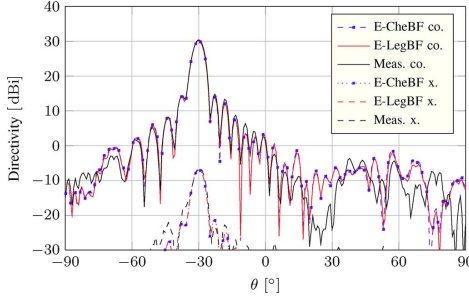


Fig. 6. Simulated and measured co- and cross-polar radiation patterns at  $\phi = 0^\circ$ .

TABLE II  
PERFORMANCE OF SINGULAR AND HIGHER-ORDER HIERARCHICAL LEGENDRE BASIS FUNCTIONS

	Peak Directivity	No. basis functions	No. Floquet harmonics	Computation time
E-SinBF	30.1 dBi	32	4141	45 s
E-CheBF	30.1 dBi	18	4141	25 s
S-LegBF	30.1 dBi	180	841	1 min 35 s
E-LegBF	30.1 dBi	84	481	17 s
Meas.	30.3 dBi	—	—	—

with less computation time, provided no acceleration techniques are used in the SDMoM. For thicker substrates, where a total of only two to eight entire-domain singular basis functions are sufficient for the accurate characterization of the array elements, approximately 24–40 E-LegBF are required, and the computation times for the two cases are practically identical.

#### IV. CONCLUSION

The use of higher-order hierarchical Legendre basis functions for the analysis of printed reflectarrays has been presented. The higher-order hierarchical Legendre basis functions can be applied to arbitrarily shaped array elements and have better convergence rate compared to first-order basis functions, e.g., rooftop basis functions. For elements that can be described using a single mesh element, the higher-order hierarchical Legendre basis functions can be defined on the entire patch, thus becoming entire-domain basis functions. For these cases, where singular basis functions are known for accurately accounting for the singularities of the electric current on the patch edges, it is demonstrated that the higher-order hierarchical Legendre basis functions are capable of producing results of the same accuracy as those obtained using singular basis functions. In addition, higher-order hierarchical Legendre basis functions require less Floquet harmonics than singular basis functions, thus a good compromise between the number of Floquet harmonics and unknowns can be obtained using higher-order hierarchical Legendre basis functions.

An offset reflectarray has been designed, manufactured, and measured to serve as a reference. The agreement with measurements is extremely good, thus demonstrating the capabilities of the higher-order hierarchical Legendre basis functions.

#### ACKNOWLEDGMENT

Dr. S. Pivnenko, Technical University of Denmark, is acknowledged for the measurements of the reflectarray sample.

#### REFERENCES

- [1] J. Huang and J. A. Encinar, *Reflectarray Antennas*. Piscataway, NJ: IEEE Press, 2008.
- [2] D. M. Pozar, S. D. Targonski, and H. D. Syrigos, "Design of millimeter wave microstrip reflectarrays," *IEEE Trans. Antennas Propag.*, vol. 45, no. 2, pp. 287–296, Feb. 1997.
- [3] R. Mittra, C. H. Chan, and T. Cwik, "Techniques for analyzing frequency selective surfaces—A review," *Proc. IEEE*, vol. 76, no. 12, pp. 1593–1615, Dec. 1988.
- [4] W. C. Chew and Q. Liu, "Resonance frequency of a rectangular microstrip patch," *IEEE Trans. Antennas Propag.*, vol. 36, no. 8, pp. 1045–1056, Aug. 1988.
- [5] A. M. Lerer and A. G. Schuchinsky, "Full-wave analysis of three-dimensional planar structures," *IEEE Trans. Microw. Theory Tech.*, vol. 41, no. 11, pp. 2002–2015, Nov. 1993.
- [6] S. M. Rao, D. R. Wilton, and A. W. Glisson, "Electromagnetic scattering by surfaces of arbitrary shape," *IEEE Trans. Antennas Propag.*, vol. AP-30, no. 3, pp. 409–418, May 1982.
- [7] A. W. Glisson and D. R. Wilton, "Simple and efficient numerical methods for problems of electromagnetic radiation and scattering from surfaces," *IEEE Trans. Antennas Propag.*, vol. AP-28, no. 5, pp. 593–603, Sep. 1980.
- [8] E. Jørgensen, J. Volakis, P. Meincke, and O. Breinbjerg, "Higher order hierarchical Legendre basis functions for electromagnetic modeling," *IEEE Trans. Antennas Propag.*, vol. 52, no. 11, pp. 2985–2995, Nov. 2004.
- [9] S. R. Rengarajan, "Choice of basis functions for accurate characterization of infinite array of microstrip reflectarray elements," *IEEE Antennas Wireless Propag. Lett.*, vol. 4, pp. 47–50, 2005.
- [10] R. R. Boix, M. J. Freire, and F. Medina, "New method for the efficient summation of double infinite series arising from the spectral domain analysis of frequency selective surfaces," *IEEE Trans. Antennas Propag.*, vol. 52, no. 4, pp. 1080–1094, Apr. 2004.
- [11] G. Cano, F. Medina, and M. Horno, "On the efficient implementation of SDA for boxed strip-like and slot-like structures," *IEEE Trans. Microw. Theory Tech.*, vol. 46, no. 11, pp. 1801–1806, Nov. 1998.
- [12] S.-O. Park, C. A. Balanis, and C. R. Birtcher, "Analytical evaluation of the asymptotic impedance matrix of a grounded dielectric slab with roof-top functions," *IEEE Trans. Antennas Propag.*, vol. 46, no. 2, pp. 251–259, Feb. 1998.
- [13] M. R. Chaharmir, J. Shaker, N. Gagnon, and D. Lee, "Design of broadband, single layer dual-band large reflectarray using multi open loop elements," *IEEE Trans. Antennas Propag.*, vol. 58, no. 9, pp. 2875–2883, Sep. 2010.
- [14] M. E. Bialkowski and K. H. Sayidmarie, "Investigations into phase characteristics of a single-layer reflectarray employing patch or ring elements of variable size," *IEEE Trans. Antennas Propag.*, vol. 56, no. 11, pp. 3366–3372, Nov. 2008.
- [15] C. Han, C. Rodenbeck, J. Huang, and K. Chang, "A C/Ka dual frequency dual layer circularly polarized reflectarray antenna with microstrip ring elements," *IEEE Trans. Antennas Propag.*, vol. 52, no. 11, pp. 2871–2876, Nov. 2004.
- [16] D. Cadoret, A. Laisne, R. Gillard, and H. Legay, "A new reflectarray cell using microstrip patches loaded with slots," *Microw. Opt. Technol. Lett.*, vol. 44, no. 3, pp. 270–272, 2005.
- [17] P. De Vita, A. Freni, G. L. Dassano, P. Pirinoli, and R. E. Zich, "Broad-band element for high-gain single-layer printed reflectarray antenna," *Electron. Lett.*, vol. 43, no. 23, pp. 1247–1249, 2007.
- [18] L. Moustafa, R. Gillard, F. Peris, R. Loison, H. Legay, and E. Girard, "The phoenix cell: A new reflectarray cell with large bandwidth and rebirth capabilities," *IEEE Antennas Wireless Propag. Lett.*, vol. 10, pp. 71–74, 2011.
- [19] Technical University of Denmark, Kgs. Lyngby, Denmark, "DTU-ESA spherical near-field antenna test facility," 2011 [Online]. Available: <http://www.dtu.dk/centre/ems/English/research/facilities.aspx>
- [20] M. Zhou, S. B. Sørensen, E. Jørgensen, P. Meincke, O. S. Kim, and O. Breinbjerg, "An accurate technique for calculation of radiation from printed reflectarrays," *IEEE Antennas Wireless Propag. Lett.*, vol. 10, pp. 1081–1084, 2011.
- [21] K. Pontoppidan, Ed., "GRASP, Technical description," TICRA Engineering Consultants, Copenhagen, Denmark, 2008.

## PAPER III

---

# DIRECT OPTIMIZATION OF PRINTED REFLECTARRAYS FOR CONTOURED BEAM SATELLITE ANTENNA APPLICATIONS

Min Zhou, Stig B. Sørensen, Oleksiy S. Kim, Erik Jørgensen,  
Peter Meincke, and Olav Breinbjerg

*Status*

Submitted: June 2012

Revised: October 2012

### **Bibliography**

- [J3] M. Zhou, S. B. Sørensen, O. S. Kim, E. Jørgensen, P. Meincke, and O. Breinbjerg, “Direct optimization of printed reflectarrays for contoured beam satellite antenna applications”, *Submitted to IEEE Trans. Antennas Propag.*, 2012.



# Direct Optimization of Printed Reflectarrays for Contoured Beam Satellite Antenna Applications

Min Zhou, *Student Member, IEEE*, Stig B. Sørensen, Oleksiy S. Kim, Erik Jørgensen, *Member, IEEE*, Peter Meincke, *Member, IEEE*, and Olav Breinbjerg, *Member, IEEE*

**Abstract**—An accurate and efficient direct optimization technique for the design of contoured beam reflectarrays is presented. It is based on the spectral domain method of moments assuming local periodicity and minimax optimization. Contrary to the conventional phase-only optimization techniques, the geometrical parameters of the array elements are directly optimized to fulfill the contoured beam requirements, thus maintaining a direct relation between optimization goals and optimization variables, and hence resulting in more optimal designs. Both co- and cross-polar radiation patterns of the reflectarray can be optimized for multiple frequencies, polarizations, and feed illuminations. Several contoured beam reflectarrays, that radiate a high-gain beam on a European coverage, have been designed and compared to similar designs obtained using the phase-only optimization technique. The comparisons show that the designs obtained using the proposed direct optimization technique are superior in performance, both for multi-frequency and dual-polarization designs. A reflectarray breadboard has been manufactured and measured at the DTU-ESA Spherical Near-Field Antenna Test Facility to validate the proposed technique. An excellent agreement of the simulated and measured patterns is obtained.

**Index Terms**—Contoured beam, reflectarray, accurate antenna analysis, pattern synthesis, optimization, satellite antenna

## I. INTRODUCTION

PRINTED reflectarrays provide a way for realizing low-cost, high-gain antennas for space applications and are the subject of increasing research interest [1]–[3]. For satellite broadcasting and telecommunication applications, where highly shaped contoured beams are required to illuminate specific geographical areas, the design requirements are extremely stringent and an accurate yet efficient design procedure is essential to meet the requirements. The shaped reflector antenna is a mature technology, both in terms of manufacturing and simulation tools, and is therefore used in many space missions to fulfill the coverage, cross-polarization, and isolation specifications. However, it suffers from large volume and mass, as well as high cost of the manufacturing, in particular the mold, which depends on the antenna requirements and can therefore not be reused for other missions. Printed reflectarrays

consist of a flat surface, they are light, and for a specific coverage only the array elements are varied, thus many of the recurring costs associated with shaped reflector antennas can be eliminated. Printed reflectarrays have been used for shaped beam applications with promising results [4]–[11].

To cover the required geographical areas, the electrical size of contoured beam reflectarrays is very large, similar to shaped reflectors, and an accurate yet efficient design procedure is therefore a challenging task. Contoured beam reflectarray design is often done using a phase-only optimization technique (POT) [5], [6] which involves two steps: first, a phase-only pattern synthesis is performed to determine the phase distribution on the reflectarray surface [5], [12]; and second, the array elements are optimized, element by element, to match the phase distribution by using an analysis routine based on the spectral domain method of moments (SDMoM) [13], [14] assuming local periodicity (LP) [15], [16].

Although the POT is efficient, a direct optimization technique, where all the array elements are simultaneously optimized, can potentially produce more optimal designs. Such a technique was presented in [17]–[19] and is based on the intersection approach from [20]. In [17], a small contoured beam reflectarray was designed, fabricated, and measured. However, significant discrepancies between simulations and measurements were observed, and it was concluded that further work is needed to improve the accuracy of the reflectarray analysis. The work in [18], [19] is an extension of the technique presented in [17] where also the position of the array elements can be included in the optimization. Since the array elements can be located in a strongly distorted grid, a full-wave method of moments (MoM) is used in the optimization. As a result, the overall synthesis becomes very time consuming.

In this work, we present a new direct optimization technique. It is efficient and has an accuracy comparable to the techniques used for the design of conventional shaped reflector antennas. It is based on a minimax optimization algorithm and the SDMoM assuming LP. To ensure an accurate, flexible, and efficient design procedure, several aspects in the analysis are taken into account. First, an accurate technique to calculate the far-field must be used [21], [22]. Second, higher-order hierarchical Legendre basis functions as described in [23] are applied in the SDMoM. It is demonstrated in [24] that these basis functions yield results of the same accuracy as those obtained using singular basis functions, and they are furthermore applicable to arbitrarily shaped array elements. Finally, the incident field on each reflectarray element must be accurately represented in the SDMoM computations [25], thus,

Manuscript received June 22, 2012; revised October 8, 2012. The reflectarray antenna production and measurement is supported by the European Space Agency (ESTEC contract No.4000101041).

M. Zhou is with TICRA, Copenhagen, Denmark, and also with the Department of Electrical Engineering, Electromagnetic Systems, Technical University of Denmark, Kgs. Lyngby, Denmark (e-mail: mz@ticra.com).

E. Jørgensen, S.B. Sørensen, and P. Meincke are with TICRA, Copenhagen, Denmark (e-mail: ticra@ticra.com).

O.S. Kim and O. Breinbjerg are with the Department of Electrical Engineering, Electromagnetic Systems, Technical University of Denmark, Kgs. Lyngby, Denmark (e-mail: osk@elektro.dtu.dk, ob@elektro.dtu.dk).

measured near-field feed patterns are used in the calculations. The analysis accuracy has been established by comparison with measurements of reference reflectarrays.

To demonstrate the capabilities of the proposed direct optimization technique, several contoured beam reflectarrays that radiate a high-gain beam on a European coverage have been designed. They have been compared to similar designs obtained using the POT, and the comparisons show that the reflectarrays designed with the new direct optimization technique are superior in performance. A reflectarray breadboard has been manufactured at the Technical University of Denmark (DTU) and measured at the DTU-ESA Spherical Near-Field Antenna Test Facility [26]. An excellent agreement between simulations and measurements is obtained, thus validating the direct optimization technique.

The paper is organized as follows. Section II describes the direct optimization technique. The reflectarray designs are described in Section III. In Section IV, simulations are compared to the measured data, and conclusions are given in Section V.

All the computations reported in this work are carried out on a 2.8 GHz dual-core Intel processor laptop computer.

The time factor  $e^{j\omega t}$  is assumed and suppressed throughout the paper.

## II. DIRECT OPTIMIZATION TECHNIQUE

The direct optimization technique (DOT) uses the same optimization procedure that is used in the TICRA software package POS [27], which is the de facto standard software tool for the design of shaped reflector antennas. It uses a gradient minimax algorithm for non-linear optimization. Since it is gradient based, a good initial point is required to ensure rapid convergence and to avoid non-optimum local minima.

### A. Optimization Procedure

The contoured beam requirements are specified in a number of far-field points in the  $u$ - $v$  plane where  $u = \sin \theta \cos \phi$  and  $v = \sin \theta \sin \phi$ . The object function  $F(\mathbf{x})$ , which consists of a set of residuals  $f_i(\mathbf{x})$ , is minimized during the optimization according to

$$\text{minimize } F(\mathbf{x}) = \max\{f_1(\mathbf{x}), f_2(\mathbf{x}), \dots, f_{N_s}(\mathbf{x})\}, \quad (1)$$

where  $\mathbf{x}$  is a vector containing the optimization variables, and  $N_x$  and  $N_s$  are the number of optimization variables and far-field specifications, respectively. Each residual has the form

$$f_i(\mathbf{x}) = w_i(D_{s,i} - D_i(\mathbf{x})), \quad i = 1, 2, \dots, N_s. \quad (2)$$

Herein,  $D_{s,i}$  and  $D_i(\mathbf{x})$  are the specified and realized directivity, respectively, in dBi for a specified polarization component, and  $w_i$  is a weight factor. The optimization variables are the geometrical parameters of the array element, e.g. side length, position, and orientation of a square patch. By optimizing the variables, the residuals are minimized and a reflectarray that best possible fulfills the coverage specifications is obtained. In this way, a direct relation between the geometrical parameters and the far-field is maintained.

The minimization of the residuals can be done simultaneously for a number of frequencies, for multiple polarizations, and for different feed illuminations, to obtain a desired bandwidth. Both co- and cross-polar radiation can be optimized, hence enabling the possibility of including cross-polar and sidelobe suppression in the optimization. The optimization of the cross-polar radiation from the entire reflectarray is an important feature as previous works on minimizing the cross-polar radiation have mostly focused on looking at the scattering response of the periodic cell [10], [28], [29] or on appropriate arrangement of the array elements [30], [31], but not by means of direct optimization of the cross-polar radiation. The optimization of the cross-polar radiation is possible in the techniques presented in [18], [19], but the results for the cross-polar radiation has not been reported.

In this paper, we restrict us to square patches located in a regular grid such that only the side lengths of the patches are used as optimization variables. Upper and lower bounds for the patches sizes are specified in the optimization. The SDMoM algorithm used in the DOT is based on [32], which is applicable for multilayer dielectric substrate configurations. In this work, only single layer configurations are considered, but the DOT can be readily applied to multilayer configurations.

### B. Far-field Calculation

In [21], several techniques to calculate the radiation from printed reflectarrays are compared. Two techniques yielded accurate results; a Floquet harmonics technique [21, technique II], and a continuous spectrum technique [21, technique III]. Both techniques are based on the field equivalence principle [33, p.106]. Comparison with measurements shows that an enhanced accuracy is obtained using the continuous spectrum technique, mainly in the back hemisphere. Although this technique is more accurate, it is not suited for optimization purposes, since it requires higher computation time and storage. Consequently, the Floquet harmonics technique has been selected for the calculation of the far-field during the optimization. However, for the evaluation of the final optimized reflectarray, the far-field is calculated using the continuous spectrum technique. For completeness, the Floquet harmonics technique is described in detail in the following.

Equivalent currents are calculated in the plane of the array elements and assumed to be zero on the back side and at the edges of the reflectarray. The electric and magnetic equivalent currents of array element  $n$  are defined by

$$\mathbf{J}_S^n = \hat{n} \times \mathbf{H}^n, \quad (3a)$$

$$\mathbf{M}_S^n = -\hat{n} \times \mathbf{E}^n, \quad (3b)$$

where  $\mathbf{E}^n, \mathbf{H}^n$  are the total electric and magnetic fields on the top surface of the  $n$ 'th unit-cell, and  $\hat{n}$  is the outward normal unit vector to that surface. The electric and magnetic fields  $\mathbf{E}^n, \mathbf{H}^n$  are computed by the fundamental Floquet plane wave harmonic of the SDMoM formulation [21].

In the SDMoM computations, each array element is assumed to be illuminated by a locally plane wave. To obtain an accurate representation of the incident field, a spherical wave expansion of measured or accurately simulated feed patterns is

used to compute the polarization, amplitude, and phase of the incident plane wave on each array element. The total tangential electric field on the unit-cell surface is given by

$$\mathbf{E}_t^n = \mathbf{E}_{s,t}^n + \mathbf{E}_{i,t}^n = (\bar{\mathbf{S}}_n + \bar{\mathbf{I}}) \mathbf{E}_{i,t}^n, \quad (4)$$

where  $\mathbf{E}_{s,t}^n$  is the tangential components of the scattered plane wave of array element  $n$ ,  $\mathbf{E}_{i,t}^n$  is the tangential components of the incident plane wave on array element  $n$ ,  $\bar{\mathbf{I}}$  is the identity matrix, and  $\bar{\mathbf{S}}_n$  the scattering coefficient matrix which is calculated using the fundamental Floquet harmonic. The magnetic field  $\mathbf{H}^n$  can be readily obtained using the plane wave relation.

The reflectarray far-field can be computed as a sum of the contributions of each array element

$$\mathbf{E}_{\text{far}} = \sum_{n=1}^{N_e} \mathbf{E}_{\text{far}}^n, \quad (5)$$

where  $N_e$  is the number of array elements. Since  $\mathbf{E}^n, \mathbf{H}^n$  are plane waves, the integral involved in calculating the far-field contribution from array element  $n$  can be evaluated analytically for rectangular cells as

$$\mathbf{E}_{\text{far}}^n(\hat{r}) = \frac{j k_0^2}{4\pi} \left[ ((\mathbf{J}_S^n \cdot \hat{r})\hat{r} - \mathbf{J}_S^n) \eta_0 + \hat{r} \times \mathbf{M}_S^n \right] e^{j k_0 \hat{r} \cdot \mathbf{r}_n} \cdot \text{sinc}\left(\frac{(k_0 u - \beta_x^n) u_x}{2}\right) \text{sinc}\left(\frac{(k_0 v - \beta_y^n) u_y}{2}\right). \quad (6)$$

Herein,  $k_0$  is the free-space wavenumber,  $\eta_0$  the free-space impedance,  $\hat{r}$  the unit vector towards the observation point,  $u_x, u_y$  the  $x$  and  $y$  dimensions of the unit-cell,  $\beta_x^n, \beta_y^n$  the  $x$  and  $y$  components of the propagation vector of the fundamental Floquet harmonic for array element  $n$ ,  $\mathbf{r}_n$  the position of array element  $n$ , and  $\text{sinc}(x) = \sin x/x$ .

### C. Choice of Basis Functions

To ensure an accurate yet efficient calculation of  $\bar{\mathbf{S}}_n$ , suitable basis functions must be selected to reduce the number of basis functions and Floquet harmonics. For canonically shaped array elements e.g. rectangular patches, entire domain basis functions with the correct edge conditions are known to provide fast convergence in the SDMoM with respect to the number of basis functions [34]–[36]. However, due to their singular behavior, the Fourier spectrum is wide, which increases the number of Floquet harmonics. For arbitrarily shaped elements, the common choices are first-order basis functions, e.g. Rao-Wilton-Glisson (RWG) [37] or rooftop [38] basis functions. However, the number of basis functions is high for these cases.

In this work, higher-order hierarchical Legendre basis functions as described in [23] are applied in the SDMoM. It was demonstrated in [24] that these basis functions are capable of giving results of the same accuracy as those obtained using entire domain singular basis functions. Furthermore, higher-order hierarchical Legendre basis functions can be applied to arbitrarily shaped array elements with improved performance compared to first-order basis functions. The flexibility of the higher-order hierarchical Legendre basis functions enables

the optimization of reflectarrays consisting of non-canonical element shapes, e.g. those reported in [39]–[41], which is important in the analysis of printed reflectarrays.

### D. Scattering Matrix Look-Up Table

Although the SDMoM combined with LP and higher-order hierarchical Legendre basis functions is computationally efficient with only a fraction of a second in computation time per array element, it is not fast enough for optimization where the analysis must be performed repeatedly. Furthermore, the optimization requires derivatives with respect to the optimization variables, which will further increase the computation time if these derivatives have to be computed numerically by finite difference approximations.

To circumvent the calculation of scattering matrices of all array elements at each iteration, the scattering matrices can be calculated in advance and stored in a look-up table which is accessed during the optimization. This approach has been successfully used in other works [10], [18], [19], [42] and is also used here in the DOT. The scattering matrix is a function of many parameters, e.g. illumination angles  $(\theta^i, \phi^i)$ , geometry of the array element, unit-cell dimensions, dielectric substrate properties, and frequency. It is thus important to find an economic way to store and interpolate these data to obtain a look-up table that is small and fast to compute.

The representation of the scattering matrices can be done in various ways, e.g. splines. However, due to the resonance properties of printed elements, the scattering matrix has a strong variation at resonance, hence splines are unsuited. The representation of the scattering matrices by means of local cubic interpolation [43, Chap. 25] on the other hand is efficient and stable. We have found that a sufficient accuracy can be obtained using relatively few scattering matrix sample values. For a center fed  $20 \times 20$  square wavelengths reflectarray consisting of square patches and a focal distance to diameter ratio  $(f/D)$  of one, approximately  $N_{\text{el}} = 60$  patch sizes and  $N_\theta = 12$  sample values in  $\theta^i$  are adequate. The variation of the scattering coefficients in  $\phi^i$  can be represented by a finite Fourier series expansion

$$\bar{\mathbf{S}}(\theta^i, \phi^i) = \sum_{s=-N_m}^{N_m} \bar{\mathbf{c}}_s(\theta^i) e^{js\phi^i}. \quad (7)$$

The Fourier coefficients  $\bar{\mathbf{c}}_s$  can be computed exactly by [44, Appen. A4]

$$\bar{\mathbf{c}}_s = \frac{\Delta\phi}{2\pi} \sum_{l=1}^{2N_m+1} \bar{\mathbf{S}}(\theta^i, \phi_l^i) e^{-js\phi_l^i}, \quad (8)$$

where  $\Delta\phi = 2\pi/(2N_m + 1)$  and  $\phi_l^i = \Delta\phi(l - 1)$ . We have found that  $N_m = 2$  is sufficient, resulting in a total of only  $N_\phi = 5$  sample values in  $\phi^i$ . Thus for a given frequency, substrate, and unit-cell size, the total number of scattering matrix samples needed in the look-up table to obtain an accurate interpolation is  $N_{\text{total}} = N_\theta N_\phi N_{\text{el}} = 12 \cdot 5 \cdot 60 = 3600$ . Each scattering matrix sample contains four 16 byte complex numbers, thus resulting in a look-up table of a total size of only 225 kB per frequency. The computation time to calculate the

look-up table for one frequency is approximately two minutes. For reflectarrays with other dimensions or feed positions,  $N_\theta$  and  $N_\phi$  may differ, but  $N_{el}$  remains the same.

For array elements with several adjustable parameters, the total number of scattering matrices samples per frequency increases rapidly as it becomes  $N_{total} = N_\theta N_\phi N_{el}^2 N_{el}^{N_f} \dots N_{el}^{N_f}$ , where  $N_f$  is the number of adjustable parameters. This increases the computation time and the storage requirements of the look-up table significantly. For example, an array element with three adjustable parameters which are optimized for 3 frequencies gives  $N_{total} = 13 \cdot 10^6$ , yielding a storage requirement of approximately 2 GB. However, once the look-up table has been calculated, it can be reused in the optimization and needs only to be recalculated if another substrate, frequency, or unit-cell size is used.

Using local cubic interpolation, the derivatives with respect to the geometrical parameters of the array element can be computed by differentiation of the local cubic polynomial. Thus, the gradients needed during the optimization can be determined analytically, which is more accurate and faster than numerical difference approximations.

### E. Phase-Only Optimization Technique

In order to avoid the optimization being trapped in a local minimum, a good starting point is required. Depending on the complexity and the requirements of the specified contour, identical array elements can be used as the starting point. This produces an initial pattern that resembles the feed pattern and is a good initial start in certain cases, e.g. multi-frequency designs. Another choice is to use an initial defocused elliptical beam obtained by a proper phase variation over the reflectarray surface. However, this is problematic for multi-frequency designs as the phases depend on the frequency. On the other hand, for single frequency designs an elliptical beam can be a very good starting point.

Alternatively, a reflectarray designed using the POT can be used as the starting point. The POT is simple and fast and is commonly used method for the design of contoured beam reflectarrays [5], [6], [10], [11]. First, a phase-only pattern synthesis is performed to determine the phase distribution required on the reflectarray surface, and hereafter the array elements are determined, element by element, to match the phase distribution. Although the technique is simple and has proven to be useful, it suffers from the disadvantage that intermediate optimization steps are necessary to fulfill a given phase distribution. This intermediate step breaks the direct relation between the geometrical parameters and the far-field performance and can give non-optimal designs. A brief outline of our POT implementation is given in the following.

To obtain the phase distribution on the reflectarray surface, an approach similar to that described in [12] is used. For dual-polarized multi-frequency designs, several phase distributions are obtained, one for each polarization and frequency. The array elements are subsequently optimized, element by element, to comply with these phase distributions by minimizing the

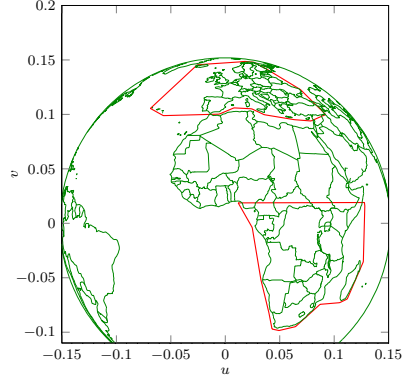


Fig. 1. European and southern African coverages seen from the longitude  $0^\circ$  geostationary orbital position.

TABLE I  
REFLECTARRAY DATA

Center frequency	10 GHz
Frequency range	9 – 11 GHz
Number of elements	50×50
Reflectarray dimensions	600 mm × 600 mm
Relative permittivity	$\epsilon_r = 3.66$
Substrate thickness	$d = 1.524$ mm
Loss tangent	$\tan \delta = 0.0037$
Feed distance to center of array	$d_f = 0.6$ m
Feed offset angle	$\theta^i = 30^\circ$ , $\phi^i = 0^\circ$

error function

$$e_n = \sum_{l=1}^L C_l |\psi_{n,r}^l - \psi_{n,c}^l|. \quad (9)$$

Herein,  $L$  is the number of phase distributions,  $\psi_{n,r}^l$  and  $\psi_{n,c}^l$  the required and computed phase-shift, respectively, of array element  $n$ , and  $C_l$  weighting coefficients, which can be different for each phase distribution. The selection of  $C_l$  is usually done empirically to obtain the best performance of the optimized design.

To find array elements that match all phase distributions simultaneously is in most cases not possible. Consequently, the array elements are determined as a compromise between the different phase distributions, resulting in non-optimal designs.

### III. REFLECTARRAY DESIGN

To demonstrate the capabilities of the DOT and its advantages against POT, we consider several offset contoured beam reflectarrays that radiate a high-gain beam on a European coverage with the possibility of having sidelobe suppression within a southern African contour. The coverages are shown in Fig. 1 as red polygons. The reflectarray parameters are summarized in Table I with respect to the coordinate system shown in Fig. 2.

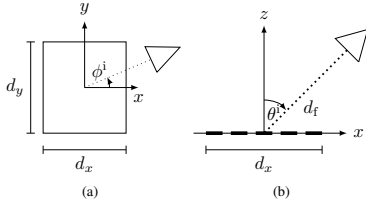


Fig. 2. Reflectarray geometrical parameters in (a) the  $xy$ -plane and (b) the  $xz$ -plane.

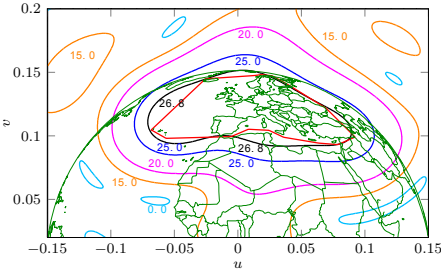


Fig. 3. Simulated co-polar radiation patterns of Design A-II at 10 GHz.

Square patches are used in these designs. Although these array elements may not provide the most optimal designs, they are sufficient for the comparison of the different design techniques.

Two reflectarray designs are considered; a multi-frequency single-polarized reflectarray design, and a single frequency dual-polarized reflectarray design. The design process for the two cases are described in the following sections.

#### A. Multi-Frequency Single-polarized Reflectarray

The goal of this design is to maximize the directivity within the European coverage in the frequency range 9 – 11 GHz for a single feed polarization. A linearly polarized Gaussian beam with a taper of  $-15$  dB at  $30^\circ$  is used as feed.

Two reflectarrays were designed, one using the POT, and one using the DOT. A scattering matrix look-up table for frequencies  $f = 9, 10, 11$  GHz has been calculated using a total computation time of approximately five minutes and a storage requirement of 1.1 MB.

For the POT design (Design A-I), phase distributions at the center and the extreme frequencies were obtained and subsequently used in the minimization of (9) with  $l = 1, 2, 3$  corresponding to  $f_l = 9, 10, 11$  GHz, respectively. The optimization process was repeated several times, alternating  $C_l$  to obtain the optimal performance within the frequency range. The best design showed a minimum directivity within the coverage of 25.4 dBi in the entire frequency range.

For the DOT design (Design A-II), identical patches was used as the starting point for the optimization. The reflectarray

TABLE II  
PERFORMANCE OF MULTI-FREQUENCY REFLECTARRAY DESIGNS

Frequency (GHz)	Design A-I POT: Minimum Directivity (dBi)	Design A-II DOT: Minimum Directivity (dBi)
8.5	24.2	24.9
9.0	25.4	26.5
9.5	25.5	26.7
10.0	25.4	26.8
10.5	25.4	26.6
11.0	25.4	26.5
11.5	23.2	23.4

was optimized at the center and extreme frequencies simultaneously. The radiation pattern of Design A-II at 10 GHz is shown in Fig. 3 where a minimum directivity of 26.8 dBi is achieved.

In Table II, the performance of the two designs are summarized. A comparison clearly shows the advantages of the DOT, where more than 1 dB in the minimum directivity is gained compared to the phase-only design. Also, the phase-only design is highly dependent on the value of  $C_l$ , which have to be obtained empirically. This is circumvented in the DOT.

For Design A-I, the computation time was approximately 20 minutes for a fixed set of  $C_l$ . The optimization time for Design A-II was approximately 30 minutes.

It should be noted that the phase of the scattered field for a periodic array of square patches is known to be very sensitive to frequency variations near the resonance, thus resulting in a narrow bandwidth [16], [41]. Nonetheless, Design A-II has been optimized to have a minimum directivity of 26.5 dBi in a frequency bandwidth of 20%. It is expected that better results can be achieved by using more broadband array elements e.g. the ones proposed in [39] or multilayer configurations as in [5], [16].

#### B. Single Frequency Dual-polarized Reflectarray

In this example, we consider a high-gain beam on the European coverage with cross-polar suppression within the same coverage, and sidelobe suppression within the southern African contour. The reflectarray is optimized for two orthogonal linear polarizations, H- and V-polarization<sup>1</sup>, and only at 10 GHz. For this design, a corrugated horn, whose measured radiation pattern is available, is used as a feed. Again, two reflectarrays were designed, one using the POT, and one using the DOT.

For the POT design (Design B-I), two phase distributions were determined, one for each polarization. In [11], rectangular patches were used and the optimization for the two orthogonal polarizations was accomplished by adjusting the two orthogonal dimensions of the rectangular patches. In our designs, square patches are used and only one dimension can be varied. Thus, the optimization for the two polarizations

<sup>1</sup>The reflectarray is assumed to be mounted on a satellite such that H-polarization is defined to be in the feed offset plane ( $xz$ -plane in Fig. 2b), and V-polarization in the orthogonal plane.



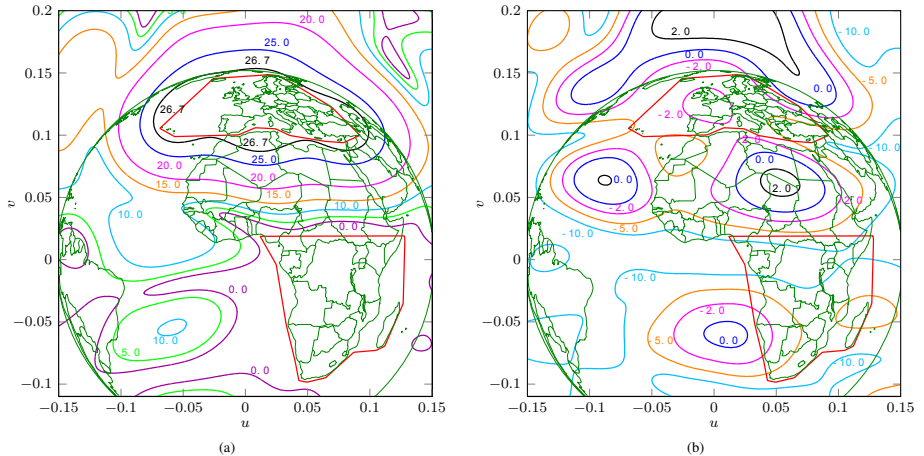


Fig. 4. Simulated (a) co-polar and (b) cross-polar radiation pattern of Design B-II for H-polarization at 10 GHz.

TABLE III  
PERFORMANCE OF DUAL-POLARIZED REFLECTARRAY DESIGNS AT 10 GHz

	Design B-I		Design B-II	
	POT		DOT	
	H-pol.	V-pol.	H-pol.	V-pol.
Min. directivity (dBi)	26.6	26.5	26.7	26.5
Min. XPD (dB)	26.5	26.7	28.6	27.0
Min. isolation (dB)	20.3	24.3	26.7	27.9

is done simultaneously by minimizing (9) with  $l = 1, 2$  corresponding to H- and V-polarization, respectively. The  $C_l$  were selected to be identical in this case.

The far-field showed a minimum directivity within the coverage of 26.5 dBi and a minimum cross polarization discrimination (XPD) around 26.5 dB for both polarizations. For the co-polar radiation on the southern African coverage, the minimum isolation (Europe/Africa) for H- and V-polarization is 20.3 dB and 24.3 dB, respectively.

For the DOT design, an elliptical beam was used as the starting point for the optimization. The radiation pattern of this optimized design (Design B-II) for H-polarization at 10 GHz is shown in Fig. 4. It is seen that a minimum directivity of 26.7 dBi is obtained. The minimum XPD and isolation levels are at 28.6 dB and 26.8 dB, respectively. For the V-polarization, the design has a very similar performance.

The performance of the designs is compared in Table III. The comparison shows that a better design is achieved using the DOT than with the POT. However, the improvements are not as significant as for the case of the multi-frequency design. This is explained by the fact that the phase distributions required for the two polarizations used in the POT are rather similar. Thus the minimization of the error function does not possess the same complexity as it does for a multi-frequency

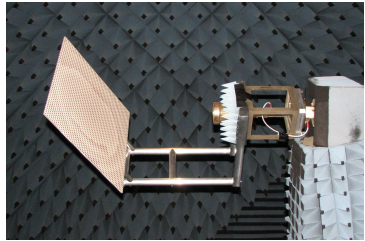


Fig. 5. Reflectarray breadboard in the DTU-ESA Spherical Near-Field Antenna Test Facility.

design.

The overall optimization time for Design B-I was around 15 minutes, whereas the overall optimization time, including the calculation of the look-up table, for Design B-II was approximately 40 minutes.

It is a known fact that the response of a periodic array of square patches is different under oblique incidence [45]. As a result, the response for each orthogonal polarization is slightly different and the dimensions of the square patches are determined as a compromise between the two polarizations. It is expected that an enhanced performance can be achieved using rectangular patches.

#### IV. VALIDATION BY MEASUREMENTS

To validate the DOT, a reflectarray breadboard has been manufactured at the Technical University of Denmark (DTU) and measured at the DTU-ESA Spherical Near-Field Antenna Test Facility [26], see Fig. 5. The breadboard is based on an

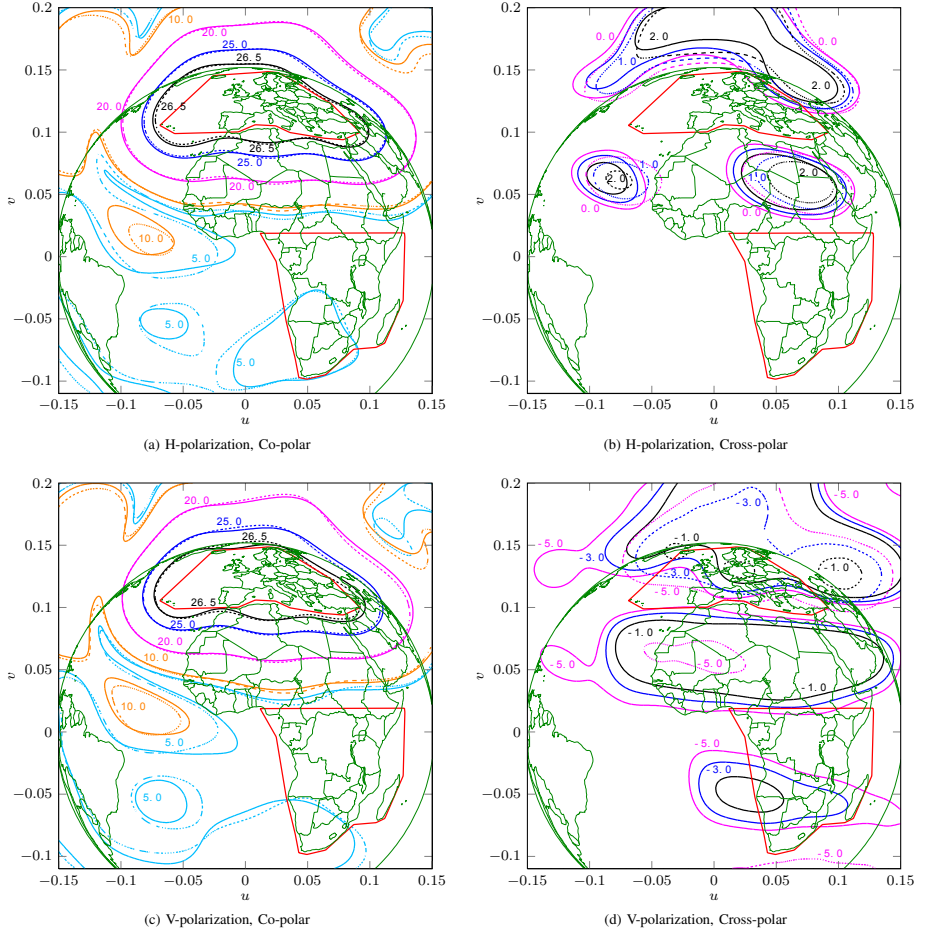


Fig. 6. Simulated (solid lines) and measured (dotted lines) radiation patterns of the manufactured breadboard for both H- and V-polarizations at 10 GHz.

earlier version of Design B-II, where the performance of the reflectarray is not optimal. Nevertheless, it is sufficient to serve as reference to verify the accuracy of the proposed technique. The dielectric substrate is Rogers RO4350B with a substrate thickness of  $d = 0.762$  mm. The breadboard was measured at a series of frequencies from 9.6 GHz to 10.5 GHz. For the peak directivity, the measurements have a  $1\sigma$  uncertainty of 0.05 dB.

To account for the presence of the support structures, the scattering from the struts is included in the simulations using the MoM add-on in GRASP [46].

The simulated and measured radiation patterns at 10 GHz for V- and H-polarization are shown in Fig. 6. The agreement between simulations and measurements is extremely good for both polarizations. It is seen that the high-gain contours curves practically coincide.

The performance of the breadboard for both polarizations is summarized in Table IV. It is seen that an excellent agreement is obtained for the peak directivity and minimum directivity within the European coverage. Also the isolation levels are in good agreement.

Regarding the XPD levels, discrepancies up to approxi-

TABLE IV  
MEASURED VERSUS SIMULATED DATA AT 10 GHz

	Peak directivity (dBi)	Min. directivity (dBi)	Min. XPD (dB)	Min. isolation (dB)
Measurement (H-pol.)	28.3	26.5	27.1	17.5
Simulation (H-pol.)	28.2	26.6	25.0	17.8
Measurement (V-pol.)	27.9	26.5	27.7	18.4
Simulation (V-pol.)	27.9	26.5	25.5	17.2

mately 2 dB are observed. This is expected since the cross-polar level is approximately 30 dB below the co-polar peak, and factors e.g. scattering from the edges come into play.

In Fig. 7, the simulated and measured minimum directivity for both polarizations are shown for the measured frequencies. The breadboard was only optimized at 10 GHz, hence the decrease in the minimum directivity in the frequency range. The maximum deviation between simulations and measurements is within  $\pm 0.1$  dB, thus demonstrating the good agreement between simulated and measured patterns in the other measured frequencies.

These excellent agreements between simulated and measured patterns are close to those obtained for conventional shaped reflectors and thereby verify the direct optimization technique presented in this paper.

## V. CONCLUSIONS

An accurate and efficient direct optimization technique for the design of contoured beam reflectarrays is presented. It is based on the spectral domain method of moments (SDMoM) with local periodicity and a minimax optimization algorithm. Contrary to the conventional phase-only optimization techniques, the geometrical parameters of the array elements are directly optimized to fulfill the contoured beam requirements, thus maintaining a direct relation between optimization goals and optimization variables. As a result, more optimal designs can be obtained. To ensure high accuracy, efficiency, and flexibility, higher-order hierarchical Legendre basis functions are used together with a fast yet accurate far-field calculation technique. The higher-order hierarchical Legendre basis functions can give results of the same accuracy as those obtained using entire domain singular basis functions, and are applicable to any arbitrarily shaped array elements. The far-field calculation technique uses scattering matrices which are calculated in advance, stored in a look-up table, and accessed during the optimization. This circumvents the calculation of the SDMoM at each iteration and greatly reduces the overall optimization time. Both co- and cross-polar radiation can be optimized for multiple frequencies, polarizations, and feed illuminations.

To demonstrate the capabilities of the direct optimization technique, several contoured beam reflectarrays that radiate a high-gain beam on a European coverage have been designed, and compared to similar designs obtained using a phase-only optimization technique. The comparison shows that the direct optimized designs are superior in performance, both for multi-frequency and dual-polarization designs. Particularly for multi-frequency designs where more than 1 dB in the minimum

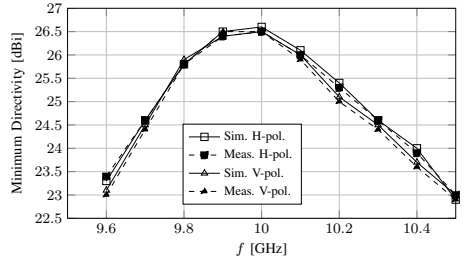


Fig. 7. Measured versus simulated minimum directivity for both polarizations for the measured frequencies.

co-polar directivity within the coverage can be gained. To validate the results, a reflectarray breadboard has been manufactured and measured at the DTU-ESA Spherical Near-Field Antenna Test Facility. An excellent agreement is obtained for the simulated and measured patterns, where the maximum deviation in the minimum directivity between simulations and measurements is within  $\pm 0.1$  dB.

## ACKNOWLEDGMENT

Dr. S. Pivnenko, Electromagnetic Systems, Technical University of Denmark (EMS-DTU), is acknowledged for the accurate measurements of the reflectarray breadboard, the mechanical workshop at EMS-DTU for the manufacturing of the reflectarray breadboard, and Dr. G. Toso, ESA-ESTEC, for providing valuable technical comments.

## REFERENCES

- [1] J. Huang and J. A. Encinar, *Reflectarray Antennas*. IEEE Press, 2008.
- [2] J. A. Encinar, "Recent advances in reflectarray antennas," in *Proc. EuCAP*, Barcelona, Spain, 2010.
- [3] A. Roederer, "Reflectarray antennas," in *Proc. EuCAP*, Berlin, Germany, 2009.
- [4] D. M. Pozar, S. D. Targonski, and R. Pokuls, "A shaped-beam microstrip patch reflectarray," *IEEE Trans. Antennas Propag.*, vol. 47, no. 7, pp. 1167–1173, 1999.
- [5] J. A. Encinar and J. A. Zornoza, "Three-layer printed reflectarrays for contoured beam space applications," *IEEE Trans. Antennas Propag.*, vol. 52, no. 5, pp. 1138–1148, 2004.
- [6] J. A. Encinar, L. S. Datashvili, J. A. Zornoza, M. Arrebola, M. Sierra-Castaner, J. L. Besada-Sanmartin, H. Baier, and H. Legay, "Dual-polarization dual-coverage reflectarray for space applications," *IEEE Trans. Antennas Propag.*, vol. 54, no. 10, pp. 2827–2837, 2006.
- [7] J. Zornoza, R. Leberer, J. Encinar, and W. Menzel, "Folded multilayer microstrip reflectarray with shaped pattern," *IEEE Trans. Antennas Propag.*, vol. 54, no. 2, pp. 510–518, 2006.
- [8] M. Arrebola, J. A. Encinar, and M. Barba, "Multifed printed reflectarray with three simultaneous shaped beams for LMDS central station antenna," *IEEE Trans. Antennas Propag.*, vol. 56, no. 6, pp. 1518–1527, 2008.
- [9] E. Carrasco, M. Arrebola, J. A. Encinar, and M. Barba, "Demonstration of a shaped beam reflectarray using aperture-coupled delay lines for LMDS central station antenna," *IEEE Trans. Antennas Propag.*, vol. 56, no. 10, pp. 3103–3111, 2008.
- [10] H. Legay, D. Bresciani, E. Labiole, R. Chiniard, E. Girard, G. Caille, L. Marnat, D. Calas, R. Gillard, and G. Toso, "A 1.3 m earth deck reflectarray for a Ku band contoured beam antenna," in *Proc. 33rd ESA Antenna Workshop*, Noordwijk, The Netherlands, 2011.

- [11] J. A. Encinar, M. Arrebola, L. D. L. Fuente, and G. Toso, "A transmit-receive reflectarray antenna for direct broadcast satellite applications," *IEEE Trans. Antennas Propag.*, vol. 59, no. 9, pp. 3255–3264, 2011.
- [12] A. Capozzoli, C. Curcio, G. D'Elia, and A. Lisenio, "Fast phase-only synthesis of conformal reflectarrays," *IET Microw. Antennas Propag.*, vol. 4, no. 12, pp. 1989–2000, 2010.
- [13] D. Pozar and D. Schaubert, "Analysis of an infinite array of rectangular microstrip patches with idealized probe feeds," *IEEE Trans. Antennas Propag.*, vol. 32, no. 10, pp. 1101–1107, 1984.
- [14] R. Mittra, C. H. Chan, and T. Cwik, "Techniques for analyzing frequency selective surfaces – a review," *Proc. IEEE*, vol. 76, no. 12, pp. 1593–1615, 1988.
- [15] D. M. Pozar, S. D. Targonski, and H. D. Syrigos, "Design of millimeter wave microstrip reflectarrays," *IEEE Trans. Antennas Propag.*, vol. 45, no. 2, pp. 287–296, 1997.
- [16] J. A. Encinar, "Design of two-layer printed reflectarrays using patches of variable size," *IEEE Trans. Antennas Propag.*, vol. 49, no. 10, pp. 1403–1410, 2001.
- [17] O. M. Bucci, A. Capozzoli, G. D'Elia, P. Maietta, and S. Russo, "An advanced reflectarray design technique," in *Proc. 28th ESA Antenna Workshop*, Noordwijk, The Netherlands, 2005.
- [18] A. Capozzoli, C. Curcio, A. Lisenio, M. Migliorelli, and G. Toso, "Aperiodic conformal reflectarrays," in *Proc. IEEE AP-S Int. Symp.*, Spokane, Washington, USA, 2011, pp. 361 – 364.
- [19] —, "Power pattern synthesis of advanced flat aperiodic reflectarrays," in *Proc. 33th ESA Antenna Workshop*, Noordwijk, The Netherlands, 2011.
- [20] O. M. Bucci, G. D'Elia, G. Mazzarella, and G. Panariello, "Antenna pattern synthesis: a new general approach," *Proc. IEEE*, vol. 82, no. 3, pp. 358 – 371, 1994.
- [21] M. Zhou, S. B. Sørensen, E. Jørgensen, P. Meincke, O. S. Kim, and O. Breinbjerg, "An accurate technique for calculation of radiation from printed reflectarrays," *IEEE Antennas Wireless Propag. Lett.*, vol. 10, pp. 1081–1084, 2011.
- [22] M. Zhou, S. B. Sørensen, O. S. Kim, S. Pivnenko, and G. Toso, "Investigations on accurate analysis of microstrip reflectarrays," in *Proc. 33rd ESA Antenna Workshop*, Noordwijk, The Netherlands, 2011.
- [23] E. Jørgensen, J. Volakis, P. Meincke, and O. Breinbjerg, "Higher order hierarchical Legendre basis functions for electromagnetic modeling," *IEEE Trans. Antennas Propag.*, vol. 52, no. 11, pp. 2985 – 2995, 2004.
- [24] M. Zhou, E. Jørgensen, O. S. Kim, S. B. Sørensen, P. Meincke, and O. Breinbjerg, "Accurate and efficient analysis of printed reflectarrays with arbitrary elements using higher-order hierarchical Legendre basis functions," *IEEE Antennas Wireless Propag. Lett.*, vol. 11, pp. 814–817, 2012.
- [25] M. Arrebola, Y. Alvarez, J. A. Encinar, and F. Las-Heras, "Accurate analysis of printed reflectarrays considering the near field of the primary feed," *IET Microw. Antennas Propag.*, vol. 3, no. 2, pp. 187–194, 2009.
- [26] "DTU-ESA Spherical Near-Field Antenna Test Facility," <http://www.dtu.dk/centre/ems/English/research/facilities.aspx>.
- [27] *POS, User's Manual*. TICRA Engineering Consultants, 2011.
- [28] J. A. Encinar and M. Arrebola, "Reduction of cross-polarization in contoured beam reflectarrays using a three-layer configuration," in *Proc. IEEE AP-S Int. Symp.*, Honolulu, Hawaii, USA, 2007.
- [29] C. Tienda, J. A. Encinar, M. Barba, and M. Arrebola, "Reduction of cross-polarization in offset reflectarrays using two layers of varying-sized patches," *Microwave Opt. Technol. Lett.*, vol. 54, no. 11, pp. 2449–2454, 2012.
- [30] D. C. Chang and M. C. Huang, "Multiple-polarization microstrip reflectarray antenna with high efficiency and low cross-polarization," *IEEE Trans. Antennas Propag.*, vol. 43, no. 8, pp. 829–834, 1995.
- [31] H. Hasani, M. Kanyab, and A. Mirkamali, "Low cross-polarization reflectarray antenna," *IEEE Trans. Antennas Propag.*, vol. 59, no. 5, pp. 1752–1756, 2011.
- [32] G. Kristensson, S. Poulsen, and S. Rikte, "Propagators and scattering of electromagnetic waves in planar bianisotropic slabs - an application to frequency selective structures," *Progr. Electromagn. Res. (PIER)*, vol. 48, pp. 1–25, 2004.
- [33] R. F. Harrington, *Time-Harmonic Electromagnetic Fields*. McGraw-Hill, Inc., 1961.
- [34] W. C. Chew and Q. Liu, "Resonance frequency of a rectangular microstrip patch," *IEEE Trans. Antennas Propag.*, vol. 36, no. 8, pp. 1045–1056, 1988.
- [35] A. M. Lerer and A. G. Schuchinsky, "Full-wave analysis of three-dimensional planar structures," *IEEE Trans. Microwave Theory Tech.*, vol. 41, no. 11, pp. 2002–2015, 1993.
- [36] S. R. Rengarajan, "Choice of basis functions for accurate characterization of infinite array of microstrip reflectarray elements," *IEEE Antennas Wireless Propag. Lett.*, vol. 4, pp. 47–50, 2005.
- [37] S. M. Rao, D. R. Wilton, and A. W. Glisson, "Electromagnetic scattering by surfaces of arbitrary shape," *IEEE Trans. Antennas Propag.*, vol. 30, no. 3, pp. 409–418, 1982.
- [38] A. W. Glisson and D. R. Wilton, "Simple and efficient numerical methods for problems of electromagnetic radiation and scattering from surfaces," *IEEE Trans. Antennas Propag.*, vol. 28, no. 5, pp. 593–603, 1980.
- [39] M. R. Chaharmir, J. Shaker, N. Gagnon, and D. Lee, "Design of broadband, single layer dual-band large reflectarray using multi open loop elements," *IEEE Trans. Antennas Propag.*, vol. 58, no. 9, pp. 2875 – 2883, 2010.
- [40] M. R. Chaharmir, J. Shaker, and H. Legay, "Dual-band Ka/X reflectarray with broadband loop elements," *IET Microw. Antennas Propag.*, vol. 4, no. 2, pp. 225–231, 2010.
- [41] M. Bozzi, S. Germani, and L. Perregini, "Performance comparison of different element shapes used in printed reflectarrays," *IEEE Antennas Wireless Propag. Lett.*, vol. 2, no. 1, pp. 219–222, 2003.
- [42] L. Marmat, R. Loison, R. Gillard, D. Bresciani, and H. Legay, "Accurate synthesis of a dual linearly polarized reflectarray," in *Proc. EuCAP*, Berlin, Germany, 2009.
- [43] M. Abramowitz and I. A. Stegun, Eds., *Handbook of Mathematical Functions*, 9th ed. Dover Publications, New York, 1970.
- [44] J. E. Hansen, Ed., *Spherical Near-Field Antenna Measurements*. Peter Peregrinus Ltd., 1988.
- [45] S. D. Targonski and D. M. Pozar, "Analysis and design of a microstrip reflectarray using patches of variable size," in *Proc. IEEE AP-S Int. Symp.*, Seattle, Washington, USA, 1994.
- [46] K. Pontoppidan, Ed., *GRASP, Technical Description*. TICRA Engineering Consultants, 2008.



## PAPER IV

---

# THE GENERALIZED DIRECT OPTIMIZATION TECHNIQUE FOR PRINTED REFLECTARRAYS

Min Zhou, Stig B. Sørensen, Oleksiy S. Kim, Erik Jørgensen,  
Peter Meincke, Olav Breinbjerg, and Giovanni Toso

*Status*

Submitted: October 2012

### **Bibliography**

- [J4] M. Zhou, S. B. Sørensen, O. S. Kim, E. Jørgensen, P. Meincke, O. Breinbjerg, and G. Toso, “The generalized direct optimization technique for printed reflectarrays,” *Submitted to IEEE Trans. Antennas Propag.*, 2012.



# The Generalized Direct Optimization Technique for Printed Reflectarrays

Min Zhou, *Student Member, IEEE*, Stig B. Sørensen, Oleksiy S. Kim, Erik Jørgensen, *Member, IEEE*, Peter Meincke, *Member, IEEE*, Olav Breinbjerg, *Member, IEEE*, and Giovanni Toso, *Senior Member, IEEE*,

**Abstract**—A generalized direct optimization technique (GDOT) for the design of printed reflectarrays using arbitrarily shaped elements with irregular orientation and position is presented. The GDOT is based on the spectral domain method of moments (SD-MoM) assuming local periodicity (LP) and a minimax optimization algorithm. The accuracy of the LP-SDMoM for the design of reflectarrays with irregularly positioned and oriented array elements has been verified by comparisons with full wave method of moments. Three contoured beam reflectarrays, forming a high-gain beam on a European coverage, have been designed: a broadband design, a circularly polarized design using the variable rotation technique, and a design with irregularly positioned array elements. The latter has been manufactured and measured at the DTU-ESA Spherical Near-Field Antenna Test Facility. An excellent agreement between simulated and measured patterns have been obtained, showing accuracies that are comparable to those obtained for conventional shaped reflectors.

**Index Terms**—Contoured beam, reflectarray, accurate antenna analysis, optimization, irregular reflectarrays, satellite antenna

## I. INTRODUCTION

FOR satellite broadcasting and telecommunication applications, the most often used antenna is the shaped reflector antenna. Although this antenna is based on a mature technology, both in terms of manufacturing and simulation tools, it suffers from having large volume and mass, as well as manufacturing cost. In particular the mold depends on the specific antenna requirements and can not be reused for other missions. Printed reflectarrays, on the other hand, consist of a flat surface, they are light, easy and cheap to manufacture, and can be packed more compactly, saving volume during the launch phase. In addition, for a specific coverage, only the array elements are modified, thus significant recurring costs associated with shaped reflector antennas are avoided. Using printed reflectarrays, low cost, high-gain antennas for space applications can be realized and they have therefore been the

subject of increasing research and development activities [1]–[4].

To obtain a specific far-field pattern with a printed reflectarray, several degrees of freedom can be used, e.g. the size [5]–[7], the shape [8]–[12], the orientation [13]–[15], and the position [16], [17] of the array elements. An accurate and efficient design procedure, capable of including all these parameters, is a challenging task. Recently, the European Space Agency (ESA) has promoted activities to improve and extend the analysis and synthesis procedures for reflectarrays including all the degrees of freedom [18]–[20].

The conventional approach for the design of contoured/multi beam reflectarrays uses a phase-only optimization technique (POT) [21], [22], involving two steps (for pencil beam reflectarrays, the first step is skipped); first, a phase-only synthesis determines the phase distribution on the reflectarray surface; second, the array elements are adjusted, element by element, to comply with the synthesized phase distribution. Several contoured beam reflectarrays have been designed using this technique [21]–[24]. The POT is efficient since the analysis of all array elements at each iteration is avoided. However, a direct optimization technique, where all the array elements are simultaneously optimized, tends to produce improved designs. Such a direct technique was presented in [19], where several contoured beam reflectarrays were designed and compared to similar designs obtained using the POT. The comparisons showed that the designs obtained using the direct optimization technique are superior in performance, both for multi-frequency and dual-polarization designs.

The direct optimization technique reported in [19] is meant for reflectarrays where the array elements are located in a regular grid. Furthermore, only the size of square patches was used as a degree of freedom. It is believed that reflectarrays with even better performance may be designed if additional degrees of freedom, e.g. the position and orientation of the array elements, are included in the optimization. Such a technique was presented in [17], [25]. Therein, the array elements were located in a strongly irregular grid and the analysis of each array element was performed using a full-wave method of moments (MoM) that included the nearest neighboring elements. Thus, the overall synthesis was very time consuming.

In this work, we generalize the direct optimization technique of [19] to include several degrees of freedom. These are the position and orientation as well as size and shape parameters of printed reflectarray elements. The generalized direct optimiza-

Manuscript received October 10, 2012. The reflectarray antenna production and measurement is supported by the European Space Agency (ESTEC contract No. 4000101041).

M. Zhou is with TICRA, Copenhagen, Denmark, and also with the Department of Electrical Engineering, Electromagnetic Systems, Technical University of Denmark, Kgs. Lyngby, Denmark (e-mail: mz@ticra.com)

E. Jørgensen, S.B. Sørensen, and P. Meincke are with TICRA, Copenhagen, Denmark (e-mail: ticra@ticra.com)

O.S. Kim and O. Breinbjerg are with the Department of Electrical Engineering, Electromagnetic Systems, Technical University of Denmark, Kgs. Lyngby, Denmark (e-mail: osk@elektro.dtu.dk, ob@elektro.dtu.dk)

G. Toso is with the European Space Agency ESA-ESTEC, Noordwijk, The Netherlands (e-mail: giovanni.toso@esa.int)



tion technique (GDOT) is based on the spectral domain method of moments (SDMoM) assuming local periodicity (LP) [6], [7]. The accuracy of the LP-SDMoM for reflectarrays with regularly positioned elements is extremely good. The use of this technique for the design and analysis of reflectarrays with irregularly positioned and oriented array elements is new, and thus the accuracy of the LP-SDMoM for such reflectarrays has to be established. We show in this work that the LP-SDMoM is sufficiently accurate and can be used to analyze and optimize reflectarrays based on arbitrarily shaped elements with irregular position and orientation.

Three contoured beam reflectarrays forming a high-gain beam on a European coverage have been designed to illustrate the capabilities of the GDOT: a broadband dual linearly polarized design, a circularly polarized design based on the variable rotation technique [13], and a linearly polarized design with irregularly positioned array elements. The latter has been manufactured at the Technical University of Denmark (DTU) and measured at the DTU-ESA Spherical Near-Field Antenna Test Facility [26]. The agreement between simulations and measurements is very good, thus verifying the accuracy of the GDOT.

This paper is organized as follows. Section II describes the GDOT. The reflectarray designs are described in Section III. In Section IV, simulations are compared to the measurements, and conclusions are given in Section V.

## II. GENERALIZED DIRECT OPTIMIZATION TECHNIQUE

In this section, the analysis and optimization methods used in the direct optimization technique are reviewed and generalized to include the position as well as the orientation of arbitrarily shaped and sized array elements into the optimization.

### A. Analysis and Optimization Methods

The GDOT is based on a minimax algorithm, which is a gradient based method for non-linear minimax optimization. It is the optimization used in the TICRA software packages POS [27] and CHAMP [28].

The far-field objectives for the reflectarray are specified in a number of far-field points in the  $(u, v)$ -plane where  $u = \sin \theta \cos \phi$ ,  $v = \sin \theta \sin \phi$ , and  $(\theta, \phi)$  the polar and azimuthal angles. At each optimization iteration, the maximum difference between realized and specified objectives is minimized. The optimization variables are the geometrical parameters of the array elements, e.g. the size, orientation, and position of the array element. Both co- and cross-polar radiation patterns can be optimized for multiple frequencies, polarizations, and feed illuminations.

For the far-field calculations, two techniques are considered, the Floquet harmonics technique [29, Technique II], and the continuous spectrum technique [29, Technique III]. Whereas the continuous spectrum technique is slightly more accurate, the Floquet harmonics technique is more efficient. Thus, the Floquet harmonics technique is used to calculate the far-field during the optimization, whereas the continuous spectrum technique is used to evaluate the final optimized reflectarray.

The Floquet harmonics technique is based on the field equivalence principle [30, p. 106] and uses the scattering matrices to calculate the equivalent currents. The scattering matrix  $\bar{S}$  for a single array element is defined as

$$\mathbf{E}^s = \bar{S} \cdot \mathbf{E}^i, \quad (1)$$

and is calculated from the fundamental Floquet harmonic through the LP-SDMoM formulation. Herein,  $\mathbf{E}^s$  and  $\mathbf{E}^i$  are the scattered and incident plane wave, respectively. To ensure an accurate and efficient calculation of the scattering matrices, higher-order hierarchical Legendre basis functions [31] are used to model the electric currents on the array elements. For canonically shaped array elements e.g. rectangular patches, singular entire domain basis functions with the correct edge conditions, reproducing the singularities of the electric current at the edges of the array elements, have proven to yield accurate results [32]. It is shown in [33] that the higher-order hierarchical Legendre basis functions can be applied to any arbitrarily shaped array elements, and are at the same time capable of yielding results of the same accuracy as those obtained using singular basis functions. The versatility of the higher-order hierarchical Legendre basis functions is a key feature in the GDOT as it enables the optimization of reflectarrays consisting of non-canonical element shapes, e.g. concentric square/ring loops, phoenix elements, and many others [8]–[12]. In this work, we consider several element shapes, namely square patches, concentric square loops, square loop/patch combination, and triple dipoles.

To avoid the calculation of the scattering matrices of all array elements at each optimization iteration, the scattering matrices can be calculated in advance and stored in a look-up table [17], [23], which is accessed during the optimization by means of local cubic interpolation [34, Chap. 25]. For a given frequency, dielectric substrate, and unit-cell size, the scattering matrix depends on the illumination angles and the geometry of the array element. For the cases we have considered, a sufficient accuracy can be obtained by using approximately  $N_{el} = 60$  element sizes and  $N_\theta = 12$  sample values in the incident polar angle  $\theta^i$ . The variation of the scattering coefficients in the incident azimuthal angle  $\phi^i$  is  $2\pi$ -periodic and can thus be represented by a finite Fourier series expansion

$$\bar{S}(\theta^i, \phi^i) = \sum_{s=-N_m}^{N_m} \bar{c}_s(\theta^i) e^{js\phi^i}, \quad (2)$$

where [35, App. A4]

$$\bar{c}_s = \frac{\Delta\phi}{2\pi} \sum_{p=1}^{2N_m+1} \bar{S}(\theta^i, \phi_p^i) e^{-js\phi_p^i}. \quad (3)$$

Herein,  $\Delta\phi = 2\pi/(2N_m + 1)$  and  $\phi_p^i = \Delta\phi(p - 1)$ . We have observed, for the reflectarrays presented in this paper, that  $N_m = 2$  is adequate, yielding a total of only  $N_\phi = 5$  sample values in  $\phi^i$ . Thus for a given frequency, substrate, and unit-cell size, the total number of scattering matrix samples needed in the look-up table to obtain an accurate interpolation is  $N_{total} = N_\theta N_\phi N_{el} = 12 \cdot 5 \cdot 60 = 3600$ . This can be computed within a couple of minutes on a standard laptop

computer. The look-up table can be reused and needs only to be recalculated if other substrates, frequencies, or unit-cell sizes are used.

### B. Irregularly Orientated Array Elements

In order to exploit the orientation of the array elements in the GDOT, the look-up table has to be extended to include also the rotation angle  $\psi$  of the array element, see Fig. 1.

The rotation angle  $\psi$  is  $2\pi$ -periodic and hence the variation of the scattering matrices in  $\psi$  can be represented by a finite Fourier series expansion. Thus, the equation in (2) is replaced by

$$\bar{\mathbf{S}}(\theta^i, \phi^i, \psi) = \sum_{s=-N_m}^{N_m} \sum_{r=-N_n}^{N_n} \bar{\mathbf{c}}_{sr}(\theta^i) e^{js\phi^i} e^{jr\psi}. \quad (4)$$

In this way, the variations in both  $\psi$  and  $\phi^i$  are accounted for. The Fourier coefficients  $\bar{\mathbf{c}}_{sr}$  are given by

$$\bar{\mathbf{c}}_{sr} = \frac{\Delta\phi\Delta\psi}{4\pi^2} \sum_{p=1}^{2N_m+1} \sum_{q=1}^{2N_n+1} \bar{\mathbf{S}}(\theta^i, \phi_p^i, \psi_q) e^{-js\phi_p^i} e^{-jr\psi_q}, \quad (5)$$

where  $\Delta\psi = 2\pi/(2N_n + 1)$  and  $\psi_q = \Delta\psi(q - 1)$ . The value of  $N_n$  depends on the shape and size of the array element. For the elements presented in this work,  $N_n = 5$ , giving a total  $N_\psi = 11$  sample values, is sufficient for an accurate representation of the variation in  $\psi$ . The total number of scattering matrix samples needed in the look-up table is now  $N_{\text{total}} = N_\theta N_\phi N_{\text{el}} N_\psi = 12 \cdot 5 \cdot 60 \cdot 11 = 39600$  per frequency. The derivatives with respect to  $\psi$ , which are required in the optimization, are readily obtained analytically by differentiation of (4).

### C. Irregularly Positioned Array Elements

In order to utilize the position of the array elements in the GDOT, an irregular distribution of element positions is obtained through a mapping from a regular to an irregular grid. In this work, the mapping is obtained by adding a distortion to the regular grid.

Let us define  $(\alpha, \beta)$  as normalized coordinates in the regular grid such that  $|\alpha| \leq 1$  and  $|\beta| \leq 1$ . Then, the new normalized coordinates in the irregular grid are given by  $(\alpha', \beta') = (\alpha + f_x, \beta + f_y)$ , where the distortion functions are

$$f_x(\alpha, \beta) = (\alpha - 1)(\alpha + 1) \sum_{p=0}^P \sum_{q=0}^Q c_{pq} T_p(\alpha) T_q(\beta), \quad (6a)$$

$$f_y(\alpha, \beta) = (\beta - 1)(\beta + 1) \sum_{p=0}^P \sum_{q=0}^Q d_{pq} T_p(\alpha) T_q(\beta). \quad (6b)$$

Herein,  $T_i$  is the Chebyshev polynomial of order  $i$ , and  $c_{pq}$  and  $d_{pq}$  are the distortion coefficients. In contrast to [17], where the edges of the reflectarray are not constrained, the terms in front of the summations ensure that the edges of the reflectarray are kept fixed to avoid any undesired increase in antenna size introduced by the mapping.

The degree of the distortion is determined by the values of  $c_{pq}$  and  $d_{pq}$  and the polynomial order  $i$ . To avoid distortions

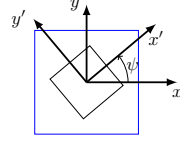


Fig. 1. A rotated square patch in a unit-cell, where the rotation angle is denoted by  $\psi$ .

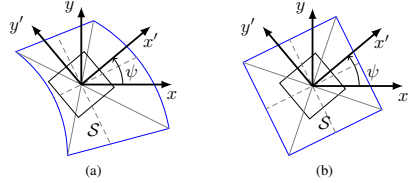


Fig. 2. An example of (a) a distorted cell and (b) its equivalent square cell. Both cells have the area  $\mathcal{S}$ . The center of the patch is located at the intersection of the two solid diagonal lines of the distorted cell. The rotation of the patch is given by the rotation angle  $\psi$  with respect to the coordinate system of the regular grid.

with overlapping array elements, upper and lower bounds are specified for  $c_{pq}$  and  $d_{pq}$ , and the polynomial order should not exceed 4. Only a few, 2 to 6, distortion coefficients are needed to achieve strong irregularities, as shown in Section II-E. The distortion coefficients  $c_{pq}$  and  $d_{pq}$  are the variables used to optimize the positions of the array elements. In this way, the optimization of the individual array element position, which can be rather complicated, is avoided.

Unlike the other optimization variables, the derivatives with respect to  $c_{pq}$  and  $d_{pq}$  can not be determined analytically since a change in  $c_{pq}$  or  $d_{pq}$  affects all array elements. As a result, the derivatives are computed numerically by finite difference approximations at the cost of higher computation time.

### D. Analysis of the Distorted Cell

Due to the grid distortion, the array elements are positioned in a non-periodic lattice and the LP-SDMoM can not be directly applied. Therefore, an equivalent unit-cell has to be defined to approximate locally each distorted cell. The center of the array element within the distorted cell is positioned at the center of the distorted cell, which is defined as the intersection of the two diagonal lines of the distorted cell, see Fig. 2a. Let us now define an equivalent square cell with the same area as the distorted cell. The equivalent cell has the same center as the distorted cell and is oriented in parallel with the bisector lines of the two diagonal lines of the distorted cell. This is illustrated in Fig. 2b, where the bisector lines are shown by dashed lines. The equivalent cell is used in the LP-SDMoM to calculate the scattering matrices.

The analysis procedure for reflectarrays with irregularly positioned elements is now the same as for those with regularly positioned elements, except that the unit-cells of the array elements are of different sizes. As a result, the look-up table has

TABLE I  
PENCIL BEAM REFLECTARRAY DATA

Center frequency	10 GHz
Reflectarray dimensions	405 mm × 405 mm
Number of elements	30 × 30
Relative permittivity	$\epsilon_r = 3.66$
Loss tangent	$\tan \delta = 0.0037$
Substrate thickness	$h = 1.524$ mm
Feed distance to center of array	$d_f = 0.6$ m
Feed offset angle	$\theta^i = 30^\circ$ , $\phi^i = 0^\circ$

to be further extended to include also samples of different sized unit-cells. The number of unit-cell samples needed depends on the degree of the grid distortion. For the results presented in this paper,  $N_{\text{cell}} = 50$  samples are sufficient, yielding a look-up table that requires  $N_{\text{total}} = N_\theta N_\phi N_{\text{el}} N_\psi N_{\text{cell}} = 12 \cdot 5 \cdot 60 \cdot 11 \cdot 50 = 1980000$  scattering matrix calculations per frequency. The computation time on a standard laptop is several hours, which is a significant increase compared to the regular array case. It is, however, still acceptable since the look-up table only needs to be calculated once prior to the optimization.

#### E. Analysis Accuracy

The use of the LP-SDMoM for the design and analysis of reflectarrays with irregularly positioned and oriented array elements is new, and thus the accuracy of the technique for such reflectarrays has to be established.

To this end, two offset pencil beam reflectarrays with different distortions have been designed, the first design with the beam towards the specular direction and the second with the beam towards the broadside direction. The distorted grids are kept fixed and only the size and orientation of the array elements are optimized. The values of  $c_{pq}$  and  $d_{pq}$  are selected empirically to ensure a strong but realistic distortion. The feed is a linear polarized Gaussian beam with a taper of  $-15$  dB at  $30^\circ$ . The geometrical parameters are summarized in Table I with respect to the coordinate system shown in Fig. 3. The mask layouts of the optimized reflectarrays are shown in

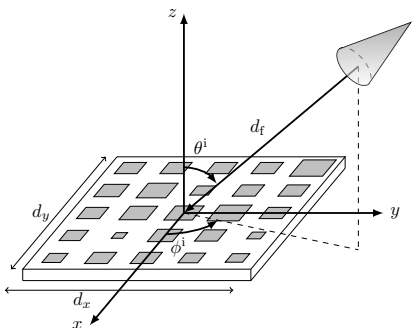
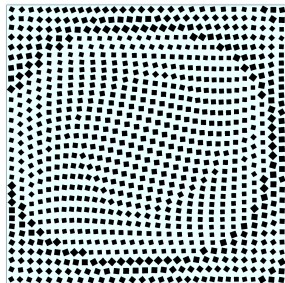
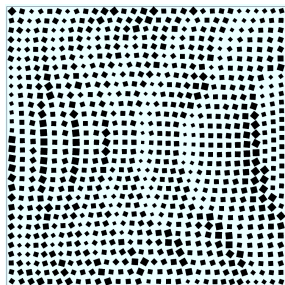


Fig. 3. Reflectarray geometrical parameters.



(a)



(b)

Fig. 4. Pencil beam reflectarrays with irregularly positioned and oriented array elements. The reflectarrays are designed to radiate a pencil beam towards (a) the specular direction and (b) the broadside direction.

Fig. 4. The number of distortion coefficients for the specular and broadside cases are 2 and 6, respectively.

A full wave MoM is used as reference. For the calculation of the currents on the array elements, the MoM relies on the spatial dyadic Green's function for a grounded dielectric slab [36], thus assuming infinite substrate and ground plane.

The radiation patterns for the two reflectarrays calculated using LP-SDMoM and MoM are shown in Fig. 5. The continuous spectrum technique is used to calculate the far-field in both methods, thus accounting for the finite size of the reflectarrays [29]. A very good agreement between the two methods is observed. For the specular case, the predicted peak directivity using both methods is 30.7 dBi, whereas for the broadside case, LP-SDMoM and MoM yield 31.1 dBi and 31.0 dBi, respectively. Also the cross-polar radiation levels are extremely close; the deviations are around 1–3 dB at  $-40$  dB below the co-polar peak. The good accuracy of the LP-SDMoM, despite the strong irregularities, can be attributed to the systematic manner in which the grids are distorted by (6). Several irregular designs have been optimized and analyzed using both LP-SDMoM and MoM, and it was observed that the accuracy of LP-SDMoM is generally good in all cases.

This shows that the LP-SDMoM is accurate and can be used to analyze and optimize reflectarrays with irregularly

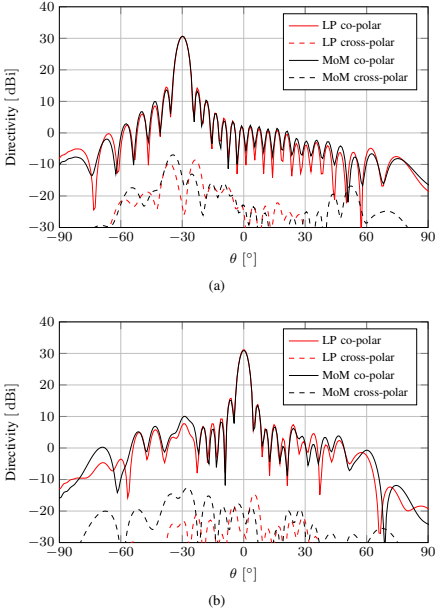


Fig. 5. Comparison of the radiation pattern at  $\phi = 0$  calculated using LP-SDMoM and MoM for (a) the specular radiation case and (b) the broadside radiation case.

positioned and oriented array elements.

### III. REFLECTARRAY DESIGN

In this section, we design several offset contoured beam reflectarrays with the aim to demonstrate the capabilities of the GDOT. We consider a high-gain European coverage with the possibility of enforcing sidelobe suppression within a southern African coverage. The coverages seen from the longitude  $0^\circ$  geostationary orbital position are shown as red polygons in Fig. 6.

Three reflectarrays are designed: a dual linearly polarized broadband design, a circularly polarized design based on the variable rotation technique [13], and a linearly polarized design with irregularly positioned array elements. The reflectarray parameters are the same as those listed in Table I, except that the dimensions of the designs are  $600 \times 600 \text{ mm}^2$ , corresponding to approximately  $20 \times 20 \lambda_0^2$ , with  $\lambda_0$  being the free space wavelength, at the center frequency 10 GHz. In addition, the substrate thickness is different for the three designs.

Although some measures are done during the design process to ensure a good antenna performance, e.g. by selecting appropriate array elements, the purpose of these designs is not to obtain the best possible reflectarray but to illustrate the capabilities of the GDOT to yield an optimum design within a given set of parameters.

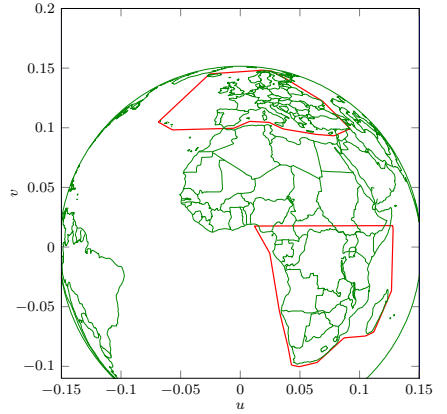


Fig. 6. European and southern African coverages seen from the longitude  $0^\circ$  geostationary orbital position.

#### A. Broadband Design

The goal of this design (Design A) is to maximize the directivity within the European coverage in the frequency range 9 – 11 GHz for two linear polarizations, V- and H-polarization, and at the same time minimize the cross-polar radiation within the same coverage. H-polarization is in the offset plane ( $xz$ -plane in Fig. 3) and V-polarization in the orthogonal plane.

The bandwidth of printed reflectarrays is controlled by two main factors: the bandwidth of the array element, and the bandwidth limitation introduced by the differential phase delay [37]. While the differential phase delay is the limiting factor for reflectarrays of large electrical sizes ( $> 50\lambda_0$ ) and small focal distance to diameter (F/D) ratios, the bandwidth of the array elements is the dominating factor for smaller reflectarrays [37].

For broadband performances, the variation of the phase of the scattering coefficient as function of the geometrical parameters should be slow and almost parallel at different frequencies [1], [7], [9], [12]. The concentric square loops have been demonstrated to have good phase responses that provides a good bandwidth [8], [9]. They have several parameters that can be adjusted to control the phase of the scattering coefficient: the lengths and widths of the outer and inner loops. In Fig. 7, the phase of the scattering coefficient of concentric square loops in a periodic environment for different widths of the inner loop  $w_2$  is shown. The phase is calculated at 10 GHz under normal plane wave incidence and displayed as a function of the length of the outer loop  $L_1$ . The substrate thickness is  $h = 3.048 \text{ mm}$  and the size of the square unit-cell is  $d = 10.5 \text{ mm}$ . Based on a number of simulations, the width of the outer loop is  $w_1 = 0.075L_1$  and the length of the inner loop is  $L_2 = 0.75L_1$ . This is to ensure a slow phase response versus  $L_1$  and at the same time maintain a

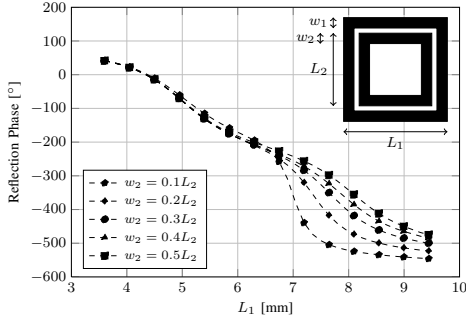


Fig. 7. The phase of the scattering coefficient of concentric square loops in a periodic environment as function of the outer loop length  $L_1$  for different inner loop widths  $w_2$ . The inner loop length is  $L_2 = 0.75L_1$ , the width of the outer loop is  $w_1 = 0.075L_1$ .

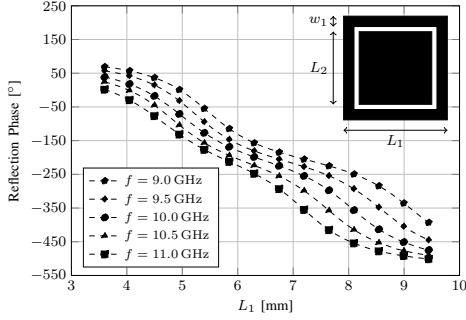


Fig. 8. The phase of the scattering coefficient of a square loop/patch combination element in a periodic environment as function of the outer loop length  $L_1$  for different frequencies. The inner loop length is  $L_2 = 0.75L_1$ , the width of the outer loop is  $w_1 = 0.075L_1$ .

phase variation over  $360^\circ$ , which is required for the design of reflectarrays. It is seen in Fig. 7 that the slope of the phase curve decreases for increasing  $L_1$  when  $w_2$  is wide. The case where  $w_2 = 0.5L_2$  is equivalent to the case where the inner loop is replaced by a square patch. Here, the reflection phase varies slowly as function of  $L_1$ . The phase response as function of  $L_1$  for different frequencies between 9–11 GHz is shown in Fig. 8. It is seen that the phase curves versus  $L_1$  are close to being parallel at the different frequencies. A similar result has been observed in [38]. Due to these properties, this square loop/patch combination is used in Design A. In the optimization,  $w_1$  and  $L_2$  are fixed according to Fig. 8 and only  $L_1$  is optimized. A scattering matrix look-up table for frequencies  $f = 9, 10, 11$  GHz has been calculated for this design.

As a starting point of the optimization, identical elements are used. A Gaussian beam with a taper of  $-15$  dB at  $30^\circ$  is used as a feed. The optimized reflectarray consists of  $57 \times$

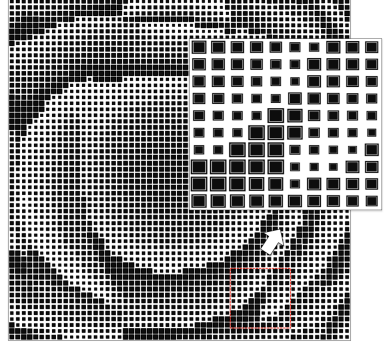


Fig. 9. The mask layout of Design A.

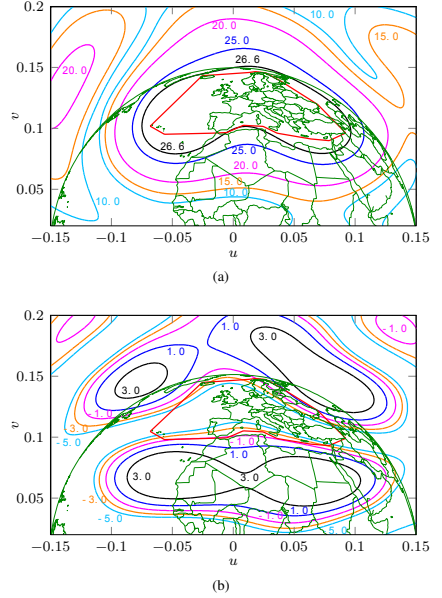


Fig. 10. Simulated radiation patterns of Design A for H-polarization at 10 GHz, (a) co-polar pattern and (b) cross-polar pattern.

57 elements and the mask layout of the design is shown in Fig. 9. The radiation pattern at 10 GHz for H-polarization is shown in Fig. 10, and it shows that a minimum directivity of 26.6 dBi is obtained within the European coverage and that the cross-polar radiation has been successfully suppressed to below 1 dBi within the same coverage.

The performance of the design is summarized in Table II. It is seen that the minimum directivity is above 26.4 dBi

TABLE II  
PERFORMANCE OF DUAL-POLARIZED BROADBAND REFLECTARRAY  
DESIGN

Frequency (GHz)	H-polarization		V-polarization	
	Minimum Directivity (dBi)	Minimum XPD (dB)	Minimum Directivity (dBi)	Minimum XPD (dB)
8.5	24.7	27.1	24.8	28.1
9.0	26.6	26.7	26.5	26.6
9.5	26.4	26.4	26.4	26.9
10.0	26.6	26.4	26.5	27.6
10.5	26.5	25.0	26.4	27.4
11.0	26.6	24.1	26.4	28.4
11.5	24.9	22.9	25.1	26.3

for both polarizations between 9 – 11 GHz and drops to approximately 25 dBi at 8.5 GHz and 11.5 GHz, which are outside of the desired frequency range. This shows that the reflectarray has been successfully optimized to operate in the specified frequency range of 20% bandwidth.

In this design, only  $L_1$  has been optimized, while  $w_1$  and  $L_2$  were fixed. It is expected that better performances can be obtained if  $w_1$  and  $L_2$  are also included as optimization variables. However, this would be at the cost of higher computation time and scattering matrix look-up table size. Furthermore, it is also believed that better designs can be obtained by using a rectangular loop/patch combination as array elements.

### B. Circularly Polarized Design

In this design (Design B), a right hand circularly polarized (RHCP) reflectarray that radiates a high-gain beam on the European coverage in the frequency range 9 – 11 GHz is realized by utilizing the variable rotation technique (VRT) [13], [14]. The VRT uses identical array elements with different angular rotations to achieve a given far-field beam. Suppose an array element is illuminated by a circularly polarized incident wave, then by rotating the array element by angle  $\psi$  (Fig. 1), the phase of the scattered field of the array element is shifted by  $2\psi$ . Thus, by adjusting the rotation angles of all array

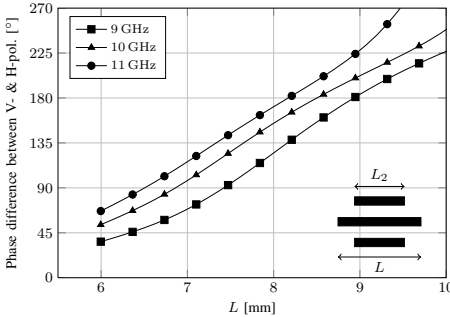


Fig. 11. The phase difference between V- and H-polarization as function of the center dipole length  $L$ . The lengths of the two parallel dipoles are both  $L_2 = 0.65L$ . The widths of the dipoles are  $w = 0.1L$ .

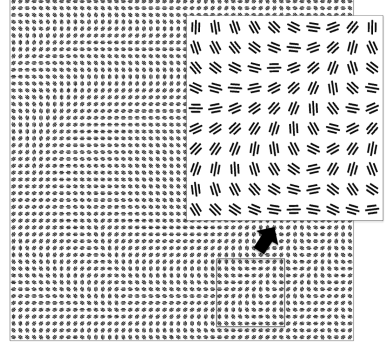


Fig. 12. The mask layout of Design B.

elements, a given phase distribution can be realized to radiate a specified far-field beam [13].

It is shown in [13], and explicitly stated in [39], that the phase of the scattering coefficient for two orthogonal linear polarizations, e.g. V- and H-polarization, has to be different by  $180^\circ$ , so that the scattered field has the same sense of circular polarization as the incident wave with a phase shift of  $\pm 2\psi$  depending on the polarization of the incident wave. Thus, by selecting an array element that can realize the  $180^\circ$  phase difference is the key for the use of the VRT. For broadband performances, the  $180^\circ$  phase difference between the orthogonal polarizations has to be realized in a wide frequency range.

In this design, we use the triple dipole element [40] as the array element. In Fig. 11, the phase difference between V- and H-polarization of the triple dipole element is shown for different frequencies as function of the center dipole length  $L$ . The length of the two parallel dipoles is  $L_2 = 0.65L$ , and the width of each dipole is  $w = 0.1L$ . The substrate thickness is  $h = 3.5$  mm and the unit-cell size  $d = 12$  mm. The phase is calculated for a normally incident plane wave and shown for  $f = 9, 10, 11$  GHz. Based on the phase difference, a dipole length of  $L = 8.5$  mm has been selected for the optimization, so that a phase difference of  $180^\circ$  between V- and H-polarization is achieved at 10 GHz. At 9 GHz and 11 GHz, the phase difference changes to approximately  $155^\circ$  and  $197^\circ$ , respectively. The specified bandwidth of 20% is rather large and the triple dipole element does not provide the necessary phase difference of  $180^\circ$  in the entire frequency range. However, it has significantly better performance compared to more simple elements e.g. single dipoles.

In this design, only the rotation angles of the triple dipoles are optimized. No cross-polar suppression has been specified for the optimization of this design. As the starting point of the optimization, all the dipoles are oriented with  $\psi = 0$ . A RHCP Gaussian beam with a taper of  $-15$  dB at  $30^\circ$  is used as feed. The optimized reflectarray consists of  $50 \times 50$  elements and the mask layout is shown in Fig. 12. It is seen in Table III, where

TABLE III  
PERFORMANCE OF CIRCULARLY POLARIZED REFLECTARRAY DESIGN

Frequency (GHz)	20% design		10% design	
	Minimum Directivity (dBi)	Minimum XPD (dB)	Minimum Directivity (dBi)	Minimum XPD (dB)
8.5	25.0	16.4	22.6	15.2
9.0	26.6	24.7	25.3	24.1
9.5	26.7	23.0	26.6	24.0
10.0	26.8	20.7	26.7	24.1
10.5	26.8	20.5	26.7	27.0
11.0	26.7	17.3	25.3	21.5
11.5	25.1	14.8	23.9	12.2

the performance of the design (20% design) in the frequency range 8.5 – 11.5 GHz is listed, that a minimum directivity within the European coverage above 26.6 dBi is achieved in the frequency range 9 – 11 GHz. The minimum directivity decreases outside the specified frequency range, as expected.

The minimum XPD within the frequency range is relatively low with the best value of 24.7 dB at 9 GHz. In the attempt to reduce the cross-polar radiation, a design with cross-polar suppression has also been optimized. However, approximately 2 dB in the minimum directivity was lost, and the cross-polar radiation was only suppressed to a minimum XPD of approximately 20 dB in the desired frequency range. This is a direct consequence of the large bandwidth specified in the optimization. A similar design including cross-polar suppression for a bandwidth of 10% (9.5 – 10.5 GHz) was also optimized and the performance is listed in Table III (10% design). A minimum directivity of 26.6 dBi in the specified frequency range is maintained, but the minimum XPD has been improved to 24.0 dB. This shows that the VRT is rather sensitive with respect to the required 180° phase difference, particularly regarding the cross-polar radiation.

It is expected that better performance can be achieved if an array element with 180° phase difference between V- and H-polarization in a wider frequency range can be found.

#### C. Irregularly Positioned Design

In this design (Design C), we consider a reflectarray with irregularly positioned array elements. The reflectarray radiate a high-gain beam within the European coverage with cross-polar suppression within the same coverage and sidelobe suppression within the southern African contour. The reflectarray consists of  $50 \times 50$  array elements and is optimized for H-polarization and only at 10 GHz. The substrate thickness is  $h = 0.762$  mm. A corrugated horn with a taper of  $-17.5$  dB at 30° at 10 GHz is used as feed. The feed has been measured at the DTU-ESA Spherical Near-Field Test Facility, and this feed pattern is used in the optimization. Square patches are used as array elements and the patch sizes are the optimization parameters. In addition to the patch sizes, 10 grid distortion coefficients are included in the optimization.

The mask layout of the optimized reflectarray is shown in Fig. 13. Simulations show a minimum directivity of 27.3 dBi within the European coverage and a minimum isolation level of 27.2 dB. In addition, the cross-polar radiation has been suppressed to below 0 dBi, yielding a minimum XPD of 27.8 dB.

Design C has been compared to a similar reflectarray with regularly positioned elements that has been optimized for the same goals as Design C. The comparison showed an improvement of 1 dB in the XPD level for Design C, indicating that a better performance in the cross-polar radiation can be obtained by using an irregular array instead of a regular one. However, this improvement is small and is obtained for a single polarization design. Reflectarrays with irregularly and regularly positioned elements optimized for both V- and H-polarizations have also been designed and compared with the aim to investigate the performance for dual-polarization applications. Good results for both polarizations can be obtained with a regular array, while with the grid distortions and square patches used in this work, no further improvement is gained by using an irregular array.

The distortions used in this work are based on Chebyshev polynomials of different orders. These polynomials do not depend nor imitate any of the physical behaviors of the reflectarray and are thus purely mathematical. In order to fully exploit the potential of the irregularity of the element positions, other types of distortions that utilizes the physics of the antenna should be investigated. A circular or elliptical grid distortion that for instance follows the feed illumination taper over the reflectarray surface could be an example. Such a distortion can be realized by using Zernike polynomials and can be readily included in the GDOT. This is subject to future work.

#### IV. VALIDATION BY MEASUREMENTS

To verify the accuracy of the GDOT, Design C has been manufactured at DTU and measured at the DTU-ESA Spherical Near-Field Antenna Test Facility. The reflectarray broadband was measured at a series of frequencies from 9.6 GHz to 10.5 GHz in both V- and H-polarizations. For the peak directivity, the measurements have a  $1\sigma$  uncertainty of 0.05 dB.

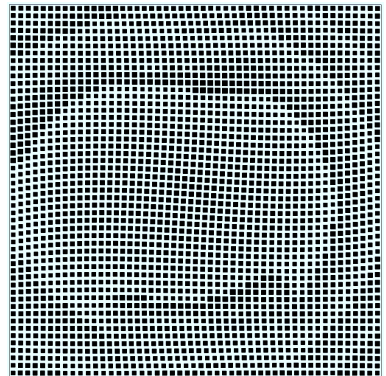


Fig. 13. The mask layout of Design C.

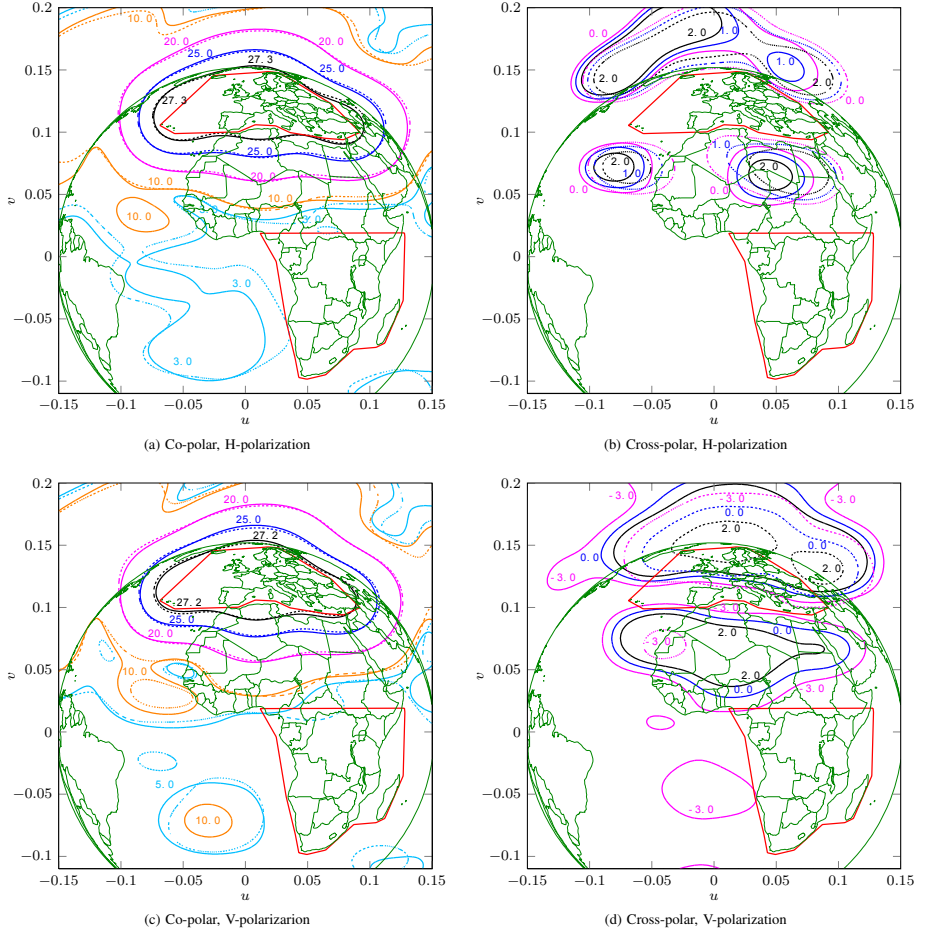


Fig. 14. Simulated (solid lines) and measured (dotted lines) radiation patterns of the manufactured reflectarray breadboard for H- and V-polarization at 10 GHz.

To account for the presence of the support structures, the scattering from the struts is included in the analysis using the MoM add-on in GRASP [41].

In Fig. 14, the simulated (solid lines) and measured (dotted lines) radiation patterns for H- and V-polarizations at 10 GHz are shown. As expected, the reflectarray has a low co-polar radiation within the southern African coverage and a low cross-polar radiation within the European coverage in H-polarization. A comparison of the solid and dotted lines shows an excellent agreement between simulations and measurements. The performance of the breadboard is summarized

in Table IV, and it is seen that the peak directivity and minimum directivity within the European coverage are very well predicted, even though the breadboard is based on an irregular grid. Even the cross-polar radiation levels, which are approximately 30 dB below the co-polar peak are accurately predicted. The breadboard was only optimized for H-polarization, hence the lower minimum XPD and isolations levels in V-polarization. The accuracy in the other measured frequencies is also very good, where the maximum discrepancy in the minimum directivity within the European coverage is 0.1 dB.



TABLE IV  
MEASURED VERSUS SIMULATED DATA AT 10 GHz

	Peak directivity (dBi)	Min. directivity (dBi)	Min. XPD (dB)	Min. isolation (dB)
Measurement (H)	29.2	27.3	27.2	24.3
Simulation (H)	29.2	27.3	27.8	27.2
Measurement (V)	29.4	27.1	24.5	20.2
Simulation (V)	29.4	27.1	21.0	20.5

These excellent agreements between simulations and measurements clearly verifies the accuracy of the GDOT.

## V. CONCLUSION

An accurate and efficient generalized direct optimization technique (GDOT) for the design of printed reflectarrays using arbitrary element shape with irregular orientation and position is presented. It is based on the spectral domain method of moments (SDMoM) assuming local periodicity (LP) and a minimax optimization algorithm. The geometrical parameters of the array elements, i.e. size, orientation, and position, are directly optimized to fulfill the far-field requirements. The optimization uses scattering matrices which are calculated in advance, stored in a look-up table, and accessed during the optimization by a local cubic interpolation. Both co- and cross-polar radiation can be optimized for multiple frequencies, polarizations, and feed illuminations. The design procedure has been described and the accuracy of the LP-SDMoM for the design of reflectarrays with irregularly positioned and oriented array elements has been verified by comparisons with full wave method of moments solutions. It is shown that the LP-SDMoM is accurate.

To show the capabilities of the GDOT, three offset contoured beam reflectarrays forming a high-gain beam on a European coverage have been designed: a linearly polarized broadband design; a circularly polarized design using the variable rotation technique; and a linearly polarized design with irregularly positioned array elements. The latter has been manufactured at the Technical University of Denmark (DTU) and measured at the DTU-ESA Spherical Near-Field Antenna Test Facility. An excellent agreement between simulated and measured patterns is obtained, thus verifying the accuracy of the GDOT.

## ACKNOWLEDGMENT

Dr. S. Pivnenko, Electromagnetic Systems, Department of Electrical Engineering, Technical University of Denmark (EMS-DTU), is acknowledged for the accurate measurements of the reflectarray breadboard, Mr. T. G. Smith (EMS-DTU) for valuable comments, and the mechanical workshop at EMS-DTU for the manufacturing of the reflectarray breadboard.

## REFERENCES

- [1] J. Huang and J. A. Encinar, *Reflectarray Antennas*. IEEE Press, 2008.
- [2] J. A. Encinar, "Recent advances in reflectarray antennas," in *Proc. EuCAP*, Barcelona, Spain, 2010.
- [3] H. Legay, D. Bresciani, E. Girard, R. Chiniard, E. Labiole, O. Vendier, and G. Caille, "Recent developments on reflectarray antennas at Thales Alenia Space," in *Proc. EuCAP*, Berlin, Germany, 2009.

- [4] A. Roederer, "Reflectarray antennas," in *Proc. EuCAP*, Berlin, Germany, 2009.
- [5] D. M. Pozar and T. A. Metzler, "Analysis of a reflectarray antenna using microstrip patches of variable size," *Electron. Lett.*, vol. 29, no. 8, pp. 657–658, 1993.
- [6] D. M. Pozar, S. D. Targonski, and H. D. Syrigos, "Design of millimeter wave microstrip reflectarrays," *IEEE Trans. Antennas Propag.*, vol. 45, no. 2, pp. 287–296, 1997.
- [7] J. A. Encinar, "Design of two-layer printed reflectarrays using patches of variable size," *IEEE Trans. Antennas Propag.*, vol. 49, no. 10, pp. 1403–1410, 2001.
- [8] M. R. Chaharmir, J. Shaker, N. Gagnon, and D. Lee, "Design of broadband, single layer dual-band large reflectarray using multi open loop elements," *IEEE Trans. Antennas Propag.*, vol. 58, no. 9, pp. 2875–2883, 2010.
- [9] M. E. Bialkowski and K. H. Sayidmarie, "Investigations into phase characteristics of a single-layer reflectarray employing patch or ring elements of variable size," *IEEE Trans. Antennas Propag.*, vol. 56, no. 11, pp. 3366–3372, 2008.
- [10] D. Cadoret, A. Laisne, R. Gillard, and H. Legay, "A new reflectarray cell using microstrip patches loaded with slots," *Microwave Opt. Technol. Lett.*, vol. 44, no. 3, pp. 270–272, 2005.
- [11] L. Moustafa, R. Gillard, F. Peris, R. Loison, H. Legay, and E. Girard, "The phoenix cell: a new reflectarray cell with large bandwidth and rebirth capabilities," *IEEE Antennas Wireless Propag. Lett.*, vol. 10, pp. 71–74, 2011.
- [12] M. Bozzi, S. Germani, and L. Perregini, "Performance comparison of different element shapes used in printed reflectarrays," *IEEE Antennas Wireless Propag. Lett.*, vol. 2, no. 1, pp. 219–222, 2003.
- [13] J. Huang and R. J. Pogorzelski, "A Ka-band microstrip reflectarray with elements having variable rotation angles," *IEEE Trans. Antennas Propag.*, vol. 46, no. 5, pp. 650–656, 1998.
- [14] B. Strassner, C. Han, and K. Chang, "Circularly polarized reflectarray with microstrip ring elements having variable rotation angles," *IEEE Trans. Antennas Propag.*, vol. 52, no. 4, pp. 1122–1125, 2004.
- [15] C. Han, C. Rodenbeck, J. Huang, and K. Chang, "A/Ca dual frequency dual layer circularly polarized reflectarray antenna with microstrip ring elements," *IEEE Trans. Antennas Propag.*, vol. 52, no. 11, pp. 2871–2876, 2004.
- [16] D. Kurup, M. Himdi, and A. Rydberg, "Design of an unequally spaced reflectarray," *IEEE Antennas Wireless Propag. Lett.*, vol. 2, pp. 33–35, 2003.
- [17] A. Capozzoli, C. Curcio, A. Lisenio, M. Migliorelli, and G. Toso, "Power pattern synthesis of advanced flat aperiodic reflectarrays," in *Proc. 33th ESA Antenna Workshop*, Noordwijk, The Netherlands, 2011.
- [18] A. Capozzoli, C. Curcio, G. D'Elia, A. Lisenio, G. Toso, and P. Vinetti, "Aperiodic and non-planar array of electromagnetic scatterers, and reflectarray antenna comprising the same," International Patent WO20111033388, September 2009.
- [19] M. Zhou, S. B. Sørensen, O. S. Kim, E. Jørgensen, P. Meincke, and O. Breinbjerg, "Direct optimization of printed reflectarrays for contoured beam satellite antenna applications," *Submitted to IEEE Trans. Antennas Propag.*, 2012.
- [20] M. Zhou, S. B. Sørensen, P. Meincke, E. Jørgensen, O. S. Kim, O. Breinbjerg, and G. Toso, "An accurate and efficient design tool for large contoured beam reflectarrays," in *Proc. ESA Workshop on Large Deployable Antennas*, Noordwijk, The Netherlands, 2012.
- [21] J. A. Encinar and J. A. Zornoza, "Three-layer printed reflectarrays for contoured beam space applications," *IEEE Trans. Antennas Propag.*, vol. 52, no. 5, pp. 1138–1148, 2004.
- [22] J. A. Encinar, L. S. Datashvili, J. A. Zornoza, M. Arrebola, M. Sierra-Castaner, J. L. Besada-Sanmartin, H. Baier, and H. Legay, "Dual-polarization dual-coverage reflectarray for space applications," *IEEE Trans. Antennas Propag.*, vol. 54, no. 10, pp. 2827–2837, 2006.
- [23] H. Legay, D. Bresciani, E. Labiole, R. Chiniard, E. Girard, G. Caille, L. Marnat, D. Calas, R. Gillard, and G. Toso, "A 1.3 m earth deck reflectarray for a Ku band contoured beam antenna," in *Proc. 33rd ESA Antenna Workshop*, Noordwijk, The Netherlands, 2011.
- [24] J. A. Encinar, M. Arrebola, L. D. L. Fuente, and G. Toso, "A transmit-receive reflectarray antenna for direct broadband satellite applications," *IEEE Trans. Antennas Propag.*, vol. 59, no. 9, pp. 3255–3264, 2011.
- [25] A. Capozzoli, C. Curcio, A. Lisenio, M. Migliorelli, and G. Toso, "Aperiodic conformal reflectarrays," in *Proc. IEEE AP-S Int. Symp.*, Spokane, Washington, USA, 2011.
- [26] "DTU-ESA Spherical Near-Field Antenna Test Facility," <http://www.dtu.dk/centre/ems/english/research/facilities.aspx>.
- [27] *POS, User's Manual*. TICRA Engineering Consultants, 2011.

- [28] *CHAMP, User's Manual*. TICRA Engineering Consultants, 2011.
- [29] M. Zhou, S. B. Sørensen, E. Jørgensen, P. Meincke, O. S. Kim, and O. Breinbjerg, "An accurate technique for calculation of radiation from printed reflectarrays," *IEEE Antennas Wireless Propag. Lett.*, vol. 10, pp. 1081–1084, 2011.
- [30] R. F. Harrington, *Time-Harmonic Electromagnetic Fields*. McGraw-Hill, Inc., 1961.
- [31] E. Jørgensen, J. Volakis, P. Meincke, and O. Breinbjerg, "Higher order hierarchical Legendre basis functions for electromagnetic modeling," *IEEE Trans. Antennas Propag.*, vol. 52, no. 11, pp. 2985 – 2995, 2004.
- [32] S. R. Rengarajan, "Choice of basis functions for accurate characterization of infinite array of microstrip reflectarray elements," *IEEE Antennas Wireless Propag. Lett.*, vol. 4, pp. 47–50, 2005.
- [33] M. Zhou, E. Jørgensen, O. S. Kim, S. B. Sørensen, P. Meincke, and O. Breinbjerg, "Accurate and efficient analysis of printed reflectarrays with arbitrary elements using higher-order hierarchical Legendre basis functions," *IEEE Antennas Wireless Propag. Lett.*, vol. 11, pp. 814–817, 2012.
- [34] M. Abramowitz and I. A. Stegun, Eds., *Handbook of Mathematical Functions*, 9th ed. Dover Publications, New York, 1970.
- [35] J. E. Hansen, Ed., *Spherical Near-Field Antenna Measurements*. Peter Peregrinus Ltd., 1988.
- [36] Y. Chow, J. Yang, D. Fang, and G. Howard, "A closed-form spatial Green's function for the thick microstrip substrate," *IEEE Trans. Microwave Theory Tech.*, vol. 39, no. 3, pp. 588 – 592, 1991.
- [37] D. M. Pozar, "Bandwidth of reflectarrays," *Electron. Lett.*, vol. 39, no. 21, pp. 1490–1491, 2003.
- [38] Q.-Y. Li, Y.-C. Jiao, and G. Zhao, "A novel microstrip rectangular-patch/ring- combination reflectarray element and its application," *IEEE Antennas Wireless Propag. Lett.*, vol. 8, pp. 1119–1122, 2009.
- [39] T. G. Smith, N. V. Larsen, U. V. Gothelf, O. S. Kim, and O. Breinbjerg, "20/30 GHz dual-band circularly polarized reflectarray antenna based on the concentric split loop element," in *Proc. 34th ESA Antenna Workshop*, Noordwijk, The Netherlands, 2012.
- [40] L. Li, Q. Chen, Q. Yuan, K. Sawaya, T. Maruyama, T. Furuno, and S. Uebayashi, "Novel broadband planar reflectarray with parasitic dipoles for wireless communication applications," *IEEE Antennas Wireless Propag. Lett.*, vol. 8, pp. 881–885, 2009.
- [41] K. Pontoppidan, Ed., *GRASP, Technical Description*. TICRA Engineering Consultants, 2008.



## CONFERENCE PAPER I

---

# INVESTIGATIONS ON ACCURATE ANALYSIS OF MICROSTRIP REFLECTARRAYS

Min Zhou, Stig B. Sørensen, Oleksiy S. Kim, Sergey Pivnenko,  
and Giovanni Toso

*Status*

Presented: October 2011

### **Bibliography**

- [C2] M. Zhou, S. B. Sørensen, O. S. Kim, S. Pivnenko, and G. Toso, “Investigations on accurate analysis of microstrip reflectarray”, *Proc. 33rd ESA Antenna Workshop*, Noordwijk, The Netherlands, 2011.



# Investigations on Accurate Analysis of Microstrip Reflectarrays

Min Zhou, Stig B. Sørensen, Oleksiy S. Kim, Sergey Pivnenko, and Giovanni Toso

**Abstract**—An investigation on accurate analysis of microstrip reflectarrays is presented. Sources of error in reflectarray analysis are examined and solutions to these issues are proposed. The focus is on two sources of error, namely the determination of the equivalent currents to calculate the radiation pattern, and the inaccurate mutual coupling between array elements due to the lack of periodicity. To serve as reference, two offset reflectarray antennas have been designed, manufactured and measured at the DTU-ESA Spherical Near-Field Antenna Test Facility. Comparisons of simulated and measured data are presented to verify and demonstrate the improved results using the proposed solutions.

**Index Terms**—Microstrip reflectarrays, accurate antenna analysis, method of moments (MoM), antenna radiation pattern, horn antennas, measurements.

## I. INTRODUCTION

MICROSTRIP reflectarrays are becoming viable alternatives to reflector antennas for satellite applications and have been the subject of increasing research interest [1]–[4]. To obtain high-gain performance for satellite applications, the electric size of reflectarrays is usually very large, and therefore an efficient and accurate analysis is a challenging task. The commonly adopted analysis method is based on the spectral domain Method of Moments (SDMoM) assuming local periodicity (LP), that is, an individual array element is embedded in an infinite array of identical elements [5]. This approach has been demonstrated to be efficient for reflectarrays made of varying-sized patches, and many advanced reflectarrays have been designed using this technique [3]. However, reflectarrays are aperiodic by nature and the local periodicity assumption gives rise to discrepancies between simulated and measured radiation patterns. Efficient full-wave simulation techniques have been applied on entire reflectarrays for accurate determination of the currents on the array elements [6]–[9]. However, discrepancies between simulations and measurements can still be observed, and the increase in computation time makes the methods unaffordable for optimization processes. For space applications, where the accuracy demands are high, an efficient and accurate analysis method is important to precisely determine the radiation properties of reflectarrays, and it is

essential for optimization purposes. The objective of this work is to understand the sources of error in reflectarray analysis and to propose solutions to these.

This paper is organized as follows. Section II describes some of the sources of error in reflectarray analysis. The benchmark antennas are described in Section III. In Section IV, simulations are compared with measurements, and conclusions are given in Section V.

## II. SOURCES OF ERROR

In reflectarray analysis, several factors can give rise to errors, e.g. the representation of the incident field, the choice of basis functions, the technique used to calculate the radiation patterns, the lack of periodicity, the truncation of the ground plane, scattering from the support structures etc. All these factors should be accounted for correctly in order to obtain an accurate analysis.

### A. Representation of the Incident Field

In the SDMoM computations, each array element is assumed to be illuminated by a locally plane wave. The pattern of the feed is usually approximated by a far field model using a  $\cos^q(\theta)$  function or a Gaussian beam [1, Sec. 3.8], and is used to compute the polarization of the incident plane wave on each array element. This approximation is usually inaccurate due to the idealized feed pattern. The analysis accuracy can be improved by using the real pattern of the feed obtained by either measurements [10] or commercially available simulation tools e.g. CHAMP [11]. However, the assumption of plane wave incidence in the SDMoM is only valid if the reflectarray surface is located sufficiently far away from the feed. Alternatively, a plane wave expansion of the feed radiation over the reflectarray surface can be computed. The SDMoM analysis is then performed for each plane wave and subsequently added to yield the final result. In this approach, the representation of the incident field is exact, however at the cost of computation time. For the reflectarray antennas to be described in Section III, it was found that the assumption of plane wave incidence is a sufficient representation of the incident field.

### B. Choice of Basis Functions

The choice of basis functions in the SDMoM computations is important. Roof-tops and entire domain trigonometric basis functions are popular choices. However, for resonant microstrip array elements, the convergence of the SDMoM solution becomes poor and in certain cases convergence is never

M. Zhou is with TICRA, Copenhagen, Denmark, and also with the Department of Electrical Engineering, Electromagnetic Systems, Technical University of Denmark, Kgs. Lyngby, Denmark.

S.B. Sørensen is with TICRA, Copenhagen, Denmark.

O.S. Kim and S. Pivnenko are with the Department of Electrical Engineering, Electromagnetic Systems, Technical University of Denmark, Kgs. Lyngby, Denmark.

G. Toso is with the European Space Agency ESA-ESTEC, Noordwijk, The Netherlands.

achieved using these basis functions. Consequently, singular basis functions with correct edge conditions are required for accurate characterization of the array elements [12]. However, singular basis functions require additional Floquet modes to achieve convergence, thus increasing the total computation time. In this paper, higher order hierarchical Legendre basis functions as described in [13] are used. These basis functions can be applied to any non-canonical element types, and at the same time yield results that are identical to those obtained with singular basis functions using less computation time [14].

### C. Aperiodicity

Reflectarrays are inherently aperiodic due to the need to compensate for the spatial phase delay from the feed. Thus the periodicity assumption in the LP approach can give inaccurate results.

One way to reduce these errors is to use the "Surrounded Element Approach" (SEA) proposed in [15]. The analysis in SEA is based on a finite approach where no periodicity is applied. It includes the actual neighboring elements that surrounds the element under consideration, thus accounting for the mutual coupling more accurately. In [15], the analysis was based on a FDTD implementation assuming plane wave incidence, and many neighboring elements were required to obtain an improved result. Even though the reported computation time were in terms of hours, we find this technique interesting and promising. Therefore, an integral equation (IE) formulation using a spatial dyadic Green's function (DGF) [16] is currently being implemented. Using an IE formulation, the plane wave incidence assumption is avoided and the total computation time may be reduced. Preliminary results indicate that the SEA is especially accurate in predicting the radiation pattern of the cross-polarization component.

Another approach, which is a combination of the LP approach and the SEA, is introduced in [14], the "Extended Local Periodicity" (ELP) approach. Similar to the LP approach, the ELP approach is also based on periodicity, but the periodicity is applied on an extended unit cell which includes the actual 8 neighboring elements that surround the element under consideration. SDMoM is applied to the extended unit cell and the unknown currents on the element under consideration is determined. This is repeated for the next element with the extended unit cell now including the new element under consideration and its 8 neighbors. The inclusion of the nearest surrounding neighbors increases the total computation time, since the number of basis functions is larger and additional Floquet modes are required. While an analysis of a realistic reflectarray takes a couple of seconds using the LP approach, the ELP approach requires 40-60 minutes. This increase is significant and must be decreased if the approach is to be used for optimization purposes. Acceleration techniques on this matter can be found in the literature [17], [18] and are currently being investigated.

Recently, there have been interests in completely aperiodic reflectarrays that aim to exploit all available degrees of freedom of the array elements e.g. element positions and orientations [19], [20]. The array elements are located in

irregular grids and the periodic assumption in the LP approach is inaccurate. It is expected that the SEA and the ELP approach are better candidates for analysis of such reflectarrays.

### D. Truncation Effects

Due to the periodicity assumption in the LP and ELP approaches, the truncation of the ground plane is not taken into account in the determination of the currents on the array elements. Nor is it accounted for in the IE formulations since the spatial DGF assumes infinite ground plane. An efficient and accurate solution to this issue should be investigated.

### E. Radiation Pattern Calculations

In the literature on accurate analysis of reflectarrays, the main focus has been on the determination of the currents on the array elements, and the technique used to calculate the radiation pattern has received less attention. However, the latter is equally important.

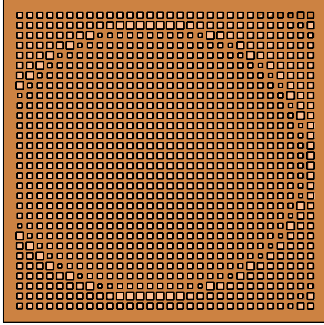
The conventional technique, which will be referred to as technique I, to calculate the radiation pattern is to invoke the field equivalence principle to calculate equivalent electric and magnetic surface currents in the plane of the array elements [21], [22]. The equivalent electric and magnetic currents are defined as

$$\mathbf{J}_S = \sum_i \mathbf{J}_i = \sum_i \hat{\mathbf{z}} \times \mathbf{H}_i, \quad (1)$$

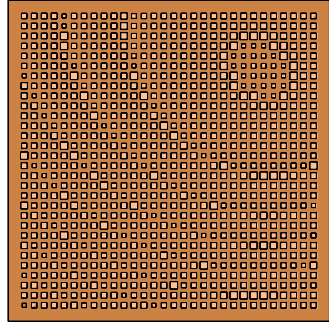
$$\mathbf{M}_S = \sum_i \mathbf{M}_i = - \sum_i \hat{\mathbf{z}} \times \mathbf{E}_i, \quad (2)$$

where index  $i$  runs over all array elements. The electric and magnetic fields,  $\mathbf{E}_i$  and  $\mathbf{H}_i$ , respectively, are approximated using the fundamental Floquet mode from the discrete spectrum in the SDMoM simulations. By integrating the equivalent currents, the far field radiation pattern can be determined. There are several disadvantages with this technique. Firstly, the ground plane in reflectarrays is often extended at the edges for practical reasons [22], [23]. The extended ground plane contributes to the far field radiation and is not accounted for in this technique. This can be circumvented by placing unit cells with no elements at the edges to cover the area of the extended ground plane. However, this procedure is rather impractical and not suitable for commercial codes. Secondly, equivalent currents are discontinuous at cell boundaries. These discontinuities can contribute to phase and amplitude errors in the equivalent currents, thus resulting in an erroneous relation between the equivalent electric and magnetic currents. As a result, the radiation in the back hemisphere can be wrong [24].

To avoid the issues associated with technique I, a novel technique as described in [24] can be used. This technique will be referred to as technique II and it also utilizes the field equivalence principle. Instead of calculating the equivalent currents using the discrete spectrum from the SDMoM simulations, a continuous spectrum is employed. In this technique, the extended ground plane is automatically accounted for. Additionally, no discontinuities are created in the equivalent currents, and the equivalent electric and magnetic currents are correctly related through the continuous spectrum, thus



(a) Antenna I



(b) Antenna II

Fig. 1. Reflectarray mask for the antenna I and II.

enabling an accurate calculation of the radiation pattern on the entire far field sphere.

### III. BENCHMARK ANTENNAS

To serve as benchmark cases, two offset microstrip reflectarray antennas were designed. The designs are focused on the aforementioned sources of error and are intended to exaggerate these sources such that they can be separated. The radiation patterns of the antennas were measured at the DTU-ESA Spherical Near-Field Antenna Test Facility [25] and serve as reference solutions.

The reflectarray in Fig. 1a is designed to exaggerate the truncation effects. To do so, a strong edge illumination is required and the aperiodicity effects must be reduced. To this end, a smooth patch variation is obtained by reducing the spatial phase delay by placing the feed far from the reflectarray surface, and by directing a pencil beam towards the specular direction.

The reflectarray in Fig. 1b is designed to exaggerate the aperiodicity in reflectarrays by having a pencil beam towards  $\theta = 35^\circ$  and  $\phi = 135^\circ$  in the coordinate system in Fig. 2. To ensure that the truncation effects are negligible, the feed is located close to the reflectarray surface such that a low edge illumination can be achieved with a high gain feed.

For both antennas, the substrate is Rogers RO4350B with a relative permittivity of  $\epsilon_r = 3.66$  and a loss tangent of  $\tan \delta = 0.0037$ . The ground plane and substrate for both antennas are slightly extended at the edges as seen in Fig. 1. The geometrical parameters of the reflectarrays are shown in Fig. 2 and summarized in Table I.

Two horn antennas were used as feed, a corrugated horn (Fig. 3a), and a Potter horn (Fig. 3b). Each horn was used on both antennas giving a total of 4 different reflectarray configurations. The corrugated horn has at 10 GHz a taper of  $-17.5$  dB at  $30^\circ$  whereas the Potter horn has a taper of  $-7$  dB at  $30^\circ$ .

The reflectarrays and their support structures were manufactured at the Technical University of Denmark. For the

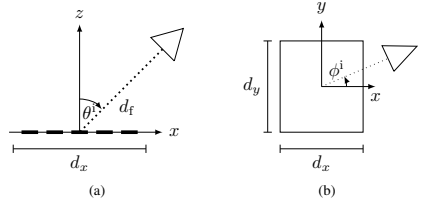


Fig. 2. Geometrical parameters of the reflectarray (a) the  $xz$ -plane (b) the  $xy$ -plane.

TABLE I  
BENCHMARK ANTENNA DATA

Frequency	10 GHz
Number of elements	$30 \times 30$
Reflectarray dimensions	435 mm $\times$ 435 mm
Substrate thickness	0.762 mm
Relative permittivity ( $\epsilon_r$ )	3.66
Loss tangent ( $\tan \delta$ )	0.0037
<b>Antenna I</b>	
Feed distance:	$d_t = 0.6$ m
Feed orientation:	$\theta^i = 30^\circ$ , $\phi^i = 0^\circ$
Main beam direction:	$\theta = -30^\circ$ , $\phi = 0^\circ$
<b>Antenna II</b>	
Feed distance:	$d_t = 0.35$ m
Feed orientation:	$\theta^i = 45^\circ$ , $\phi^i = 0^\circ$
Main beam direction:	$\theta = 35^\circ$ , $\phi = 135^\circ$

measurements, see Fig. 4, the estimated  $1\sigma$  uncertainty for the peak directivity is 0.07 dB. In addition to the reflectarray measurements, the feed horns were also measured and the measured data was used to represent the incident field on the reflectarray surface in the analysis.

These reflectarray antennas and their associated radiation patterns constitute a scientific contribution in itself, since the results currently available in the literature are not completely



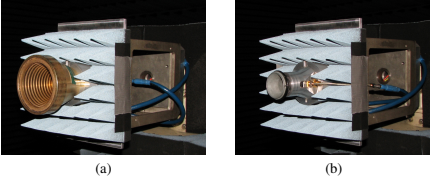
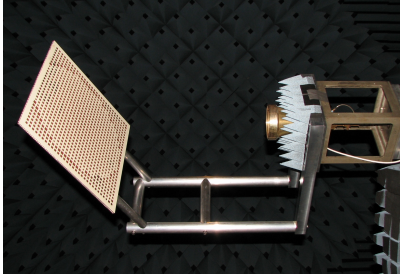
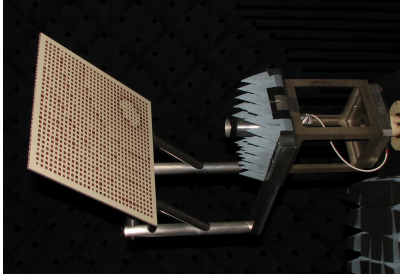


Fig. 3. The two horn antennas used in the benchmark cases, (a) the corrugated horn, (b) the Potter horn.



(a) Antenna I with the corrugated horn



(b) Antenna II with the Potter horn

Fig. 4. Benchmark antennas at the DTU-ESA Spherical Near-Field Antenna Test Facility.

specified in terms of geometrical parameters or feed radiation pattern, or the accuracy of the measurements. In addition, the available results are for complex full-size reflectarrays where many sources of errors are present at the same time and cannot be distinguished.

#### IV. SIMULATIONS VS. MEASUREMENTS

Radiation patterns obtained at 10 GHz by measurements and simulations are presented in this section. To account for the presence of the support structures, the scattering from the struts is included in the analysis using the MoM add-on in GRASP [26]. All radiation patterns are depicted in a coordinate system defined with the  $z$ -axis directed towards the main beam direction.

#### A. Radiation Pattern Calculations

To demonstrate the accuracy of the aforementioned techniques to calculate the radiation pattern, technique I and II are used to compute the radiation patterns for antennas I and II, and compared with measurements in Fig. 5 and Fig. 6. For these results, the currents on the array elements are determined using the LP approach. To illustrate the effect of the extended substrate, this contribution is not included in technique I.

The far field co-polar radiation patterns for antenna I are shown in Fig. 5. The Potter horn is used in this case to give a strong edge illumination,  $-7$  to  $-1$  dB. It is seen that the improvement using technique II is clear, especially in Fig. 5b where the simulated and measured pattern practically coincide. The discrepancies observed in Fig. 5a around  $\theta = 45^\circ$  are due to the blockage of the measurement tower.

The far field co-polar radiation patterns for antenna II are depicted in Fig. 6. A low edge illumination of approximately  $-25$  to  $-12$  dB is achieved in this case using the corrugated horn as feed. Even in this case where the edges are weakly illuminated, the enhancement of the analysis accuracy is apparent. The side lobes are much better predicted using technique II compared to technique I. The discrepancies are mainly attributed to the strong aperiodicity.

The improvements in Fig. 5 and Fig. 6 using technique II are due to the inclusion of the extended ground plane. It is shown in [24] that a similar accuracy in the forward hemisphere can be achieved with technique I if empty unit cells are placed at the edges to cover the area extended by the substrate. Since very good agreements can be achieved when the aperiodicity effects are minimized, it can be concluded that the error introduced by the truncation of the ground plane is of small importance for the determination of the currents on the array elements, but has to be accounted for in the calculation of the far field radiation pattern.

With respect to the radiation in the back hemisphere, technique I can yield wrong results as shown in Fig. 7. In this figure, the results from Fig. 6b are shown also in the back hemisphere. It is seen that in the direction of the main beam's image around  $\theta = 145^\circ$ , an erroneous beam is predicted by technique I. This is caused by the incorrect relation between the equivalent electric and magnetic currents in technique I as previously mentioned. This issue is avoided using technique II since the equivalent currents are correctly related to each other, thus yielding good results in the entire far field sphere.

#### B. Aperiodicity

To illustrate the aperiodicity effects, results for antenna II computed using the LP and ELP approaches are compared with the measurements and shown in Fig. 8. Technique II is used to calculate the radiation patterns, and the Potter horn is used as feed yielding an edge illumination of approximately  $-20$  to  $-5$  dB.

It is seen that the overall accuracy over the entire far field sphere is good, also for the LP case. This is due to the technique used to calculate the radiation pattern and the inclusion of the radiation from the support structures. However, it is observed that the ELP approach is generally

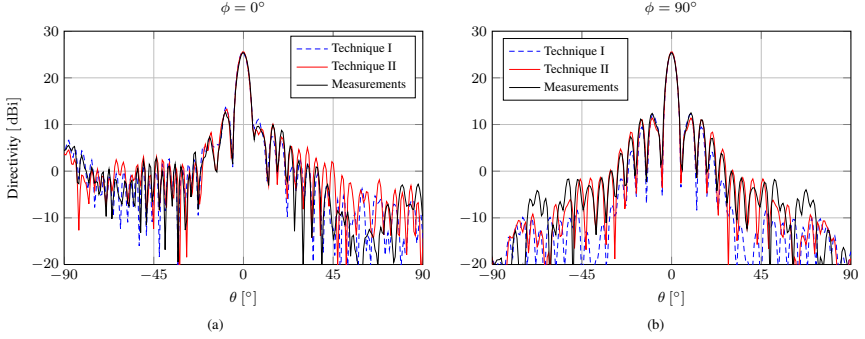


Fig. 5. Comparison of radiation pattern calculated using technique I and II with measurements for antenna I.

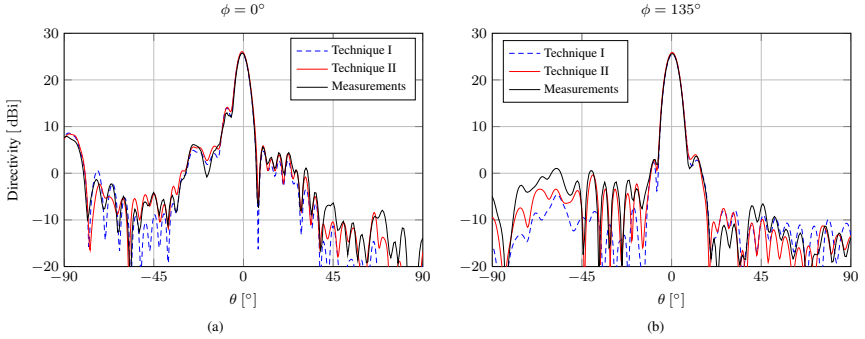


Fig. 6. Comparison of radiation pattern calculated using technique I and II with measurements for antenna II.

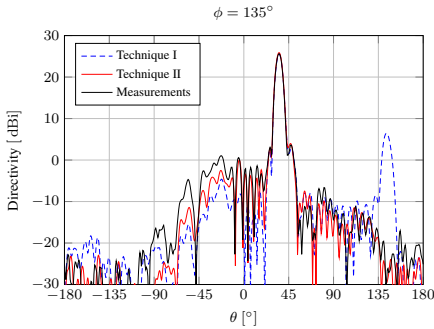


Fig. 7. The results from Fig. 6b shown also in the back hemisphere.

more accurate e.g.  $-90 < \theta < -40$  in Fig. 8b. To see the improvements more clearly, a close up of the radiation pattern from Fig. 8a is depicted in Fig. 9. It is apparent that the accuracy is enhanced using the ELP approach. The peak directivity is measured to  $D_{\text{meas}} = 26.1$  dBi. The LP approach predicts  $D_{\text{meas}} = 26.8$  dBi whereas ELP yields an improved value of  $D_{\text{meas}} = 25.9$  dBi. For the far field cross-polar radiation patterns, the results obtained using the LP and ELP approaches are rather similar and improvements were not observed.

## V. CONCLUSIONS

An investigation on accurate analysis of microstrip reflector-arrays has been carried out and is presented in this paper. Several sources of error in reflectarray analysis have been examined, e.g. the representation of the incident field, the choice of basis functions, aperiodicity, and truncation effects, as well as the technique used to calculate the radiation pattern. To serve as benchmark cases, two offset reflectarray antennas have been designed, manufactured and measured at the DTU-ESA

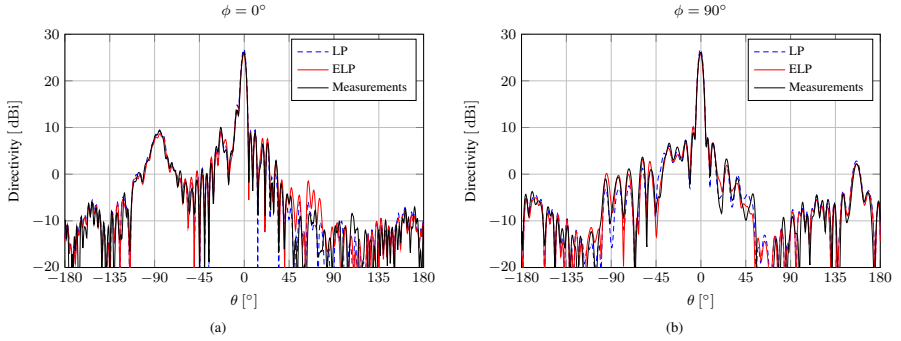


Fig. 8. Comparison of simulations using LP and ELP, and measurements for antenna II. The Potter horn is used as feed.

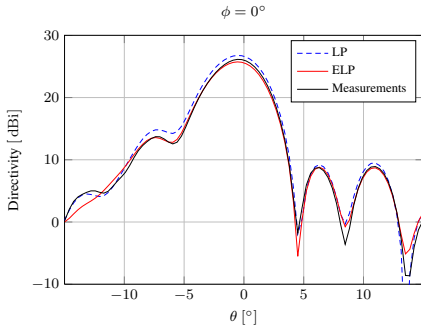


Fig. 9. Close up of the comparison shown in Fig. 8a.

Spherical Near-Field Antenna Test Facility. The two designs aim to exaggerate the errors introduced by the truncation of the ground plane, and the lack of periodicity, respectively. Comparisons of simulated and measured radiation patterns show that the errors introduced by the truncation of the ground plane are of small importance for the determination of the currents on the array elements and can thus be neglected. The errors introduced by the aperiodicity on the other hand can be significant and the conventional local periodicity assumption can be inaccurate. To circumvent this, the extended local periodicity approach can be utilized. In addition, the comparisons shown that the choice of the technique to calculate the radiation pattern is very important with respect to the analysis accuracy. The finite substrate and ground plane size of the reflectarray must be taken into account and techniques that neglect this give inaccurate results.

The results presented in this paper show that accurate analysis of reflectarrays can be achieved if the sources of error are treated correctly. However, several challenges remain and are presently being investigated.

#### ACKNOWLEDGMENT

This work is supported by the European Space Agency (ESA) within the ESTEC contract No.4000101041.

#### REFERENCES

- [1] J. Huang and J. A. Encinar, *Reflectarray Antennas*. IEEE Press, 2008.
- [2] J. A. Encinar, "Recent advances in reflectarray antennas," in *Proc. EuCAP*, Barcelona, Spain, 2010.
- [3] H. Legay, D. Bresciani, E. Girard, R. Chiniard, E. Labiole, O. Vendier, and G. Caille, "Recent developments on reflectarray antennas at thales alenia space," in *Proc. EuCAP*, Berlin, Germany, 2009, pp. 2515 – 2519.
- [4] J. Shaker, M. Chaharmir, M. Cuhaci, and A. Itipiboon, "Reflectarray research at the communications research centre canada," *IEEE Antennas Propag. Mag.*, vol. 50, no. 4, pp. 31 – 52, Aug 2008.
- [5] D. M. Pozar, S. D. Targonski, and H. D. Syrigos, "Design of millimeter wave microstrip reflectarrays," *IEEE Trans. Antennas Propag.*, vol. 45, no. 2, pp. 287–296, 1997.
- [6] M. Berçigli, P. D. Vita, R. Guidi, A. Freni, P. Pirinoli, L. Matekovits, G. Vecchi, and M. Bandinelli, "Hybrid SFX/MLayAIM method for the analysis and optimization of large reflectarrays and planar arrays with metallic lenses," in *Proc. EuCap*, 2010.
- [7] F. Catedra, I. Gonzalez, A. Tayebi, and J. Gomez, "Full wave analysis of reflectarrays antennas," in *Proc. 30th ESA Antenna Workshop*, Noordwijk, The Netherlands, 2008.
- [8] P. D. Vita, A. Freni, M. Berçigli, M. Bandinelli, and M. Sabbadini, "Fast and accurate modeling of quasi-periodic layered structures," in *Proc. 30th ESA Antenna Workshop*, Noordwijk, The Netherlands, 2008.
- [9] J. Rius, J. Parron, A. Heldring, J. Tamayo, and E. Ubeda, "Fast iterative solution of integral equations with method of moments and matrix decomposition algorithm – singular value decomposition," *IEEE Trans. Antennas Propag.*, vol. 56, no. 8, pp. 2314 – 2324, 2008.
- [10] M. Arrebola, Y. Alvarez, J. A. Encinar, and F. Las-Heras, "Accurate analysis of printed reflectarrays considering the near field of the primary feed," *IET Microw. Antennas Propag.*, vol. 3, no. 2, pp. 187–194, 2009.
- [11] "CHAMP: Corrugated Horn Analysis by Modal Processing," TICRA, Denmark, <http://www.ticra.com>.
- [12] S. R. Rengarajan, "Choice of basis functions for accurate characterization of infinite array of microstrip reflectarray elements," *IEEE Antennas Wireless Propag. Lett.*, vol. 4, pp. 47 – 50, 2005.
- [13] E. Jørgensen, J. Volakis, P. Meincke, and O. Breinbjerg, "Higher order hierarchical Legendre basis functions for electromagnetic modeling," *IEEE Trans. Antennas Propag.*, vol. 52, no. 11, pp. 2985 – 2995, 2004.
- [14] M. Zhou, S. B. Sørensen, E. Jørgensen, P. Meincke, O. S. Kim, and O. Breinbjerg, "Analysis of printed reflectarrays using extended local periodicity," in *Proc. EuCAP*, Rome, Italy, 2011, pp. 1408 – 1412.
- [15] M. A. Milon, D. Cadoret, R. Gillard, and H. Legay, "Surrounded-element approach for the simulation of reflectarray radiating cells," *IET Microw. Antennas Propag.*, vol. 1, no. 2, pp. 289–293, 2007.

- [16] Y. Chow, J. Yang, D. Fang, and G. Howard, "A closed-form spatial Green's function for the thick microstrip substrate," *IEEE Trans. Microwave Theory Tech.*, vol. 39, no. 3, pp. 588 – 592, 1991.
- [17] R. Boix, M. Freire, and F. Medina, "New method for the efficient summation of double infinite series arising from the spectral domain analysis of frequency selective surfaces," *IEEE Trans. Antennas Propag.*, vol. 52, no. 4, pp. 1080 – 1094, 2004.
- [18] A. L. Fructors, R. R. Boix, and F. Mesa, "A contribution to the efficient computation of multilayered periodic green's functions," in *Proc. EuCAP*, Rome, Italy, 2011, pp. 2471 – 2474.
- [19] A. Capozzoli, C. Curcio, E. Iavazzo, A. Lisenò, M. Migliorelli, and G. Toso, "Phase-only synthesis of a-periodic reflectarrays," in *Proc. EuCAP*, Rome, Italy, 2011, pp. 987 – 991.
- [20] A. Capozzoli, C. Curcio, A. Lisenò, M. Migliorelli, and G. Toso, "Aperiodic conformal reflectarrays," in *Proc. IEEE AP-S Int. Symp.*, Spokane, Washington, USA, 2011, pp. 361 – 364.
- [21] S. R. Rengarajan, "Reciprocity considerations in microstrip reflectarrays," *IEEE Antennas Wireless Propag. Lett.*, vol. 8, pp. 1206–1209, 2009.
- [22] M. Arrebola, J. A. Encinar, and M. Barba, "Multifed printed reflectarray with three simultaneous shaped beams for LMDS central station antenna," *IEEE Trans. Antennas Propag.*, vol. 56, no. 6, pp. 1518–1527, 2008.
- [23] J. Encinar, M. Barba, J. Page, M. Arrebola, A. Pacheco, and K. Klooster, "Experimental validation of a reflectarray antenna in ka-band," in *Proc. IEEE AP-S Int. Symp.*, Spokane, Washington, USA, 2011, pp. 353 – 356.
- [24] M. Zhou, S. B. Sørensen, E. Jørgensen, P. Meincke, O. S. Kim, and O. Breinbjerg, "An accurate technique for calculation of radiation from printed reflectarrays," *IEEE Antennas Wireless Propag. Lett.*, vol. 10, pp. 1081–1084, 2011.
- [25] "DTU-ESA Spherical Near-Field Antenna Test Facility," <http://www.dtu.dk/centre/ems/English/research/facilities.aspx>.
- [26] K. Pontoppidan, Ed., *GRASP9, Technical Description*. TICRA Engineering Consultants, 2008.



## CONFERENCE PAPER II

---

# AN ACCURATE AND EFFICIENT DESIGN TOOL FOR LARGE CONTOURED BEAM REFLECTARRAYS

Min Zhou, Stig B. Sørensen, Peter Meincke, Erik Jørgensen, Oleksiy S. Kim,  
Olav Breinbjerg, and Giovanni Toso

*Status*

Presented: October 2012

### **Bibliography**

- [C5] M. Zhou, S. B. Sørensen, P. Meincke, E. Jørgensen, O. S. Kim, O. Breinbjerg, and G. Toso, “An accurate and efficient design tool for large contoured beam reflectarrays”, *Proc. ESA Workshop on Large Deployable Antennas*, Noordwijk, The Netherlands, 2012.



# An Accurate and Efficient Design Tool for Large Contoured Beam Reflectarrays

Min Zhou, Stig B. Sørensen, Erik Jørgensen, Peter Meincke, Oleksiy S. Kim, Olav Breinbjerg, and Giovanni Toso

**Abstract**—An accurate and efficient tool for the design of contoured beam reflectarrays is presented. It is based on the Spectral Domain Method of Moments, the Local Periodicity approach, and a minimax optimization algorithm. Contrary to the conventional phase-only optimization techniques, the geometrical parameters of the array elements are directly optimized to fulfill the far-field requirements. The design tool can be used to optimize reflectarrays based on a regular grid as well as an irregular grid. Both co- and cross-polar radiation can be optimized for multiple frequencies, polarizations, and feed illuminations. Two offset contoured beam reflectarrays that radiate a high-gain beam on an European coverage have been designed, manufactured, and measured at the DTU-ESA Spherical Near-Field Antenna Test Facility. An excellent agreement is obtained for the simulated and measured patterns. To show the design tool's ability to optimize electrically large reflectarrays, a  $50 \times 50$  square wavelengths contoured beam reflectarray has been designed.

**Index Terms**—Printed reflectarrays, accurate antenna analysis, method of moments (MoM), measurements, contoured beam, optimization, satellite antennas

## I. INTRODUCTION

PRINTED reflectarrays provide a way for realizing low-cost, high-gain antennas for space applications and are the subject of increasing research interest [1]–[3]. For satellite broadcasting and telecommunication applications, the most often used antenna is the shaped reflector antenna. Although the shaped reflector antenna is a mature technology, both in terms of manufacturing and simulation tools, they suffer from large volume and mass, as well as high cost of manufacturing. Printed reflectarrays on the other hand consist of a flat surface, they are light, easy and cheap to manufacture, and can be packed more compactly, saving volume for the launch.

To obtain a certain antenna performance, several degrees of freedom in printed reflectarrays can be utilized, e.g. the size [4], the shape [5]–[7], the orientation [8], and the position [9], [10] of the array elements, as well as the shape of the reflecting surface [11] of the reflectarray. An accurate and efficient design procedure that is capable of including all these parameters is a challenging task.

The conventional approach for the design of contoured beam reflectarrays is using a phase-only optimization technique

(POT) [12], [13]. Initially, a phase-only synthesis is performed to determine the phase distribution on the reflectarray surface. The array elements are subsequently optimized, element by element, to match the required phase distribution. Several contoured beam reflectarrays have been designed using this technique [13]–[15].

Although the POT is efficient, since the analysis of all array elements at each iteration is avoided, a direct optimization technique, where all the array elements are simultaneously optimized, may produce more optimal designs. Such approaches are presented in [16], [17]. In [16], a small contoured beam reflectarray was designed and measured. However, significant discrepancies between simulations and measurements were observed, and it was concluded that further work is needed to improve the accuracy of the analysis. In [17], a direct optimization technique where also the position of the array elements can be included in the optimization is presented. The array elements are located in a strongly distorted grid and a full-wave Method of Moments (MoM) is used in the optimization. This involves a high computational burden.

In this work, we present a new direct optimization technique, which is both efficient and accurate. It is based on the Spectral Domain Method of Moments (SDMoM) assuming Local Periodicity (LP) and a minimax optimization algorithm. The direct optimization technique can be used for the design of reflectarrays based on a regular grid as well as for reflectarrays based on an irregular grid. To verify the accuracy of the direct optimization technique, two offset contoured beam reflectarrays that radiate a high-gain beam on an European coverage have been designed, manufactured, and measured at the DTU-ESA Spherical Near-Field Antenna Test Facility [18]. An excellent agreement is obtained between simulations and measurements, thus validating the direct optimization technique and the LP approach.

Some of the results presented in this paper have been published elsewhere [19], [20], but are included to give a complete overview of the direct optimization technique.

This paper is organized as follows. Section II describes the direct optimization technique. The reflectarray samples are described in Section III where also the simulations are compared to the measured data. In Section IV, the design of a  $50 \times 50$  square wavelengths contoured beam reflectarray is presented, and conclusions and on-going work are given in Section V.

## II. DIRECT OPTIMIZATION TECHNIQUE

The direct optimization technique (DOT) is based on a gradient-based method for non-linear minimax optimization.

M. Zhou is with TICRA, Copenhagen, Denmark, and also with the Department of Electrical Engineering, Electromagnetic Systems, Technical University of Denmark, Kgs. Lyngby, Denmark

S.B. Sørensen, E. Jørgensen, and P. Meincke are with TICRA, Copenhagen, Denmark

O.S. Kim and O. Breinbjerg are with the Department of Electrical Engineering, Electromagnetic Systems, Technical University of Denmark, Kgs. Lyngby, Denmark

G. Toso is with the European Space Agency ESA-ESTEC, Noordwijk, The Netherlands



The far-field requirements are specified in a number of far-field stations in the  $u$ - $v$  plane where  $u = \sin \theta \cos \phi$  and  $v = \sin \theta \sin \phi$ . At each iteration, the maximum difference between realized and specified objectives are minimized. The optimization variables are the geometrical parameters of the array elements, e.g. the size and position of the array element. Both co- and cross-polar radiation can be optimized for multiple frequencies, polarizations, and feed illuminations.

To calculate the far-field during the optimization, the Floquet harmonics technique [21, Technique II] is used. It is based on the field equivalence principle and uses the scattering matrices determined from the fundamental Floquet harmonics through the SDMoM formulation. To evaluate the final optimized reflectarray, the more accurate continuous spectrum technique [21, Technique III] is used.

To ensure an accurate and yet efficient calculation of the scattering matrices, higher-order hierarchical Legendre basis functions as described in [22] are used to represent the electric currents on the array elements. These basis functions can be applied to any arbitrarily shaped array elements, and have been demonstrated to yield very accurate results [23]. The versatility of the higher-order hierarchical Legendre basis functions is an important feature in the DOT as it enables the optimization of reflectarrays consisting of non-canonical element shapes, e.g. those reported in [5]–[7].

To utilize the position of the array elements in the DOT, an irregular distribution of element positions is obtained through a mapping from a regular to an irregular grid. Constraints on the mapping must be enforced to ensure the area of the reflectarray surface is efficiently utilized. In [17], the edges of the reflectarray are not constrained. In our case, the edges are kept fixed to avoid any undesired increase in the antenna size.

The mapping used in this work is acquired by adding a distortion to the regular grid. Let us define  $(\alpha, \beta)$  as normalized coordinates in the regular grid such  $|\alpha| \leq 1$  and  $|\beta| \leq 1$ . The new normalized coordinates in the irregular grid is then given by  $(\alpha', \beta') = (\alpha + f_x, \beta + f_y)$ , where

$$f_x(\alpha, \beta) = (\alpha - 1)(\alpha + 1) \sum_{p=0}^P \sum_{q=0}^Q c_{pq} T_p(\alpha) T_q(\beta), \quad (1a)$$

$$f_y(\alpha, \beta) = (\beta - 1)(\beta + 1) \sum_{p=0}^P \sum_{q=0}^Q d_{pq} T_p(\alpha) T_q(\beta). \quad (1b)$$

Herein,  $T_i$  is the Chebyshev polynomial of order  $i$ , and  $c_{pq}$  and  $d_{pq}$  are the distortion coefficients. The factors in front of the summations are boundary conditions that ensure the edges of the reflectarray are kept fixed.

The degree of the distortion is governed by the values of  $c_{pq}$  and  $d_{pq}$  and the order  $i$ . To avoid strong distortions, where array elements overlap, bounds are specified for the values of  $c_{pq}$  and  $d_{pq}$ , and the maximum order of the Chebyshev polynomials should not exceed 4. To achieve strong irregularities, only 2-6 distortion coefficients are needed [19]. The distortion coefficients  $c_{pq}$  and  $d_{pq}$  are included as optimization variables to optimize the positions of the array elements.

Due to the grid distortion, the array elements are now positioned in a non-periodic lattice and the LP approach can no

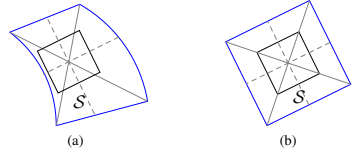


Fig. 1. An example of (a) a distorted cell and (b) its equivalent square cell.

longer be applied. Therefore, a new unit-cell must be defined to approximate locally these non-periodic cells. Let us define the center of the distorted cell as the intersection of the two diagonal lines of the distorted cell. The array element is rotated to orient in parallel of the bisector lines of the two diagonal lines of the distorted cell, and located at the center of the distorted cell. This is illustrated in Fig. 1a, where the diagonal and bisector lines are shown as the solid and dashed lines, respectively. Now, we define an equivalent square cell with the same area as the distorted cell. The equivalent cell has the same center as the distorted cell and is oriented parallel to the bisector lines in the distorted cell. This is shown in Fig. 1b. The equivalent cell is used in the LP computations to calculate the scattering matrices. It was shown in [19] that the accuracy of the LP approach for the analysis reflectarrays with irregularly positioned array elements is very good, even for the cross-polar radiation. Consequently, the LP approach can be used to analyze and optimize reflectarrays with regularly positioned as well as irregularly positioned array elements.

To circumvent the calculation of the scattering matrices of all array elements at each optimization iteration, the scattering matrices are calculated in advance and stored in a look-up table, which is accessed during the optimization. For a given frequency and substrate, the scattering matrices depend on: illumination angles, geometry of the array element, and unit-cell dimensions. For the reflectarrays presented in this paper, we have found that a sufficient accuracy can be obtained by using approximately  $N_{el} = 60$  patch samples,  $N_{inc} = 60$  incident angles, and  $N_{cell} = 50$  different unit-cell sizes, yielding a total of  $N_{total} = N_{el} N_{inc} N_{cell} = 60 \cdot 60 \cdot 50 = 180000$  scattering matrix calculations per frequency. The computation time on a standard laptop computer is approximately one hour. The look-up table can be reused and needs only to be recalculated if another substrate or frequency is used.

For large reflectarrays, where the number of array elements exceeds 10000, the number of optimization variables becomes prohibitively large and the computational burden of the optimization is too high to be run on a standard laptop computer. Thus, to reduce the number of optimization variables, cubic splines have been included in the DOT to represent the sizes of the array elements

$$s(x, y) = \sum_i \sum_j b_{ij} B_i(x) B_j(y). \quad (2)$$

Herein,  $s(x, y)$  describes the sizes of the array elements at coordinates  $(x, y)$ ,  $b_{ij}$  are the spline coefficients, and  $B_i(x)$  and  $B_j(y)$  are the cubic splines. The spline coefficients  $b_{ij}$  are the optimization variables used to optimize the sizes of

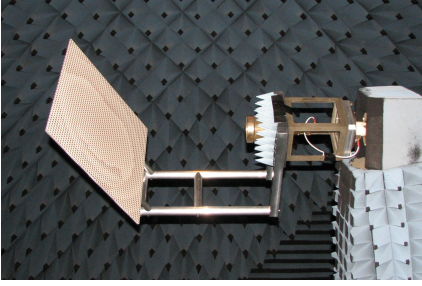


Fig. 2. Sample I in the DTU-ESA Spherical Near-Field Antenna Test Facility.

the array elements. However, the variation of the dimensions of the array element over the reflectarray surface can have discontinuities when the scattered phase is required to jump after a complete  $360^\circ$  cycle. Such discontinuities are hard to represent using splines. As a result, a design obtained using splines is inferior compared to a design where the array elements are directly optimized (unless the number of splines and array elements are equal). It is expected the spline representation can be improved if a periodic mapping between  $s(x, y)$  and the sizes of the array elements is used such the discontinuities can be taken into account. This is subject to ongoing work. Nevertheless, the current spline implementation can be used to generate a design, which can be used as a starting point for the more rigorous optimization where the array elements are directly optimized. In this way, the number of optimization iterations, and hence the overall computation time, that is needed for the rigorous optimization, can be reduced.

For more details on the analysis methods and the look-up table used in the DOT, the reader is referred to [21], [23]–[25].

### III. VALIDATION BY MEASUREMENTS

To validate the DOT, two offset contoured beam reflectarrays that radiate a high-gain beam on an European coverage with cross-polar suppression within the same coverage and sidelobe suppression within a southern African contour have been designed, manufactured, and measured at the DTU-ESA Spherical Near-Field Antenna Test Facility, see Fig. 2. The coverages seen from the longitude  $0^\circ$  geostationary orbital position are shown in Fig. 3. The reflectarray parameters are summarized in Table I with respect to the coordinate system depicted in Fig. 4.

#### A. Reflectarray Samples

The mask layout of the two reflectarray samples are shown in Fig. 5.

The reflectarray in Fig. 5a, sample I, is a regular reflectarray where the array elements are positioned in a regular grid. It is optimized for two orthogonal linear polarizations, V and H, at 10 GHz. The reflectarray in Fig. 5b, sample II, is optimized with the same optimization goals as for sample I, but only

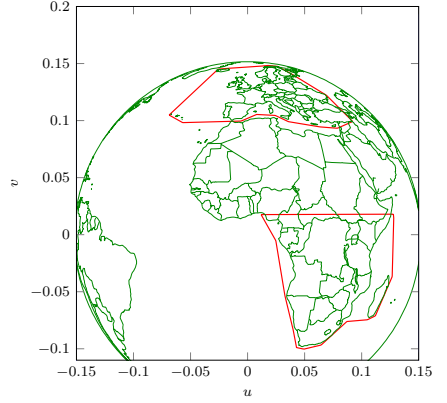


Fig. 3. European and southern African coverages seen from the longitude  $0^\circ$  geostationary orbital position.

TABLE I  
REFLECTARRAY SAMPLE DATA

Frequency	10 GHz
Reflectarray dimension	600 mm $\times$ 600 mm
Number of elements	50 $\times$ 50
Relative permittivity	$\epsilon_r = 3.66$
Loss tangent	$\tan \delta = 0.0037$
Substrate thickness	$h = 0.762$ mm
Feed distance	$d_f = 0.6$ m
Feed offset angle	$\theta^i = 30^\circ$ , $\phi^i = 0^\circ$
Main coverage	European coverage
Cross-polar suppression	European coverage
Sidelobe suppression	Southern African coverage

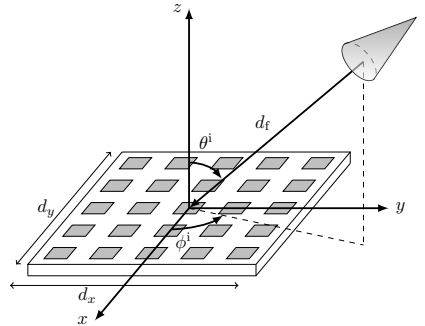
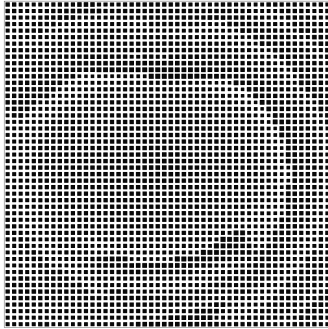


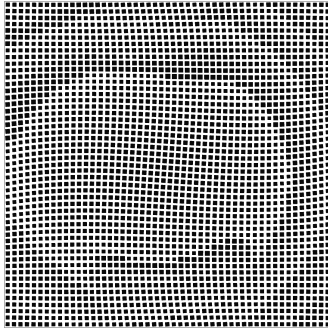
Fig. 4. Reflectarray geometrical parameters.

H-polarization and also at 10 GHz. However, the sample is an irregular design where the array elements are positioned in an irregular grid. For this design, 10 distortion coefficients are included in the optimization.

For both samples, a corrugated horn with a taper of



(a)



(b)

Fig. 5. Reflectarray layout of (a) sample I and (b) sample II.

$-17.5$  dB at  $30^\circ$  at  $10$  GHz is used as feed. The feed has been measured at the DTU-ESA-Spherical Near-Field Test Facility, and its measured pattern is used in the optimization.

The reflectarrays samples were measured for both V- and H-polarizations at a series of frequencies from  $9.6$  GHz to  $10.5$  GHz. For the peak directivity, the measurements have a  $1\sigma$  uncertainty of  $0.05$  dB.

### B. Simulations Versus Measurements

In Fig. 6 and Fig. 7, the radiation patterns of sample I and II for H-polarization at  $10$  GHz are shown. It is seen that both antennas radiate a high-gain beam on the European coverage. For sample I, which is optimized for dual-polarization, a minimum co-polar directivity of  $26.5$  dBi is obtained, whereas sample II, which is optimized for a single polarization, has a minimum directivity of  $27.3$  dBi. The measured cross-polar radiation has been successfully suppressed below  $0$  dBi for both samples. It is also seen for sample II in Fig. 7b that the co-polar radiation on the southern African coverage has been suppressed below  $3$  dBi. This is however not the case for sample I where the co-polar radiation within the southern African coverage is higher than expected. During the design

TABLE II  
MEASURED VERSUS SIMULATED DATA AT  $10$  GHz

Sample I	Peak	Min.	Min.	Min.
	directivity	directivity	XPB	isolation
	(dBi)	(dBi)	(dB)	(dB)
Meas. (H)	28.3	26.5	27.1	17.5
Sim. (H)	28.2	26.6	25.0	17.8
Meas. (V)	27.9	26.5	27.7	18.4
Sim. (V)	27.9	26.5	25.5	17.2
Sample II	Peak	Min.	Min.	Min.
	directivity	directivity	XPB	isolation
	(dBi)	(dBi)	(dB)	(dB)
Meas. (H)	29.2	27.3	27.2	24.3
Sim. (H)	29.2	27.3	27.8	27.2
Meas. (V)	29.4	27.1	24.5	20.2
Sim. (V)	29.4	27.1	21.0	20.5

of sample I, the expected isolation level was above  $25$  dB, but the measurements showed an isolation level around  $17$  dB. The source of error was found to be an inadequate number of basis functions used in the SDMoM to characterize the electric currents on the patches during the design process. The analysis was not entirely converged in the entire forward hemisphere and resulted in a non-optimum design. By increasing the number of basis functions, we obtain the results shown in Fig. 6.

A comparison of the solid and dotted lines, in Fig. 6 and 7, shows an excellent agreement between simulations and measurements, where the high gain curves practically coincide. Also the accuracy for the lower levels is very good. This is the case for both samples I and II. The performance of the samples are summarized in Table II. It is seen that the peak and minimum directivity within the European coverage are perfectly predicted for both samples in both polarizations. Even for the XPB and the isolations level, which are approximately  $30$  dB below the co-polar peak, the accuracy is good. The accuracy for the other measured frequencies is also very good; in all cases the maximum difference in the minimum co-polar directivity is  $0.1$  dB.

These excellent agreements between simulations and measurements for the presented reflectarrays are similar to those obtained for conventional shaped reflector antennas, and clearly demonstrates the accuracy of the proposed DOT.

### IV. DESIGN OF LARGE CONTOURED BEAM REFLECTARRAY

To demonstrate the DOT's ability to design electrically large reflectarrays, an offset  $1.5 \times 1.5$  m<sup>2</sup> contoured beam reflectarray that radiate a high-gain beam on the European coverage in the frequency range  $9.5$ – $10.5$  GHz is designed. At the center frequency  $10$  GHz, the dimension of the reflectarray corresponds to  $50 \times 50 \lambda_0^2$ , with  $\lambda_0$  being the free-space wavelength. It is optimized for both V- and H-polarizations including cross-polar suppressions within the European coverage. A linearly polarized Gaussian beam with a taper of  $-25$  dB at  $30^\circ$  is used as feed and square patches positioned in a regular grid are used as array elements. A scattering matrix look-up table for frequencies  $f = 9.5, 10, 10.5$  GHz has been calculated. The geometrical parameters are summarized in Table III.

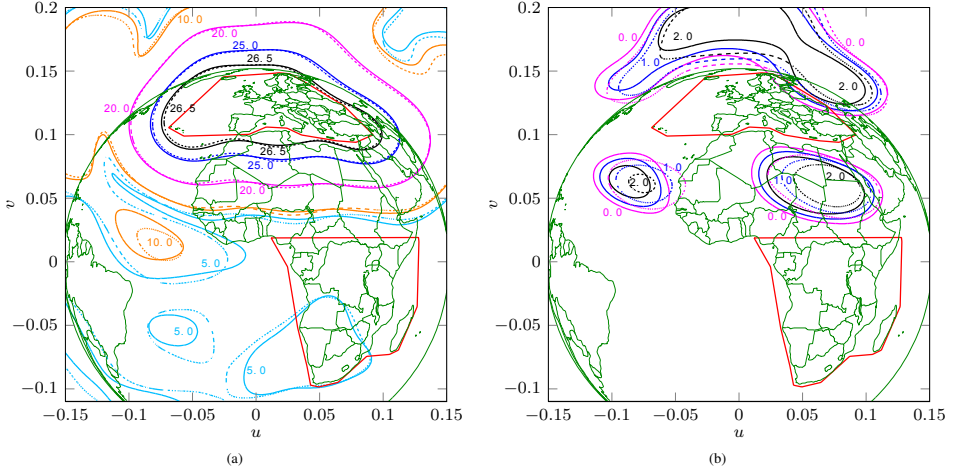


Fig. 6. Simulated (solid) and measured (dotted) radiation patterns of sample I for H-polarization at 10 GHz, (a) co-polar pattern and (b) cross-polar pattern.

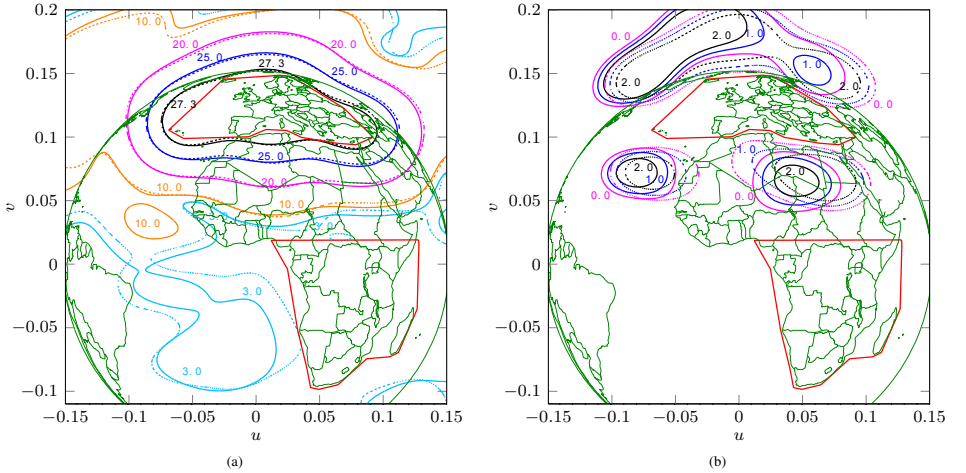


Fig. 7. Simulated (solid) and measured (dotted) radiation patterns of sample II for H-polarization at 10 GHz, (a) co-polar pattern and (b) cross-polar pattern.

Initially, a reflectarray optimized using  $50 \times 50$  splines is designed. A minimum co-polar directivity of 27.5 dBi within the European coverage is achieved in the specified frequency range for both polarizations. This design is subsequently used as the starting point for the final design where all patches are directly optimized. The final layout of the reflectarray is shown in Fig. 8 and the performance summarized in Table IV. It is seen that the minimum directivity is above 28.3 dBi in

the 9.5–10.5 GHz frequency range for both polarizations, and that the minimum XPD is around 27.0 dB. It is expected that the XPD levels can be improved if a reduction in the minimum directivity is allowed. At 9 GHz and 11 GHz, which are outside of the specified frequency range, the minimum directivity drops several dBs, thus demonstrating that the reflectarray has been successfully optimized to operate in the specified frequency range. Compared to the two previous reflectarray

TABLE III  
REFLECTARRAY DATA

Frequency	9.5 – 10.5 GHz
Reflectarray dimension	1.5 m × 1.5 m
Number of elements	110 × 110
Relative permittivity	$\epsilon_r = 3.66$
Loss tangent	$\tan \delta = 0.0037$
Substrate thickness	$h = 1.524$ mm
Feed distance	$d_f = 1.5$ m
Feed offset angle	$\theta^i = 30^\circ$ , $\phi^i = 0^\circ$
Main coverage	European coverage
Cross-polar suppression	European coverage

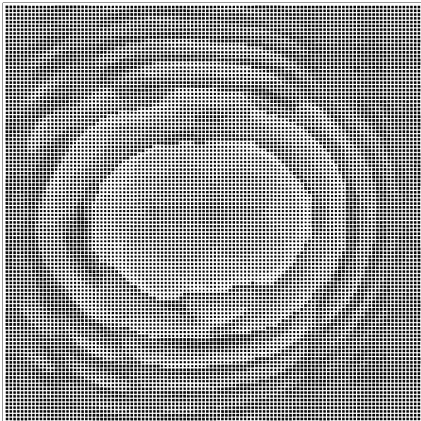


Fig. 8. Reflectarray layout of  $50 \times 50 \lambda_0^2$  design.

samples, the minimum directivity is improved by less than 2 dB, even though the antenna area is more than 4 times larger. This is expected as this design is a multi-frequency design, and that the minimum directivity for contoured beam antenna scales differently with respect to the antenna size than pencil beam antennas [26].

Due to the large electrical size of the reflectarray, the far-field requirements are specified in many far-field stations within the coverage [27]. With the cross-polar suppression, dual polarization, and three frequencies included in the optimization, the total number of far-field samples in the optimization is approximately 8200. This, together with  $110 \times 110$  optimization variables, is rather demanding, resulting in an overall optimization time slightly below 20 hours using an 1.86 GHz 8 core Intel Xeon processor computer. Compared to POS for the design of shaped reflectors, the overall computation time is still high, and techniques to reduce this is currently being investigated.

Although square patches are used in this design, a 10% bandwidth is still achieved. However, it is expected that an improved performance can be obtained by using more advanced array elements e.g. rectangular patches or those reported in [6].

## V. CONCLUSION AND ON-GOING WORK

An accurate and efficient direct optimization technique (DOT) for the design of contoured beam reflectarrays is presented. It is based on the Spectral Domain Method of Moments, Local Periodicity approach, and a minimax optimization algorithm. Contrary to the conventional phase-only optimization techniques, the geometrical parameters of the array elements are directly optimized to fulfill the contoured beam requirements. To ensure an accurate and efficient optimization procedure, higher-order hierarchical Legendre basis functions are used together with a fast yet accurate far-field calculation technique. The DOT can be used to design reflectarrays based on a regular grid as well as an irregular grid. Both co- and cross-polar radiation can be optimized for multiple frequencies, polarizations, and feed illuminations.

To show the accuracy of the DOT, two offset contoured beam reflectarrays that radiate a high-gain beam on an European coverage have been designed, manufactured, and measured at the DTU-ESA Spherical Near-Field Antenna Test Facility. Excellent agreements are obtained for the simulated and measured patterns, showing accuracies that are comparable to those obtained for shaped reflectors. To demonstrate the DOT's ability to optimize electrically large reflectarrays, a  $50 \times 50$  square wavelengths dual polarized contoured beam reflectarrays has been designed.

Several further developments of the DOT are on-going and worth mentioning. First, the orientation of the array elements can be added as optimization variables and exploited as extra degrees of freedom with the aim of improving the performance. This can also be used for the design of circularly polarized reflectarrays. Second, only square patches on a single layer substrate with rectangular rim are presented in this work. The DOT is applicable for more advanced and broadband elements, but will also allow multi-layer configurations with circular or elliptical rim. Finally, techniques for reducing the overall optimization time are currently being investigated.

## ACKNOWLEDGMENTS

This work is supported by the European Space Agency (ESA) within the ESTEC contract No.4000101041, and Dr. S. Pivnenko, Technical University of Denmark, is acknowledged for the accurate measurements of the reflectarray samples.

## ACKNOWLEDGMENT

## REFERENCES

- [1] J. A. Encinar, "Recent advances in reflectarray antennas," in *Proc. EuCAP*, Barcelona, Spain, 2010.
- [2] H. Legay, D. Bresciani, E. Girard, R. Chiniard, E. Labiole, O. Vendier, and G. Caille, "Recent developments on reflectarray antennas at Thales Alenia Space," in *Proc. EuCAP*, Berlin, Germany, 2009.
- [3] A. Roederer, "Reflectarray antennas," in *Proc. EuCAP*, Berlin, Germany, 2009.
- [4] D. M. Pozar, S. D. Targonski, and H. D. Syrigos, "Design of millimeter wave microstrip reflectarrays," *IEEE Trans. Antennas Propag.*, vol. 45, no. 2, pp. 287–296, 1997.
- [5] M. E. Białkowski and K. H. Sayidmarie, "Investigations into phase characteristics of a single-layer reflectarray employing patch or ring elements of variable size," *IEEE Trans. Antennas Propag.*, vol. 56, no. 11, pp. 3366–3372, 2008.

TABLE IV  
PERFORMANCE OF  $50 \times 50 \lambda_0^2$  REFLECTARRAY DESIGN

Frequency (GHz)	H-polarization		V-polarization	
	Minimum Directivity (dBi)	Minimum XPD (dB)	Minimum Directivity(dBi)	Minimum XPD (dB)
9.0	23.4	25.2	22.8	18.8
9.5	28.7	27.0	28.4	26.7
10.0	28.7	27.8	28.3	28.0
10.5	28.5	28.0	28.3	27.5
11.0	23.5	23.1	25.0	27.1

- [6] L. Moustafa, R. Gillard, F. Peris, R. Loison, H. Legay, and E. Girard, "The phoenix cell: a new reflectarray cell with large bandwidth and rebirth capabilities," *IEEE Antennas Wireless Propag. Lett.*, vol. 10, pp. 71–74, 2011.
- [7] M. Bozzi, S. Germani, and L. Perregrini, "Performance comparison of different element shapes used in printed reflectarrays," *IEEE Antennas Wireless Propag. Lett.*, vol. 2, no. 1, pp. 219–222, 2003.
- [8] J. Huang and R. J. Pogorzelski, "A Ka-band microstrip reflectarray with elements having variable rotation angles," *IEEE Trans. Antennas Propag.*, vol. 46, no. 5, pp. 650–656, 1998.
- [9] D. Kurup, M. Himdi, and A. Rydberg, "Design of an unequally spaced reflectarray," *IEEE Antennas Wireless Propag. Lett.*, vol. 2, pp. 33–35, 2003.
- [10] A. Capozzoli, C. Curcio, E. Iavazzo, A. Lisenò, M. Migliorelli, and G. Toso, "Phase-only synthesis of a-periodic reflectarrays," in *Proc. EuCAP*, Rome, Italy, 2011, pp. 987–991.
- [11] J. A. Encinar, M. Arrebola, and G. Toso, "A parabolic reflectarray for a bandwidth improved contoured beam coverage," in *Proc. EuCAP*, Edinburgh, UK, 2007.
- [12] J. A. Encinar and J. A. Zornoza, "Three-layer printed reflectarrays for contoured beam space applications," *IEEE Trans. Antennas Propag.*, vol. 52, no. 5, pp. 1138–1148, 2004.
- [13] J. A. Encinar, L. S. Datashvili, J. A. Zornoza, M. Arrebola, M. Sierra-Castaner, J. L. Besada-Sanmartin, H. Baier, and H. Legay, "Dual-polarization dual-coverage reflectarray for space applications," *IEEE Trans. Antennas Propag.*, vol. 54, no. 10, pp. 2827–2837, 2006.
- [14] H. Legay, D. Bresciani, E. Labiole, R. Chiniard, E. Girard, G. Caille, L. Marnat, D. Calas, R. Gillard, and G. Toso, "A 1.3 m earth deck reflectarray for a Ku band contoured beam antenna," in *Proc. 33rd ESA Antenna Workshop*, Noordwijk, The Netherlands, 2011.
- [15] J. A. Encinar, M. Arrebola, L. D. L. Fuente, and G. Toso, "A transmit-receive reflectarray antenna for direct broadcast satellite applications," *IEEE Trans. Antennas Propag.*, vol. 59, no. 9, pp. 3255–3264, 2011.
- [16] O. M. Bucci, A. Capozzoli, G. D'Elia, P. Maietta, and S. Russo, "An advanced reflectarray design technique," in *Proc. 28th ESA Antenna Workshop*, Noordwijk, The Netherlands, 2005.
- [17] A. Capozzoli, C. Curcio, A. Lisenò, M. Migliorelli, and G. Toso, "Power pattern synthesis of advanced flat aperiodic reflectarrays," in *Proc. 33th ESA Antenna Workshop*, Noordwijk, The Netherlands, 2011.
- [18] "DTU-ESA Spherical Near-Field Antenna Test Facility," <http://www.dtu.dk/centre/ems/English/research/facilities.aspx>.
- [19] M. Zhou, S. B. Sørensen, P. Meincke, E. Jørgensen, O. S. Kim, O. Breinbjerg, and G. Toso, "Design and analysis of printed reflectarrays with irregularly positioned array elements," in *Proc. EuCAP*, Prague, Czech Republic, 2012.
- [20] —, "Design of dual-polarized contoured beam reflectarrays with cross-polar and sidelobe suppressions," in *Proc. IEEE AP-S Int. Symp.*, Chicago, Illinois, USA, 2012.
- [21] M. Zhou, S. B. Sørensen, E. Jørgensen, P. Meincke, O. S. Kim, and O. Breinbjerg, "An accurate technique for calculation of radiation from printed reflectarrays," *IEEE Antennas Wireless Propag. Lett.*, vol. 10, pp. 1081–1084, 2011.
- [22] E. Jørgensen, J. Volakis, P. Meincke, and O. Breinbjerg, "Higher order hierarchical Legendre basis functions for electromagnetic modeling," *IEEE Trans. Antennas Propag.*, vol. 52, no. 11, pp. 2985–2995, 2004.
- [23] M. Zhou, E. Jørgensen, O. S. Kim, S. B. Sørensen, P. Meincke, and O. Breinbjerg, "Accurate and efficient analysis of printed reflectarrays with arbitrary elements using higher-order hierarchical Legendre basis functions," *IEEE Antennas Wireless Propag. Lett.*, vol. 11, pp. 814–817, 2012.
- [24] M. Zhou, S. B. Sørensen, E. Jørgensen, P. Meincke, O. S. Kim, and O. Breinbjerg, "Direct optimization of printed reflectarrays for contoured beam satellite antennas applications," *Submitted to IEEE Trans. Antennas Propag.*, 2012.
- [25] M. Zhou, S. B. Sørensen, E. Jørgensen, P. Meincke, O. S. Kim, O. Breinbjerg, and G. Toso, "Generalized direct optimization technique for printed reflectarrays," *In writing*, 2012.
- [26] S. B. Sørensen, R. Jørgensen, and K. Pontoppidan, "Synthesis of the aperture field for a contoured beam," in *Proc. 7th ICAP*, York, United Kingdom, 1991.
- [27] *POS, User's Manual*. TICRA Engineering Consultants, 2011.



## BIBLIOGRAPHY

---

- [1] J. Huang and J. A. Encinar, *Reflectarray Antennas*. IEEE Press, 2008.
- [2] J. A. Encinar, “Recent advances in reflectarray antennas,” in *Proc. EuCAP*, Barcelona, Spain, 2010.
- [3] H. Legay, D. Bresciani, E. Girard, R. Chiniard, E. Labiole, O. Vendier, and G. Caille, “Recent developments on reflectarray antennas at Thales Alenia Space,” in *Proc. EuCAP*, Berlin, Germany, 2009.
- [4] A. Roederer, “Reflectarray antennas,” in *Proc. EuCAP*, Berlin, Germany, 2009.
- [5] D. Berry, R. Malech, and W. Kennedy, “The reflectarray antenna,” *IEEE Trans. Antennas Propag.*, vol. 11, no. 6, pp. 645–651, 1963.
- [6] C. S. Malagisi, “Microstrip disc element reflect array,” *Eascon '78*, pp. 186–192, 1978.
- [7] R. Munson, H. Haddad, and J. Hanlen, “Microstrip reflectarray for satellite communication and radar cross-section enhancement and reduction,” *US Patent 4,684,952*, 1987.
- [8] J. Huang, “Microstrip reflectarray,” in *Proc. IEEE AP-S Int. Symp.*, vol. 2, London, Ontario, Canada, 1991, pp. 612–615.
- [9] D. C. Chang and M. C. Huang, “Microstrip reflectarray antenna with offset feed,” *Electron. Lett.*, vol. 28, no. 16, pp. 1489–1491, 1992.
- [10] —, “Multiple-polarization microstrip reflectarray antenna with high efficiency and low cross-polarization,” *IEEE Trans. Antennas Propag.*, vol. 43, no. 8, pp. 829–834, 1995.
- [11] Y. Zhuang, K. L. Wu, C. Wu, and J. Litva, “Microstrip reflectarrays: Full-wave analysis and design scheme,” in *Proc. IEEE AP-S Int. Symp.*, Ann Arbor, Michigan, USA, 1993.
- [12] —, “Modelling studies of microstrip reflectarrays,” *IEE Proceedings - Microwaves, Antennas and Propagation*, vol. 142, no. 1, pp. 78–80, 1995.
- [13] R. D. Javor, X.-D. Wu, and K. Chang, “Beam steering of a microstrip flat reflectarray antenna,” in *Proc. IEEE AP-S Int. Symp.*, Seattle, Washington, USA, 1994.



- [14] —, “Design and performance of a microstrip reflectarray antenna,” *IEEE Trans. Antennas Propag.*, vol. 43, no. 9, pp. 932–939, 1995.
- [15] D. M. Pozar and T. A. Metzler, “Analysis of a reflectarray antenna using microstrip patches of variable size,” *Electron. Lett.*, vol. 29, no. 8, pp. 657–658, 1993.
- [16] S. D. Targonski and D. M. Pozar, “Analysis and design of a microstrip reflectarray using patches of variable size,” in *Proc. IEEE AP-S Int. Symp.*, Seattle, Washington, USA, 1994.
- [17] D. M. Pozar, S. D. Targonski, and H. D. Syrigos, “Design of millimeter wave microstrip reflectarrays,” *IEEE Trans. Antennas Propag.*, vol. 45, no. 2, pp. 287–296, 1997.
- [18] D. Pilz and W. Menzel, “Full wave analysis of a planar reflector antenna,” *Proceedings of 1997 Asia-Pacific Microwave Conference*, vol. 1, pp. 225–227 vol.1, 1997.
- [19] K. Y. Sze and L. Shafal, “Analysis of phase variation due to varying patch length in a microstrip reflectarray,” in *Proc. IEEE AP-S Int. Symp.*, Atlanta, Georgia, USA, 1998.
- [20] Y. J. Guo and S. K. Barton, “Phase correcting zonal reflector incorporating rings,” *IEEE Trans. Antennas Propag.*, vol. 43, no. 4, pp. 350–355, 1995.
- [21] D. M. Pozar and S. D. Targonski, “A microstrip reflectarray using crossed dipoles,” in *Proc. IEEE AP-S Int. Symp.*, Atlanta, Georgia, USA, 1998.
- [22] D. Cadoret, A. Laisne, R. Gillard, L. Le Coq, and H. Legay, “Design and measurement of new reflectarray antenna using microstrip patches loaded with slot,” *Electron. Lett.*, vol. 41, no. 11, pp. 623–624, 2005.
- [23] J. Huang and R. J. Pogorzelski, “A Ka-band microstrip reflectarray with elements having variable rotation angles,” *IEEE Trans. Antennas Propag.*, vol. 46, no. 5, pp. 650–656, 1998.
- [24] C. Han and K. Chang, “Ka-band reflectarray using ring elements,” *Electron. Lett.*, vol. 39, no. 6, pp. 491–493, 2003.
- [25] B. Strassner, C. Han, and K. Chang, “Circularly polarized reflectarray with microstrip ring elements having variable rotation angles,” *IEEE Trans. Antennas Propag.*, vol. 52, no. 4, pp. 1122–1125, 2004.
- [26] C. Han, J. Huang, and K. Chang, “Cassegrain offset subreflector-fed X/Ka dual-band reflectarray with thin membranes,” *IEEE Trans. Antennas Propag.*, vol. 54, no. 10, pp. 2838–2844, 2006.
- [27] —, “A high efficiency offset-fed X/Ka-dual-band reflectarray using thin membranes,” *IEEE Trans. Antennas Propag.*, vol. 53, no. 9, pp. 2792–2798, 2005.
- [28] J. A. Encinar, “Design of a dual frequency reflectarray using microstrip stacked patches of variable size,” *Electron. Lett.*, vol. 32, no. 12, pp. 1049–1050, 1996.

- [29] C. Han, C. Rodenbeck, J. Huang, and K. Chang, "A C/Ka dual frequency dual layer circularly polarized reflectarray antenna with microstrip ring elements," *IEEE Trans. Antennas Propag.*, vol. 52, no. 11, pp. 2871–2876, 2004.
- [30] S.-H. Hsu, C. Han, J. Huang, and K. Chang, "An offset linear-array-fed Ku/Ka dual-band reflectarray for planet cloud/precipitation radar," *IEEE Trans. Antennas Propag.*, vol. 55, no. 11 2, pp. 3114–3122, 2007.
- [31] M. R. Chaharmir, J. Shaker, and H. Legay, "Dual-band Ka/X reflectarray with broadband loop elements," *IET Microw. Antennas Propag.*, vol. 4, no. 2, pp. 225–231, 2010.
- [32] J. Shaker, C. Pike, and M. Cuhaci, "A dual orthogonal cassegrain flat reflector for ka-band application," *Microwave Opt. Technol. Lett.*, vol. 24, no. 1, pp. 7–11, 2000.
- [33] S.-W. Oh, J.-K. Lee, J. Huang, and K. Chang, "A six-band reflectarray antenna," in *Proc. IEEE AP-S Int. Symp.*, Charleston, South Carolina, USA, Jun. 2009.
- [34] J. Shaker and M. Cuhaci, "Multi-band, multi-polarisation reflector-reflectarray antenna with simplified feed system and mutually independent radiation patterns," *Proc. Inst. Elect. Eng. Microw., Antennas Propag.*, vol. 152, no. 2, pp. 97–101, 2005.
- [35] Z.-H. Wu, W.-X. Zhang, Z.-G. Liu, and W. Shen, "A dual-layered wideband microstrip reflectarray antenna with variable polarization," *Microwave Opt. Technol. Lett.*, vol. 48, no. 7, pp. 1429–1432, 2006.
- [36] D. M. Pozar, S. D. Targonski, and R. Pokuls, "A shaped-beam microstrip patch reflectarray," *IEEE Trans. Antennas Propag.*, vol. 47, no. 7, pp. 1167–1173, 1999.
- [37] J. A. Encinar and J. A. Zornoza, "Three-layer printed reflectarrays for contoured beam space applications," *IEEE Trans. Antennas Propag.*, vol. 52, no. 5, pp. 1138–1148, 2004.
- [38] J. A. Encinar, L. S. Datashvili, J. A. Zornoza, M. Arrebola, M. Sierra-Castaner, J. L. Besada-Sanmartin, H. Baier, and H. Legay, "Dual-polarization dual-coverage reflectarray for space applications," *IEEE Trans. Antennas Propag.*, vol. 54, no. 10, pp. 2827–2837, 2006.
- [39] E. Carrasco, M. Arrebola, J. A. Encinar, and M. Barba, "Demonstration of a shaped beam reflectarray using aperture-coupled delay lines for LMDS central station antenna," *IEEE Trans. Antennas Propag.*, vol. 56, no. 10, pp. 3103–3111, 2008.
- [40] J. A. Encinar, M. Arrebola, L. D. L. Fuente, and G. Toso, "A transmit-receive reflectarray antenna for direct broadcast satellite applications," *IEEE Trans. Antennas Propag.*, vol. 59, no. 9, pp. 3255–3264, 2011.
- [41] H. Legay, D. Bresciani, E. Labiole, R. Chiniard, E. Girard, G. Caille, L. Marnat, D. Calas, R. Gillard, and G. Toso, "A 1.3 m earth deck reflectarray for a Ku band contoured beam antenna," in *Proc. 33rd ESA Antenna Workshop*, Noordwijk, The Netherlands, 2011.

- [42] M. Arrebola, J. A. Encinar, and M. Barba, "Multifed printed reflectarray with three simultaneous shaped beams for LMDS central station antenna," *IEEE Trans. Antennas Propag.*, vol. 56, no. 6, pp. 1518–1527, 2008.
- [43] P. Nayeri, F. Yang, and A. Elsherbeni, "Design and experiment of a single-feed quad-beam reflectarray antenna," *IEEE Trans. Antennas Propag.*, vol. 60, no. 2, pp. 1166–1171, 2012.
- [44] M. E. Bialkowski, A. W. Robinson, and H. J. Song, "Design, development, and testing of x-band amplifying reflectarrays," *IEEE Trans. Antennas Propag.*, vol. 50, no. 8, pp. 1065–1076, 2002.
- [45] S. V. Hum, M. Okoniewski, and R. J. Davies, "Realizing an electronically tunable reflectarray using varactor diode-tuned elements," *IEEE Microw. Wireless Compon. Lett.*, vol. 15, no. 6, pp. 422–424, 2005.
- [46] —, "Modeling and design of electronically tunable reflectarrays," *IEEE Trans. Antennas Propag.*, vol. 55, no. 8, pp. 2200–2210, 2007.
- [47] J. P. Gianvittorio and Y. Rahmat-Samii, "Reconfigurable patch antennas for steerable reflectarray applications," *IEEE Trans. Antennas Propag.*, vol. 54, no. 5, pp. 1388–1392, 2006.
- [48] M. Riel and J. J. Laurin, "Design of an electronically beam scanning reflectarray using aperture-coupled elements," *IEEE Trans. Antennas Propag.*, vol. 55, no. 5, pp. 1260–1266, 2007.
- [49] L. Cabria, J. A. Garcia, and A. Mediavilla, "Controlling the scattered field in a reflectarray element using a novel technique," *Microwave Opt. Technol. Lett.*, vol. 48, no. 4, pp. 808–810, 2006.
- [50] H. Legay, E. Girard, R. Chiniard, D. Bresciani, G. Caille, E. Labiole, L. Schreider, and O. Vendier, "Antenna with selectable or reconfigurable sub-reflectarrays for flexible coverage," in *Proc. 32nd ESA Antenna Workshop*, Noordwijk, The Netherlands, 2010.
- [51] H. Legay, Y. Cailloce, O. Vendier, G. Caille, J. Perruisseau-Carrier, M. Lathi, J. P. Polizzi, U. Oestermann, P. Pons, and N. Raveu, "Satellite antennas based on MEMS tunable reflectarrays," in *Proc. EuCAP*, Edinburgh, UK, 2007.
- [52] J. Perruisseau-Carrier, "Dual-polarized and polarization-flexible reflective cells with dynamic phase control," *IEEE Trans. Antennas Propag.*, vol. 58, no. 5, pp. 1494–1502, 2010.
- [53] H. Rajagopalan, Y. Rahmat-Samii, and W. Imbriale, "RF MEMS actuated reconfigurable reflectarray patch-slot element," *IEEE Trans. Antennas Propag.*, vol. 56, no. 12, pp. 3689–3699, 2008.
- [54] D. Pilz and W. Menzel, "Folded reflectarray antenna," *Electron. Lett.*, vol. 34, no. 9, pp. 832–833, 1998.

- [55] —, “Printed millimeter-wave reflectarrays,” *Annales des Telecommunications*, vol. 56, pp. 51–60, 2001.
- [56] W. Menzel, D. Pilz, and M. Al-Tikriti, “Millimeter-wave folded reflector antennas with high gain, low loss, and low profile,” *IEEE Antennas Propag. Mag.*, vol. 44, no. 3, pp. 24–29, 2002.
- [57] J. Zornoza, R. Leberer, J. Encinar, and W. Menzel, “Folded multilayer microstrip reflectarray with shaped pattern,” *IEEE Trans. Antennas Propag.*, vol. 54, no. 2, pp. 510 – 518, 2006.
- [58] J. Huang and A. Fera, “A 1-m x-band inflatable reflectarray antenna,” *Microwave Opt. Technol. Lett.*, vol. 20, no. 2, pp. 97–99, 1999.
- [59] —, “Inflatable microstrip reflectarray antennas at X and Ka-band frequencies,” in *Proc. IEEE AP-S Int. Symp.*, Orlando, Florida, USA, 1999.
- [60] J. Huang, “Bandwidth study of microstrip reflectarray and a novel phased reflectarray concept,” in *Proc. IEEE AP-S Int. Symp.*, Newport Beach, California, 1995.
- [61] D. M. Pozar, “Bandwidth of reflectarrays,” *Electron. Lett.*, vol. 39, no. 21, pp. 1490–1491, 2003.
- [62] J. A. Encinar, “Design of two-layer printed reflectarrays using patches of variable size,” *IEEE Trans. Antennas Propag.*, vol. 49, no. 10, pp. 1403–1410, 2001.
- [63] J. A. Encinar and J. A. Zornoza, “Broadband design of three-layer printed reflectarrays,” *IEEE Trans. Antennas Propag.*, vol. 51, no. 7, pp. 1662–1664, 2003.
- [64] M. E. Bialkowski and K. H. Sayidmarie, “Investigations into phase characteristics of a single-layer reflectarray employing patch or ring elements of variable size,” *IEEE Trans. Antennas Propag.*, vol. 56, no. 11, pp. 3366–3372, 2008.
- [65] M. R. Chaharmir, J. Shaker, M. Cuhaci, and A. Ittipiboon, “Broadband reflectarray antenna with double cross loops,” *Electron. Lett.*, vol. 42, no. 2, pp. 65–66, 2006.
- [66] —, “A broadband reflectarray antenna with double square rings,” *Microwave Opt. Technol. Lett.*, vol. 48, no. 7, pp. 1317–1324, 2006.
- [67] M. R. Chaharmir, J. Shaker, and H. Legay, “Broadband design of a single layer large reflectarray using multi cross loop elements,” *IEEE Trans. Antennas Propag.*, vol. 57, no. 10 2, pp. 3363–3366, 2009.
- [68] M. R. Chaharmir, J. Shaker, and N. Gagnon, “Broadband dual-band linear orthogonal polarisation reflectarray,” *Electron. Lett.*, vol. 45, no. 1, pp. 13–14, 2009.
- [69] M. R. Chaharmir and J. Shaker, “Broadband reflectarray with combination of cross and rectangle loop elements,” *Electron. Lett.*, vol. 44, no. 11, pp. 658–659, 2008.

- [70] H. Li, B. Z. Wang, W. Shao, and H. Li, "Novel broadband reflectarray antenna with compound-cross-loop elements for millimeter-wave application," *J. Electro-mag. Waves Appl.*, vol. 21, no. 10, pp. 1333–1340, 2007.
- [71] H. Hasani, M. Kamyab, and A. Mirkamali, "Broadband reflectarray antenna incorporating disk elements with attached phase-delay lines," *IEEE Antennas Wireless Propag. Lett.*, vol. PP, no. 99, 2010.
- [72] A. W. Robinson, M. E. Bialkowski, and H. J. Song, "A passive reflect array with dual-feed microstrip patch elements," *Microwave Opt. Technol. Lett.*, vol. 23, no. 5, pp. 295–299, 1999.
- [73] E. Carrasco, M. Barba, and J. A. Encinar, "Aperture-coupled reflectarray element with wide range of phase delay," *Electron. Lett.*, vol. 42, no. 12, pp. 667–668, 2006.
- [74] —, "Reflectarray element based on aperture-coupled patches with slots and lines of variable length," *IEEE Trans. Antennas Propag.*, vol. 55, no. 3 2, pp. 820–825, 2007.
- [75] D. M. Pozar, "Wideband reflectarrays using artificial impedance surfaces," *Electron. Lett.*, vol. 43, no. 3, pp. 148–149, 2007.
- [76] G. Zhao, Y. Jiao, F. Zhang, and F. Zhang, "A subwavelength element for broadband circularly polarized reflectarrays," *IEEE Antennas Wireless Propag. Lett.*, vol. 9, pp. 330–333, 2010.
- [77] P. Nayeri, F. Yang, and A. Elsherbeni, "Broadband reflectarray antennas using double-layer subwavelength patch elements," *IEEE Antennas Wireless Propag. Lett.*, vol. 9, pp. 1139–1142, 2010.
- [78] P. Nayeri, F. Yang, and A. Z. Elsherbeni, "Bandwidth improvement of reflectarray antennas using closely spaced elements," *Progr. Electromagn. Res. C*, vol. 18, pp. 19–29, 2011.
- [79] M. Bozzi, S. Germani, and L. Perregrini, "Performance comparison of different element shapes used in printed reflectarrays," *IEEE Antennas Wireless Propag. Lett.*, vol. 2, no. 1, pp. 219–222, 2003.
- [80] F. Zubir and M. K. A. Rahim, "Simulated fractals shape for unit cell reflectarray," *2009 Asia-Pacific Microwave Conference*, pp. 583–586, 2009.
- [81] L. Moustafa, R. Gillard, F. Peris, R. Loison, H. Legay, and E. Girard, "The phoenix cell: a new reflectarray cell with large bandwidth and rebirth capabilities," *IEEE Antennas Wireless Propag. Lett.*, vol. 10, pp. 71–74, 2011.
- [82] L. Li, Q. Chen, Q. Yuan, K. Sawaya, T. Maruyama, T. Furuno, and S. Uebayashi, "Novel broadband planar reflectarray with parasitic dipoles for wireless communication applications," *IEEE Antennas Wireless Propag. Lett.*, vol. 8, pp. 881–885, 2009.

- [83] Q.-Y. Li, Y.-C. Jiao, and G. Zhao, "A novel microstrip rectangular-patch/ring-combination reflectarray element and its application," *IEEE Antennas Wireless Propag. Lett.*, vol. 8, pp. 1119–1122, 2009.
- [84] P. De Vita, A. Freni, G. L. Dassano, P. Pirinoli, and R. E. Zich, "Broadband element for high-gain single-layer printed reflectarray antenna," *Electron. Lett.*, vol. 43, no. 23, pp. 1247–1249, 2007.
- [85] E. Carrasco, J. A. Encinar, and M. Barba, "Bandwidth improvement in large reflectarrays by using true-time delay," *IEEE Trans. Antennas Propag.*, vol. 56, no. 8, pp. 2496–2503, 2008.
- [86] J. A. Encinar, M. Arrebola, and G. Toso, "A parabolic reflectarray for a bandwidth improved contoured beam coverage," in *Proc. EuCAP*, Edinburgh, UK, 2007.
- [87] M. R. Chaharmir, J. Shaker, N. Gagnon, and D. Lee, "Design of broadband, single layer dual-band large reflectarray using multi open loop elements," *IEEE Trans. Antennas Propag.*, vol. 58, no. 9, pp. 2875 – 2883, 2010.
- [88] D. Kurup, M. Himdi, and A. Rydberg, "Design of an unequally spaced reflectarray," *IEEE Antennas Wireless Propag. Lett.*, vol. 2, pp. 33–35, 2003.
- [89] A. Capozzoli, C. Curcio, E. Iavazzo, A. Lisenò, M. Migliorelli, and G. Toso, "Phase-only synthesis of a-periodic reflectarrays," in *Proc. EuCAP*, Rome, Italy, 2011.
- [90] D. Pozar and D. Schaubert, "Analysis of an infinite array of rectangular microstrip patches with idealized probe feeds," *IEEE Trans. Antennas Propag.*, vol. 32, no. 10, pp. 1101–1107, 1984.
- [91] D. M. Pozar, "Analysis of an infinite phased array of aperture coupled microstrip patches," *IEEE Trans. Antennas Propag.*, vol. 37, no. 4, pp. 418–425, 1989.
- [92] R. Mittra, C. H. Chan, and T. Cwik, "Techniques for analyzing frequency selective surfaces – a review," *Proc. IEEE*, vol. 76, no. 12, pp. 1593–1615, 1988.
- [93] "DTU-ESA Spherical Near-Field Antenna Test Facility," <http://www.dtu.dk/centre/ems/English/research/facilities.aspx>.
- [94] K. Pontoppidan, Ed., *GRASP, Technical Description*. TICRA Engineering Consultants, 2008.
- [95] *POS, User's Manual*. TICRA Engineering Consultants, 2011.
- [96] F. Venneri, G. Angiulli, and G. Di Massa, "Design of microstrip reflect array using data from isolated patch analysis," *Microwave Opt. Technol. Lett.*, vol. 34, no. 6, pp. 411–414, 2002.
- [97] I. Bardi, R. Remski, D. Perry, and Z. Cendes, "Plane wave scattering from frequency-selective surfaces by the finite-element method," *IEEE Trans. Magn.*, vol. 38, no. 2, pp. 641–644, 2002.

- [98] P. Harms, R. Mittra, and W. Ko, "Implementation of the periodic boundary condition in the finite-difference time-domain algorithm for FSS structures," *IEEE Trans. Antennas Propag.*, vol. 42, no. 9, pp. 1317–1324, 1994.
- [99] M. Arrebola, L. Haro, and J. Encinar, "Analysis of dual-reflector antennas with a reflectarray as subreflector," *IEEE Antennas Propag. Mag.*, vol. 50, no. 6, pp. 39–51, 2008.
- [100] W. Hu, M. Arrebola, R. Cahill, J. A. Encinar, V. Fusco, H. S. Gamble, Y. Alvarez, and F. Las-Heras, "94 ghz dual-reflector antenna with reflectarray subreflector," *IEEE Trans. Antennas Propag.*, vol. 57, no. 10, pp. 3043–3050, 2009.
- [101] M. A. Milon, D. Cadoret, R. Gillard, and H. Legay, "Surrounded-element approach for the simulation of reflectarray radiating cells," *IET Microw. Antennas Propag.*, vol. 1, no. 2, pp. 289–293, 2007.
- [102] M. A. Milon, R. Gillard, D. Cadoret, and H. Legay, "Comparison between the "infinite array" approach and the "surrounded-element" approach for the simulation of reflectarray antennas," in *Proc. IEEE AP-S Int. Symp.*, Albuquerque, New Mexico, USA, 2006.
- [103] H. Li, B.-Z. Wang, L. Guo, W. Shao, and P. Du, "A far field pattern analysis technique for reflectarrays including mutual coupling between elements," *J. Electromag. Waves Appl.*, vol. 23, pp. 87–95, 2009.
- [104] M. Arrebola, Y. Alvarez, J. A. Encinar, and F. Las-Heras, "Accurate analysis of printed reflectarrays considering the near field of the primary feed," *IET Microw. Antennas Propag.*, vol. 3, no. 2, pp. 187–194, 2009.
- [105] S. M. Rao, D. R. Wilton, and A. W. Glisson, "Electromagnetic scattering by surfaces of arbitrary shape," *IEEE Trans. Antennas Propag.*, vol. 30, no. 3, pp. 409–418, 1982.
- [106] A. W. Glisson and D. R. Wilton, "Simple and efficient numerical methods for problems of electromagnetic radiation and scattering from surfaces," *IEEE Trans. Antennas Propag.*, vol. 28, no. 5, pp. 593–603, 1980.
- [107] M. Bozzi and L. Perregrini, "Analysis of multilayered printed frequency selective surfaces by the mom/bi-rme method," *IEEE Trans. Antennas Propag.*, vol. 51, no. 10, pp. 2830–2836, 2003.
- [108] S. R. Rengarajan, "Choice of basis functions for accurate characterization of infinite array of microstrip reflectarray elements," *IEEE Antennas Wireless Propag. Lett.*, vol. 4, pp. 47–50, 2005.
- [109] F. De Vita, P. De Vita, A. Di Maria, and A. Freni, "An efficient technique for the analysis of reflectarrays," *Automatika*, vol. 49, no. 1-2, pp. 21–25, 2008.
- [110] M. Bercigli, M. Bandinelli, P. De Vita, A. Freni, and G. Vecchi, "Acceleration methods for full-wave modelling of reflectarrays," in *Proc. EuCap*, Edinburgh, UK, 2007.

- [111] J. Rius, J. Parron, A. Heldring, J. Tamayo, and E. Ubeda, "Fast iterative solution of integral equations with method of moments and matrix decomposition algorithm – singular value decomposition," *IEEE Trans. Antennas Propag.*, vol. 56, no. 8, pp. 2314 – 2324, 2008.
- [112] F. Catedra, I. Gonzalez, A. Tayebi, and J. Gomez, "Full wave analysis of reflectarrays antennas," in *Proc. 30th ESA Antenna Workshop*, Noordwijk, The Netherlands, 2008.
- [113] S. R. Rengarajan, "Reciprocity considerations in microstrip reflectarrays," *IEEE Antennas Wireless Propag. Lett.*, vol. 8, pp. 1206–1209, 2009.
- [114] D. Cadoret, A. Laisne, R. Gillard, and H. Legay, "A new reflectarray cell using microstrip patches loaded with slots," *Microwave Opt. Technol. Lett.*, vol. 44, no. 3, pp. 270–272, 2005.
- [115] H. Rajagopalan and Y. Rahmat-Samii, "Dielectric and conductor loss quantification for microstrip reflectarray: Simulations and measurements," *IEEE Trans. Antennas Propag.*, vol. 56, no. 4, pp. 1192–1196, 2008.
- [116] M. Albooyeh, N. Komjani, and M. S. Mahani, "A circularly polarized element for reflectarray antennas," *IEEE Antennas Wireless Propag. Lett.*, vol. 8, pp. 319–322, 2009.
- [117] S. W. Oh, C. H. Ahn, and K. Chang, "Reflectarray element using variable ring with slot on ground plane," *Electron. Lett.*, vol. 45, no. 24, pp. 1206–1207, 2009.
- [118] H. Salti, R. Gillard, R. Loison, and L. Le Coq, "A reflectarray antenna based on multiscale phase-shifting cell concept," *IEEE Antennas Wireless Propag. Lett.*, vol. 8, pp. 363–366, 2009.
- [119] H. Hasani, M. Kamyab, and A. Mirkamali, "Low cross-polarization reflectarray antenna," *IEEE Trans. Antennas Propag.*, vol. 59, no. 5, pp. 1752–1756, 2011.
- [120] H. Legay, E. Girard, G. Caille, Y. Cailloce, N. Raveu, H. Aubert, P. Pons, R. Gillard, J. Pollizzi, M. V. d. Voorst, J. Perruissey, A. Skrivervik, J. Lenkkeri, M. Lahti, U. Oestermann, and E. Jung, "MEMS controlled reflectarray elements," in *Proc. 29th ESA Antenna Workshop*, Noordwijk, The Netherlands, 2007.
- [121] E. Carrasco, M. Barba, and J. A. Encinar, "Design and validation of gathered elements for steerable-beam reflectarrays based on patches aperture-coupled to delay lines," *IEEE Trans. Antennas Propag.*, vol. 59, no. 5, pp. 1756–1761, 2011.
- [122] W. Hu, R. Cahill, J. A. Encinar, R. Dickie, H. Gamble, V. Fusco, and N. Grant, "Design and measurement of reconfigurable millimeter wave reflectarray cells with nematic liquid crystal," *IEEE Trans. Antennas Propag.*, vol. 56, no. 10, pp. 3112–3117, 2008.
- [123] M. Hajian, A. Coccia, and L. P. Ligthart, "Design, analysis and measurements of reflected phased array microstrip antennas at ka-band using passive stubs," in *Proc. EuCAP*, 2006.



- [124] W. C. Chew and Q. Liu, "Resonance frequency of a rectangular microstrip patch," *IEEE Trans. Antennas Propag.*, vol. 36, no. 8, pp. 1045–1056, 1988.
- [125] E. Jørgensen, J. Volakis, P. Meincke, and O. Breinbjerg, "Higher order hierarchical Legendre basis functions for electromagnetic modeling," *IEEE Trans. Antennas Propag.*, vol. 52, no. 11, pp. 2985 – 2995, 2004.
- [126] R. F. Harrington, *Time-Harmonic Electromagnetic Fields*. McGraw-Hill, Inc., 1961.
- [127] O. M. Bucci, A. Capozzoli, G. D'Elia, and S. Musto, "A new approach to the power pattern synthesis of reflectarrays," in *Proc. URSI EMTS Symp.*, Pisa, Italy, 2004, pp. 1053–1055.
- [128] A. Capozzoli, C. Curcio, G. D'Elia, and A. Liseno, "Fast phase-only synthesis of conformal reflectarrays," *IET Microw. Antennas Propag.*, vol. 4, no. 12, pp. 1989–2000, 2010.
- [129] H. Legay, D. Bresciani, R. Chiniard, E. Girard, G. Caille, E. Labiole, and R. Gillard, "Demonstration model of a reflectarray for telecommunication antenna, Final report," Thales Alenia Space, Toulouse, France, Tech. Rep., March 2012.
- [130] L. Marnat, R. Loison, R. Gillard, D. Bresciani, and H. Legay, "Optimization strategies for dual polarized reflectarrays," in *Proc. 30th ESA Antenna Workshop*, Noordwijk, The Netherlands, 2008.
- [131] —, "Accurate synthesis of a dual linearly polarized reflectarray," in *Proc. EuCAP*, Berlin, Germany, 2009.
- [132] —, "Comparison of synthesis strategies for a dual-polarized reflectarray," *Int. J. Antennas Propag.*, vol. 2012, 2012, Article ID 708429.
- [133] O. M. Bucci, A. Capozzoli, G. D'Elia, P. Maietta, and S. Russo, "An advanced reflectarray design technique," in *Proc. 28th ESA Antenna Workshop*, Noordwijk, The Netherlands, 2005.
- [134] A. Capozzoli, C. Curcio, A. Liseno, M. Migliorelli, and G. Toso, "Power pattern synthesis of advanced flat aperiodic reflectarrays," in *Proc. 33th ESA Antenna Workshop*, Noordwijk, The Netherlands, 2011.
- [135] J. A. Encinar and M. Arrebola, "Reduction of cross-polarization in contoured beam reflectarrays using a three-layer configuration," in *Proc. IEEE AP-S Int. Symp.*, Honolulu, Hawaii, USA, 2007.
- [136] C. Tienda, J. A. Encinar, M. Barba, and M. Arrebola, "Reduction of cross-polarization in offset reflectarrays using two layers of varying-sized patches," *Microwave Opt. Technol. Lett.*, vol. 54, no. 11, pp. 2449–2454, 2012.
- [137] K. Michalski and D. Zheng, "Electromagnetic scattering and radiation by surfaces of arbitrary shape in layered media. Part i: Theory," *IEEE Trans. Antennas Propag.*, vol. 38, no. 3, pp. 335–344, 1990.

- [138] K. Michalski and J. R. Mosig, "Multilayered media Green's functions in integral equation formulations," *IEEE Trans. Antennas Propag.*, vol. 45, no. 3, pp. 508 – 519, 1997.
- [139] K. Michalski and D. Zheng, "Analysis of microstrip resonators of arbitrary shape," *IEEE Trans. Microwave Theory Tech.*, vol. 40, no. 1, pp. 112–119, 1992.
- [140] A. Capozzoli, C. Curcio, A. Lisenio, M. Migliorelli, and G. Toso, "Aperiodic conformal reflectarrays," in *Proc. IEEE AP-S Int. Symp.*, Spokane, Washington, USA, 2011.
- [141] T. G. Smith, N. V. Larsen, U. V. Gothelf, O. S. Kim, and O. Breinbjerg, "20/30 GHz dual-band circularly polarized reflectarray antenna based on the concentric split loop element," in *Proc. 34th ESA Antenna Workshop*, Noordwijk, The Netherlands, 2012.
- [142] M. Abramowitz and I. A. Stegun, Eds., *Handbook of Mathematical Functions*, 9th ed. Dover Publications, New York, 1970.
- [143] E. Jørgensen, O. S. Kim, P. Meincke, and O. Breinbjerg, "Higher order hierarchical discretization scheme for surface integral equations for layered media," *IEEE Trans. Geosci. Remote Sensing*, vol. 42, no. 4, pp. 764–772, 2004.
- [144] R. Jedlicka, M. Poe, and K. Carver, "Measured mutual coupling between microstrip antennas," *IEEE Trans. Antennas Propag.*, vol. 29, no. 1, pp. 147–149, 1981.
- [145] M. A. Khayat, J. T. Williams, D. R. Jackson, and S. A. Long, "Mutual coupling between reduced surface-wave microstrip antennas," *IEEE Trans. Antennas Propag.*, vol. 48, no. 10, pp. 1581–1593, 2000.
- [146] Y. Chow, J. Yang, D. Fang, and G. Howard, "A closed-form spatial Green's function for the thick microstrip substrate," *IEEE Trans. Microwave Theory Tech.*, vol. 39, no. 3, pp. 588 – 592, 1991.
- [147] G. Dural and M. Aksun, "Closed-form Green's functions for general sources and stratified media," *IEEE Trans. Microwave Theory Tech.*, vol. 43, no. 7, pp. 1545–1552, 1995.
- [148] R. R. Boix, M. J. Freire, and F. Medina, "New method for the efficient summation of double infinite series arising from the spectral domain analysis of frequency selective surfaces," *IEEE Trans. Antennas Propag.*, vol. 52, no. 4, pp. 1080–1094, 2004.
- [149] G. Cano, F. Medina, and M. Horno, "On the efficient implementation of SDA for boxed strip-like and slot-like structures," *IEEE Trans. Microwave Theory Tech.*, vol. 46, no. 11, pp. 1801–1806, 1998.
- [150] S.-O. Park, C. A. Balanis, and C. R. Birtcher, "Analytical evaluation of the asymptotic impedance matrix of a grounded dielectric slab with roof-top functions," *IEEE Trans. Antennas Propag.*, vol. 46, no. 2, pp. 251–259, 1998.

- [151] J. R. Mosig and F. E. Gardiol, "A dynamical radiation model for microstrip structures," in *Advances in Electronics and Electron Physics*, P. W. Hawkes, Ed. New York: Academic, 1982, vol. 59, pp. 139–237.
- [152] W. C. Chew, *Waves and Fields in Inhomogeneous Media*. IEEE Press, 1995.
- [153] J. J. Yang, Y. L. Chow, and D. G. Fang, "Discrete complex images of a three-dimensional dipole above and within a lossy ground," *Proc. Inst. Elect. Eng. H*, vol. 138, no. 4, pp. 319–326, 1991.
- [154] M. Aksun and R. Mittra, "Derivation of closed-form Green's functions for a general microstrip geometry," *IEEE Trans. Microwave Theory Tech.*, vol. 40, no. 11, pp. 2055–2062, 1992.
- [155] M. Aksun, "A robust approach for the derivation of closed-form Green's functions," *IEEE Trans. Microwave Theory Tech.*, vol. 44, no. 5, pp. 651–658, 1996.
- [156] Y. Hua and T. Sarkar, "Generalized pencil-of-function method for extracting poles of an EM system from its transient response," *IEEE Trans. Antennas Propag.*, vol. 37, no. 2, pp. 229–234, 1989.
- [157] A. Erteza and B. Park, "Nonuniqueness of resolution of hertz vector in presence of a boundary, and the horizontal dipole problem," *IEEE Trans. Antennas Propag.*, vol. 17, no. 3, pp. 376–378, 1969.